UNIVERSITY OF SOUTHERN QUEENSLAND

Fibre optic pressure transducers for disturbance measurements in transient aerodynamic research facilities

A dissertation submitted by

S. Ahmad Sharifian, M Eng

For the award of

Doctor of Philosophy

2003

CERTIFICATION OF DISSERTATION

I certify that the ideas, experimental work, results, analyses, software and conclusions in this dissertation are entirely my own effort, except where otherwise acknowledged. I also certify that the work is original and has not been previously submitted for any award, except where otherwise acknowledged.

Ahmad Sharifian 28.3.2003

Signature of Candidate Date

ENDORSEMENT

_____ _____

Signature of Principal Supervisor Date

_____ _____

Signature of Associate Supervisor Date

Abstract

Experiments in the study of transient aerodynamics typically require pressure measurements with a high spatial and temporal resolution. Existing commercial pressure transducers are expensive and they provide a spatial resolution only on the order of millimetres. The full bandwidth of commercial devices (which extends to around 200 kHz) can only be utilised by exposing the transducer to the flow environment with very little thermal or mechanical protection. If insufficient protection is provided, the expensive commercial devices are likely to be damaged.

Inexpensive pressure sensors based on extrinsic Fabry-Perot fibre optic interferometry are capable of measurement with a high spatial and temporal resolution. Thermal protection or isolation for these sensors is still required, but they can be exposed directly to the flow if the sensors are disposable (low cost). Excessive thermal or mechanical protection is not required for these sensors because the damaging heat transfer and particle impacts that may occur in transient aerodynamic facilities generally occur after the useful test flow.

In this dissertation, a variety of construction techniques for diaphragm-based Fabry-Perot fibre optic pressure sensors were investigated and the advantages and disadvantages of all techniques are compared. The results indicate that using a zirconia ferrule as the substrate, a liquid adhesive as the bonding layer, and a polished copper foil as the diaphragm provide the best results. It is demonstrated that a spatial resolution on the order of 0.1 mm and a bandwidth to more than 100 kHz can be achieved with such constructions.

A variety of problems such as hysteresis, response irregularity, low visibility and sensor non-repeatability were observed. By using a thinner bonding layer, a larger bonding area, longer cavity length, increased calibration period, and applying load cycling to the diaphragm, the hysteresis was minimized. Sensor response irregularity was also minimized using a polished diaphragm. Visibility increased to about 90% using active control of the cavity length during the construction process. Non-repeatability was found to be a consequence of adhesive viscoelasticity and this effect was minimized using a thin layer of adhesive to bond the diaphragm to the substrate. Due to the effects of adhesive viscoelasticity, the pressure sensors indicate an error of up to 10% of mean value for the reflected shock pressure. This error could

not be further reduced in the current sensors configuration. Some new configurations are proposed to decrease the effect of sensor non-repeatability.

The effect of pretensioning the diaphragm was investigated analytically but the results do not indicate any considerable advantage for the levels of pretension likely to be achieved in practice. However, the results do indicate that pretension effects caused by an environmental temperature change can damage the sensor during storage. The effect of the initial diaphragm deflection on the sensor performance and temperature sensitivity was modelled and the results show that an initial diaphragm deflection can improve the sensor performance.

The effect of the thermal isolation layer on the sensor performance was also investigated and the results show that for a shock tube diaphragm bursting pressure ratio up to 5.7, heat transfer does not contribute to sensor errors for the first millisecond after shock reflection. However, it was found that the use of a thin layer of low viscosity grease can protect the sensor for about 20 ms while only decreasing its natural frequency by typically 17%. The grease layer was also found to decrease the settling time of a low damping ratio sensor by 40%. The sensor was successfully employed to identify an acoustic disturbance in a shock tube.

Acknowledgments

The work presented in this thesis would not have been possible without help of the following people and friends.

I would like to give a very special thanks to my Supervisor, Dr. David Buttsworth for his guidance and willingness to support me in a variety of different ways throughout the duration of this project. His encouragement, assistance during experiments, key advice, enormous knowledge and enthusiasm, and his comprehensive reading and correcting of my draft thesis will never be forgotten. I will always be indebted to him for the independence he allowed me and for bearing with my poor English expression, especially in the early stages of my work.

I wish to thank all of my teachers and friends during previous studies. Without their help, I would never have obtained the basic knowledge necessary to undertake this thesis.

I wish to give a special thanks to my deceased mum, who passed away during this work. I will never forget her and her encouragement to study during my childhood and school time. Her love and support was unwavering. In fact, she ordered other family members not to tell me about her deteriorating health condition in her final days of life because she did not want to interrupt my research. That is only one of many examples of her respect to my future.

I also wish to acknowledge the support of the Applied Optics and Photonics Group at Heriot-Watt University. In particular, I would like to thank Dr. W.N. MacPherson, Dr J.S. Barton, and Prof. J.D.C Jones for providing copies of papers and a dissertation, providing some key materials in an emergency, and answering some important questions.

I must of course thank other members of the Faculty of Engineering and Surveying, in particular Dr. Nigel Hancock, my Co-Supervisor and Bob Fulcher, Head of the Mechanical Discipline for their invaluable assistance throughout my years at the University of Southern Queensland (USQ). I must also thank Chris Snook for his help in using engineering software and Dr. Harry Ku for his advice in the material laboratories.

I am grateful for the hard work and practical advice obtained from the staff within the mechanical, electrical, and physics workshops/laboratories. Without their help, none of this research would have been possible. Special thanks must go to John

Benecke and Adrian Blokland in the mechanical laboratories. Mohan Trada was also of great assistance – he not only provided all the necessary instruments and offered assistance whenever it was needed, but he also made many excellent recommendations to improve the experiments. In electronics laboratories, Terry Byrne and Dean Beliveau always gave me excellent advice and Don Gelhaar and Chris Lock supplied all the required parts in the minimum possible time. The sense of humour of Chris Galligan, Brian Aston, and Stephan Brennan never prevented them from doing quality work in a timely manner. Graham Holmes is thanked for his assistance in the physics laboratory.

I would like to give a special thanks to Michael Mclachan, Operation Manager for his patience and advice, Jim Scott for his concern for safety issues during the experiments and, Lez Scott who purchased all the necessary items in the minimum time.

I would also like to thank Dick Young and Tanya Stockler for their great job in organising the financial support associated with my seminars, conferences and purchasing.

I also acknowledge Ms Christine Bartllet for organising all necessary scholarship related support during my work.

I wish to thank Dr. Ali Aysen. It is hard to imagine how I could complete this work without his advice, encouragement and good sense of humour.

I would also like to thank David Orton and David Boland for provision of computer facilities. Furthermore, I wish to acknowledge Dr. Harry Harris and Professor ThanhTran-Cong, who were the Associate Deans of Research during this work. Their encouragement and positive views were a great help throughout this work.

I am also grateful beyond measure to Sonia Hilo for her proof reading, her patience and her support. She spent much of her free time during evenings and weekends, particularly in the last 6 months assisting me and I will never forget her help.

Finally, I would like to thank the Research and Higher Degree Committee which awarded me an International Postgraduate Research Scholarship (IPRS) and provided me with the opportunity to do this work.

Contents

List of Figures

List of Tables

Chapter 1: Introduction

1.1 Transient aerodynamic facilities

Aerodynamic facilities that simulate high Mach number flows can be categorised as short duration (transient) facilities and continuous or near continuous facilities. Achieving a high Mach number is less important than achieving the correct flow enthalpy when attempting to simulate the flow around re-entry bodies. This is because most of the critical aerodynamic uncertainties are associated with the stagnation region, and the high temperatures achieved in the real stagnation region have a profound effect on the gas dynamics (Anderson 1989). Continuous facilities cannot provide high enthalpy flows due to design problems associated with heat transfer especially in nozzle and reservoir regions. Transient aerodynamic facilities are very attractive due to their ability to provide high enthalpy flows (Schultz & Jones 1973).

The maximum achievable stagnation temperature or enthalpy is an inverse function of flow duration. For example, expansion tubes can provide stagnation enthalpies on the order of 100 MJ/kg but only for tens of microseconds (Morgan 1997). The useful flow duration in shock tunnels is longer (on the order of milliseconds) but the maximum stagnation enthalpy decreases to around 20 MJ/kg. Hotshot facilities that produce useful flows for around 100 ms have a maximum stagnation enthalpy of around 4 MJ/kg. Blowdown tunnels are near continuous facilities that can provide long flow durations (measured in tens of minutes) but the maximum stagnation enthalpy is generally somewhat less than 4 MJ/kg (Schultz & Jones 1973).

Pressure is a fundamental parameter that must be quantified in most aerodynamic applications. In transient facilities where the flow duration can be as short as tens of microseconds (eg expansion tubes), a fast response device is necessary in order to characterise the mean flow conditions. Disturbances that typically arise in wind tunnels are stronger than those that occur in actual atmospheric flight environments and it is recognised that these disturbances can have a significant influence on certain unsteady and time-averaged flow properties (Beckwith 1975). Thus, for proper characterisation of flow conditions produced by some transient facilities, pressure measurements with a response time in order of 1 μs are required in order to correctly

identify the mean flow and any possible perturbations (such as those discussed by Jacobs 1994).

1.2 Limitations of commercial pressure transducers

Commercial high bandwidth pressure transducers such as piezoelectric and piezoresistive transducers can be used in transient aerodynamic facilities. For example, response times on the order of microseconds often quoted for the commercial piezoelectric pressure transducers (see Section 2.3.5). However, such transducers can be expensive (around $1500 Australian) and this makes it important to avoid directly exposing them to the flows produced by transient facilities because thermal or mechanical damage is likely to be caused by the high temperature flows which sometimes contain particles.

A common method to avoid particle impacts is to protect the transducers in a recessed cavity. For static pressure measurements, a small cavity transfers the static pressure directly to the transducer diaphragm. The recessed cavity increases the measurement system rise time depending on the actual geometry, but for a typical configuration, the net rise time is typically between about 10 and 15 μs (Doolan 1997). In Pitot pressure configurations, additional mechanical protection also is required to protect transducers from high speed diaphragm fragments (which generally arrive after the useful test flow). In this Pitot probe arrangement, the recessed cavity faces directly upstream and a baffle is placed within the cavity to act as a filter for the fragments and avoid direct particle impacts on the diaphragm. This system appears to increases the pressure measurement system rise time to about 4 μs (Doolan 1997). Hence, pressure measurements made using a commercial sensor in a recessed cavity are unlikely to have a sufficiently high bandwidth for a complete characterisation of transient wind tunnel flows.

Thermal protection is also used for commercial transducers and this often takes the form of a relatively thin layer of RTV (Room Temperature Vulcanised rubber). This thermal protection layer may further alter the system response, depending on the relative diaphragm stiffness and mass.

1.3 Objectives

The aim of this research is to develop a pressure sensor that can be employed in transient flows and is capable of providing accurate fast response measurements in such environments.

To make a useful addition to the array of pressure measurement devices that are already available for use in transient aerodynamic facilities, the sensors should:

1) have a high spatial resolution (the size should be less than 1 mm);

2) have a natural frequency greater than 500 kHz;

3) have a designable pressure range with an accuracy of 2% of mean pressure; and

4) be of low-cost, such that they can be regarded as sacrificial.

1.4 Approach

This work builds on that performed at Heriot-Watt University by MacPherson (1999). The sensor developed in that work consisted of a copper foil bonded to a zirconia ferrule substrate. The relatively expensive interrogation system was located outside the test flow environment, and the components for the sensor itself would have cost in the order of $20 Australian. Rise times of about 1 μs appear achievable with these devices and their spatial resolution is far better than commercial pressure transducers (see Fig. 6.1). Since the original work by MacPherson, further sensor development has occurred at Heriot-Watt University resulting in the production of a silicon micromachined sensor (see Section 3.6.3.2) that shows lower temperature sensitivity and superior performance (Gander et al. 2002).

In contrast, the work described in this thesis has persisted with the ‘glued diaphragm’ approach and attempted to optimise it since a low cost and hence sacrificial pressure sensor arrangement is being sought for transient aerodynamic facilities such as shock tunnels and expansion tubes. If a suitable (inexpensive) pressure sensor can be developed, thermal isolation will probably still be required in order to minimize the thermal effects which may be interpreted as a pressure response during the useful test flow. In this case, the thickness of the thermal isolation layer can be minimized to protect the sensor only during the useful test flow (usually around a few ms or less) as this will maintain a high bandwidth sensor response. Heat that penetrates to the

diaphragm after this time is not a particular issue provided the pressure sensor is inexpensive. Similarly, mechanical/pneumatic protection which can potentially destroy the bandwidth of the measurement system will not be required if the sensor is sacrificial.

1.5 Overview of remaining chapters

Some basic pressure measurement devices including those currently used in transient aerodynamic facilities are discussed in Chapter 2. There is an emphasis on piezoelectric pressure transducers, piezoresistive pressure transducers, bar gauges, and pressure sensitive paints as these methods have a demonstrated potential for pressure measurements in transient aerodynamic facilities. Some of the different techniques for dynamic calibration of pressure transducers are also discussed in Chapter 2.

Fibre optic pressure sensors are described separately in Chapter 3. These sensors are divided into intensity modulating, polarization, refractive index, evanescent, and interferometric sensors. Due to the importance of interferometric pressure sensors, some common interferometers such as Mach-Zehnder, Michelson and Fabry-Perot are discussed with a focus on the Fabry-Perot interferometer.

Chapter 4 reviews the principal components that are used in the interferometer system and describes the system operation including some key equations. This chapter also introduces some sources of nonlinearity in fibre optic systems which can limit their application. Justification for the selection of the particular fibre optic interrogation system is presented at the end of the chapter.

Chapter 5 reviews important mechanical and optical properties in design of a diaphragm for fibre optic pressure sensors and introduces important equations that can be used in design. Effects of pretension on the diaphragm strength and natural frequency are also discussed and some sample calculations are presented.

A variety of techniques for the construction of fibre optic pressure sensors are presented in Chapter 6. The effects of diaphragm roughness on the sensor performance are also measured. Temperature sensitivity of the fibre optic pressure sensor is calculated and the results are compared with the results from experiments.

The shock tube, different components used for sensor embedding, and pressure sensitivity of sensors during quasi-static calibration are also presented in Chapter 6.

The fibre optic pressure sensors constructed according to the methods of Chapter 6 show a considerable hysteresis. Chapter 7 discusses and evaluates the potential sources of hysteresis. Chapter 7 also demonstrates some new techniques to minimize the sensor hysteresis.

Chapter 8 describes the performance of fibre optic pressure sensor during shock tube experiments. The intention was to use a shielded piezoelectric pressure transducer as a reference to evaluate the fibre optic pressure sensor response. However, as the shock tube diaphragm rupture pressure was not controlled, it was necessary to first calibrate a computational fluid dynamics (CFD) code with data from the piezoelectric transducer and then use the validated numerical simulations as the reference instead. The shock response from a sample fibre optic pressure sensor is presented and the possible sources of errors are identified. The effect of two different kinds of thermal isolation layers on the sensor response and natural frequency were identified. Results from a fibre optic pressure sensor mounted in the end wall of the shock tube are then presented as a demonstration of the capacity of the technique for the identification of acoustic disturbances in the shock tube.

Chapter 9 discusses the key conclusions that have arisen from this project.

Chapter 2: Pressure transducers for the study of transient aerodynamics

2.1 Introduction

Pressure is a key parameter in many flow systems. Many instruments are already available to measure pressure in different environments. This chapter presents a selective review of these instruments and discusses their relevance to transient aerodynamic facilities. Due to the large variety of optical pressure transducers and their particular relevance to the current research, discussion of these devices is delayed until Chapter 3.

A pressure transducer is a device that converts an applied pressure into an electrical or mechanical signal (for example, see Dally, Rifley & McConnell 1993; Figliola & Beasley 2000). Two steps are involved in this process: 1) sensing the pressure; and 2) converting it into a more convenient form to read or record the data (Finkelstein & Gratton 1994; Figliola & Beasley 2000). The sensing step is usually associated with the elastic deformation of a flexible member (Finkelstein & Gratton 1994) such as a Bourdon tube, bellows or a diaphragms (TPC training systems 1979) and these devices are discussed in Section 2.2. There are many different methods to convert the deformation to a readable signal including the mechanical rotation of a pointer, and the change of an electrical parameter such as resistance or capacitance, or the change of a magnetic characteristic such as inductance or reluctance (TPC training system 1979; Doebellin 1990). Section 2.3 discusses these methods of conversion. Due to the prevalence of piezoelectric and piezoresistive transducers in transient aerodynamic facilities, these are discussed separately within Section 2.3. Pressure sensitive paints (PSP) have recently been employed in short duration flows (about 40 ms) and they have shown a relatively short response time (Asai 2001). As PSPs rely on different operating principles to the other transducers, they are discussed separately in Section 2.4. Bar gauges are a special type of pressure transducer especially designed for transient aerodynamic facilities and these are discussed in Section 2.5.

The characterisation of transducer performance is an important part of new transducer development and standard methods are discussed in Section 2.6. Deadweight testers are very basic instruments normally used to calibrate other devices. Some of the available techniques to measure the natural frequency, response time, and accuracy of measured pressures are also discussed in Section 2.6. The last section in this chapter (Section 2.7) compares the pressure transducers presented in this chapter and discusses the potential for their application in the measurement of disturbance in transient aerodynamic facilities.

2.2 Sensing elements

A wide variety of sensing elements such as Bourdon tubes, diaphragms, and bellows are used for pressure measurement in industry (for example, see Gopel, Hesse & Zemel 1989; Doebellin 1990). Their deflection may directly actuate a pointer through suitable linkages, or it may be converted to an electrical signal (Doebellin 1990).

2.2.1 Bourdon tubes and bellows

Bellows and especially Bourdon tubes are the most common pressure sensitive elements (TPC training systems 1979). Their various configurations are presented in Fig. 2.1. They all rely on elastic deformation under pressure. Bourdon tubes are made with metal and in different styles include the C, spiral, helix, and twisted shapes (TPC training systems 1979). Bellows generally consist of a cylinder with flexible sides and rigid ends which can deflect under pressure. Bellows can be used as a sensing part of some transducers such as potentiometers and differential transformers (Doebellin 1990). The metal which is used for the tubes and bellows would normally be corrosion resistant and support repeated loading without any fatigue, hysteresis, and creep (TPC training systems 1979). Due to their low natural frequency, they cannot be used for fast response measurement and would normally be restricted to the measurement of pressure variations at less than 1 Hz.

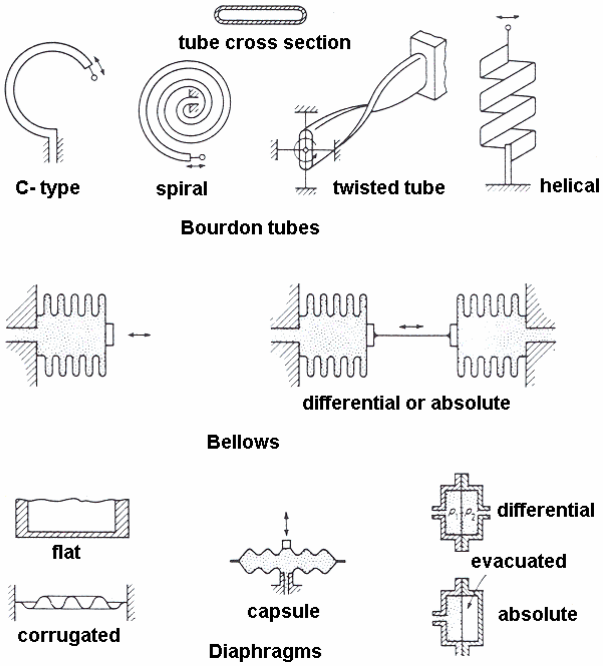

Figure 2.1 Elastic pressure sensing elements (adapted from Doebellin 1990).

2.2.2 Diaphragms

The simplest geometry for the elastic sensing element is a diaphragm. Diaphragms can be configured in single or capsule arrangements (TPC training system 1979; Dally, Rifley & McConnell 1993), as shown in Fig. 2.1. Diaphragm deflection is related to the difference between the pressures applied on either side, so they can show absolute or relative pressure depending on the reference pressure. In the case of a capsule diaphragm, two diaphragms are welded together and the measurand pressure is applied to the inside of the capsule. Capsule diaphragms have a higher pressure sensitivity than a single diaphragm of the same size but a longer response time. Further increase in pressure sensitivity can be achieved by using an array of capsules (Dally, Rifley & McConnell 1993).

Diaphragms can be used for pressures up to 200 MPa; for higher pressure, cylinders are often used (Dally, Rifley & McConnell 1993). Typical industrial diaphragms have a natural frequency of up to 50 kHz; they can be used for dynamic pressure measurements with a response times less than 0.1 ms (Dally, Rifley & McConnell 1993).

2.3 Transducers

2.3.1 Variable resistance transducers

The two most commonly used forms of variable resistance transducer are the potentiometer and strain gauge. Potentiometers are the simplest and cheapest transducers (Carstens 1993), and typical arrangements are illustrated in Fig. 2.2. They include a linear or angular wiper connected to a sensing element. The movement of the wiper arm, which is connected to an electrical resistance, changes the output voltage and thereby indicates the pressure applied on the sensing element. The response time of all the various potentiometers is limited by the high inertia of the wiper assemblies. They are used only for static or quasi-static measurements (Dally, Rifley & McConnell 1993) (bandwidths up to 2 kHz (M-System Technology n.d.)).

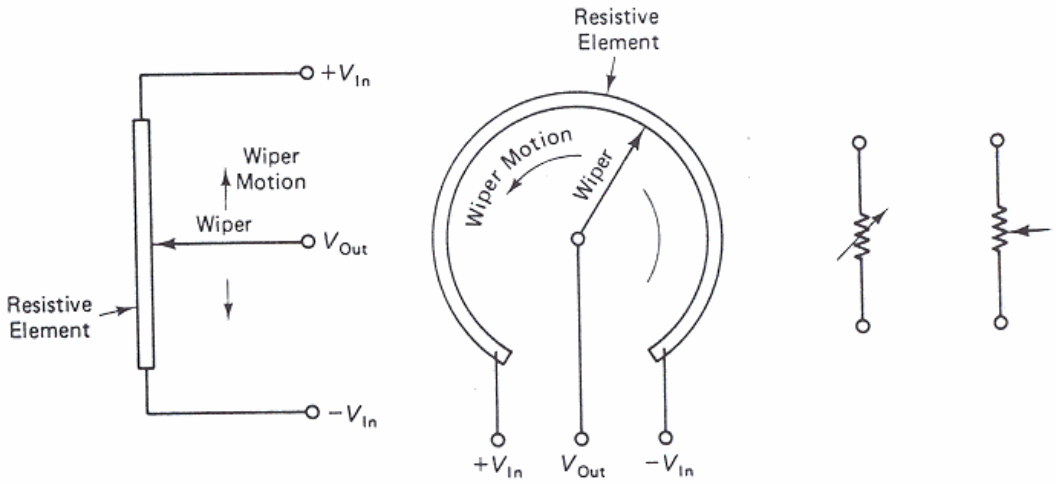

Figure 2.2 Potentiometer (reproduced from Carstens 1993).

The strain sensitivity of metals was first observed in copper and iron by Lord Kelvin in 1856 (Dally, Rifley & McConnell 1993). The strain gauge is a device that changes electrical resistance due to strain (TPC training systems 1979). Strain gauges can be directly bonded to a flat or corrugated metal diaphragm (Doebellin 1990), and a typical configuration is shown in Fig. 2.3. An applied pressure changes the diaphragm strain and thus strain gauge resistance which is usually detected in the form of a voltage from a suitable Wheatstone bridge arrangement.

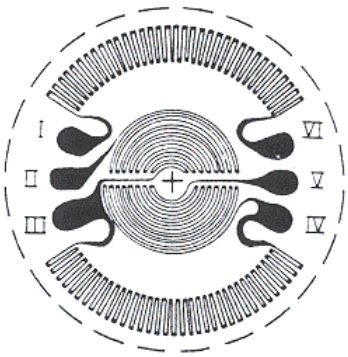

Figure 2.3 Strain gauges used in a pressure transducer (adapted from Doebellin 1990).

There are three kinds of strain gauges: metal wire, metal foil, and semiconductor (TPC training systems 1979). Metal wire and foil gauges show a strong temperature sensitivity. Their change of resistance is generally low in comparison with their total resistance; however, these problems can largely be solved using a suitable electrical bridge circuit (TPC training systems 1979).

The response time of strain gauge pressure transducers is normally limited by the response time of the diaphragm and electrical circuits; ideally they can be used in short response time applications. However, the area necessary for strain gauge bonding does not permit the use of a very small (less than a few mm (Gopel, Hesse & Zemel 1989)) diaphragm. Piezoresistive transducers (discussed in Section 2.3.4) overcome these difficulties by employing semiconductor strain gauges that are an integral part of the diaphragm.

2.3.2 Magnetic transducers

Inductance characterises the ability of a coil to oppose any change in the current passing through it. Reluctance characterises the capacity to induce a signal in a second coil (Carstens 1993). Inductance and reluctance vary when an iron core inside a coil or between two coils move. The iron core can be coupled to a sensing element and therefore a change of measurand (pressure), which moves the iron core, can be detected when a current is passed through the primary coil.

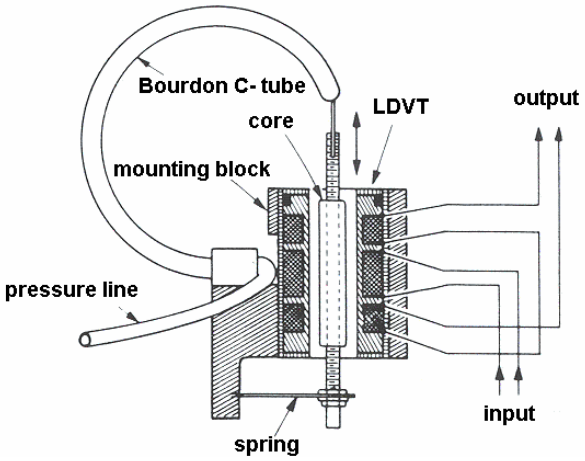

Figure 2.4 Pressure transducer that uses a Bourdon tube as sensing element and LDVT (adapted from Dally, Rifley & McConnell 1993).

The most popular magnetic transducer is a linear variable differential transformer (LVDT) (Dally, Rifley & McConnell 1993). Due to the lack of contact between core and coils, the working life of an LVDT is long and friction and hysteresis are eliminated. The small core mass and lack of friction gives them a capacity for dynamic measurements up to 500 Hz (Dally, Rifley & McConnell 1993), although a special kind of inductive transducer has demonstrated a frequency range up to 15 kHz (Pownall 1993). Figure 2.4 shows a LDVT coupled to a Bourdon gauge as the sensing element. This particular system has a natural frequency of up to 10 Hz.

2.3.3 Capacitive transducers

The capacitance between two plates depends on the distance between them and this distance can be altered by a sensing element. In this kind of transducer, one plate of the capacitor can be employed as a diaphragm (Gopel, Hesse & Zemel 1989). Capacitive transducers can have extreme ruggedness, high accuracy, long life, and can work under harsh conditions (Gopel, Hesse & Zemel 1989) such as temperatures up to 1100^{o}C (Carstens 1993). Capacitance sensors constructed using silicon technology can be very small (Pownall 1993). Disadvantages of capacitance transducers include their temperature sensitivity (Figliola & Beasley 2000), small output signals, and the influence of cable capacitance (Pownall 1993). Furthermore, increases in the frequency of the pressure fluctuation reduce their sensitivity,

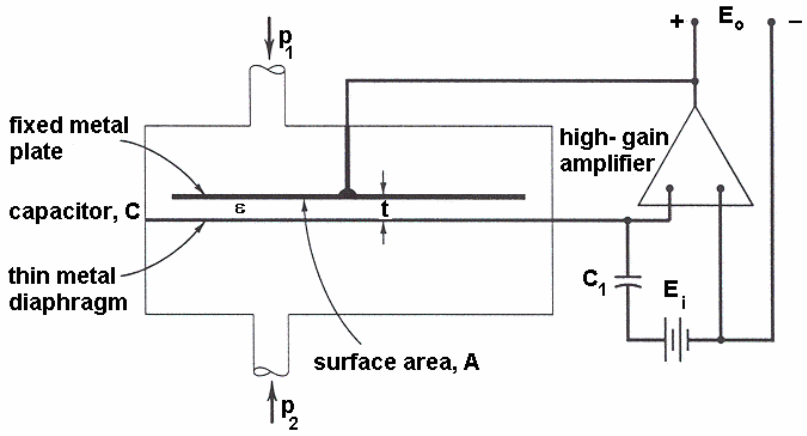

Figure 2.5 Capacitive pressure transducer (adapted from Figliola & Beasley 2000).

therefore making their frequency response somewhat limited (Carstens 1993). Figure 2.5 illustrates some features of a capacitive pressure transducer.

2.3.4 Piezoresistive transducers

Piezoresistive sensors take advantage of the change of conductivity associated with a pressure induced strain in a semiconductor; they are usually fabricated from silicon. They can be made as a strain gauge and bonded to a diaphragm (Doebellin 1990), or they can be formed as an integral strain gauge diaphragm device. Piezoresistive strain gauges show 50 times more sensitivity than conventional metallic strain gauges (Figliola & Beasley 2000), and furthermore, silicon has lower thermo-elastic and creep effects. Their usual working pressure range is between 0.1 kPa to 100 MPa (Pownall 1993). However, they should be protected from aggressive materials and their maximum operating temperature is about 120^{o}C and they break easily if the pressure exceeds the maximum working pressure (Pownall 1993). Furthermore, silicon is not a good material for operating in wet conditions (Figliola & Beasley 2000). The natural frequency of silicon diaphragms can be greater than 70 kHz, and they show a small acceleration sensitivity, generally around 100 Pa/g. Various configurations are possible, and Fig. 2.6 shows a typical piezoresistive diaphragm pressure transducer.

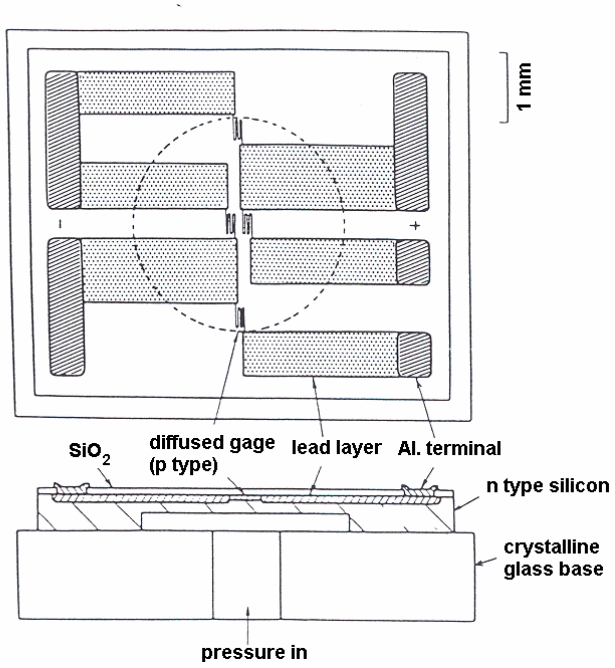

Figure 2.6 Structure of semiconductor pressure sensor (adapted from Gopel, Hesse & Zemel 1989).

2.3.5 Piezoelectric pressure transducers

The Curie brothers discovered anisotropic crystals in 1880 (Eggins 1996). These materials such as quartz, tourmaline, Rochelle salt, and barium titanate do not have a centre of symmetry and produce an electric charge when subjected to a sudden change of pressure (for example, see Carstens 1993; Eggins 1996). Quartz is the most common material used in piezoelectric pressure transducers due to their high modulus of elasticity, low hysteresis, linearity and high natural frequency (Dally, Rifley & McConnell 1993). The natural frequency of the crystals alone can be around 10 MHz (Eggins 1996), however, the actual natural frequency of the transducer arrangement is dependent on the mass of crystal, mechanical design, and metallic electrodes coated onto the crystal (Dally, Rifley & McConnell 1993; Eggins 1996). The actual natural frequency many piezoelectric transducers is between about 0.25 MHz and 0.5 MHz while still maintaining a high pressure sensitivity (Dally, Rifley & McConnell 1993).

Piezoelectric pressure transducers are the most common transducer used for transient pressure measurement due to their high natural frequency (Finkelstein & Gratton 1994). They do not show sensitivity to slow changes of pressure and therefore, they

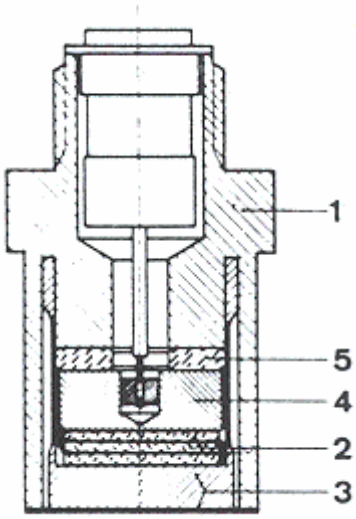

Figure 2.7 Piezoelectric pressure transducer with acceleration compensation: 1) housing; 2) quartz crystal; 3) diaphragm assembly; 4) compensating mass; and 5) compensating quartz (reproduced from Doebellin 1990).

cannot be employed for static pressure measurements. Piezoelectric pressure transducers show a sensitivity to acceleration and if they are employed to measure low pressures with strong vibration, they may need an acceleration compensated design. Figure 2.7 illustrates such a piezoelectric pressure transducer.

2.4 Pressure sensitive paint

Pressure sensitive paint (PSP) is a relatively new method for pressure measurement. This technique is based on oxygen quenching of luminescent molecules dispersed in a film, which is coated onto a test surface (Pitotech 2002). In this method, a light

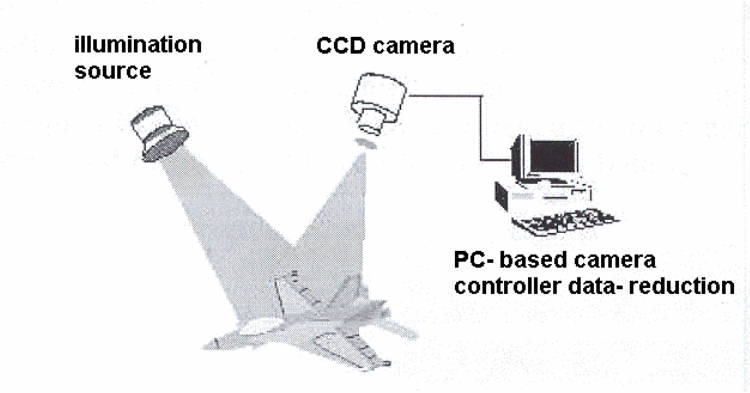

Figure 2.8 Basic configuration of PSP application (adapted from Asai 2001).

with an appropriate wavelength (λ_{ex}) radiates the film, which stimulates the probe molecules to a higher, quasi-stable state. The molecules return again to the initial state either by releasing photons in the form of red shifted photoluminescence or through non-radiative decay, resulting in thermal energy or quenching (Abbitt, Fuentes & Carroll 1996). The released photons have a wavelength (λ_{em}) that is inversely proportional to the pressure applied to the surface if the light intensity and mole fraction of oxygen are held constant. This technique is shown schematically in Fig. 2.8.

The advantages of PSPs include their capacity for accurate and spatially continuous pressure measurements. The technique is not particularly expensive, however, PSPs are sensitive to temperature (about 1%/^{o}C) and their response time is on the order of hundreds of microseconds. The response time is proportional to the square of the thickness of the paint layer and inversely proportional to the diffusivity of oxygen in binder. Decreasing the layer thickness to reduce the response time reduces the signal to noise ratio and so there are limitations to the maximum achievable bandwidth (Scharier 2002). Nevertheless, technique improvements are continuing and measurements with a 10 kHz bandwidth in a hypersonic wind tunnel have been reported (Asai 2001).

2.5 Bar gauge

Shielding a piezoelectric pressure transducer to reduce thermal effects or the possibility of particle impacts increases its response time. In an attempt to produce a robust pressure transducer with a fast response, bar gauges were designed at the University of Wales (Davies & Lippaitt 1964). These sensors were applied at the Australian National University for use in the T3 free piston shock tunnel, for the first time (Mudford, Stalker & Shields 1980). Common piezoelectric pressure transducers

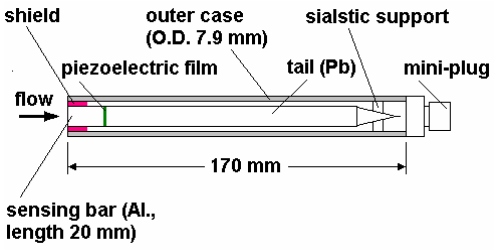

Figure 2.9 Bar gauge configuration (adapted from Neely & Morgan 1994).

use a diaphragm as the sensing element. The bar gauge (see Fig. 2.9) uses a metallic bar in front of a piezoelectric film. Pressure acts on the exposed face of the bar and produces a stress wave. The stress wave, with an intensity proportional to the applied pressure, moves along the bar and acts on a thin piezoelectric film. The electrical charge produced by the film is converted to a voltage and amplified. Figure 2.9 shows the bar gauge configuration used in this work (Neely & Morgan 1994).

The aluminium bar against which the flow impacts had a diameter of about 3 mm and was mounted within an outer case (O.D. 7.9 mm) and supported by a shield. The length of the aluminium bar should be long enough to protect the piezoelectric film from any thermal effect, however, a long bar ahead of the piezoelectric film causes an increased delay time. To minimize the delay time, aluminium was selected for the bar material as it has a high sound velocity (4877 m/s) (The engineering toolbox n.d.). To delay reflection of the stress wave from the downstream end of the device, a long tail was connected to the other side of the film (Fig. 2.9). This bar was made from a tin-lead alloy to decrease the wave speed and provide a longer gauge operating period. The bar gauge showed a linear output (about 2.17 mV/kPa) and a response time of about 4 μs (Neely & Morgan 1994). In its original form, the response time was less then 2 μs (Mudford, Stalker & Shields 1980).

In an attempt to improve the conventional bar gauge sensitivity, a steel disc of 9 mm diameter and 1 mm thickness was attached to the front of the bar (see Fig. 2.10). This disk also improved the aerodynamic shielding and the survivability of the gauge. The rise time of the bar gauge in this configuration was reported to be about 5 μs (Macrossan, Chiu & Mee 2001). Further modifications from the original configuration include two strain gauges mounted onto opposite sides of a single brass bar in a bending compensation arrangement.

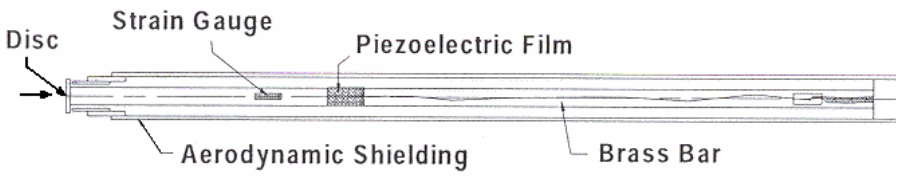

Figure 2.10 Modified bar gauge used at the University of Queensland (reproduced from Macrossan, Chiu & Mee 2000).

2.6 Transducer characterisation

2.6.1 Deadweight testers

A deadweight tester is a device used to calibrate other pressure gauges. Figure 2.11 shows the basic configuration of a typical deadweight tester. The tester chamber is filled with oil and the volume can be adjusted with a plunger or a pump. The chamber also includes a vertical cylinder and piston. The pressure in the chamber can be increased by loading the piston with standard weights. The adjustable plunger should be moved until the piston disconnects from chamber body and completely floats. The pressure generated by such devices are usually between 0.07 kPa and 70 MPa (Figliola & Beasley 2000), with errors as low as 0.01%.

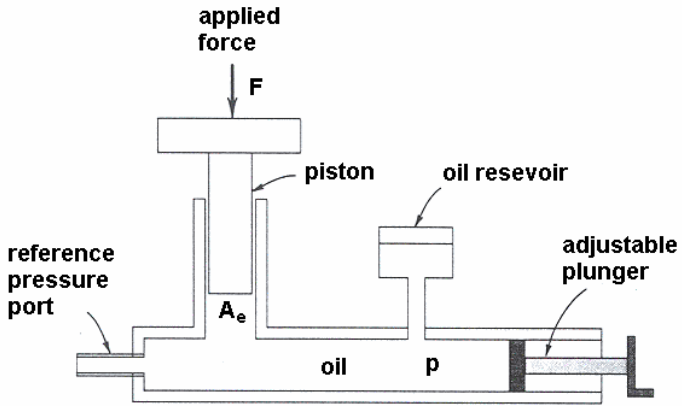

Figure 2.11 Deadweight tester (adapted from Figliola & Beasley 2000).

The variation of local gravity, installation unbalance, thermal expansion, elastic deformation of piston under pressure, and air buoyancy effects contribute to the errors in the deadweight tester operation. The necessary clearance between the piston and the cylinder creates uncertainty for the reference area. This clearance also leads to a small oil flow between the piston and the cylinder, and the consequent shear stress contributes an additional error. This error can be minimized by using a high viscosity oil. A method to reduce possible the dry friction between the piston and the cylinder is to cause rotation of the piston (Doebellin 1990).

2.6.2 Dynamic calibration

The natural frequency and damping ratio of transducers can be measured through dynamic calibration. Common methods for dynamic calibration include a thin

diaphragm technique, a ball drop technique, and a shock tube technique (Doebellin 1990; Figliola & Beasley 2000).

A thin diaphragm technique can be used for transducer natural frequencies up to A thin diaphragm technique can be used for transducer natural frequencies up to about 1 kHz (Doebellin 1990). Figure 2.12 illustrates the configuration. Two different pressures (P_1 and P_2) are applied on the two sides of a diaphragm and the diaphragm can be ruptured by a solenoid-actuated knife. After bursting, the pressure P_2 rises to approximately P_1 very quickly.

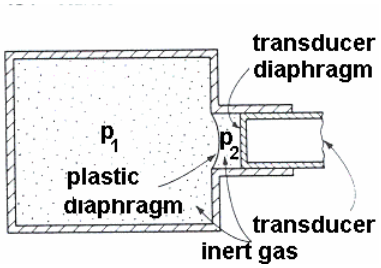

Figure 2.12 Thin diaphragm apparatus configuration (adapted from Doebellin 1990).

The step load rise time should be less than about one quarter of the transducer rise time, otherwise the natural frequency will not be excited (Doebellin 1990). The thin diaphragm device described in the Doebellin work (1990) had a rise time of about 0.25 ms, so it could be used to measure transducers rise times that are greater than approximately 1 ms.

A simple impulse method involves dropping a small steel ball onto the pressure sensitive diaphragm. The impact excites the natural frequency and the results have been found to correlate quite well with the shock tube method (Doebellin 1990).

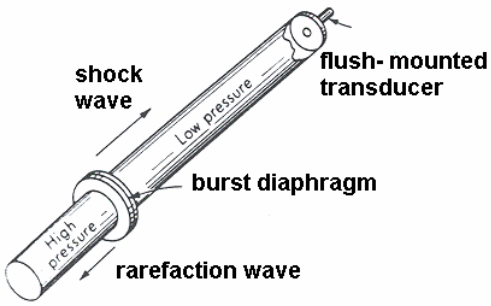

Figure 2.13 Illustration of a pressure transducer calibration shock tube (adapted from Doebellin, 1990).

Faster step loading of pressure transducers can be achieved using a shock tube, Fig. 2.13. The shock tube is a long tube divided into two sections by a diaphragm. The pressure is different in the two sections and the transducer is mounted in the end wall of the low-pressure section. A rise of pressure in the high-pressure section or a mechanically controlled needle can burst the diaphragm. A shock wave will be created which propagates toward the end wall and transducer at a speed higher than the speed of sound in the low pressure gas. The shock thickness is in the order of 1 μm (Figliola & Beasley 2000), so the load rise time is around 2 ns for a shock speed of 500 m/s. This rise time increases if the transducer is not flush mounted in the end wall or is placed on the side of the tube. In the case of a transducer mounted on the side wall, the load rise time increases to $t=(d+h)/W$ where d, h, W designate the diaphragm diameter, shock thickness and shock speed respectively.

2.7 Conclusion

Various pressure sensors and transducers have been reviewed. Generally, they do not show sufficiently short response times for the measurement of high frequency fluctuations (up to around 100 kHz) in transient aerodynamic facilities. The exceptions are: 1) piezoresistive; 2) piezoelectric; and 3) bar gauge devices.

Piezoelectric pressure transducers have the highest natural frequency. Acceleration compensated devices generally have a large diaphragm diameter, around 5 mm. Another disadvantage is their cost (often more than $1500 Australian), which makes it important to shield them (either mechanically or pneumatically) in the harsh flow environments often encountered in transient aerodynamic facilities. Shielding the diaphragm can greatly reduce the system natural frequency below the frequencies of interest. (The effects of mechanical shielding are discussed in Chapter 5.)

Piezoresistive transducers have a good response times but the pressure sensitive area usually has a diameter on the order of at least 1 mm. Using Micro-Electro-Mechanical Systems (MEMS) technology provides the capacity for high spatial resolution sensors (Huang et al. 2000). However, as with peizoelectric sensors, these devices are often expensive and must therefore normally be shielded from the transient flow environment, which again results in a lowering of the system natural frequency perhaps to below the frequencies of interest.

The bar gauge has a long length and limited useful measurement period. Their long length makes them inappropriate for some applications. However, they have been successfully applied as a relatively low cost solution for Pitot pressure measurements in transient aerodynamic facilities. The primary disadvantage of bar gauges in some aerodynamic disturbance measurement applications is their spatial resolution which has so far been restricted to a maximum of about 3 mm.

In summary, piezoelectric transducers, piezoresistive transducers and bar gauges can all be used in transient aerodynamic facilities depending on measurement requirements. However, the piezoelectric and piezoresistive gauges are relatively expensive and therefore should be shielded, and this limits their bandwidth. Bar gauges appear to be a good solution (low cost yet high bandwidth) for many applications, however, the spatial resolution of bar gauges remains comparable with commercial devices. Thus there is scope for fibre optic pressure sensors to make a substantial contribution due to cost and spatial resolution advantages as will be seen in Chapter 3.

Chapter 3: Review of fibre optic pressure sensors

3.1 Introduction

Fibre optic pressure sensors have the potential to measure pressure in aerodynamic facilities. They have advantages such as small size, low weight, neutral to electromagnetic interference (EMI) and radio frequency interference (RFI), no risk of fire and sparks, intrinsically safe in explosive environments, high bandwidth and accuracy (Krohn 1988; Pal 1992).

Fibre optic pressure sensors are generally divided into two categories, extrinsic and intrinsic (Finkelstein & Grattan 1994). With intrinsic sensors, the pressure modulates the transmission properties of the sensing fibre while in extrinsic sensors, the modulation takes place outside the fibre (Pal 1992). The most common fibre optic pressure sensors techniques are based on either intensity or phase modulation (Pal 1992; Moseley & Crocker 1996). Difficulties with fibre optic pressure sensors arise due to source variations and in case of phase mode operation, sensitivity to other physical effects such as temperature changes (Moseley & Crocker 1996).

In this chapter, a selection of fibre optic pressure sensors is reviewed. There is an emphasis on interferometric techniques and in particular, Fabry-Perot systems because they have a higher-pressure sensitivity, the potential to be made in a small size, and they have shown high bandwidth (MacPherson 1999). The inherent bandwidth limitation of the fibre optic pressure sensors is due to the bandwidth of the light (about 10^{14} Hz). In practice however, the measurement bandwidth is limited by the bandwidth of the optical detection system that is usually in the order of MHz.

3.2 Intensity modulating, Transmissive sensors

Transmissive sensors (which are extrinsic devices) include two fibres, one connected to the source and the other to the detector. The percentage of light transmitted from one fibre to the other changes with pressure and can be calibrated. Transmissive sensors can be divided into two basic categories. In the first category, intensity modulation is provided by the relative movement of two fibres whereas in the second

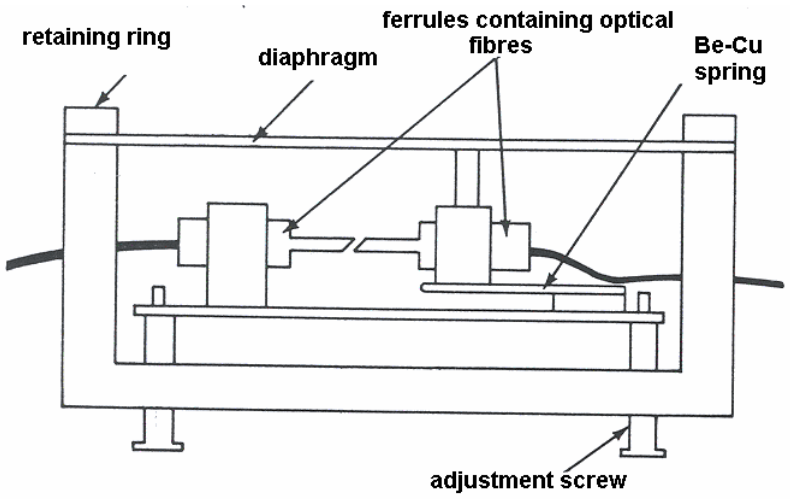

Figure 3.1 Example of an intensity modulated fibre optic pressure sensor (adapted from Krohn 1988).

category, the relative movement of a shutter provides the modulation (Krohn 1988; Pal 1992).

In the first category, the relative movement can include relative displacement of two fibres (transverse or longitudinal), or a change of angles between two fibres. Figure 3.1 shows one of these sensors, which works on the basis of transverse displacement caused by deflection of a diaphragm.

Figure 3.2 shows a reflective diaphragm-type pressure transducer. The light intensity transmitted to the second fibre is changed directly by deflection of a diaphragm. Single mode or multi mode fibres can be used as the wave guide. The response of

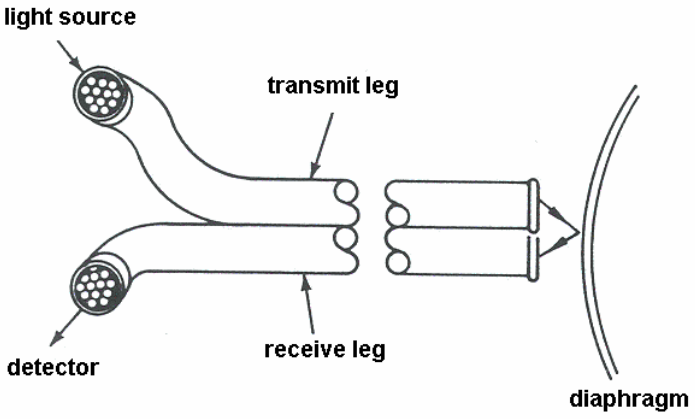

Figure 3.2 Reflective fibre optic pressure sensor using a diaphragm for intensity modulation (adapted from Krohn 1988).

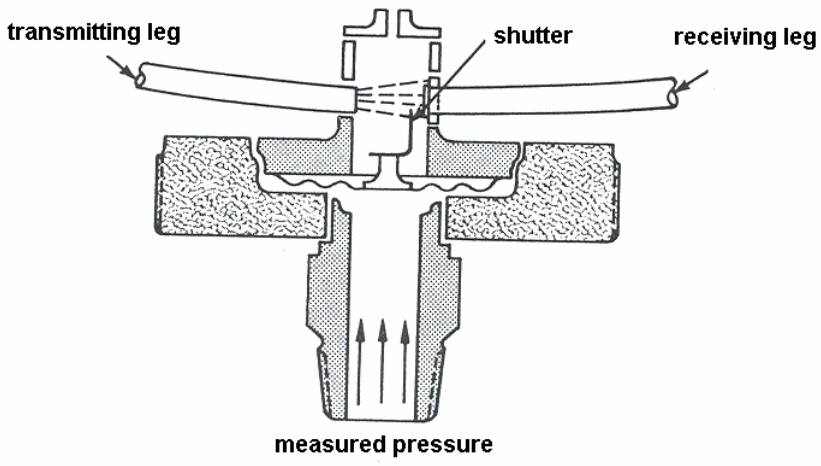

Figure 3.3 Transmissive fibre optic pressure sensor using a shutter to modulate the intensity (adapted from Krohn 1988).

devices like that illustrated in Fig. 3.2 is not usually linear but can be corrected with a suitable electronic circuit. Commercial varieties of these sensors are available and they show little hysteresis (Krohn 1988).

Figure 3.3 shows one sensor in the second category (transmission is modulated by a shutter). The light is interrupted by a shutter, which moves due to a change of pressure.

A grating can be used in place of the shutter in the optical path as illustrated in Fig.

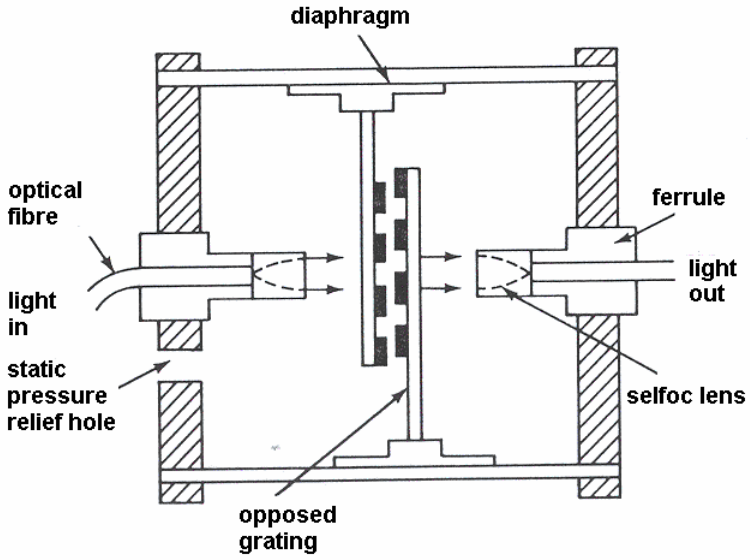

Figure 3.4 Transmissive fibre optic pressure sensor using a moving grating to modulate the intensity (adapted from Krohn 1988).

3.4. The relative movement of the two gratings (caused by pressure applied to a diaphragm), alters the fraction of light transmitted to the second fibre. Through optimisation of the grating geometry, very sensitive transmissive sensors have been constructed (Krohn 1988).

3.3 Microbending sensors

Bending increases the energy loss within optical fibres, and this process is used in microbending pressure sensors as shown in Fig. 3.5. Hence, microbending sensors can be classified as intrinsic devices.

With reference to Fig. 3.5c, increasing the pressure decreases the distance between two plates which increases the optical loss within the fibre. The transmitted light intensity can be calibrated to measure the pressure. The parameters that affect loss

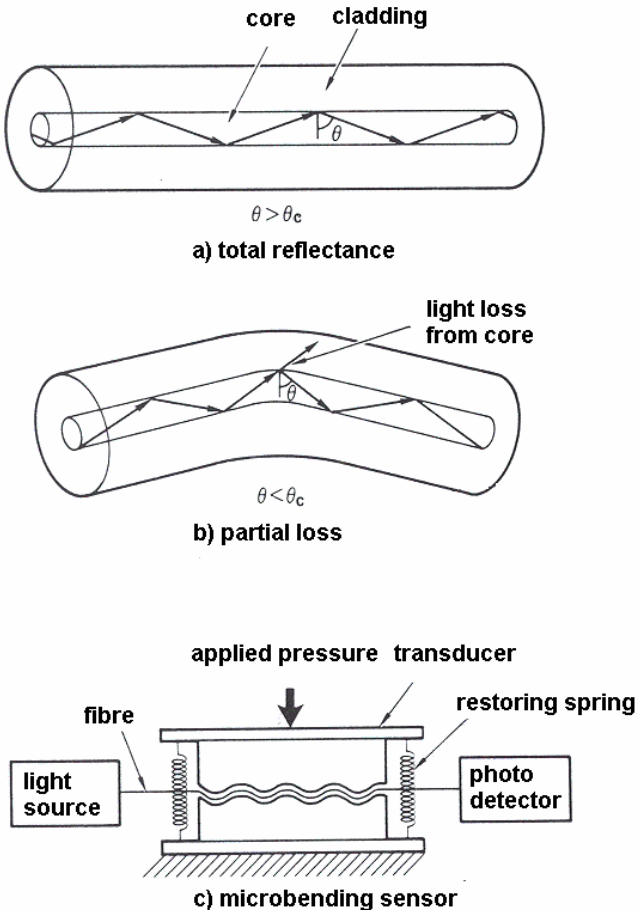

Figure 3.5 Microbend light loss sensor: a) straight fibre which has no bend loss; b) small bend creates transmission loss; and c) microbend sensor (adapted from Gopel, Hesse & Zemel 1989).

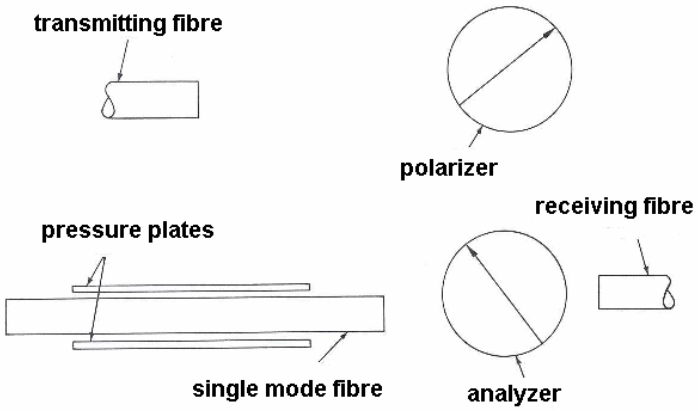

Figure 3.6 Intrinsic polarizing fibre optic pressure sensor (adapted from Krohn 1988).

are fibre numerical aperture, core size, cladding size, core to cladding ratio and microbending curvatures. This system has an advantage in that the contamination in the flow cannot damage the sensor as it is a closed system, but disadvantages include limited dynamic response and relaxation of the fibre bending (Krohn 1988). A thorough description of these sensors is given by Lagakos, Cole & Bucaro (1987).

3.4 Polarization & refractive index sensors

Figure 3.6 illustrates an intrinsic fibre optic pressure sensor based on polarization effects. Pressure induces a transverse strain to the fibre, which causes birefringence. In the present context, birefringence means the fibre core refractive indices are

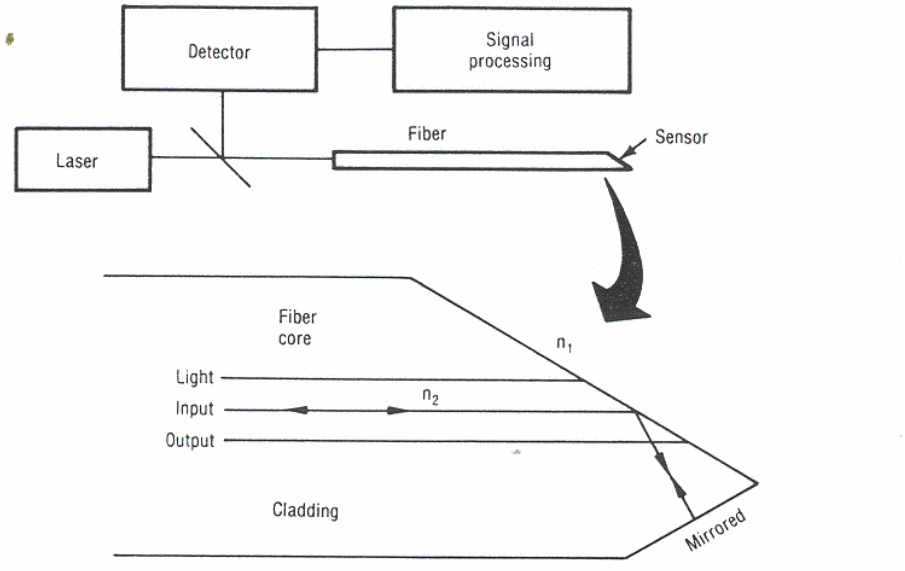

Figure 3.7 NTIR fibre optic pressure sensor (reproduced from Krohn 1988).

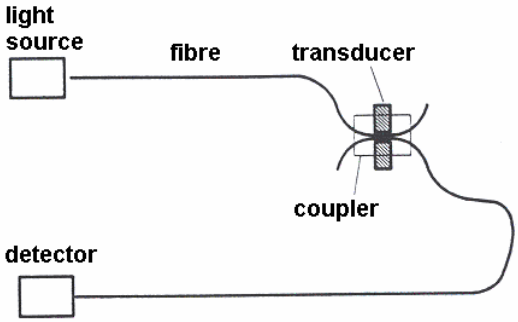

Figure 3.8 Evanescent coupler sensor (adapted from Yu & Yang 1997).

different in the parallel and perpendicular directions. Birefringence causes a change in polarisation state and can be detected. Considering this effect, the light will be polarized at the entrance of the sensor and the output intensity of light in the other polarization direction, which is related to applied pressure, will be identified using an analyser and detector.

An example of an intrinsic sensor based on the pressure induced change of refractive index is the near total internal reflection (NTIR) sensor. The configuration of the NTIR sensor, which is sometimes categorised as a reflective sensor, is shown in Fig. 3.7.

The end face of a single mode fibre is cut at an angle just below the critical angle and the input light reflects from the end face and the mirror as illustrated in Fig. 3.7. The intensity of the reflected light modulates due to the applied pressure. This is because the pressure alters the critical angle due to change of refractive indices in different directions (as discussed earlier in this section). The main advantage of these sensors is their extremely small size (Krohn 1988).

3.5 Evanescent sensors

The light is not totally confined within the core of the single mode fibre – it penetrates inside the cladding layer. This portion of the light is called the evanescent wave. When light passes through a coupler, the fraction of light transferred from one fibre to the other is dependant on the distance between the two cores. This distance can be modulated by pressure. Figure 3.8 shows the configuration of a sensor based on this effect. These sensors can be classed as intrinsic devices.

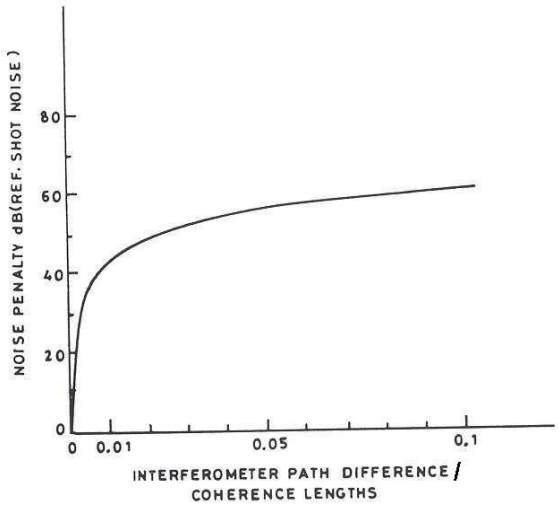

Figure 3.9 Noise as a function of optical path difference in interferometric pressure sensors (reproduced from Pal 1992).

3.6 Interferometric sensors

Interferometric pressure sensors typically have high sensitivity, wide bandwidth and accuracy (Krohn 1988). They can be based on either intrinsic or extrinsic designs. The high sensitivity of some interferometric sensors is a consequence of the low wavelength of light which is on the order of 1 μm (Pal 1992). Such advantages attract many applications, however interferometric sensors have some important limitations such as source coherence and laser phase noise.

Two light beams are required for interferometry and the difference between their optical path affects the signal to noise ratio. Interferometry will not be possible if the optical path difference exceeds the coherence length. The coherence length (l_c) is related to the coherence of the source ($\Delta\lambda$)(see Section 4.2.1.5) and its wavelength (λ) according to,

$$l_c \approx \lambda^2 / \Delta\lambda \tag{3.1}$$

Noise can become a problem in some applications if the optical path difference is on the order of 0.1% of coherence length (Pal 1992). A typical effect of optical path difference on noise is shown in Fig. 3.9.

Increasing the optical path difference also affects the visibility. (Visibility is discussed in some detail in Section 3.7). Equation (3.2) shows the relation between

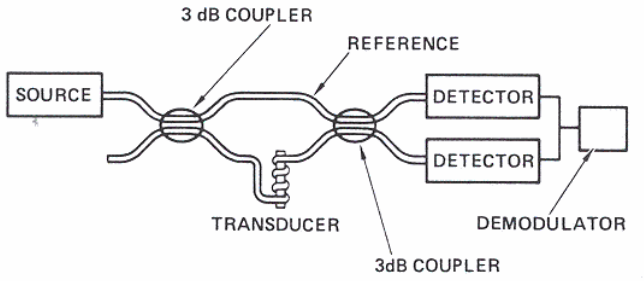

Figure 3.10 A Mach-Zehnder optical fibre interferometer (reproduced from Gopel, Hesse & Zemel 1989).

the visibility (V), coherence length (l_c), and optical path difference (Δl) if the intensity of two beams is equal and polarization effects are neglected.

$$V = \exp\left(-\frac{|\Delta l|}{l_c}\right) \tag{3.2}$$

3.6.1 Mach-Zehnder

The configuration of an optical fibre Mach-Zehnder interferometer is shown in Fig. 3.10. The light emitted from a laser source is directed to a coupler and divided into two fibres. The beams from these two fibres interfere after they have been combined by passing through another coupler. The beam travelling along one of the fibres situated between the two couplers is used as the reference and the other fibre forms the sensing leg of the system. The fibre length or its refractive index can be modulated by an applied pressure. This alters the optical path length in the sensing leg and causes a change in intensity of light at the detectors.

3.6.2 Michelson

Instead of using two couplers, the light can be returned from the reference and sensing legs using mirrors as shown in Fig. 3.11. This arrangement is known as the Michelson interferometer and it is generally a cheaper arrangement than that of the Mach-Zehnder interferometer.

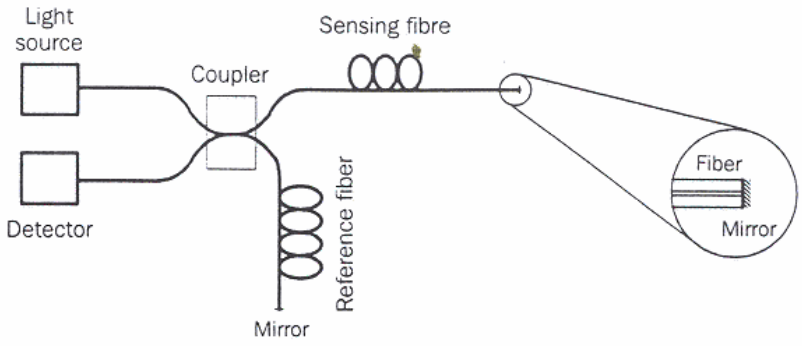

Figure 3.11 A Michelson optical fibre interferometer (reproduced from Yu & Yang 1997).

3.6.3 Fabry-Perot

The Fabry-Perot interferometer has a simpler configuration than the Michelson interferometer. It uses only one fibre to transmit both required light beams. An example of a Fabry-Perot interferometer is shown in Fig. 3.12. Fabry-Perot interferometers can show high temperature sensitivity (Yu & Yin 2002), which is not desirable for a pressure sensor.

The light emitted from the laser is directed to the sensor after passing through the beam splitter (or coupler). The illustrated arrangement (Fig. 3.12) includes a lens and

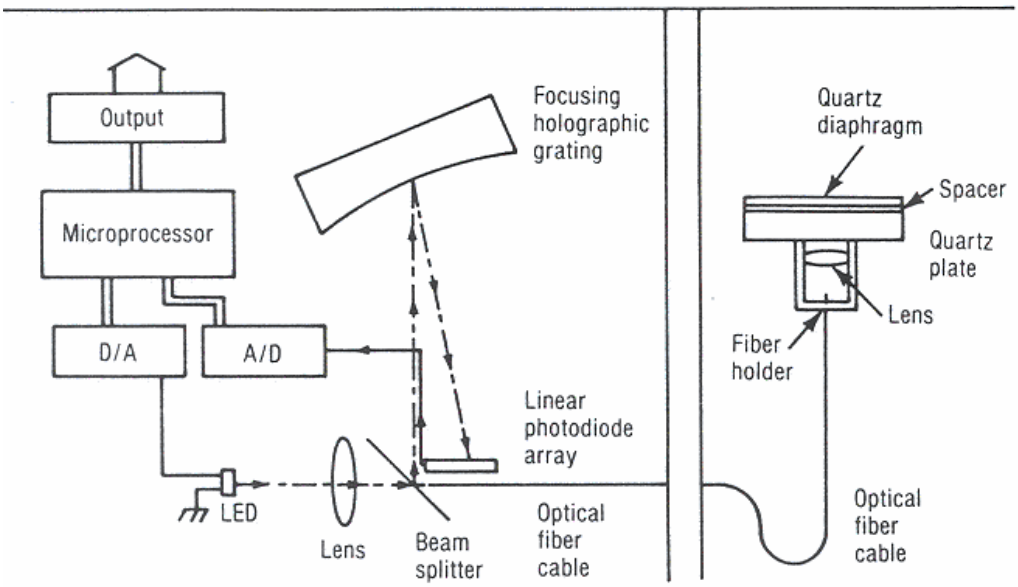

Figure 3.12 A Fabry-Perot optical fibre interferometer (reproduced from Yu & Yang 1997).

a reflective diaphragm. The optical path between lens and diaphragm can be altered due to pressure applied on the diaphragm. The change of the optical path alters the phase difference between the two reflected beams and therefore the intensity of reflected light changes due to the applied pressure. This system allows the sensor to be compact due to the use of only one fibre.

Fabry-Perot interferometers can be divided into two categories, firstly, intrinsic Fibre Fabry-Perot Interferometers (FFPI) and secondly, Extrinsic fibre Fabry-Perot Interferometers (EFPI) (Yu & Yin 2002). FFPI sensors include a single mode fibre between two reflectors and the pressure affects the optical path between the two reflectors. EFPI sensors include an air gap or some solid material between two mirrors and pressure changes the optical path across this material (Yu & Yin 2002).

3.6.3.1 Intrinsic Fabry-Perot interferometry

Three kinds of FFPI sensors are shown in Fig. 3.13. Figure 3.13a shows a sensor, which includes an internal mirror and a reflective end. This reflective surface can be produced with a cleaved or polished end. Changes of pressure alter the fibre refractive index, and therefore the optical path changes (Yu & Yin 2002). Figure 3.13b shows another FFPI sensor, which uses two internal mirrors and one non-reflective end fibre. The change of pressure can change the optical path as previously discussed. Figure 3.13c shows a similar arrangement using Fibre Bragg Grating (FBG) mirrors and a non-reflective fibre end (Yu & Yin 2002).

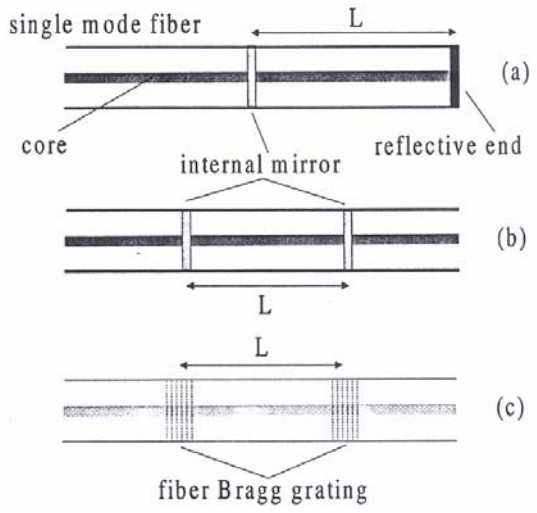

Figure 3.13 FFPI sensor configurations: a) cavity formed by an internal mirror and fibre end; b) cavity formed by two internal mirrors; and c) cavity formed by two fibre Bragg gratings. (reproduced from Yu & Yin 2002).

3.6.3.2 Extrinsic fibre based Fabry-Perot interferometry

Four different configurations of EFPI sensors are presented in Fig. 3.14. Figure 3.14a shows the earliest and the most useful EFPI sensor (Yu & Yin 2002). In this arrangement, some light is reflected from a cleaved or polished end of fibre while the other light required for interferometry is reflected from the diaphragm. Such sensors can have a very short cavity length, which makes it possible to use LEDs as a light source and use multimode optical fibre (Yu & Yin 2002).

Instead of a reflective diaphragm and air cavity, a transparent solid material can be used as shown in Fig. 3.14b. The applied pressure on the transparent material changes its physical dimension and refractive index. This modulated optical path difference can be calibrated to measure the pressure. Another EFPI sensor configuration is illustrated in Fig. 3.14c where two fibres are positioned in a capillary tube separated by a small distance. The Fresnel backreflection and reflected light in entrance to the second fibre which acts as a mirror, provides the two required beams. A similar configuration called In-Line Fibre Etalon (ILFE) uses two single mode fibres and the air gap is filled with a spliced hollow core fibre as shown in Fig. 3.14d.

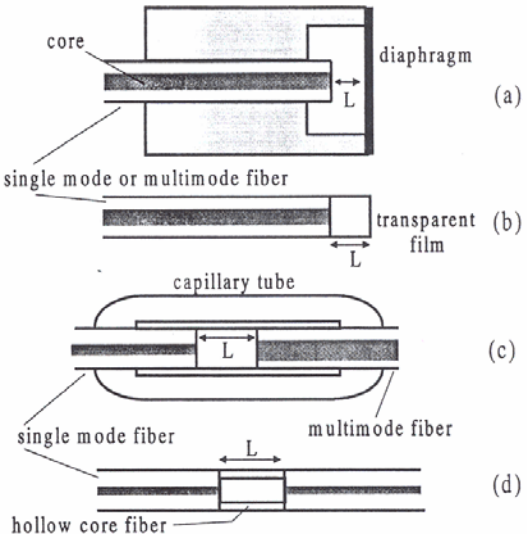

Figure 3.14 EFPI sensor configurations: a) reflective diaphragm sensor; b) transparent sensor; c) two opposite fibres sensor; and d) hollow core fibre sensor (reproduced from Yu & Yin 2002).

The light is not totally confined in EFPI sensors and the light exits and enters the fibre, which cause optical loss. This limits the cavity length to just a few hundred μm for most applications (Pal 1992).

At Heriot-Watt University, an extrinsic Fabry-Perot interferometer with a pressure sensor of the type shown in Fig. 3.14a was successfully developed. The interrogation system was a single wavelength interrogation system and a single mode optical fibre was used. Fresnel back reflection from the cleaved end of the addressing fibre was used as a beam and the second beam for interferometry was reflected from the diaphragm. The diaphragm was made from copper using a vacuum deposition technique. The diaphragm thickness was less than 6 μm to provide the required sensitivity and the desired pressure range was from vacuum to 400 kPa. The pressure resolution was about 2 kPa (MacPherson 1999).

The sensor had a very good spatial resolution (better than 0.2 mm) and high natural frequency (about 1 MHz) and indicated a frequency response to higher than 100 kHz. However, the sensor shows considerable hysteresis and high temperature sensitivity (about 35 kPa/^{o}C), which can cause problems in some applications. The air cavity was formed with a sealed volume at atmospheric pressure and the construction success rate was about 40%.

In recent research at Heriot-Watt University, a micromachined sensor was made using a silicon wafer as a substrate. The diaphragm was electroplated onto the wafer instead of using glue. The size of the sensor was about 0.5 mm × 0.5 mm × 0.3 mm. It was successfully applied to the measurement of pressure in a turbine (Gander et al., 2002).

3.7 Extrinsic Fabry-Perot cavity models

The reflected light intensity is related to the optical path difference in a Fabry-Perot interferometer and it changes due to the applied pressure. Many models are presented in different references to calculate the reflected intensity. The two beam model is the simplest model and is based on the assumptions (MacPherson 1999):

1. Every reflective surface gives rise to only one reflection.
2. The reflective surfaces are zero thickness and the light intensity and its phase do not change during transmission or reflection.

3. The state of polarization of the light entering the cavity does not change as it passes through the cavity.
4. The cavity length is much smaller than light coherence length and the light can be assumed perfectly coherent (in both spatial and temporal senses, as discussed in Section 4.2.1.5)

The first assumption is moderately accurate for low reflectivity surfaces. In the case of only one of the surfaces having high reflectivity, the intensity of the reflected light decreases significantly during the first few reflections and hence does not greatly affect the two beam approximation.

The zero thickness reflective surface is an idealization. For example, the light reflected from a material penetrates a certain distance inside the surface called the skin depth. Furthermore, the state of polarization in reflection can change, and no source is totally coherent, as discussed in Chapter 4.

In the two beam case, the ratio of the reflected intensity (I_r) to the light intensity at the entrance (I_0) can be calculated as (MacPherson 1999),

$$\frac{I_r}{I_0} = R_1 + R_2 + 2\sqrt{R_1 R_2}\cos\varphi \tag{3.3}$$

The reflection amplitude and its square are designated r and R respectively and subscripts 1 and 2 denote the reflective surfaces 1 and 2 respectively. The phase difference is ϕ which can be calculated as (MacPherson 1999),

$$\phi = \frac{4\pi n l}{\lambda} \tag{3.4}$$

where λ is wavelength and l is physical distance between the two surfaces and n is refractive index of medium between two surfaces.

The attenuation in fibre and coupling losses can also be considered and this leads to (MacPherson 1999),

$$I_r = kI_0(1 + V\cos\phi) \tag{3.5}$$

Coefficient k is related to the losses and V introduces the cavity visibility which is defined as (MacPherson 1999),

$$V = \frac{I_{\max} - I_{\min}}{I_{\max} + I_{\min}} \tag{3.6}$$

where I_{max} and I_{min} are the maximum and minimum reflected intensities respectively.

One coefficient commonly used in interferometry to describe the profile (or sharpness) of the reflection spectrum of the cavity is finesse which is defined as (MacPherson 1999),

$$F = \frac{4R}{(1-R)^2} \tag{3.7}$$

The two beam model is not valid if the reflectivity of the surface is high. In this case, the higher order reflected light should be considered. The reflected intensity in a multi beam cavity model can be calculated as (MacPherson 1999),

$$I_r = kI_0\left(\frac{R_1 + 2\sqrt{R_1R_2}\cos\phi + R_2}{1 + 2\sqrt{R_1R_2}\cos\phi + R_1R_2}\right) \tag{3.8}$$

It should be noted that the multi beam cavity model only relaxes the first assumption used in the two beam model. In a real cavity, factors such as poor fibre alignment, light absorption or scattering in the cavity or optical coatings, and the thickness of reflective surface can all affect the reflected intensity and cause deviation from the models.

3.8 Fabry-Perot interrogation systems

3.8.1 Single wavelength

Figure 3.15 shows a practical single wavelength Fabry-Perot interrogation system. The light from a laser diode enters a single mode fibre after passing through an optical isolator. Optical isolation of the laser is required to prevent instability caused by backreflection. The light is split into two different single mode fibres while passing through the bi directional coupler. The light in one fibre is used as an intensity reference while the light in the other fibre enters the sensor. The light reflected from sensor returns to the directional coupler and then to the signal detector.

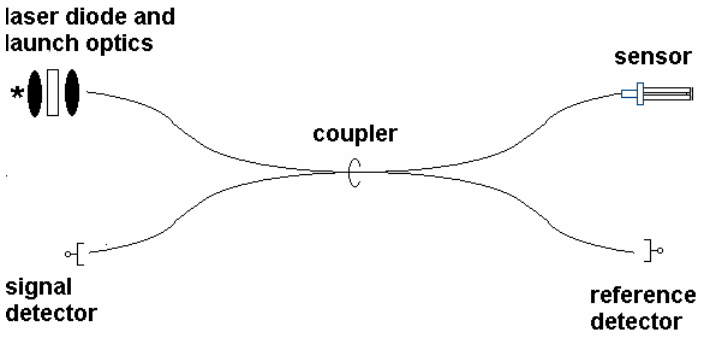

Figure 3.15 A practical Fabry-Perot interferometer using optical fibre

Single wavelength interrogation suffers three key problems. Firstly, the phase modulation must be controlled to a maximum of π radians, otherwise there will be phase ambiguity. Secondly, the laser intensity noise affects the results. Finally, any change in optical intensity loss between calibration and measurement causes an error (these changes of loss can be caused by the connection in the splicers or different fibre bending).

3.8.2 Multiple wavelength

Equation (3.5) includes three unknowns V, k, and ϕ. Two and three wavelength interrogation systems can decrease or eliminate the number of unknowns. Increasing the number of wavelengths beyond three appears impractical due to system complexity and in some cases, bandwidth limitations (MacPherson 1999).

Different configurations of multiple wavelength interrogation systems can be used for short cavities (<50 μm) and long cavities (>1mm) (MacPherson 1999). According to Eq. (3.4), a small change of wavelength for a long cavity produces a clear phase difference between two wavelengths. This small change of wavelength can be achieved with appropriate modulation of a single laser diode source (MacPherson 1999). For short cavities where a change of phase due to a small change of wavelength is not clear, two separate sources should be used. Figure 3.16 illustrates a basic two wavelengths interrogation scheme for a short cavity.

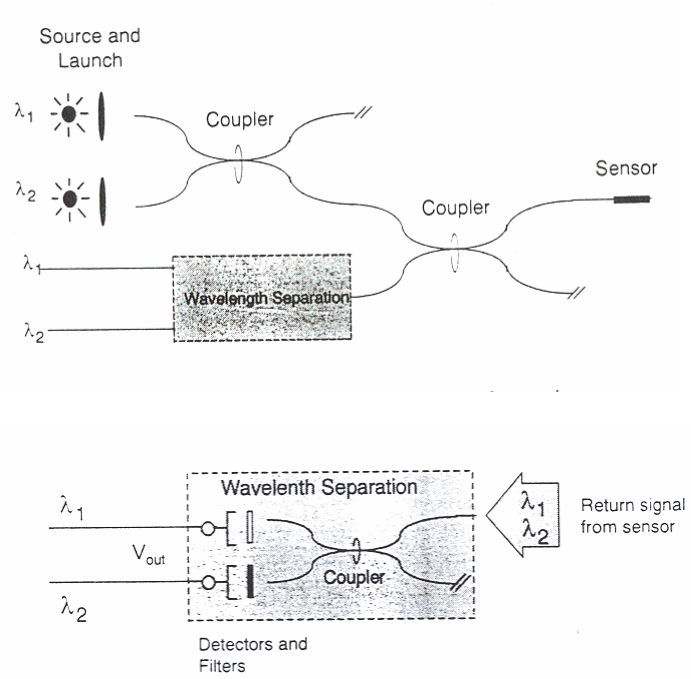

Figure 3.16 Two wavelength interrogation system (reproduced from MacPherson 1999).

Two lasers with different wavelengths launch light into the system and both beams enter into one single mode fibre after passing a 2×2 coupler (Fig. 3.16). Light enters the sensor and reflects back to the system, similar to one wavelength interrogation. This time there is a new coupler located in place of the detector and each leg includes a filter for eliminating the undesired wavelength. Two detectors simply detect the intensity of each wavelength separately. In this case, the phase ϕ_1 can be calculated as (MacPherson 1999),

$$\phi_1 = \cos^{-1}\left(\frac{S_2 - S_1}{\pm\sqrt{A^2 + B^2}}\right) - \tan^{-1}\left(\frac{A}{B}\right) \tag{3.9}$$

where S_1 and S_2 are normalised intensities and defined as,

$$S_1 = \frac{I_{r1}}{I_{O1}} = k(1 + V\cos\phi_1) \tag{3.10}$$

$$S_2 = \frac{I_{r2}}{I_{O2}} = k(1 + V\cos(\phi_1 + \delta)) \tag{3.11}$$

and

$$\delta = \frac{\lambda_1 - \lambda_2}{\lambda_2}\phi_1$$

$$A = S_1 V \sin\delta$$

$$B = S_1 V \cos\delta - S_2 V$$

The values of S_1 and S_2 can be identified from the detectors and δ is dependant on ϕ_1 and the two identified wavelengths. Equation (3.9) can be solved indirectly or by a trial and error method. The value of loss (k) is not required – it is assumed to remain constant for the two wavelengths. This assumption and additional assumptions of constant visibility for both wavelengths makes Eq. (3.9) approximate and the error increases if the two wavelengths have a significant difference.

A three wavelength interrogation system makes it possible to calculate phase without knowing k and V. This system is more complicated and three separate light sources should be employed for a short cavity length. Furthermore, instead of using 2×2 couplers, a 3×2 coupler or a 3×1 coupler should be used. MacPherson (1999) presents the necessary equations for a three wavelength interrogation system.

3.8.3 White light interferometry

White light interferometry (WLI) is another way to avoid phase ambiguity. In the present context, white light means the coherence length is much smaller than optical path difference of the two reflected light beams in the case of a Fabry-Perot interferometer (Yu & Yin 2002). LEDs, laser diodes biased near threshold, and tungsten lamps are reasonable sources for WLI. A typical Fabry-Perot WLI and its response are shown in Fig. 3.17.

The central fringe is a key point in WLI and numbers of phase change can be counted from this recognizable fringe. WLI appears impractical in applications that require fast response because of detection limitations that arise when attempting to identify a sufficiently large number of fringes. The direction of phase changes can easily be identified in contrast with coherent light interferometry discussed previously (Yu & Yin 2002).

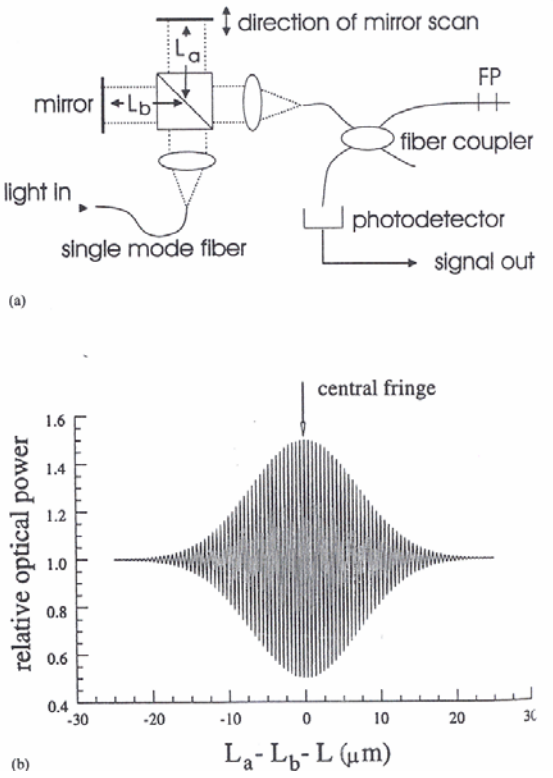

Figure 3.17 White light interferometry, L is length of FP cavity: a) optical configuration; and b) fringe pattern (reproduced from Yu & Yin 2002).

3.9 Discussion

For fibre optic pressure sensor in a shock tube, smaller sized sensors are required to provide high spatial resolution. Larger sized sensors can affect the flow and induce errors particularly in Pitot pressure arrangements. Some sensor configurations presented in this chapter require the insertion of optical fibres from opposite directions, which increases the size of the pressure sensor. Four configurations do not have this problem and have potential as a small sized sensor. They are the reflective transmissive sensor (Fig. 3.2), NTIR sensor (Fig. 3.7), Fabry-Perot sensor using a diaphragm (Fig. 3.14a), and Fabry-Perot sensor using transparent film (Fig. 3.14b).

Reflective transmissive sensors have a simple configuration and are relatively easy to construct. Due to the possible use of multimode fibre, the alignment between the diaphragm and the two fibres is not critical and therefore they are much easier to make than single mode fibre sensors. However, as they do not rely on interferometry, the change in optical path needs to be hundreds of micrometers for sufficient sensitivity (Fig. 6.2; Goff 1999). To provide such deflection, it is necessary to use a

very thin diaphragm or the diaphragm diameter should be increased relative to an interferometric sensor. According to the equations presented in Chapter 5, both thinner diaphragms and larger diameters have a lower natural frequency and therefore sensors with the highest achievable spatial and temporal resolution are unlikely to be obtained with the reflective transmission configuration.

Fabry-Perot transparent film sensors also have a simple configuration and have the potential to be the smallest possible size (about the same size as the cladding or about 125 μm), however they are difficult to make. The alignment and quality of connecting surfaces should be extremely high. The estimated pressure sensitivity is not high for the thin transparent film. Its temperature sensitivity would increase if the film thickness is increased in an attempt to improve the pressure sensitivity. However, the transparent length should be much less than half of the coherence length, which leads to relatively poor pressure sensitivity in most applications.

NTIR sensors are not interferometric sensors and therefore their pressure sensitivity is not high. However, NTIR sensors have excellent spatial resolution. Due to the change of fibre refractive index with temperature, they show a high temperature sensitivity.

Fabry-Perot sensors using a diaphragm are the final possibility. To maximize the bandwidth, the diaphragm diameter should be decreased to the size of fibre cladding. This is essentially the configuration of the Heriot-Watt sensor. The Heriot-Watt arrangement leads to relatively low cost sensors due largely to the ease of construction. Furthermore, the Heriot-Watt arrangement has a demonstrated capacity for high frequency fluctuation measurements. For these reasons, this configuration was chosen for further investigation and development in the current work.

Chapter 4: Review of principal fibre optic system components

4.1 Introduction

The Fabry-Perot interferometer is a possible option for sensitive, high spatial resolution, and fast response pressure measurement, as discussed in Chapter 3. In this chapter, the principal components required to assemble such a system are discussed. The components discussed in this chapter are: 1) the light source; 2) the optical isolator; 3) the optical fibre; 4) the coupler; and 5) the detector. The intention of this chapter is to provide an introductory review, which may prove useful to experimentalists that use these fibre optic pressure sensors.

4.2 Light source

There are many light sources such as light-emitting diodes, lasers and lamps. Among them, lasers are a high intensity, narrow spectral width, coherent, and highly directional light source. The word laser is derived from *"light amplification by stimulated emission of radiation"*.

Two common light sources in fibre optic applications are LED's and laser diodes (LD). The reasons are their small size, small emitting area, long life and capacity for high speed modulation. For interferometry applications, the spectral width of the source should be very narrow. Lasers have a narrower spectral width than the LEDs. The laser diode is adopted as a light source in this research.

4.2.1 Laser diode characteristics

4.2.1.1 Directionality

The laser beam is approximately conical and it slightly diverges with distance after a length called the Rayleigh range. The divergence angle can be different in the two directions. The light intensity is a maximum at the optical centre of the beam and it decreases exponentially with distance from the optical centre. This optical centre can differ from the mechanical centre of the laser. The radius of the light beam is usually defined as a distance where intensity drops to $1/e^2$ of its maximum value.

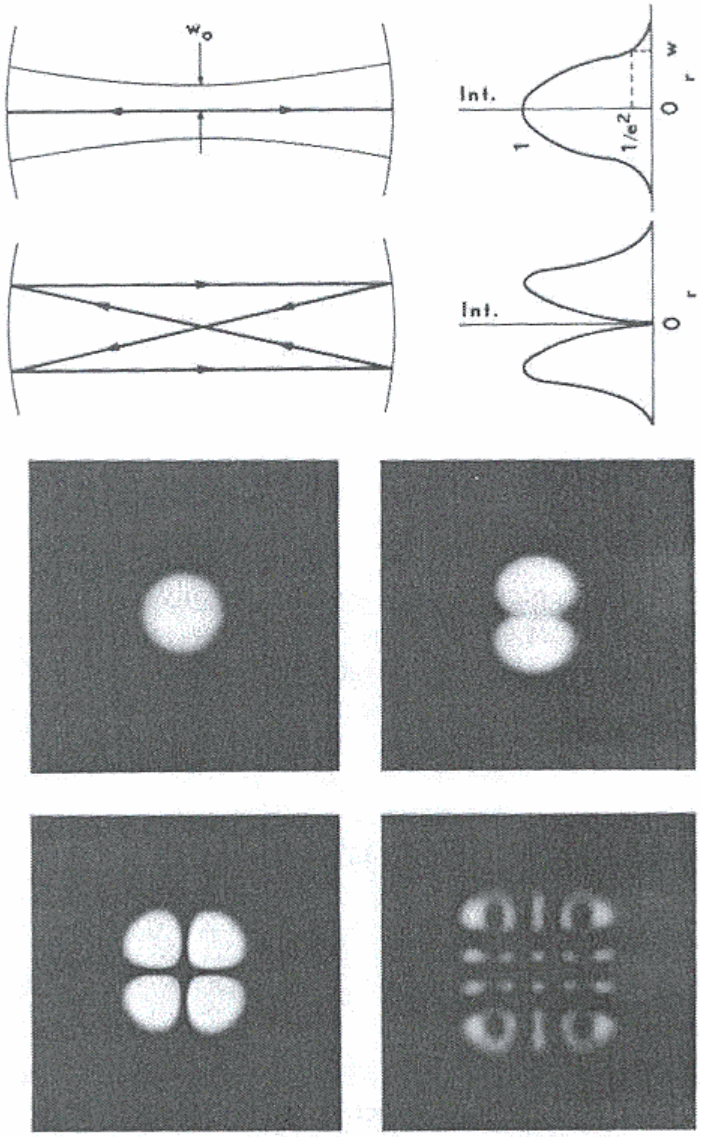

Figure 4.1 Laser transverse mode patterns (reproduced from Young 1992).

4.2.1.2 Focusability

The laser light, which is coherent and nearly collimated, can be focused to a spot with a minimum size using a lens. The minimum diameter (d) can be calculated from Eq. (4.1),

$$d \cong f\phi \tag{4.1}$$

The focal length of the lens and the divergence angle of the light are designated f and ϕ respectively. Equation (4.1) indicates that the laser light can be focused to a very small size by using a short focal length lens. This is especially important when attempting to launch light into an optical fibre with a small core size.

4.2.1.3 Transverse modes

The intensity distribution across the cross-section of the laser beam can vary depending on the laser design. Figure 4.1 shows the processes of transverse mode formation. Due to the curvature of mirrors, other stable modes can be formed in addition to the main mode as shown. Stable light reflection can occur at four points (two points on each side). These points form the maximum intensity points and intensity decreases with distance from these points. It is desirable, especially in interferometry systems, that only one mode emerges at the laser output. Manufacturers attempt to attenuate or filter the other modes, permitting only one mode to dominate at the exit of the laser.

4.2.1.4 Monochromaticity

No light is truly a single wavelength or monochromatic, however, the laser light is closer to this than any other source. No ordinary light, without significant filtering, can approach the degree of monochromaticity present in the output beam of typical lasers. The FWHM, which stands for Full Width at Half Maximum, can be used as a measure of the width of the optical spectrum. It indicates the spectral width of the light at the point where the intensity falls to half of the maximum value as illustrated in Fig. 4.2.

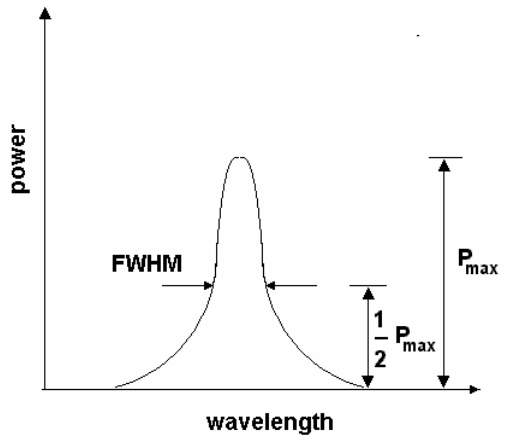

Figure 4.2 Definition of full width at half maximum (FWHM)

4.2.1.5 Coherence

There are two kinds of coherence, spatial and temporal coherence. Spatial coherence deals with the beam collimation and is related to the size and shape of light source while temporal coherence refers to the light spectral width. In pure harmonic motion of light, it is assumed that the light consists of some infinite wave trains. This is not strictly true as the radiation includes a finite number of vibrations of a fixed frequency. In interferometry, the wave trains must have a phase relation that continues during the observation period (Brown 1965). This period or coherence time indicates the period that a quasimonchromatic light beam keeps a reminiscence of the value it had at an earlier time (Klein & Furtak 1986). In interferometry applications, the source should be both spatially and temporally coherent. Figure 4.3 illustrates the concept of coherence for a tungsten lamp and a laser.

Light from a tungsten lamp lacks temporal and spatial coherence, as shown in Fig. 4.3a. If a pinhole is placed in front of the light, the spatial coherence improves (Fig. 4.3b), however, the light still lacks temporal coherence and the power in the beam is decreased. Using a narrow band filter improves the temporal coherence (Fig. 4.3c) but the power again decreases. The final result of using a pinhole and narrow band filter is a coherent light, however, the power is much less than the initial light. The light irradiated from a laser has good temporal and spatial coherence and its power can be very high (Fig. 4.3d).

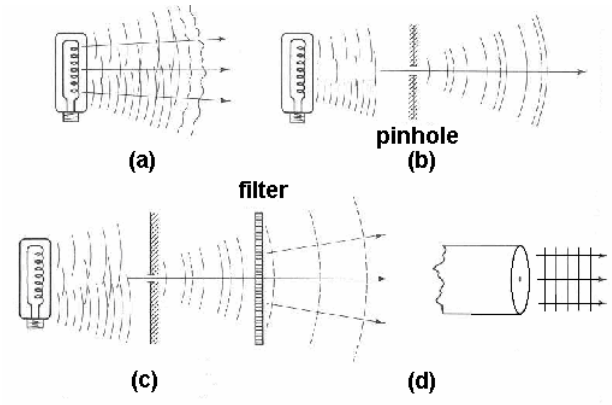

Figure 4.3 Illustration of light coherence: a) No coherence; b) Spatial coherence; c) Spatial and temporal coherence; and d) Coherent light from a laser (adapted from Pedrotti, FL & Pedrotti, LS 1987).

It should be noted that the light emitted from a multimode laser does not have better coherence than a filtered light from a thermal source. For interferometry applications, it is important that the laser operates in a single transverse and axial mode. Even for such a laser, the light is coherent only for a specific distance called coherence length. The coherence length is the distance the light travels during coherence time (see first paragraph of this section) and can be calculated using (Sharp c. 1990),

$$L_c = \frac{\lambda^2}{2\,\pi\, n\, \Delta\lambda} \tag{4.2}$$

where

L_c Coherence length

λ Light nominal wavelength

$\Delta\lambda$ Spectral width

n index of refraction of the propagation medium.

Interferometry can only be effective if the difference between the two optical paths of the two beams is less than the coherence length. For example, if the laser wavelength is 790 nm and its spectral bandwidth is 0.3 nm (which are representative figures for the lasers used in this work), the coherence length calculated from Eq. (4.2) is 215 μm.

4.2.2 Laser diode performance

The electrons within an atom have some specific discrete energy. The transition of electrons from one energy level to other is possible by absorption or emission of light. The absorbed or emitted light is in individual units called photons. Photons are electromagnetic waves and have a specific frequency and direction. For the transition between discrete energy levels, the absorbed or emitted light should have the exact energy difference between two levels. The wavelength of the absorbed or emitted photon can be calculated from its energy using (Sharp c. 1990),

$$\lambda = \frac{c}{|E_2 - E_1|/h} = \frac{1.2398}{|E_2 - E_1|} \tag{4.3}$$

where

λ Wavelength (μm)

c Velocity of light (2.998×10^{8} m/s)

h Planck's constant (4.135×10^{-15} eV/Hz)

$|E_2\text{-}E_1|$ Energy difference between states (eV)

There are two types of photon emission. The first type of emission occurs when an electron falls from a higher energy level to a lower energy level and emits a photon with the wavelength given by Eq. (4.3). This phenomenon is called spontaneous emission. The light emitted by one atom within a material has no phase relation to the light emitted by any other atom. Light is emitted in all directions and the result is an incoherent source.

The second type of emission occurs when a photon with the energy of $E_2\text{-}E_1$ and wavelength given by Eq. (4.3) interacts with an atom, which has an electron in the higher energy level of E_2. The atom is stimulated to emit a second photon with the same wavelength, phase and direction as the first photon, leaving the electron in the energy level E_1. The constructive interference of a group of photons in the same direction, phase and wavelength produces a coherent beam.

The number of electrons in a lower energy level (E_1) is usually more than higher level (E_2), therefore, more light is absorbed than that emitted. For light amplification, the number of electrons in a higher level should be more than in the lower level and this population inversion can be achieved by optical or electrical pumping.

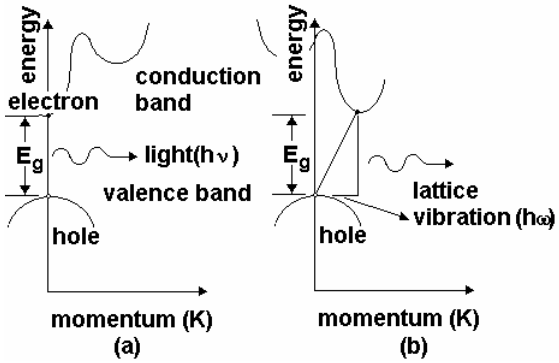

Figure 4.4 Two types of laser diodes a) direct-gap type; b) indirect-gap type (after Sharp c. 1990).

In laser diodes, the required population inversion can be achieved by applying current injection to a P-N junction. The higher and lower energy levels are associated with the conduction and valance bands respectively.

Two types of laser diodes are possible: 1) direct band gap; and 2) indirect band gap (Fig. 4.4). Laser diodes with a wavelength between 750 and 830 nm use a direct gap gallium aluminium arsenide (GaAlAs) crystal. In this type, the electron momentum remains constant and the light can be emitted easily (Fig. 4.4a). In the indirect band gap type, the transition does not occur easily due to the different momentum (Fig. 4.4b). In GaAlAs laser diodes, the ratio of the gallium to aluminium can be adjusted to vary the band gap width and thereby control the wavelength.

A laser oscillator should be used to produce a strong laser light. It usually consists of two confronting mirrors and their distance is occupied by a light amplifying material.

This structure, which is called a Fabry-Perot Resonator, is obtained in a laser diode

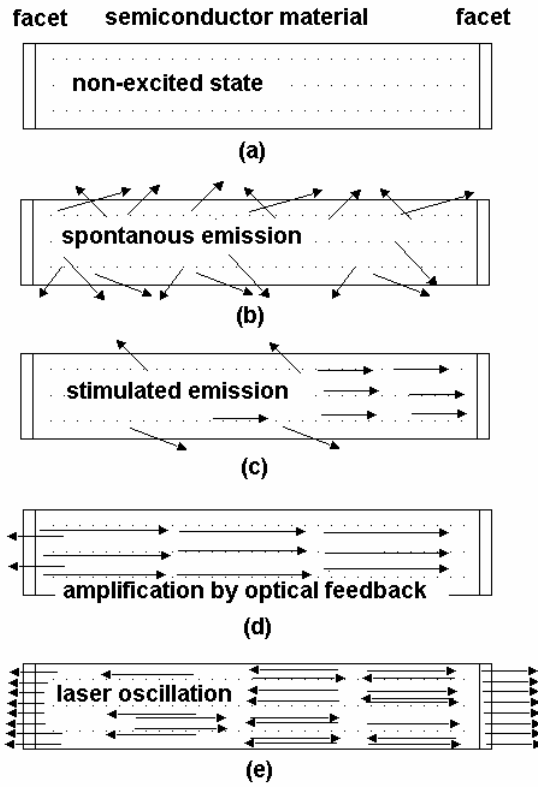

Figure 4.5 Forming laser oscillation: a) non-excited state of a laser consists Fabry-Perot resonator structure; b) spontaneous emission of laser just after excitation; c) beginning of simulated emission; d) amplification of simulated light by optical feedback; and e) laser oscillation (after Sharp c. 1990).

by cleaving the ends of the semiconductor crystal (Fig.4.5a). A special coating may be used to improve the reflectivity or transmissivity of the mirror facet.

When the laser diode begins to operate, light produced by a spontaneous emission is amplified and repeatedly reflected by two mirrors. Light emitted in directions other than the optical axes will pass through the sides of the resonator (Fig. 4.5b). Light which travels repeatedly in an optical axis direction, will be amplified by a stimulated emission (Fig. 4.5c and Fig. 4.5d). At each reflection, some parts of the light are transmitted through reflective facets. Laser oscillation begins when the amount of amplified light becomes equal to the total amount lost through the sides of the resonator, mirror facets and absorption by the semiconductor material (Fig. 4.5e).

4.2.3 Laser important factors

Important parameters that are used to characterise the performance of laser diodes and LED's are as below,

Peak wavelength. This is the wavelength at which the source emits the most power. The most common peak wavelengths for laser diodes are 780 nm, 850 nm, 1310 nm, 1550 nm, and 1625 nm.

Rise and fall time. This is a measure of how quickly the laser can be switched on or off, measured between the output levels of 10% to 90% of the maximum.

Bandwidth. It is defined as the point where the signal amplitude drops 3 dB below the normal level, which is equivalent to a reduction of 50% in power. The precise relationship between bandwidth and rise time differs for the various light sources. The rise time can be related roughly to bandwidth using,

$$BW = \frac{0.35}{\tau} \tag{4.4}$$

Where BW is in MHz if rise time (τ) is in μs**.**

Spectral width. Laser output is not monochromatic and it includes a range of wavelengths centred at the peak wavelength. This range is called the spectral width of the source.

Threshold current. This is the lowest current at which the laser begins to operate, as shown in Fig.4.6. LED's do not have threshold current.

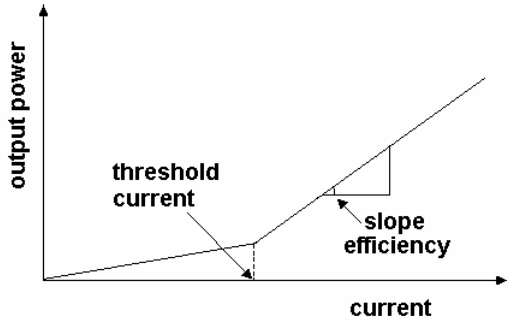

Figure 4.6 Definition of laser diodes threshold current (after Hecht & Zajak 1982).

Numerical aperture. The actual output light of laser and LED's are conical and not cylindrical. The numerical aperture is sine of this angle, which can be different in horizontal and vertical directions, as illustrated in Fig. 4.7.

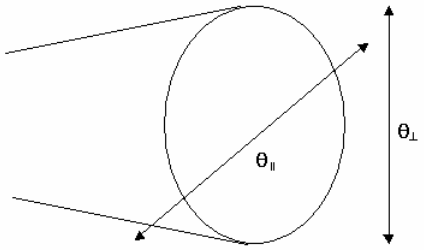

Figure 4.7 Different angles of laser light in horizontal and vertical directions (after Sharp c. 1990).

4.2.4 Laser noise

Noise is a fluctuation of laser output over time. As previously discussed, the laser diode output is proportional with the drive current above threshold current, therefore any drive current fluctuation appears as noise in laser diode output. Changes of drive current not only appear as amplitude modulation (AM) noise but also as noise in frequency and coherence (Dakin & Culshaw 1998).

Above the threshold current, the frequency noise is almost independent of current drive (Dakin & Culshaw 1998), however, this noise is especially important in interferometry system. The frequency noise of the laser converts to the phase noise error at the sensor output (Dakin & Culshaw 1998). This makes it necessary to use a battery or well smoothed power supply to drive the laser.

The light emitted from a laser or LED's has the best coherence when operated at its designed current and coherence decreases if the laser is operated at a different drive current (Dakin & Culshaw 1998).

Changes of temperature affect the output of the lasers and LEDs due to changes of refractive index and the length of the laser Fabry-Perot cavity. The peak wavelength, threshold current, and the slope efficiency (see Fig. 4.6) of the laser all vary with temperature. If the temperature increases, the threshold current increases, but the slope decreases.

4.3 Optical isolator

Backreflection from the lenses or the cleaved ends of the fibre used in the system can reflect back into the laser and destabilize its operation. The Rayleigh backscattered light and the quasi-random properties of polarization for fibres more than a few tens of metres in length can have the same effects. Use of an optical isolator is necessary

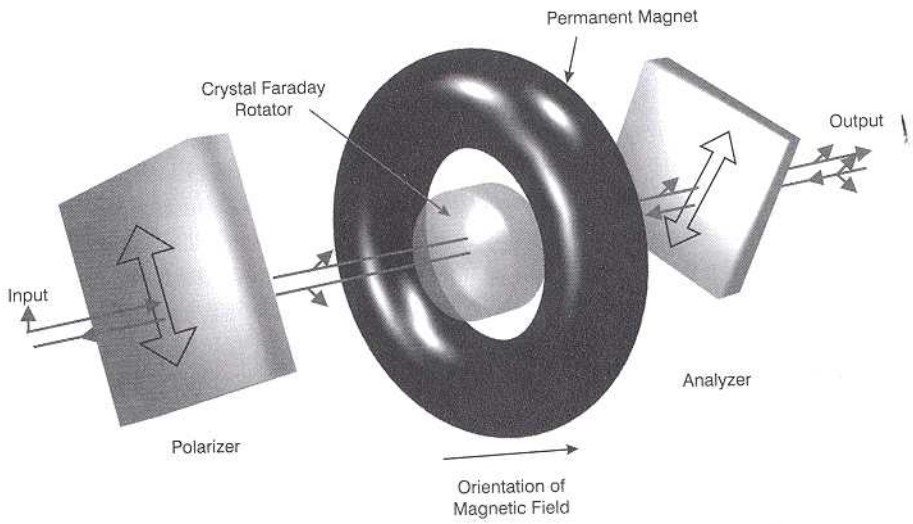

Figure 4.8 Details of an optical isolator (reproduced from Goff 1999).

to prevent this noise, however, a typical isolator achieves only -40 dB isolation and care should still be taken. The operation of one type of optical isolator is illustrated in Fig. 4.8.

The light enters the isolator from the left and passes through a polarizer. The polarized light turns through an angle of 45^{o} clockwise in a crystal Faraday rotator (as viewed in Fig. 4.8) and leaves the isolator after passing through the output polarizer. The backreflected light cannot pass the isolator. It enters from the right and after passing through the polarizer on the right, it enters the Faraday rotator. This crystal turns the light through 45^{o} again in the clockwise direction as viewed in Fig. 4.8, so the output light from the rotator is perpendicular to the polarizer on the left and cannot pass through it.

4.4 Optical fibre

An optical fibre is a waveguide and there are several major types, which have different characteristics and functions. The basic types of fibre and their performance are presented in this section.

4.4.1 Optical fibre performance

The refractive index of a transparent material is defined as the ratio of the speed of light in the vacuum (C_{vac}) to the speed of light in the material (C_{mat}),

$$n = \frac{C_{vac}}{C_{mat}} \tag{4.5}$$

Light travels in a straight line but it changes direction if the refractive index of the medium changes. This process is described by Snell's law which relates the two angles defined in Fig. 4.9 according to,

$$n_i \sin I = n_r \sin R \tag{4.6}$$

Where n_i and n_r are the refractive indexes of the initial and refractive mediums respectively. Incident and refraction angles are designated with I and R respectively.

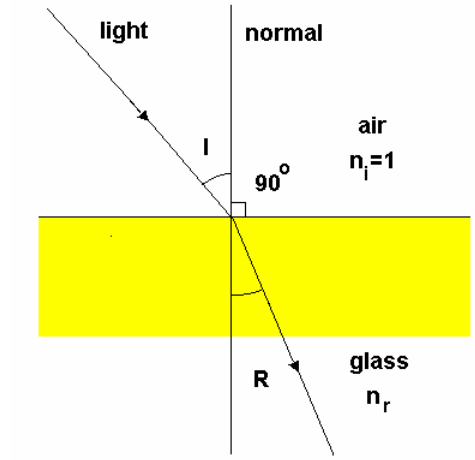

Figure 4.9 Incident and refraction angle (after Hecht & Zajak 1982).

If light enters to a medium with lower refractive index, the refraction angle increases. There is a critical angle which the refraction angle reaches 90^o (critical angle can be calculated from Eq. (4.6) by substituting sin*R*=1). In this case, the incident light is refracted along the boundary between two mediums. If the light approaches the boundary at angle greater the critical angle, the light is reflected. This effect is called total internal reflection (TIR) and is the basic concept of transmitting light in optical fibres.

Optical fibre has two main parts, the core and cladding, as shown in Fig. 4.10. The light travels inside the core. The refractive index of the core is larger than that of the cladding. The core is surrounded by cladding and therefore those rays of light that have angle smaller than the confinement angle, are confined within the core.

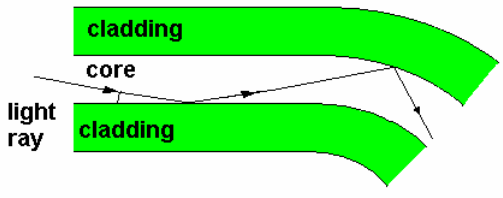

Figure 4.10 Illustration of the core and cladding in optical fibre (after Hecht & Zajak 1982).

The light travels inside the core by frequent reflection within the confinement angle (θ_c) as shown in Fig. 4.11.

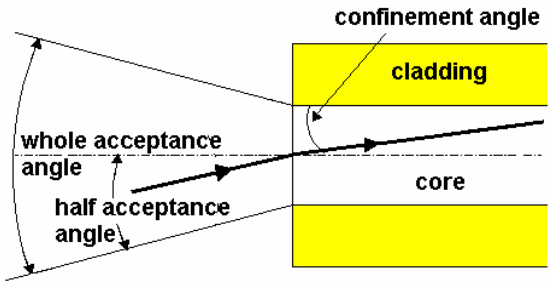

Figure 4.11 Acceptance angle of optical fibre (after Hecht & Zajak 1982).

It should be noted that half acceptance angle θ differs from the confinement angle due to the different refraction of core-cladding and core-air interfaces (see Fig. 4.11). If a light ray attempts to enter the core at an angle larger than the acceptance angle, the light will not be reflected at the interface of the core and cladding and instead it will be refracted into the cladding. The numerical aperture is defined as sine of the half acceptance angle,

$$NA = n_{ext} \sin\theta \tag{4.7}$$

where n_{ext} is the refractive index of medium surrounding the fibre. Using Eq. (4.6) it can be demonstrated that if light from a vacuum or air enters the fibre, the numerical aperture is,

$$NA = \sqrt{n_0^{\,2} - n_1^{\,2}} \tag{4.8}$$

where n_0 is the refractive index of the core and n_1 is the refractive index of the cladding.

Light can be lost from the fibre due to absorption, scattering, and leakage of light out of the core caused by environmental factors such as pressure. The magnitude of the attenuation depends on the light wavelength (amongst other factors) and it is commonly defined as the ratio of the output power to the input power. Measurements are normally made in decibels,

$$\text{dB Loss} = -10\text{Log}_{10}\left(\frac{P_{out}}{P_{in}}\right) \tag{4.9}$$

The light can travel within the core along many different paths as long as the core diameter is much larger than the wavelength of the light. These different paths have different length and the light arrives in the end of the fibre at different times. Therefore, a sharp edged pulse of light will spreads out as it travels along the fibre. This phenomenon is called pulse dispersion and the magnitude of the dispersion increases linearly with the length of fibre. This limits the analog bandwidth or the data rate of a digital data because it causes successive pulses to overlap and interfere with each other. The maximum bandwidth or data rate can be estimated using,

$$\text{Bandwidth (MHz)} = \frac{350}{\text{Dispersion (ns/km)} \times L^{\gamma}} \tag{4.10}$$

where γ is a factor that is dependent on the fibre type, but it can be taken as unity for most practical cases. The maximum bandwidth is usually quoted in the manufacturer's specifications (for a 1 km length of fibre). The maximum bandwidth for different fibre lengths can be calculated from Eq. (4.10).

For certain paths through an optical fibre, the electromagnetic fields in the light waves reinforce each other so as to form a field distribution that is stable as the light travels within the fibre. These standing waves are called modes. In other paths, a stable wave will not propagate down the fibre, so there is no identifiable mode. The number of modes (N_{m}) that can propagate in a fibre depends on the fibre's numerical aperture (NA) or acceptance angle, core diameter (D), and the light wavelength (λ). The number of modes can be estimated using (Hecht 2002),

$$N_m = \frac{(D \times NA \times \pi/\lambda)^2}{2} \tag{4.11}$$

This equation is approximate particularly when there are only a few modes. Each mode has a characteristic number, N which is associated with all rays travelling at an angle θ_N with respect to the fibre axis which is given by,

$$\theta_N \approx \lambda\left(\frac{N+1}{2Dn}\right) \tag{4.12}$$

Where for small values of θ_N, N is the mode number (the lowest mode number is zero), λ is the wavelength of the light, D is the light core diameter and n is the refractive index of the core. It should be noted that even the rays associated with the zero mode number do not travel straight along the fibre core.

It is possible that the highest modes penetrate slightly inside the cladding and travel inside the cladding for a short distance due to changes of conditions such as small bend. This can artificially increase the fibre's numerical aperture, and thus while a 1 km length of a certain fibre may have NA of 0.3, a 1 m length of the same fibre may have a NA of 0.37. The modes responsible for such effects are called leaky modes. Multimode fibres are especially sensitive to bending because after the higher modes leak out, the lower modes transform to a higher mode which in turn can leak out of the core. The bending does not need to be large- even microbending can cause serious problems.

Two additional sources of loss are absorption and Rayleigh scattering. Any impurities within the core can block some of the light and absorb its energy. Scattering can happen even due to tiny changes of refractive index or density of the core material. The amount of scattered light depends on the size of the discontinuity compared with the wavelength of the light. The amount of scattering increases dramatically as the wavelength decreases and can be calculated for solid transparent material using,

$$\text{Scattering} = A\lambda^{-4} \tag{4.13}$$

where A is a constant that depends on the homogeneity of the core material.

Dispersion can also occur in single mode fibres. Different wavelengths travel within the fibre with different speeds. As all light sources are not truly monochromatic, this dispersion (chromatic dispersion) can occur. The effects of two sources of dispersion- material dispersion and structure dispersion- can actually counteract each other at a particular wavelength. For example, standard fibre that is single mode at a wavelength of 1310 nm can have (nominally) zero dispersion (Goff 1999).

Another kind of dispersion is Polarization Mode Dispersion (PMD). Light can travel in both perpendicular polarization directions in a standard single mode fibre. As the fibre material is not perfectly isotropic, and environmental effects such as stress do

not lead to uniform effects in all directions, so the speed of light can be different in the two polarization directions and cause PMD (Goff 1999).

4.4.2 Fresnel backreflection

When the refractive index of a transparent medium changes, the angle of the light passing into the new medium can be calculated from Eq. (4.6). However, a few percent of the light power will be reflected. This phenomenon is called Fresnel reflection and the magnitude of this effect can be calculated using,

$$\text{Reflected Power (\%)} = \left(\frac{n_1 - n_2}{n_1 + n_2} \right)^2 \times 100\% \tag{4.14}$$

For example, if n_1=1.5 and $n_2 = 1$, the reflected power will be about 4% of incident light power.

4.4.3 Fibre nonlinearity

An advantage of fibre optic systems is the minor interaction between lights. However, there are some exceptions that should be considered. These processes are called nonlinear effects because they are not usually proportional to intensity (Hecht 2002).

4.4.3.1 Stimulated Brillouin scattering (SBS)

Optical power can generate small acoustic vibrations in the fibre when it exceeds a threshold power. The threshold level can be as low as few milliwatts for a single mode fibre. Acoustic waves alter the material density and produce changes of the fibre refractive index. The refractive index fluctuation scatters light and this scattered light can also generate further acoustic waves. This process is called *Stimulated Brillouin Scattering* or SBS. This periodic change of refractive index can also cause backreflection (Goff 1999). SBS limits the maximum power which can be transmitted along a fibre. This is because after saturation of the fibre, a significant fraction of power will backscatter towards the source or transmitter (Goff 1999). The SBS process also introduces substantial noise into the system.

Increasing the spectral bandwidth, fibre area, or light frequency can increase the SBS threshold. For example, a typical narrow bandwidth laser (less than 10 MHz) at a

wavelength of 1550 nm has 3 mW SBS threshold but by dithering the laser drive, the SBS threshold can be increased to 40 mW (Goff 1999).

4.4.3.2 Self-Phase modulation and Cross-Phase modulation

Change of light intensity can slightly alter the refractive index of the fibre which of course produces a change of light speed. This process is called self-phase modulation because the intensity modulation of a light changes the phase of the same light. If multiple wavelengths are used in the same fibre, the intensity change of one wavelength can affect the power of the other wavelengths and the process is called cross-phase modulation. Shift of frequency is in the opposite direction to the intensity change. The amount of the modulation depends on the rate of optical intensity change and the nonlinear coefficient of the fibre material (Hecht 2002).

4.4.3.3 Raman scattering

A molecule in a solid lattice can absorb a photon and re-emits a photon with the same energy plus or minus the energy associated with a change in the molecular vibration mode. This process can both scatter the light and change its wavelength, resulting in the generation of many different wavelengths from a nominally single wavelength source (Weik 1997; Hecht 2002).

The Raman shift can be a large effect- for example, a shift of 100 nm is possible for fibre at the 1550 nm wavelength. The effect can be even more substantial at shorter wavelengths (Hecht 2002).

4.4.4 Some kinds of optical fibre

Many kinds of optical fibre are commercially available for different applications. They are made with different materials, shapes and structures. Generally however, they can be divided into two kinds, single mode and multimode fibres.

According to Eq. (4.11), the number of modes can be decreased by decreasing the core diameter for a specific wavelength and material. Such a decrease can continue until only one mode exists within the core. Such fibres are termed single mode (SM).

It should be noted that a single mode fibre for a specific wavelength could have more modes when operated at a shorter wavelength. The minimum wavelength at which the fibre remains a single mode fibre is called the cutoff wavelength. Single mode fibre transmission avoids modal dispersion and modal noise, so SM fibres can carry signals with a much higher bandwidth than multimode fibres. Although the core diameter is the physical parameter used in the equations for single mode transmission, the core of a dielectric waveguide does not confine all the light. Some light in the guided single mode extends a short distance into the cladding. The diameter at which the intensity drops to a value of $1/e^2$ of the peak value in the core is called mode field diameter. This diameter depends on the wavelength and typically is about 10% to 15% greater than core diameter (Hecht 2002).

To prevent PMD (see Section 4.4.1), two kinds of fibre can be used: single polarization fibre and polarization maintaining fibre. Single polarization fibre has different attenuations in the different directions. It strongly attenuates the light in one direction but can transmit light well in the orthogonal direction. Therefore, only the desired polarization direction can be transmitted. Polarization maintaining fibre has internal strain or asymmetry, which effectively splits the input light into two separate polarization modes. This property is called birefringence (the refractive index of the fibre differs for the two polarizations) and prevents the light from shifting between polarizations. Attenuation of two polarizations is similar but they travel at different speeds because of the difference in the refractive index. If the light launched into the fibre already has a single polarization which is aligned properly with the fibre

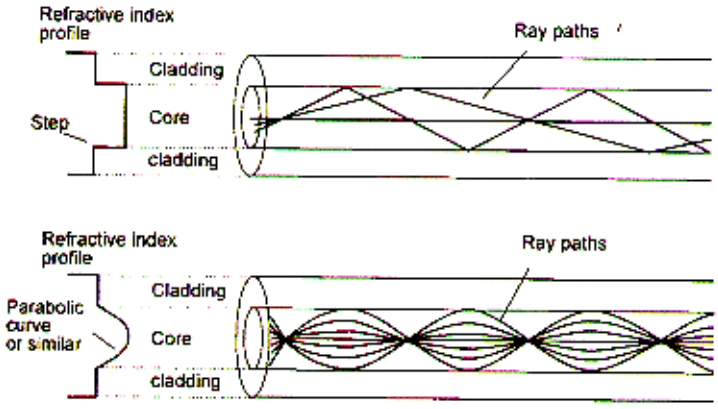

Figure 4.12 Light paths in multimode optical fibre: a) step index MM fibre; b) graded index MM fibre (reproduced from Crisp 1999).

polarization direction, the polarization will be maintained (Hecht 2002).

Another kind of fibre is multimode fibre (MM). According to Eq. (4.11), the number of modes increases when the core diameter increases. Launching light inside this type of fibre is much easier, however, due to modal dispersion as discussed in Section 4.4.1, the use of step index MM fibre in high-speed signal transmission is limited. Graded index MM fibre, in which the refractive index decreases slowly from the core into cladding, can eliminate modal dispersion (Fig. 4.12). This type of fibre increases the speed of light in longer modes and therefore, the modal dispersion can be eliminated.

4.5 Coupler

Couplers are passive components which connect three or more fibres together. They can have different ports, directionality and signal splitting ratios and they can be constructed using many different methods. One common coupler is a fused fibre coupler, as shown in Fig. 4.13. If the light enters the coupler from port 1, it splits into two ports 2 and 3. In practice, a very small part of light (typically less than 0.01%), which is the result of scattering and reflection, can travel in port 4. This design is inherently bidirectional and as light that enters from port 2 will divide into ports 1 and 4.

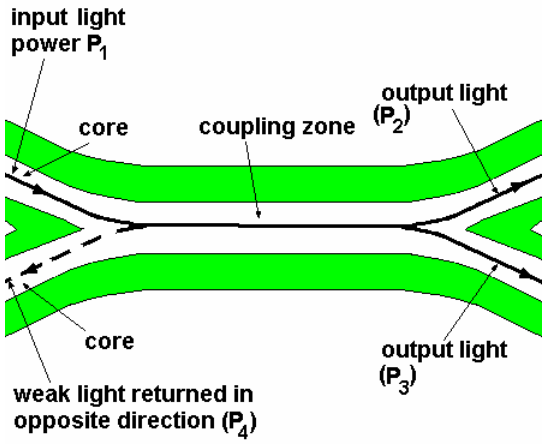

Figure 4.13 Illustration of a 2×2 fused fibre coupler (after Hecht & Zajak 1982).

Although Fig. 4.13 shows the cores from the two sides merged, they do not have to merge completely in the middle zone. A phenomenon called evanescent wave

coupling lets light pass through a thin zone of the lower refractive index (cladding) to the higher index zone (core). This is possible because some light actually travels in the inner portion of cladding (see Section 4.4.1). In MM fibre couplers, the higher-order modes leak into the cladding and into the core of the other fibre. The coupling mechanism is different for SM fibre. Light transfers between the two cores in a resonant interaction that varies with length. If all the light enters into the coupler from one fibre, it gradually transfers completely to the other, then transfers back as it travels farther, shifting back and forth cyclically. The distance over which the cycling takes place depends on the coupler design and the wavelength.

Couplers can be sensitive or insensitive to the wavelength or they can be wavelength selective, which is usually used in telecommunication networks to separate two different wavelengths. A coupler also can be sensitive to polarization and transmit the light differently in the vertical and horizontal directions. This can be a problem because most fibre optic systems do not constrain polarization. Random variations in input polarization can modulate the light output, producing noise and degrading signal quality.

4.6 Detectors

Detectors convert optical signals to an electronic form. The output of a detector is usually too weak to be used as an input for other devices. The output of a detector generally needs:

1. Preamplification;
2. Amplification;
3. Equalization; and
4. Filtering.

Preamplification is a low-noise amplification that is designed for weak signals. The output from the preamplifier is the input to an amplifier for power amplification and further voltage gain. Signals with different wavelengths may not be amplified identically causing frequency and phase distortion. An equalization circuit can balance these differences. Filtering increases the signal to noise ratio by selectively attenuating undesired noise and is often used in fibre optics.

Photon detectors are normally used in fibre optic systems. In general, there are two operational modes, in which detectors may work: photoconductive mode and photovoltaic mode. Photoconductive detectors make use of photoconductivity (change of conductivity by irradiance) in their operation and have a voltage power source such as a battery, to provide the current. Photovoltaic photodiodes use the photovoltaic effect (the production of a potential difference at the junction of two dissimilar materials) and do not require an external voltage force because they generate a voltage internally. Detectors operating in the photovoltaic mode have very low noise and high sensitivity, however their low bandwidth and slow response time makes them unsuitable in some applications.

4.6.1 Important detectors parameters

4.6.1.1 Signal quality

The quality of the signal produced by the detector and amplifier system depends on the signal and noise power. Higher noise makes it difficult to record the change of signal especially in analog systems. The signal to noise ratio (SNR) is usually defined as,

$$\text{SNR} = \frac{\text{Signal Power}}{\text{Noise Power}} \tag{4.15a}$$

Sometimes it is more convenient to define SNR as a logarithm,

$$\text{SNR (dB)} = 10 \times \text{Log}_{10} \left(\frac{\text{Signal Power}}{\text{Noise Power}} \right) \tag{4.15b}$$

4.6.1.2 Responsivity

Responsivity is defined as the ratio of the electrical output to the input optical power:

$$\text{Responsivity} = \frac{\text{Electrical Output}}{\text{Input Optical Power}} \tag{4.16}$$

Because the output of most fibre optic detectors is a current, the unit for responsivity is normally amperes per watt (A/W).

The responsivity of nearly all detectors is a function of wavelength and frequency. The frequency dependence of responsivity can generally be approximated using,

$$R(f) = \frac{R_0}{\sqrt{1 + 4\pi^2 f^2 \tau^2}} \tag{4.17}$$

where

R_0 Responsivity at zero frequency

τ Response time of detector (see Section 4.6.1.4)

4.6.1.3 Dark current and Noise Equivalent Power (NEP)

There is a small current even in the absence of any optical signal due to bias voltage and the intrinsic resistance of the detector. This current is called dark current and is extremely temperature sensitive and contributes to detector noise.

The minimum detectable optical power is limited by the noise in the operation of the detector. One source of noise is due to random emission of electrons (shot noise) which causes current fluctuations. Another noise source is the change of temperature (thermal noise or Johnson noise), which causes fluctuation in the load resistance of the detector. Shot noise and thermal noise exist in the detector and amplification circuit independent of the incoming optical power. Noise is proportional to current and bandwidth and it is minimum when there is no light. Another source of noise is the statistical fluctuation of photons or radiation noise. The electrical signal emerging from a detector and amplifier circuit includes both signal and noise. Some noise is associated with the input optical signal (optical noise), some is generated by the detector, and the amplifier circuit adds extra noise. Electromagnetic interference can cause noise when its fields induce currents in detector and amplifier conductors.

Noise Equivalent Power or NEP is defined as the minimum detectable optical power per square root bandwidth at a given frequency. NEP depends on frequency of the modulated signal, the bandwidth over which noise was measured, area of the detector, and operating temperature. NEP is usually measured at a 1 kHz modulation frequency and over a bandwidth of 1 Hz (Hecht 2002).

4.6.1.4 Response and delay time

The rise time of a detector is defined as the time the output signal takes to rise from 10% to 90% of the final level after a step in the input optical power is applied. Similarly, the fall time is defined as the time the output signal takes to drop from

90% to 10% after the input optical power is turned off. The longer of these quantities is considered the device response time, which depends on the intrinsic resistance of the detector, the geometry of the device, material composition, applied reverse voltage and other factors.

The approximate –3 dB frequency of a detector is given by,

$$f_{-3dB} = \frac{1}{2\pi R C} \tag{4.18}$$

where

R impedance that the detector operates into

C capacitance of the detector

The response time can be estimated using,

$$\tau = 2.2 \text{ R.C} \tag{4.19}$$

or

$$\tau = \frac{0.35}{f_{-3dB}} \tag{4.20}$$

Equations (4.18), (4.19) and (4.20) are almost precise for slow receivers. However, as response time decreases, these equations become more approximate as the time is needed for carriers to cross the depletion region, and the diffusion of current carriers in the photodiodes become significant.

4.6.1.5 Device geometry

The size of the detector is another important factor which should be considered. The larger the size of a detector, the longer its response time. However, the active area of a detector influences its sensitivity and for the highest sensitivity the active area should be large enough to capture all the input light.

If the output fibre has a core diameter D and a half acceptance angle θ, and is a distance S from the detector, the diameter of light spot d on detectors is,

$$d = D + 2S \tan \theta \tag{4.21}$$

If the spot size is larger than the active area of the detector, some light will be lost and sensitivity will be reduced. Most detectors have an active area larger than the

multimode core, so the problems are not usually encountered in the case of single mode fibre. However, misalignment or large distances between the fibre and the detector may cause problems.

4.6.1.6 Dynamic range

If the input optical power exceeds a certain amount, the detector begins to saturate and the relation between input and output will not be linear. NEP is defined as minimum input power that is distinguishable from noise. The range between these minimum and maximum optical powers is called the dynamic range.

4.6.1.7 Device capacitance

The capacitance of a detector is a function of the active area and the bias voltage. As the bias voltage increases, the capacitance decreases. However, bias voltages beyond 6 V do not further reduce the capacitance because the detector is already fully depleted, and in addition, such voltages can damage the detector.

Decreasing of the detector active area decreases its capacitance, however there is a limitation due to sensitivity. Illuminating a region in the edge area can cause a slow response in the detector.

4.6.1.8 Backreflection

If the fibre is coupled to the detector at a perpendicular angle, it is possible that from the detector couples back into the fibre. This backreflection is especially important in analog applications. A small angle (about 10^{o}) between the face of the detector and the fibre can decrease the backreflection.

4.6.1.9 Wavelength

The detector responsivity is related to the light wavelength and for the highest responsivity, different types of detectors should be used at different wavelengths. The responsivity of silicon detectors generally reaches a maximum between 800 nm and 900 nm.

4.6.2 Types of detector

PN photodiodes are made from P and N type semiconductors. Carriers are electrons in N type material also which has immobile positive ions. P type material is the reverse- its carriers are holes and the material also has immobile negative ions (fixed acceptor atoms). When these two types of material form a junction, the electrons from the N type and the holes from the P type diffuse across the junction and create an internal potential which prevents further diffusion, as shown in Fig. 4.14.

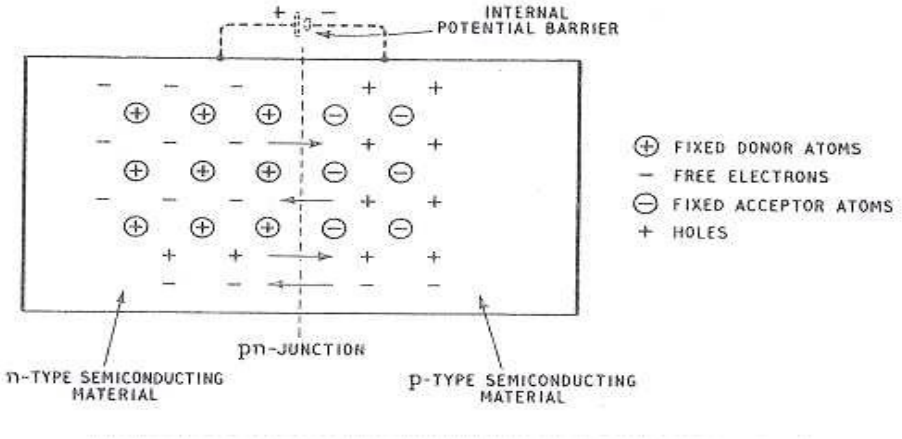

Figure 4.14 Initial conditions within a PN junction (reproduced from Amos 1990).

The region close to the junction is called the depletion area because the carriers in each material have diffused to the other side. It should be noted that it is possible that some electrons from the P type and holes from the N type drift to other side forming a weak drift current. The average distance which carriers can transverse without recombining is called the diffusion length. The thickness of the depletion area is much smaller than the diffusion length in PN diodes.

Applying a reverse bias voltage across the junction increases the thickness of the depletion area (Fig. 4.15). If a light illuminates the device, due to the narrow depletion area, most photons generally hit the PN photodiode outside of the depletion area. Photons that do impinge on the depletion zone create electron-hole pair, and due to the bias voltage they rapidly move in opposite directions. Electron-hole pairs

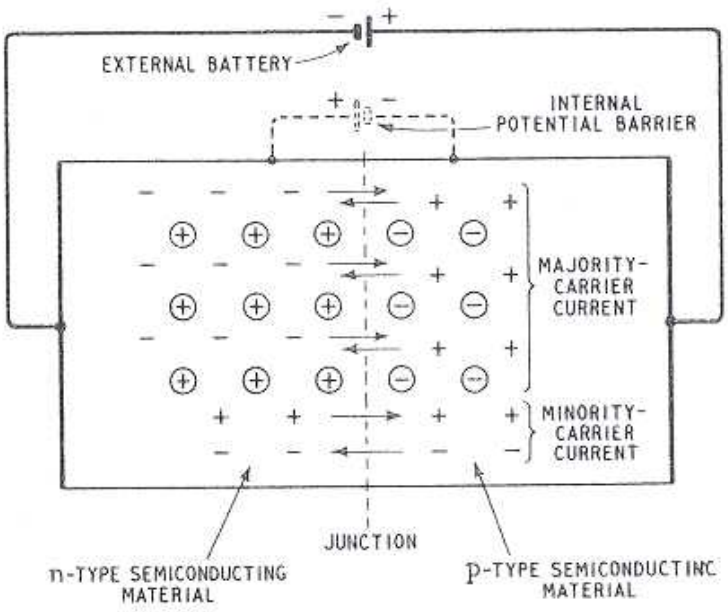

Figure 4.15 PN junction after applying bias voltage (reproduced from Amos 1990).

created by photon impingement outside the depletion area, moves slowly due to a larger distance and lower speed outside the depletion area.

The PN photodiode is similar to a variable resistor and it acts in the photoconductive mode. There is no current when there is no light (except dark current) and the current increases when the light hits the device within the diffusion length of the junction. PN photodiodes have a relatively slow response.

Increasing the thickness of the depletion area reduces the detector response time because most photons can be absorbed in the depletion area. However, further increases can also enlarge the distance over which the carrier has to travel and can have a reverse effect. Increasing the depletion area can be achieved by inserting an intrinsic semiconductor between the P and N type materials. These P-Intrinsic-N photodiodes or PIN photodiodes are faster than PN devices because most light is absorbed in the depletion area. Most of the bias voltage is concentrated across the intrinsic semiconductor because its resistivity is higher than *P* and *N* type materials. This concentration of voltage increases the speed of the carriers and reduces noise.

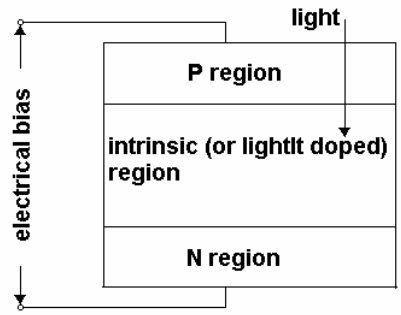

Figure 4.16 Schematic illustration of a PIN photodiode (after from Sharp c. 1990).

Typical bias voltages are between 5 V and 20 V and response time can be under 1 ns. PIN photodiodes are an adequate choice in most fibre optic systems. They have large dynamic range. Their responsivity changes with wavelength and a typical value is 0.6 A/W for a wavelength of 800 nm. They are the most commonly used solid-state detectors for visible and near infrared wavelengths.

4.7 Interrogation system review

The main factors in the design of most fibre optic interrogation systems are loss, bandwidth, response time, noise and cost. Ideally, all selected components should be well matched, but working system can still be created with some components operating off their design point.

Choosing the operating wavelength is the fundamental step in the design of a fibre optic system and it can affect all the important factors, which have been previously been discussed. The selected wavelength in this research work is approximately 780 nm. This selection, like other engineering options, has some advantages and disadvantages. The common wavelength in communication systems lies between 780 nm to 1610 nm. If a wavelength in this range is used, off- the- shelf components can be purchased which obviously reduces the cost. 780 nm is the lowest wavelength in this range and this low wavelength makes it possible to construct a sensitive pressure sensor, as discussed in Chapters 3 and 5 (see Eq. (3.4)). It permits the use of a relatively thick diaphragm, which increases the sensor natural frequency and bandwidth. According to Eq. (4.2) for a given spectral width, the lower the wavelength, the lower coherence length, and this may be a useful effect (no need to frequency dither).

Loss increases for short wavelengths in silica or glass fibres. This loss is a combination of light absorption and scattering. Losses due to absorption are not important in the present system due to the short length of fibre. The increase of scattering at the shorter wavelengths (Eq. (4.14)) even can be useful because they can eliminate their effects over coherence length, which is important for interferometric systems.

Silicon PIN detectors are relatively low cost devices and usually have their highest responsitivity around this wavelength. The laser diodes operating in the wavelength between 780 nm to 850 nm are easily available and relatively inexpensive.

However, this short wavelength (780 nm) has some disadvantages. A disadvantage of 780 nm is dispersion. As discussed earlier, the chromatic dispersion is a minimum at 1310 nm and it increases at shorter wavelength. In an interferometric system, selecting a single mode fibre decreases modal noise. Bending the multimode fibres can couple light from one mode to another mode and this significantly increases the system noise. The core diameter of single mode fibre optic is related to the operating wavelength. Launching light to a small core (necessary for low wavelength SM operation) can be difficult. Another disadvantage of low wavelength operation is related to a phenomenon called laser speckle (see Section 5.3). The roughness of a surface from which the light reflects should be less than a fraction of the operating wavelength to minimize speckle effects. Choosing a shorter wavelength causes some limitations, as discussed in Section 5.3.

The light polarization can change while travelling in fibre or upon reflection from the diaphragm. This change of polarization can decrease sensor visibility and cause it to fade in some cases. The use of polarization maintaining or single polarization fibre is recommended for interferometric systems (Gratton & Meggitt 2000). However, if a standard single mode fibre is used, it is estimated to control or minimize changes of polarization. In the present system, this is done through the use of an optical isolator, which increases the polarization of launched light. However, the polarization can still change within fibres and during reflection from diaphragm and this may decrease the sensor visibility.

After adopting 780 nm as the operating wavelength and using single mode optical fibre, the other system choices are somewhat straightforward. However, it is

important to know the maximum bandwidth and system response time particularly since the present intended use is in fast- response pressure sensors. The system response time can be calculated using (Hecht 2002),

$$\Delta t_{overall} = \sqrt{\Delta t^2{}_{transmitter} + \Delta t^2{}_{receiver} + \Delta t^2{}_{fibre}} \tag{4.22}$$

Response time measurements for the receivers at their different gain settings are presented in Appendix H. Laser response time does not affect the system response time because it operates at its steady condition in this work. Single mode fibre optic response time can be calculated using,

$$\Delta t_{\text{single mode}} = \sqrt{(D_{\text{chromatic}} \times L \times \Delta\lambda)^2 + (D_{\text{PMD}} \times \sqrt{L})^2} \tag{4.23}$$

where $D_{\text{chromatic}}$ is Chromatic dispersion and D_{PMD} is polarization-mode dispersion and L is fibre optic length and $\Delta\lambda$ is wavelength width. The length of fibre is a few metres and typical values for $D_{\text{chromatic}}$ and D_{PMD} are 3 ps/nm/km and 0.5 ps/km$^{0.5}$ respectively. Typical wavelength width is about 0.3 nm, so fibre response time is negligible (≈0.05 ns) in comparison with detector response time which is about 160 ns in the lowest detector gain. Bandwidth can be estimated from Eq. (4.4) and in the case of lowest gain for fastest detector, bandwidth is about 2.2 MHz.

The coherence length can be calculated from Eq. (4.2) and is around 200 μm for the laser diodes used in this work. As will be seen in Chapter 6, the cavity length in the sensors is about 10 μm, which means the minimum coherence length should be 20 μm. The actual coherence length (215 μm) is therefore quite satisfactory. Choosing a laser with a narrower wavelength increases the coherence length, but this is not necessary and may in fact degrade system performance. The Rayleigh backscattering due to impurities in the fibre and backscattering from several connections in the system can cause problems, especially in interferometry systems if the effects do not dissipate each other (it occurs if the coherence length is longer than the distance between the sources of scattered light). Due to the sufficiently low coherence lengths, it was not necessary to use a frequency dither.

The laser powers used in this work were between 3 mW and 30 mW. Choosing a higher power laser may not increase the signal to noise ratio due to the SBS effect. In some cases this effect was observed when using a 30 mW laser and, to decrease this effect, the fraction of light launched from the laser into the fibre was decreased.

Details of all selected fibre optic system parts are presented in Appendix K.

Chapter 5: Diaphragm design

5.1 Introduction

The diaphragm is one of the main features of the fibre optic pressure sensor, as discussed in Chapter 3. In this chapter, the important mechanical and optical properties in selecting the diaphragm material are discussed (Sections 5.2 to 5.6). The necessary equations in the design of the diaphragms are then presented in Sections 5.7 to 5.9 and the effects of pretension and thermal isolation layers on sensor performance are also discussed in these sections. Three candidate diaphragm materials are discussed in some detail (Section 5.10) and a sample calculation for a copper foil is performed to demonstrate the possibility of making a fast response sensor from this commercial foil material (Section 5.11).

5.2 Important mechanical properties

Yield strength – the stress at which a material shows a particular offset from the proportionality of stress and strain, see Fig. 5.1. An offset of 0.2% is used as the specified deviation for many materials.

Ultimate strength – the maximum stress (tensile, compressive or shear) that a material can withstand.

Proportional limit – the maximum stress at which the strain remains directly proportional to the stress (see Fig. 5.1).

Elastic limit – the maximum stress at which a material does not show any permanent deformation. The elastic limit is slightly above the proportional limit for most materials.

Proof stress – the maximum stress at which the permanent material deformation remains less than the amount that can be measured by the extensometer (see Fig. 5.1)

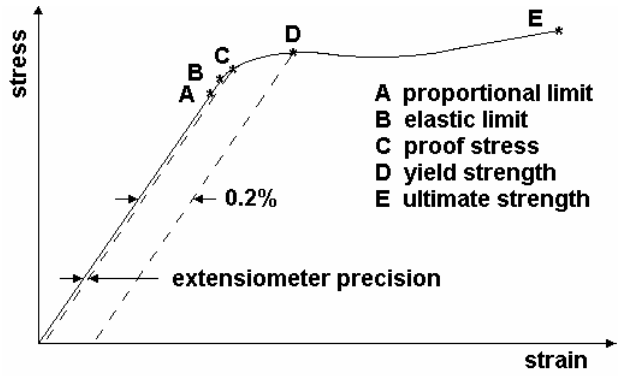

Figure 5.1 Illustrative stress-strain diagram for a ductile material.

Elastic modulus – (Young's modulus) is a measurement of stiffness, denoted by the symbol *E*, and is equal to the ratio of uniaxial stress to strain up to the proportional limit, as shown in Fig. 5.1.

$$E = \frac{\sigma}{\varepsilon} \tag{5.1}$$

The elastic modulus in tension is very important in the design of the pressure sensitive diaphragm as the diaphragm deflection is directly proportional to the elastic modulus.

Shear modulus – (or the modulus of rigidity) is the ratio of shear stress to shear strain within the proportional limit. The shear modulus is usually represented by the symbol *G*. Provided the elastic modulus and Poisson's ratio is known, it can be calculated from the elastic modulus using

$$G = \frac{E}{2(1+\nu)} \tag{5.2}$$

where *E* is the modulus of elasticity in tension and ν is Poisson's ratio.

Poisson's ratio – the ratio of the transverse to the longitudinal strain within the elastic limit for uniaxial loading. Typically Poisson's ratios vary between 0.25 and 0.35 for metals. It can be calculated from Eq. (5.2) if *G* and *E* are both known.

Ductility – a material property, which allows deformation without rupture. The lack of ductility in a material is called brittleness.

Impact strength – indicates the toughness of the material. This property is especially important for shock loading.

Hardness – indicates the resistance of a material to plastic deformation. Resistance to erosion increases with increasing hardness.

Endurance limit – the maximum cyclic stress that can be applied indefinitely without leading to failure.

Fatigue strength – the maximum cyclic stress that can be applied for a specific time (usually 10^9 cycles) without failure. Nonferrous materials usually do not have an endurance limit and fatigue strength is used instead.

Surface finish – leads to an increase in the corrosion resistance and fatigues strength of materials, however its effect on static performance is negligible.

5.3 Important optical properties

Reflectivity – the ratio of the energy of a wave reflected from a surface to the energy of the incident wave on that surface. This is especially important for a fibre optic pressure sensor, which works on the basis of reflected light as discussed in Chapter 3.

Roughness – a description of the deviation of the surface heights from the mean height value. There are no less than thirty-five different parameters for describing surface quality (Cochrane 1998). The average roughness (R_a), which is the average of the modulus of the surface heights about the mean surface height, is an industrial measure of surface finish. *RMS* roughness (R_q or σ) is the root mean square value of the surface heights about the mean surface height and is used more in theoretical analyses.

A laser source can include many waves with parallel paths. When a laser irradiates a rough surface, the reflected light is not parallel. Therefore, the reflected waves received at one point can have phase differences which arise because of different optical path lengths. Interference of these waves causes a different resultant irradiance at neighbouring points. This variation is called objective speckle (Fig. 5.2).

If an object diameter and its distance from the receiver are D and L respectively, then the statistical average of the path differences gives the average diameter S_{obj} of the speckle patches (Cloud 1998, Eq. (18.1)),

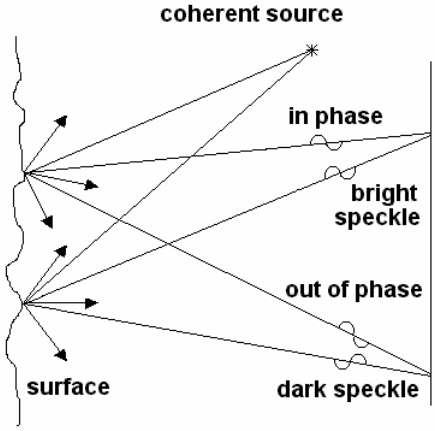

Figure 5.2 Speckles formed by interference of coherent light that is scattered or reflected from a surface (after Cloud 1998).

$$S_{obj} = 1.22\frac{L}{D}\lambda \tag{5.3}$$

The speckle wavelength can differ from the interrogation system wavelength (Cloud 1998).

5.4 Thermal effects on physical properties

Most materials are temperature sensitive which mean that their physical properties change with temperature. In particular, the modulus of elasticity of most materials decreases with an increase in temperature. The pressure sensitivity of a diaphragm will therefore increase with temperature.

Some ferromagnetic materials exhibit a different behaviour, which can be utilized to make constant-modulus alloys. NI-SPAN 902C alloy is an alloy which exhibits a controllable thermoelastic coefficient (Di Giovanni 1982). The alloy can be made to have an essentially constant modulus of elasticity from –10^{o}C to +65^{o}C and low material hysteresis (see Section 5.5) by using a specific heat treatment and cold work.

Other relevant temperature effects include: 1) oxidation of the diaphragm material; and 2) decrease in tensile strength. For example, most aluminium alloys should not be used above 100^{o}C as the tensile strength reduces sharply above this temperature.

5.5 Material hysteresis

If the pressure on the diaphragm increases and decreases during an experiment, the diaphragm deflection for the increasing and decreasing pressure phases may be measurably different because of hysteresis. The mechanism which gives rise to mechanical hysteresis is energy dissipation by friction on a molecular scale. This energy appears as heat in dynamic cycling. It is very difficult to calculate hysteresis effects, but they can be reduced or almost eliminated by the proper choice of material and stress level. Crystalline materials such as moncrystalline silicon chips, generally exhibit low hysteresis errors (Di Giovanni 1982).

For a diaphragm, which is required to work in cyclic loading conditions, the endurance limit and fatigue strength become important factors. If the allowable stress is kept to less than 35% and 50% of the ultimate stress for nonferrous and ferrous metals, respectively, then it appears that plastic deformation does not occur even on a microscopic scale (Di Giovanni 1982) and the width of hysteresis loop approaches zero.

5.6 Diaphragm stability

Sensor stability and repeatability of are very important factors – without these, accurate calibration is not feasible. Sources of non-repeatability include residual stress, plastic deformation, metallurgical changes, stress concentration, corrosion and thermal effects. Diaphragm stability can be achieved for most materials by applying a pressure that is twice the maximum working pressure provided this load does not exceed the proportional limit. This process can release residual stresses in material, however, it can also change Young's modulus and the thermal expansion coefficient by a few percent. To ensure stability over extended periods, the maximum stress should be kept to less than 30% of the yield strength. Metallic coatings usually do not improve the performance of a diaphragm, in fact they can decrease the endurance limit by 35%. A general theory to justify the endurance limit reduction has not been established yet, however fine cracks and residual stress are possible factors (Di Giovanni 1982).

5.7 Basic equations for diaphragm design

The basic equations for the calculation of stress and deflection of a circular diaphragm are presented in this section. There are numerous texts (e.g., see those listed in Di Giovanni (1982)) which derive or present these equations. They are repeated here for completeness. The key assumptions are:

1) The diaphragm is flat and has uniform thickness.

2) The diaphragm is made with an isotropic and homogenous material.

3) The stresses remain within the elastic limit.

4) All loads are perpendicular to diaphragm.

5) The diaphragm is “thin” (which in practice means its thickness is less than 20% of its diameter) (Di Giovanni 1982).

6) The deflections are “small” (which in practice means the deflection is less than 30% of thickness).

Two types of diaphragm edge support are usually considered:

1) Simply supported; and

2) Fixed (or clamped) edge.

In the simply supported case, the diaphragm is supported only by a frictionless annular knife edge and thus there is no bending stress near the diaphragm edge. In the fixed support case, a moment can be transferred to the edges and therefore bending stresses do develop at the support. Both types of support are idealised models and the behaviour of the real support is likely to have characteristic of both arrangements.

Unless otherwise noted, all equations presented in this section are from Di Giovanni (1982). The nomenclature for these equations are presented as below,

a diaphragm radius

E Young’s modulus

h diaphragm thickness

p differential pressure on diaphragm

r distance from centre of diaphragm

W membrane translation force

y defection of diaphragm

y_0 defection at diaphragm centre

ε_t peripheral deformation

ν Poisson's ratio

σ_r radial stress

$\sigma_{r,max}$ maximum radial stress in diaphragm

σ_θ tangential stress

$\sigma_{\theta,max}$ maximum tangential stress in diaphragm

5.7.1 Fixed edge circular diaphragm

The deflection of every radial location can be calculated using,

$$y = \frac{3(1-\nu^2)p}{16Eh^3}(a^2 - r^2)^2 \tag{5.4}$$

The maximum deflection occurs at the centre of the diaphragm and is given by,

$$y_0 = \frac{3(1-\nu^2)pa^4}{16Eh^3} \tag{5.5}$$

The radial stress σ_r at any distance r from the centre can be calculated using the equation,

$$\sigma_r = \pm\frac{3}{8}\frac{pa^2}{h^2}\left[(3+\nu)\frac{r^2}{a^2} - (1+\nu)\right] \tag{5.6}$$

The maximum radial stress is at the fixed edge and is

$$\sigma_{r,\max} = \pm\frac{3}{4}\frac{pa^2}{h^2} \tag{5.7}$$

The tangential stress σ_θ at any radial distance r can be calculated from the expression,

$$\sigma_\theta = \pm\frac{3}{8}\frac{pa^2}{h^2}\left[(3\nu+1)\frac{r^2}{a^2}-(1+\nu)\right] \tag{5.8}$$

The maximum tangential stress is at the centre and is given by,

$$\sigma_{\theta,\max} = \mp\frac{3}{8}(1+\nu)\frac{pa^2}{h^2} \tag{5.9}$$

Sometimes it is more convenient to relate stress to deflection (rather than to the applied load, p) in which case,

$$\sigma_r = \pm\frac{2Ehy_0}{(1-\nu^2)a^2}\left[(3+\nu)\frac{r^2}{a^2}-(1+\nu)\right] \tag{5.10}$$

and

$$\sigma_\theta = \pm\frac{2Ehy_0}{(1-\nu^2)a^2}\left[(3\nu+1)\frac{r^2}{a^2}-(1+\nu)\right] \tag{5.11}$$

5.7.2 Simply supported circular diaphragm

For a simply supported diaphragm, the deflection can be calculated using,

$$y = \frac{3}{16}\frac{(1-\nu^2)p(a^2-r^2)}{Eh^3}\left(\frac{5+\nu}{1+\nu}a^2-r^2\right) \tag{5.12}$$

The value of deflection is maximum in the centre and is given by,

$$y_0 = \frac{3}{16}\frac{Pa^4}{Eh^3}(1-\nu^2)\left(\frac{5+\nu}{1+\nu}\right) \tag{5.13}$$

Assuming ν=0.3 and comparing Eq. (5.13) with Eq. (5.5) indicates that simply supported diaphragms have a deflection in the centre approximately 4 times that of fixed edge diaphragms.

The radial stress for a simply supported edge diaphragm at any radial distance r is,

$$\sigma_r = \frac{3}{8}\frac{pa^2}{h^2}\left[(3+\nu)\left(1-\frac{r^2}{a^2}\right)\right] \tag{5.14}$$

and the tangential stress at any radial distance is,

$$\sigma_\theta = \frac{3}{8}\frac{p}{h^2}\left[a^2(3+\nu)-r^2(1+3\nu)\right] \tag{5.14}$$

The tangential stress is a maximum at the centre of the diaphragm and is equal to the radial stress.

5.7.3 Membrane effects

When the deflection of a diaphragm is large ($y_0/h>5$), especially for a thin diaphragm ($h/a<0.4$), the median plane is under tension and the diaphragm can be considered as a membrane (Di Giovanni 1982). An ideal membrane has no flexural rigidity and does not provide any bending stress resistance during deflection. It cannot resist any load when it is flat.

The characteristic equation of a membrane as developed by Andreeva (cited in Di Giovanni 1982) is:

$$\frac{pa^4}{Eh^4} = \frac{7-\nu}{3(1-\nu)}\frac{{y_0}^3}{h^3} \tag{5.16}$$

Equation (5.16) indicates that the deflection of a membrane is non linear – its rigidity increases at larger deflections.

A membrane cannot support its own weight without deflecting. If an initial tension W is applied to a membrane, the characteristic equation becomes,

$$\frac{pa^4}{Eh^4} = \frac{7-\nu}{3(1-\nu)}\frac{{y_0}^3}{h^3} + \frac{4}{1-\nu}\frac{y_0}{h}\frac{Wa}{h^2} \tag{5.17}$$

The tension W is the membrane translation force defined as,

$$W=\varepsilon_\theta\, a \tag{5.18}$$

where ε_θ is peripheral strain caused by W. The effect of the initial tension is to provide more rigidity and linearity to the membrane.

5.7.4 Deflection of a thin circular diaphragm clamped at edges for any deflection

Di Giovanni (1982) suggests that a method of superposition can be used to calculate the deflection of a very thin diaphragm ($h/a<0.15$), for any load according. Combining Eqs. (5.5) and (5.16) gives,

$$\frac{pa^4}{Eh^4} = \frac{16}{3(1-\nu^2)}\frac{y_0}{h} + \frac{7-\nu}{3(1-\nu)}\frac{{y_0}^3}{h^3} \tag{5.19}$$

5.8 Effects of pretension on diaphragm performance

It has been suggested that pretensioning the diaphragm during construction may lead to an improvement in pressure sensor performance. It is therefore desirable to evaluate the effects of pretensioning the diaphragm during construction, that is, how pretensioning can change the maximum stress, deflection, pressures and temperature sensitivity of a diaphragm.

Actual pretensioning during sensor construction could be achieved directly by applying a biaxial tension to the diaphragm or indirectly by increasing the diaphragm temperature during the adhesive curing process. In the case of increasing the diaphragm temperature during bonding to substrate, a pretensioning effect will be achieved when the diaphragm cools.

The symbols used in Section 5.7 are again employed here. New symbols introduced in this section are,

D flexural rigidity of diaphragm

f_r radial force per length

f_θ tangential force per length

H nondimensional h

P differential pressure on diaphragm

P^* P normalised using H^3

R nondimensional r

S_1 nondimensional radial stress

S_2 nondimensional tangential stress

S_{eq} nondimensional equivalent stress

Δt temperature change

T nondimensional σ_{pt}

T^* T normalised using H^2

Y nondimensional y

Y_0 nondimensional y_0

α_T thermal expansion coefficient

σ_r radial stress

σ_θ tangential stress

σ_{pt} stress due to pretensioning

5.8.1 Governing equations

Assuming the diaphragm material is homogenous and isotropic with constant material properties (e.g., properties that do not change with temperature), the differential equation governing the deflection of an axisymmetric pretensioned diaphragm under uniform loading due to pressure p is given by (Donnel 1976),

$$D\left(\frac{d^4y}{dr^4}+\frac{2}{r}\frac{d^3y}{dr^3}-\frac{1}{r^2}\frac{d^2y}{dr^2}+\frac{1}{r^3}\frac{dy}{dr}\right)=p+f_r\frac{d^2y}{dr^2}+\frac{f_\theta}{r}\frac{dy}{dr} \tag{5.20}$$

where D is the flexural rigidity,

$$D=\frac{Eh^3}{12(1-\nu^2)} \tag{5.21}$$

In the derivation of Eq. (5.20), shear stress and direct stress perpendicular to the diaphragm are not considered (this is not a restrictive assumption for thin diaphragms, $h/a<0.3$ (Donnel 1976)). Furthermore, it is assumed the radial and tangential stress due to pretensioning of the diaphragm are equal and do not change with diaphragm defection. This assumption is accurate only for small diaphragm defections. For large diaphragm deflections, the membrane effects (see Section 5.7.3) and large deflection behaviour will lead to inaccuracies with the approach taken in this section.

Assuming that the diaphragm pretensioning is due to a uniform biaxial load, the radial and tangential forces per unit length can be written,

$$f_r = f_\theta = h\sigma_{pt} \tag{5.22}$$

The governing equation can be written in non dimensional form,

$$\frac{d^4Y}{dR^4}+\frac{2}{R}\frac{d^3Y}{dR^3}-\frac{1}{R^2}\frac{d^2Y}{dR^2}+\frac{1}{R^3}\frac{dY}{dR}=\frac{P}{H^3}+\frac{T}{H^2}\frac{d^2Y}{dR^2}+\frac{1}{R}\frac{T}{H^2}\frac{dY}{dR} \tag{5.23}$$

where

$$Y=\frac{y}{a} \tag{5.24}$$

$$R=\frac{r}{a} \tag{5.25}$$

$$H=\frac{h}{a} \tag{5.26}$$

$$T=\frac{\sigma_{pt}}{\frac{E}{12(1-\nu^2)}} \tag{5.27}$$

$$P=\frac{p}{\frac{E}{12(1-\nu^2)}} \tag{5.28}$$

Further simplification of the governing equation is possible by using additional nondimensional variables,

$$P^*=\frac{P}{H^3} \tag{5.29}$$

$$T^*=\frac{T}{H^2} \tag{5.30}$$

The governing differential equations, Eq. (5.23) can be solved by a series solution assuming,

$$Y=\sum_{n=0}^{\infty}a_nR^n \tag{5.31}$$

Boundary conditions can be written in nondimensional form,

$$Y_{R=1}=0 \tag{5.32}$$

$$\left(\frac{dY}{dR}\right)_{R=0,1}=0 \tag{5.33}$$

Solving the Eq. (5.23) in the case of pretensioning ($T^*\neq 0$) gives,

$$Y = a_0 + a_2 R^2 + a_4 R^4 + a_4 \sum_{n=3}^{\infty} b_n R^{2n} \tag{5.34}$$

where

$$a_4 = \frac{\frac{P^*}{4}}{16 + T^*(2 + \sum_{n=3}^{\infty} n b_n)} \tag{5.35}$$

$$b_n = (T^*)^{n-2} \frac{1}{4^{n-3} n!^2} \tag{5.36}$$

$$a_2 = \frac{16}{T^*} a_4 - \frac{P^*}{4T^*} \tag{5.37}$$

and

$$a_0 = -a_2 - a_4 - a_4 \sum_{n=3}^{\infty} b_n \tag{5.38}$$

In the case of no pretension (T^*=0), the diaphragm defection can be calculated as,

$$Y = \frac{P^*}{64}(1 - R^2)^2 \tag{5.39}$$

5.8.2 Diaphragm strength

The maximum and minimum direct stresses within the diaphragm occur at the diaphragm surfaces and will be given by Donnel (1976),

$$\sigma_r = \frac{f_r}{h} \pm \frac{6}{h^2} D(\frac{d^2 y}{dr^2} + \frac{\nu}{r}\frac{dy}{dr}) \tag{5.40}$$

and

$$\sigma_\theta = \frac{f_\theta}{h} \pm \frac{6}{h^2} D(\frac{1}{r}\frac{dy}{dr} + \nu\frac{d^2 y}{dr^2}) \tag{5.41}$$

which can be written in nondimensional form as

$$S_1 = T \pm 6H(\frac{d^2 Y}{dR^2} + \frac{\nu}{R}\frac{dY}{dR}) \tag{5.42}$$

and

$$S_2 = T \pm 6H\left(\frac{1}{R}\frac{dY}{dR} + \nu\frac{d^2Y}{dR^2}\right) \tag{5.43}$$

The stresses can be written in nondimensional form as

$$S_1 = \frac{\sigma_r}{\frac{E}{12(1-\nu^2)}} \tag{5.44}$$

and

$$S_2 = \frac{\sigma_\theta}{\frac{E}{12(1-\nu^2)}} \tag{5.45}$$

Assuming the diaphragm material is ductile, the nondimensional equivalent stress can be written as,

$$S_{eq} = (S_1{}^2 + S_2{}^2 - S_1S_2)^{0.5} \tag{5.46}$$

5.8.3 Effect of thermal expansion on pretension

Due to differing thermal expansion coefficients for the diaphragm and substrate materials, the magnitude of pretension changes with temperature and can be expressed as,

$$\Delta\sigma_{pt} = -\frac{E}{(1-\nu)}\Delta\alpha_T\Delta t \tag{5.47}$$

The change of pretension in nondimensional form is,

$$\Delta T = -12(1+\nu)\Delta\alpha_T\Delta t \tag{5.48}$$

where $\Delta\alpha_T$ is the difference in thermal expansion coefficient of the diaphragm and substrate material, and Δt is the change of temperature. Equation (5.48) indicates that changes in pretension are directly related to changes in temperature.

5.8.4 Results and Discussion

The effect of pretension on diaphragm defection, pressure sensitivity and temperature sensitivity can be calculated using Eq. (5.34). Equation (5.48) shows the sensitivity of a diaphragm to pretension is proportionally related to sensor temperature sensitivity. The stresses can be calculated using Eqs. (5.34), (5.42), (5.43), (5.46).

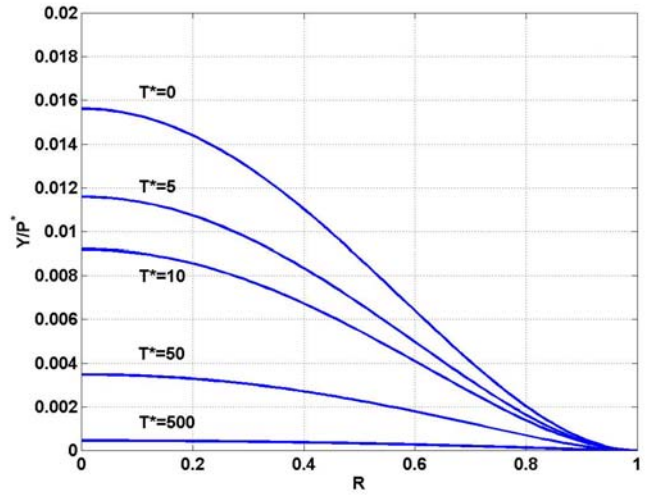

Figure 5.3 Normalised diaphragm shape, Y/P^* for various values of normalised pretension.

For all calculations presented in this section, the series in Eq. (5.34) was evaluated to n=30 and the maximum errors is estimated to be less than 1×10^{-4}% of the exact solution.

Figure 5.3 shows the effects of pretension on diaphragm deflection. The pretension decreases the central diaphragm deflection, however the shape of the diaphragm does not change. Figure 5.4 shows the effect of pretension on diaphragm pressure sensitivity. According to this figure, the pressure sensitivity changes sharply for

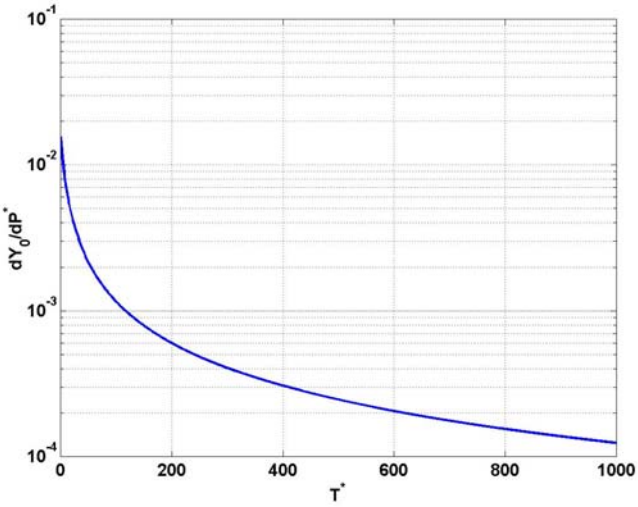

Figure 5.4 Nondimensional pressure sensitivity of the diaphragm, dY_0/dP^* as a function of normalised pretension T^*.

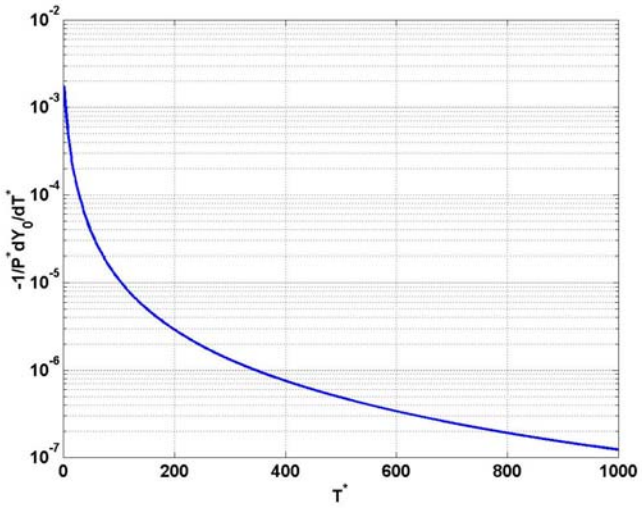

Figure 5.5 Nondimensional pretension sensitivity of the diaphragm, dY_0/dT^* normalised using P^* and presented as a function of normalised pretension T^*.

small values of pretension (T^*<1) but its effect decreases with further pretension. For example, if pretensioning was applied to a sample diaphragm (copper diaphragm with a thickness of 9 μm and a diameter of 125 μm, see Section 5.11) such that T^*=1.6, the pressure sensitivity would decrease to about 15% of its original value.

Figure 5.5 indicates that increases in pretension can decrease the temperature sensitivity of the diaphragm (which is directly related to dY_0/dT^* through Eq. (5.48)). The effect of pretension on temperature sensitivity is similar to the effect of pretension on pressure sensitivity – its effect is strong for small values of pretension but it decreases for higher values of pretension. For example, the change of temperature sensitivity for the sample diaphragm is about 25% which is more than 15% of pressure sensitivity change for the same sample diaphragm.

Figure 5.6 shows the effect of pretension on the ratio of pressure sensitivity to pretension (or temperature) sensitivity. It indicates that although the pressure sensitivity and temperature sensitivity decreases simultaneously with increasing values of pretension, the temperature sensitivity decreases more rapidly.

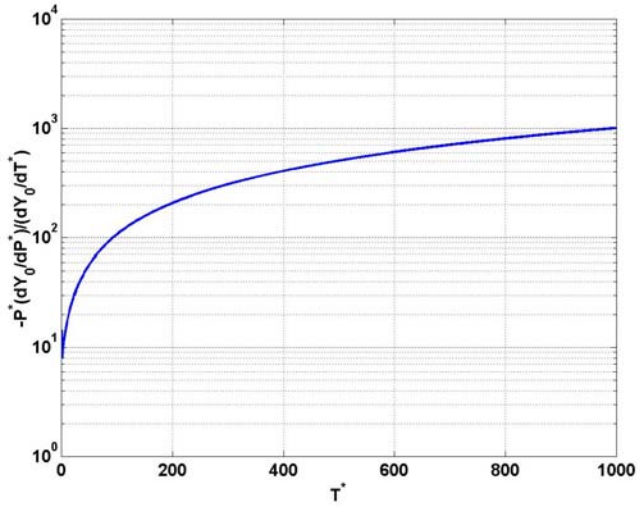

Figure 5.6 Pressure sensitivity of the diaphragm relative to its pretension sensitivity, $(dY_0/dP^*)/(dY_0/dT^*)$ scaled with the pressure P^* and presented as a function of normalised pretension T^*.

Figure 5.7 shows the effect of pretension on stress level. It indicates that for a very thin diaphragm where its thickness is less than 5% of its radius, the maximum equivalent stress decreases if the pretension does not exceed a particular value. However, for a thicker diaphragm (h/a>0.05) the stress level increases and this introduces a new design limitation for the pretension. For example, for a typical diaphragm, where H=0.048, the value of equivalent stress does not change with pretension up to T=0.01.

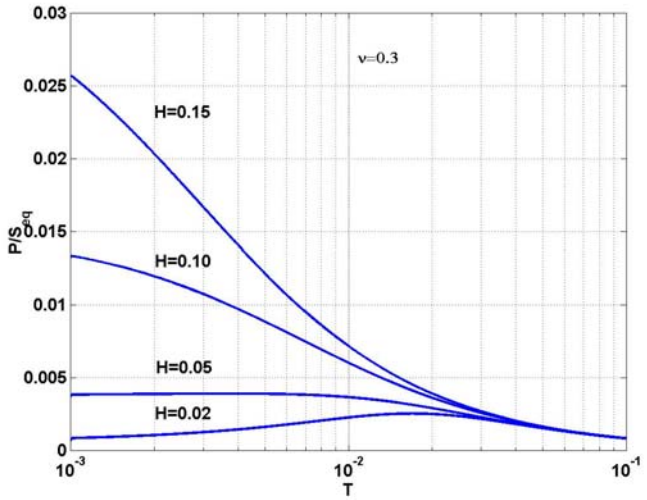

Figure 5.7 Pressure required to produce a given stress state, P/S_{eq} as a function of nondimensional pretension, T for various values of nondimensional thickness, H.

5.9 Diaphragm natural frequency

The derivation of equations for the natural frequency of circular diaphragms including the effects of pretension and thermal isolation layers is presented in Appendix G.

5.9.1 Fixed edge circular diaphragm

The response time of a diaphragm is related to its natural frequency. For a fast response sensor, it is necessary to have a high natural frequency diaphragm. The lowest (fundamental) natural frequency of a clamped edge circular diaphragm with the assumptions presented in Section 5.7 is,

$$f_n = \frac{10.21}{2\pi a^2}\sqrt{\frac{D}{h\rho}} \tag{5.49}$$

where D is the flexural rigidity as defined in Eq. (5.21).

Combining Eqs. (5.49) and (5.21) shows that the natural frequency is proportional to h/a^2, and according to the equations presented in Section 5.7.1, the stress is proportional to a^2/h^2. This means that if a/h remains constant and the diaphragm diameter decreases, then the maximum stress remains constant whilst the natural frequency increases. Therefore, one approach to fast response sensor design is to decrease the diaphragm diameter and thickness. In this approach, however, there will be a trade off with sensitivity as the diaphragm deflection varies with a^4/h^3 and thus the sensitivity will decrease in proportion to the diameter if a/h is held constant.

In practice, other factors influence the calculated natural frequency. For example, if gas is trapped behind the diaphragm, the natural frequency will increase due to a stiffening effect associated with the trapped air (Di Giovanni 1982).

5.9.2 Effects of pretension

The effects of pretension on the natural frequency of a clamped circular diaphragm are identified in Appendix G. Results for a diaphragm with $\nu=0.3$ are presented in Fig. 5.8. Pretensioning the diaphragm has only a moderate effect on the diaphragm natural frequency. For example, applying a normalised pretension of T^*=1.6 increases the natural frequency of a diaphragm without any thermal isolation layer (M=0) by only 0.5%.

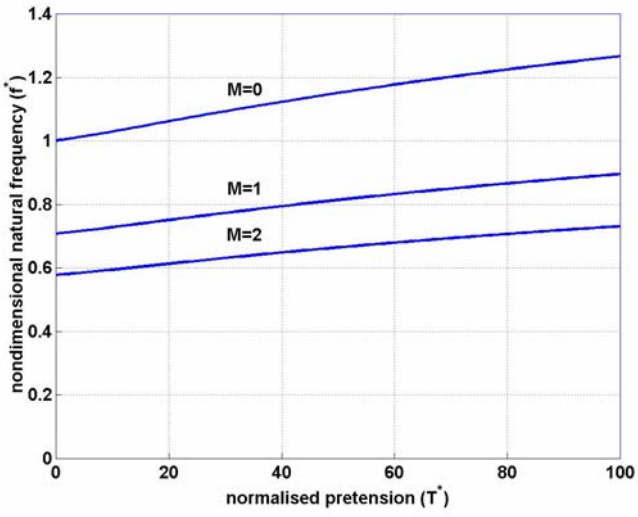

Figure 5.8 Effects of pretension and thermal protection layer on the first natural frequency of a clamped circular diaphragm (ν=0.3).

5.9.3 Effects of thermal isolation layer

As diaphragm pressure sensors can show a high temperature sensitivity (and certainly the fibre optic pressure sensors described in this work are no exception as discussed in Chapters 6 and 8), it is necessary to protect the diaphragm against the high temperature flow by applying a thermal isolation layer. The intention is to choose an isolation layer such as grease that has a very low flexural rigidity, and so does not contribute to the diaphragm's potential energy during deflection. However, such a layer can provide a large contribution to the diaphragm's kinetic energy during vibration. This results in a decrease in the diaphragm's natural frequency and details of the derivation are presented in Appendix G. The final results is presented as Eq. (5.50),

$$f = f_0 \sqrt{\frac{1}{(1+M)}} \tag{5.50}$$

where the natural frequency of diaphragm without any thermal isolation layer is designated by f_0, and M represents the ratio of ρh of the thermal isolation layer to that of the diaphragm.

According to Eq. (5.50), the thermal isolation layer can have a substantial influence on the natural frequency of the diaphragm if a thick layer is employed (Fig. 5.8). For

example, the natural frequency of copper foil diaphragm with a thickness of 9 μm (supplied by MICRO HARD Ltd, see Table 6.3) and a thermal isolation layer of grease with a thickness of 3 mm (assuming $\rho=884$ kg/m (Matweb material property data 2002)), decreases to 17% of its initial value. This shows an important limitation of using a thick isolation layer. A relatively thin layer does not substantially affect the natural frequency. For example, applying a 0.1 mm thick grease layer only decreases the natural frequency by 30%, which is a modest reduction. The required thermal isolation thickness can be calculated by considering the sensor temperature sensitivity and the required measurement duration.

5.10 Diaphragm material selection

As discussed in Section 5.9, choosing a thinner diaphragm with a proportionally smaller diameter increases the natural frequency without increasing the diaphragm stresses. This leads to using a very thin foil, which should be commercially available. Other important factors in material selection include optical reflectivity, modulus of elasticity, yield strength, hardness, roughness, thermal expansion coefficient, and cost. The choice of diaphragm material involves a trade off between these factors. For example, Invar which has a very low coefficient of thermal expansion (around $2\times10^{-6}/^{o}C$) (Goodfellow c. 1998/9) and is available in a thickness of 8 μm, has a relatively high price (more than $200 Australian, for a 25 mm× 25 mm sample) (Goodfellow c. 1998/9).

Three representative materials considered for the diaphragm were: 1) aluminium; 2) copper; and 3) silicon. Aluminium has high optical reflectivity, silicon has low thermal expansion coefficient, while copper has an average value for both these features. The properties of these three materials are presented in Table 5.1.

Table 5.1 Selected properties of aluminium, copper and silicon (Matweb 2002; goodfellow c. 1998/9; Richardson & Crook 1998).

Material Property	Aluminium (1145-H19)	Copper (cold worked)	Silicon
Density (kg/m^3)	2705	8960	2329
Hardness (Vickers)	45	100	11270 (Knoop μhard.)$^{+++}$
Modulus of Elasticity (GPa)	69	110	112.4
Poisson's ratio	0.33	0.35	0.28 (0.42)$^{+}$
Shear modulus (GPa)	26	46	49
CTE, linear 20^{o}C (μm/m/^{o}C)	23.6	16.4	2.49 (4.7-7.6)$^{+}$
Heat capacity (J/kg/^{o}C)	904	385	702
Thermal conductivity (W/m/^{o}C)	225	385	124
Tensile Strength, ultimate (MPa)	165	344*	3790^{++}
Tensile strength, yield (MPa)	145	333.4*	-
Elongation at rupture	2.5%	14%*	-
Shear modulus (GPa)	26	46*	-
Shear strength (MPa)	100	-	-
Reflectivity	96%	63%	30% – 70%

* Cochrane (1998) for copper Cold Drawn
** Goodfellow (c. 1998/1999) for temperature 0-100^{o}C
\+ Goodfellow (c. 1998/1999)
++ Richardson & Crook (1998) for a single crystal silicon
+++ Goodfellow (c. 1998/1999) gives 7 Mohrs

According to Table 5.1, aluminium shows the best reflectivity for visible light. Aluminium foils are also cheap and are readily available. However, aluminium has a high coefficient of thermal expansion and the lowest mechanical strength.

Silicon has a low coefficient of thermal expansion and hence silicon can be used to make low temperature sensitivity pressure sensors. Silicon is the strongest of three materials and will allow a very high natural frequency sensor to be constructed. However, its reflectivity is lower than the other two materials in Table 5.1.

Copper has superior mechanical and thermal properties to aluminium and is harder than aluminium, which prevents plastic deformation. However, its reflectivity is lower than aluminium in visible wavelength range. With respect to the design of a fibre optic pressure sensor diaphragm, silicon has properties superior to copper with the exception of its reflectivity.

The other important factors in the present work include the cost and availability of material in the form of a thin foil. The cost of silicon foils is much higher than the other two materials. Copper and aluminium foils have been used in this work for sensor construction.

5.11 Calculation for a sample foil

For the sample calculation in this section, a copper foil diaphragm with a thickness of 9 μm and diameter of 125 μm is considered (this corresponds to an actual form of construction used in Chapter 6). The assumed properties of the copper foil are presented in Table 5.1. The modulus of elasticity for the copper was taken as 40 GPa which differs from the Table 5.1 but is the value identified for a sample of the actual copper foil (see Appendix I). Calculations are performed using the equations presented in Section 5.7 for both fixed edge and simply supported diaphragms.

According to Fig. 5.9, which presents the results for a fixed edge support diaphragm, the centre deflection is about 50 nm for an applied pressure of 600 kPa (Figs. 5.9a, b). Assuming 600 kPa is the maximum design pressure, the change of optical path is around 100 nm, which is about a quarter of the desired change (half the illumination wavelength, or about 400 nm). However, the deflection of the adhesive and a diaphragm with a diameter larger than 125 μm (due to construction processes uncertainties) can both contribute to a deflection that is larger than this calculated value.

Comparing Figs. 5.9c and 5.9d, the radial stress has a larger magnitude than the tangential stress and the radial stress reaches its maximum value at the edge. These stresses are much less than the yield strength (maximum equivalent stress is about 57 MPa and yield strength is 336 MPa, see Appendix I), which is less than 35% of ultimate strength, so there is no particular limitation with regard to stress levels.

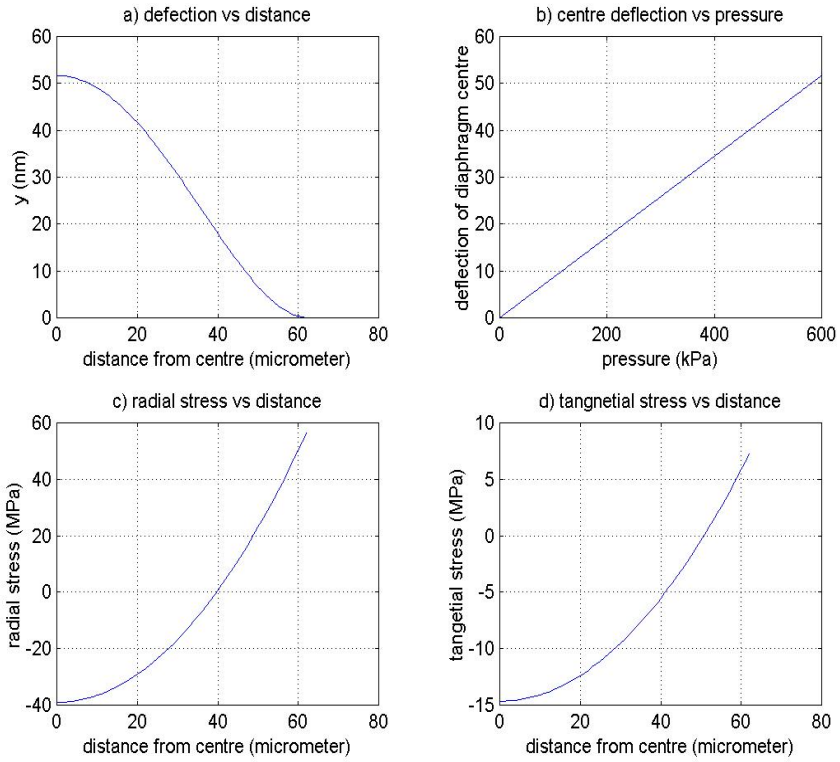

Figure 5.9 Stress and deflection for a fixed edge copper diaphragm, 9 μm thick and 125 μm diameter.

Up to an applied pressure of 1.2 MPa, the equivalent stress remains less than 35% of the ultimate strength, meaning the diaphragm should operate without any plastic deformation, even on the microscopic scale. The rupture pressure is about 3.5 MPa (at this load the equivalent stress reaches 100% of the ultimate strength). For pressures between 1.2 and 3.5 MPa, the diaphragm is expected to have some plastic deformation which causes sensor non-repeatability.

The above calculations were repeated for an aluminium foil with a thickness of 12.7 μm, and diameter of 125 μm with properties presented in Table 5.1, and a measured modulus of elasticity of 20 GPa. (These parameters correspond to an actual form of construction used in Chapter 6). The results were similar to those of the copper foil diaphragm and the equivalent stress again should not exceed 35% of the ultimate stress. However, in the aluminium foil case, the deflection is larger than for the copper due to its lower modulus of elasticity. These results show that either the copper or aluminium foil diaphragms can be employed without substantial plastic deformation even on the microscopic scale.

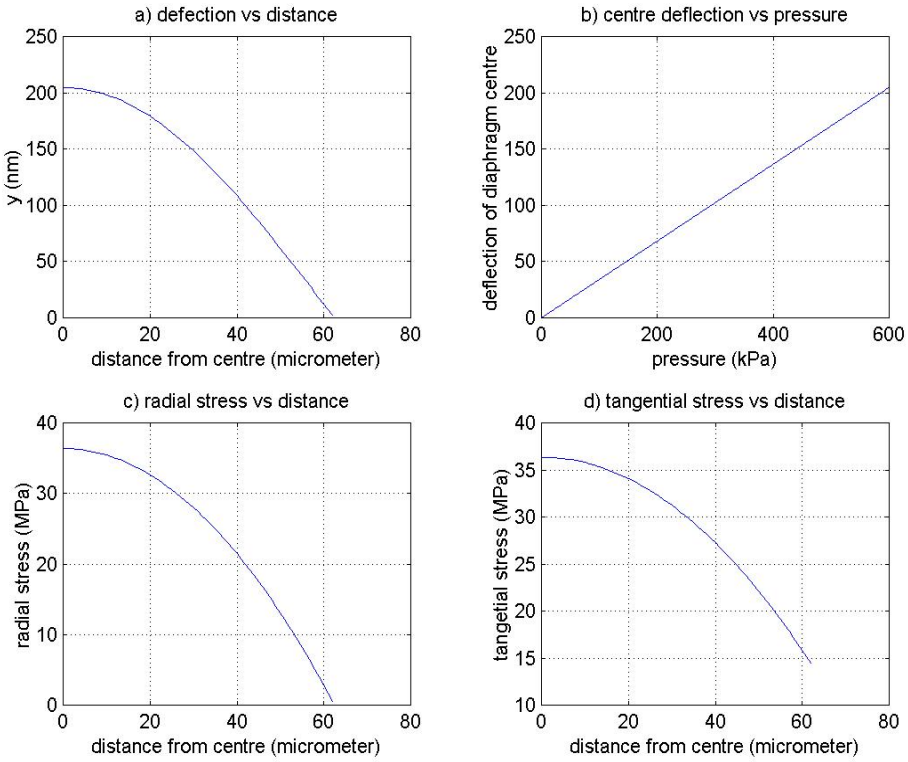

Figure 5.10 Stress and defection for a simply supported copper diaphragm, 9 μm thick and 125 μm diameter.

If the edge is simply supported, the results are somewhat different as presented in Fig. 5.10. According to these results, the deflection of the centre of the diaphragm is 4 times larger than in the fixed edge case. The magnitude of the stress is lower than in the fixed edge case and the maximum stresses occur in the centre of the diaphragm, not at the edges. The results show again that the stress is not a limiting design factor.

Even for the larger deflections associated with the simply supported diaphragm, calculations indicate that the membrane effects will have less than a 1% contribution. Therefore, membrane effects do not need to be considered in these sample calculations.

Using the equations presented in Section 5.9, the natural frequency of the fixed edge sample copper diaphragm material has been calculated and presented in Fig. 5.11 as a function of: a) the diaphragm thickness (for a radius of 62.5 μm); and b) the diaphragm radius for a thickness of 9 μm). Figure 5.11a shows that a diaphragm with

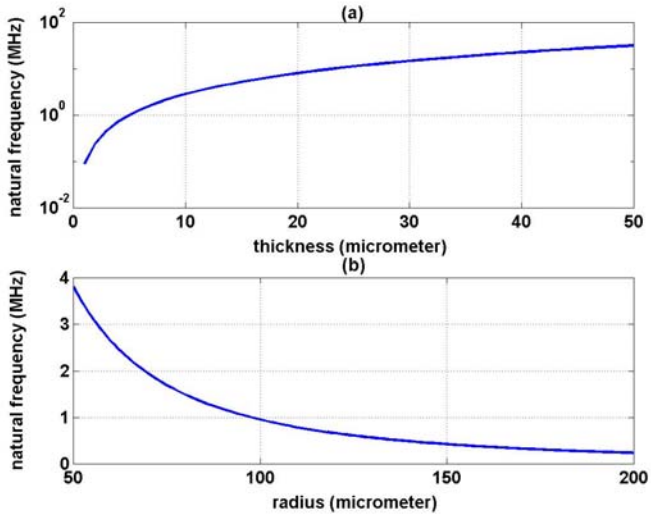

Figure 5.11 Natural frequency for a fixed edge copper diaphragm: a) as a function of thickness (for a radius of 62.5 μm); b) the diaphragm radius (for a thickness of 9 μm).

a diameter of 125 μm, has a natural frequency over 1 MHz if its thickness is more than 5 μm. Figure 5.11b indicates that a change of radius from 50 μm to 200 μm will decrease the natural frequency of the diaphragm from 3.8 MHz to about 250 kHz.

5.12 Conclusion

Important factors which affect the diaphragm performance were discussed and the important equations in design were presented. The results show that one approach to fast response sensor design is to decrease the size of diaphragm.

Copper, aluminium and silicon were discussed as potential materials. Silicon shows the best mechanical and thermal performance, however, due to its low reflectivity (in comparison with aluminium and copper) and relatively high cost it was not selected for sensor construction.

Two possible support conditions were considered: 1) fixed edge; and 2) simply supported. However, neither support arrangements are likely to be fully achieved in practice because of the construction techniques that have been adopted (Chapter 6). The actual deflections and stresses that develop are expected to lie between the calculated values for the two kinds of support conditions.

Calculations for a sample copper shows it is possible to make a fast response sensor (natural frequency more than 1 MHz) with a pressure range of up to 1.2 MPa if the

diaphragm diameter and thickness are limited to 125 μm and 9 μm respectively. The repeatability of such a sensor is expected to decrease if it is operated at higher pressures, however, the sensor may still operate for pressures up to 3.5 MPa.

The effects of pretension on the diaphragm pressure sensitivity, temperature sensitivity and natural frequency were also estimated. According to the results, the use of pretension could be beneficial because it will reduce the temperature sensitivity of the diaphragm more significantly than the pressure sensitivity which is also reduced by the use of pretension. For the likely range of pretensions that might realistically be achieved, the effect of pretension on natural frequency is negligible. This suggests that one approach to diaphragm design is to apply a pretension and to compensate its impact on pressure sensitivity by choosing a thinner diaphragm. In practice however, applying a high magnitude of pretension is difficult (as will be discussed in Chapters 6 and 8), and furthermore, it will be more difficult to maintain a high level of pretension due to relaxation of adhesive.

Considering pretension effects on diaphragm performance is important even if a pretension is not applied during construction. For example, if the sensor construction is a copper diaphragm on a zirconia substrate (Chapter 6), a decrease of room temperature can create a pretensioned diaphragm thus reduce the pressure and temperature sensitivity of the sensor. Furthermore, due to viscoelastic effects and relaxation of adhesive (see Section 8.8.3.7) caused by cyclic changes of environment temperature, the sensor could be damaged. Ideally sensors should be stored in a constant temperature environment prior to operation.

Chapter 6: Sensor construction and quasi-static calibration

6.1 Introduction

A variety of fibre optic pressure sensors were constructed using different foils, adhesives and substrates. Different construction techniques were generally established for each set of foils, substrates and adhesives. The effects of each set of material and construction technique on sensor performance have been discussed. Quasi-static pressure calibration techniques were also developed to identify the pressure sensitivity of these sensors. The temperature sensitivity of the sensors and interrogation systems were measured and compared with the results from analytical modelling.

6.2 Pressure sensor components

6.2.1 Substrates

The substrate locates the fibre and supports the pressure sensitive diaphragm. A small substrate size can lead to a high spatial resolution sensor, particularly for Pitot pressure measurement configurations. Furthermore, the substrate should include a small hole that makes it possible to insert the fibre. The size of the hole in the substrate should be small enough to assist the design of a high natural frequency diaphragm (as discussed in Chapter 5). Commercially available substrates of suitable dimensions will reduce the cost of the sensor. Two kinds of commercially available substrate were considered: 1) ferrule as used in the fibre optic industry; and 2) hypodermic tubes.

Ferrules used in the fibre optic industry are made from different materials and in different shapes. Zirconia is the most common material from which the ferrules are constructed. They are made in different sizes and shapes and their central holes are sized to accept the most common optical fibres. A typical arrangement for a zirconia ferrule is presented in Fig. 6.1.

The end face surface finish of the zirconia ferrule is excellent and the angle between the central hole and the end face can be ninety degrees to within measurement precision. The length of the central hole into which the fibre is inserted (8 mm) is

Figure 6.1 Photograph of zirconia ferrule substrate and piezoelectric pressure transducer.

sufficient to permit good alignment between the fibre and the end face. The ferrule includes a metallic base, which is convenient for fibre insertion and bonding (Fig. 6.1). The front face diameter of the ferrule is less than the cylindrical body (Fig. 6.1), and this feature is useful in protecting the diaphragm during insertion within the sensor support (which is discussed in Section 6.3.6).

The principal dimensions of the ferrule are presented in some detail in Section 6.3.7. Briefly however, the diameter of the body is 2.5 mm and the diameter of the front face is 2 mm. The diameter of the central hole is 126 μm and this is designed to suit the 125 μm diameter of single mode fibres (with cladding). This one micrometer difference in diameters makes insertion of the fibre with the glue on it relatively easy. The low thermal expansion coefficient of zirconia is another advantage (see Table 6.1). One significant disadvantage is that the outer diameter (2.5 mm) is large relative to the minimum size of the pressure sensitive diaphragm (126 μm). This means that the potential for high resolution Pitot pressure measurements cannot be fully realised unless the outer diameter is reduced. As zirconia is a hard material, the reduction of its outside diameter is an expensive (time consuming) operation (MacPherson 1999).

Table 6.1 Physical and thermal properties of zirconia*

Property	Value
density	5740 kg/m^3 (5680 kg/m^3)+
specific heat @ 25^{o}C	400-500 J/kg/K
thermal conductivity @ 20^{o}C	1.5-2.5 W/m/K (1.675 W/m/K)+
thermal expansion coefficient, 20-1000^{o}C	5-10×10^{-6} /K (7×10^{-6} /K)+
upper continuous use temperature	1000^{o}C
compressive strength	1500-2000 MPa
Hardness (Vickers)	1200 kgf/mm^2
shear strength	414 MPa
tensile modulus	200 GPa
tensile strength	>300 MPa
Melting point+	2681-2874^{o}C

* Goodfellow c. 1998/9 for zirconia stabilised with Magnesia

\+ Matweb 2002 for monoclinic zirconia

The stainless steel hypodermic tubes were also used as substrates. The hypodermic tubes potentially hold a number of advantages over the zirconia ferrules including: 1) lower cost; 2) wide range of sizes; 3) smaller outside diameter; and 4) easier to machine and modify. The sizes of the tubes used in this work are presented in Table 6.2. The internal diameter of these tubes is about 0.2-0.3 mm less than external

Table 6.2 Size of standard hypodermic tubes

Commercial designation	Outside Diameter (mm)	Length (mm)
18G × 1 ½ ″ T.W.	1.2	38
19G × 1 ½ ″ T.W.	1.1	38
20G × 1 ½ ″ U.T.W	0.9	38
21G ×1 ½ ″ U.T.W.	0.8	38
22G ×1 ½ ″ T.W.	0.7	38
23G × 1 ¼ ″ T.W.	0.6	32
25G ×1 ½ ″	0.5	38
25G ×1 “ U.T.W.	0.5	25
26G × ½ ″	0.45	13
27G × ½ ″	0.4	13

diameter. They have two primary disadvantages relative to the zirconia ferrules: 1) a higher thermal expansion coefficient; and 2) a certain amount of machining/modification is necessary to prepare the hypodermic tubes to accept the fibre and diaphragm.

6.2.2 Diaphragm

The diaphragm is an important part of the fibre optic pressure sensors. The diaphragm should be highly reflective and relatively thin, as discussed in Chapter 5. Aluminium and copper foils were chosen for the diaphragm as discussed in Chapter 5. The foils presented in Table 6.3 are commercially available and their thickness is between about 10 μm and 50 μm.

The commercial foil number 3 (in Table 6.3) is used for wrapping and decorating. This foil shows good reflectivity, but it is basically a composite construction of plastic with a layer of reflective metal. The plastic deforms permanently under load and this leads to non-repeatability of the sensor, as is discussed in Section 6.5.1. The foils numbered 1, 2, 4 and 5 show less reflectivity than foils 3 but they lead to the

Table 6.3 Properties of foils

No.	Commercial Name	Material	Manufacturer	Thickness (μm)
1	Roll Wrap	Aluminium	PHIL TAYLOR	55
2	Foil- Stronger than ordinary	Aluminium	MULTIX ALFOIL	15
3	Metallic Cello	Aluminium	WRAP SENSATION	25
4	Black Back Copper Foil	Copper	VENTURE TAPE	31
5	MASTER FOIL	Copper	VENTURE TAPE	38
6	FOIL	Aluminium 1145-O	ALL FOILS	7.2
7	FOIL	Aluminium 1145-H19	ALL FOILS	25.4
8	FOIL	Aluminium 1145-H19	ALL FOILS	38.1
9	FOIL	Copper- 110 as rolled	ALL FOILS	12.7
10	FOIL	Copper	MICRO HARD	9
11	FOIL	Aluminium		55

production of sensors with better repeatability.

Pure aluminium and copper foils with no plastic film layers (numbered 6-11) do not show the considerable problems as associated with the commercial foils. However, they are more expensive and have a lower reflectivity.

6.2.3 Adhesive

Three types of adhesive were tested for bonding the diaphragm to the substrate: 1) liquid; 2) film; and 3) tape adhesives. The properties of the various adhesives used in this work are presented in Table 6.4.

The liquid adhesives can be used with both substrates discussed in Section 6.2.1. Their setting time, bond strength and service temperature are important, and should be considered. For example, using an adhesive with a setting time of 24 hours obviously increases the construction time relative to a construction based on the 5 minute epoxy. Care should be taken when mixing the two parts of epoxies. If the mixing is not done thoroughly, the adhesive strength and stiffness may be low and the sensor construction will not be repeatable.

Tape adhesives are easy to use, however they cannot be used with hypodermic tube substrates because the available bonding area on the hypodermic tube is insufficient. There are also some difficulties in making an appropriate hole in them in order to allow reflection from the diaphragm (Section 6.6.3). Furthermore, tape adhesives have substantial plastic deformation. Their length can stretch to several times of their original length and they are not strong adhesives. One sided and double-sided tapes were tested in this work.

The film adhesives tested in this work were thicker than the tape adhesives. As with the tape adhesives, the film adhesives could only be used with the ferrules. A uniform thickness bonding layer can be obtained, but there are some construction difficulties that arise from the setting process which requires heating. The film adhesives expand during heating and possible movement of the adhesive during heating and cooling process can create problems. In particular, the air cavity can get filled with the adhesive, or the diaphragm can shift during the construction process. Forming the hole in the film adhesives (to allow reflection from the diaphragm) is easier for the film adhesives than for the tape adhesives.

Table 6.4 Properties of adhesives

Commercial Name	Manufacturer	State	Comment or additional data
Scotch Brand, Tape Adhesive Transfer 465	3M	Double sided tape	
Scotch brand, High performance adhesive 467 MP	3M	Double sided tape	
Supa Glue Gel	SELLEYS	Instant liquid	
609 Super retaining compound	LOCTITE	Liquid	
High strength epoxy adhesive	RS	Liquid	
Araldite– Super strength	SELLEYS	Liquid	6-8 hours set time, high bond strength after 3 days
Araldite– Epoxy resin 5 minute	SELLEYS	Instant liquid	
Polyester Adhesive film	BEMIS	Film adhesive	76 μm, Hardness 95A,service temperature from –20 to 115^{o}C, minimum glue line temperature 153^{o}C, softening point 125^{o}C
Polyester Adhesive film	BEMIS	Film adhesive	127 μm, Hardness 95A,service temperature from –20 to 115^{o}C, minimum glue line temperature 153^{o}C, softening point 125^{o}C
Polyester Adhesive film	BEMIS	Film adhesive	178 μm, Hardness 95A,service temperature from –20 to 115^{o}C, minimum glue line temperature 153^{o}C, softening point 125^{o}C
Loctite 324	LOCTITE	Liquid adhesive	Impact resistant and tough, especially suitable for flat dissimilar materials. Can be used with activator 7075
Loctite 325	LOCTITE	Liquid adhesive	Suitable for bonding rigid parts of metal or ceramic where exposed to thermal cycling. Can be used with activator 7075

6.2.4 Single mode optical fibre

The optical fibre is an integral part of the sensor. For optimal performance, it is important to use the same fibre which is used in the coupler. A small difference in numerical aperture can cause substantial loss and a large difference can stop the sensor from working. The fibre core size is also important and a mismatch in the sensor and coupler fibre will degrade performance in a similar way to differences in numerical aperture. If a single mode fibre is used, the minimum cut off wavelength

Table 6.5 Properties of optical fibre SMC-AO780B

Property	Value
Operating wavelength	780 nm
Core diameter	4.9 μm
Mode field diameter @ 780 nm	5.4 ± 1 μm
Cladding Diameter	125 ± 2 μm
Fibre Diameter	245±15 μm
Core/clad concentricity	≤1 μm
Clad concentricity	≤2 μm
Refractive index of primary coating	1.54
Refractive index of secondary coating	1.53
NA	0.11±0.02
Cut-Off wavelength	730±60 nm
Attenuation @ 780 nm	≤4 dB/km

of the fibre should not be less than the interrogation wavelength. The optical fibre was SMC-AO780B manufactured by Lucent – properties of this fibre are presented in Table 6.5.

6.3 Sensor construction techniques

6.3.1 Summary of configurations

Fibre optic pressure sensors were constructed in different configurations using different substrates and adhesives. They can be categorized into hypodermic substrate sensors and ferrule substrate sensors. Both categories can also be divided into subcategories depending on the adhesives and construction techniques that were used.

A ‘one-tube sensor’ is a sensor where a small sized hypodermic tube is used as the substrate. For this sensor, it was necessary to perform and observe the bonding of the diaphragm and the substrate through a stereo zoom microscope. This sensor has the smallest outside diameter, around 0.5 mm. The real size of the sensor is slightly greater than the external diameter of the hypodermic tube due to the diaphragm thickness and the glue on the sides of the tube. Figure 6.2 shows a one-tube sensor.

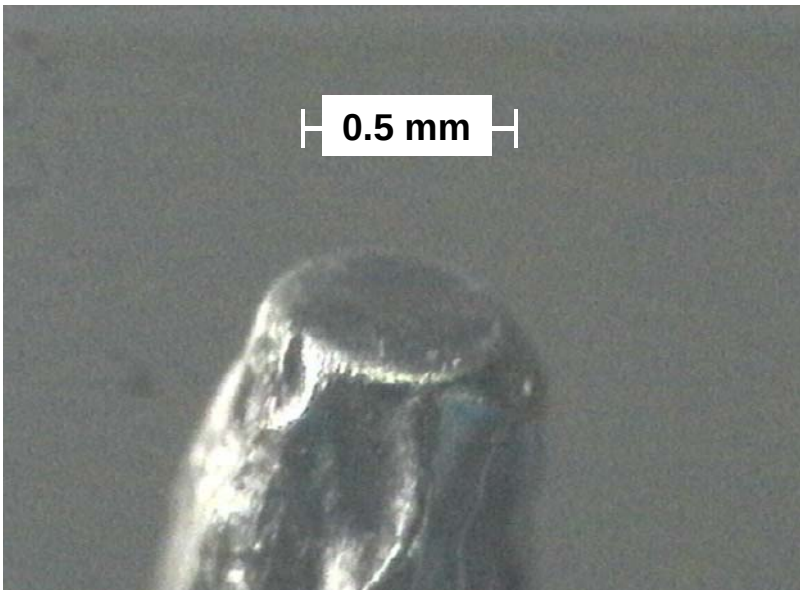

Figure 6.2 Fibre optic pressure sensor made with one hypodermic tube.

A ‘two-tube sensor’ is an alternative sensor configuration. In this configuration, the diaphragm was bonded onto one tube, the fibre was glued into a smaller sized tube and finally, the smaller tube was inserted inside the larger tube. Control of the cavity length was easier because the fibre could be glued inside one tube whilst the process was observed using a stereomicroscope. Furthermore, the quality of the diaphragm was improved due to pretension caused by pushing the smaller tube into the larger tube.

With the two-tube sensor construction method, there is virtually no possibility of contact between the end of the fibre and the diaphragm. Such contact can damage the fibre end face and affect the sensor performance. However, this sensor is larger in size (outside diameter about 0.8 mm) than the one-tube sensor and some problems in alignment between the two tubes were observed. Using a third tube to cover the two-tube sensor improves the alignment but further increases the outside diameter to about 1.2 mm.

There were two main problems associated with using hypodermic tubes as substrates. Firstly, the quality of the diaphragm was not ideal due to a slight creasing of the foil which was as a consequence of the quality of the end face of the tube. Secondly, their natural frequency was low. The smallest size hypodermic tube (27G) has an internal diameter of 0.2 mm. As discussed in Chapter 5, this larger than necessary diameter decreases the natural frequency. Using a zirconia ferrule substrate resolves these problems.

A double sided tape sensor requires a ferrule substrate. Double sided tape covers the ferrule face and after making a hole with a fibre, the diaphragm was placed on the tape. These sensors could be made in the shortest amount of time (about 90 minutes), however, good bonding between the diaphragm and the substrate was not provided and most sensors showed a leakage. Furthermore, due to the high viscoelasticity of tape adhesives, the sensors did not have a repeatable performance (see Section 8.8.3.7).

One simple configuration using tape adhesive was also tested. The diaphragm was cut into a very small size then placed onto the bonding side of the tape and finally the tape was mounted onto the substrate. In this configuration, the problem associated with making a hole in the tape was eliminated, but all problems observed in the double sided tape sensors were repeated. These sensors were completely non-repeatable and their natural frequency was very low and depended on the size of the diaphragm and elasticity of the tape.

The sensors made using film adhesives showed more repeatability than sensors made with tape adhesives and the bonding between ferrule and diaphragm was improved. However, the problems associated with change of alignment between the diaphragm and the substrate during heating reduced the construction success to less than 20%. Furthermore, due to the thickness of film adhesive (>75 μm), they had considerable contribution in diaphragm deflection, and this lead to substantial hysteresis (see Chapter 7).

By using liquid adhesives, it is possible to create thin bonding layers. This can be achieved by spinning the component to which the adhesive has been applied in a high speed drill in order to spin off the excess adhesive. These sensors showed the best response and highest repeatability with lowest hysteresis. However, the control of the diaphragm diameter was difficult and it was possible that the adhesive penetrated inside the hole. Figure 6.3 shows one of these sensors.

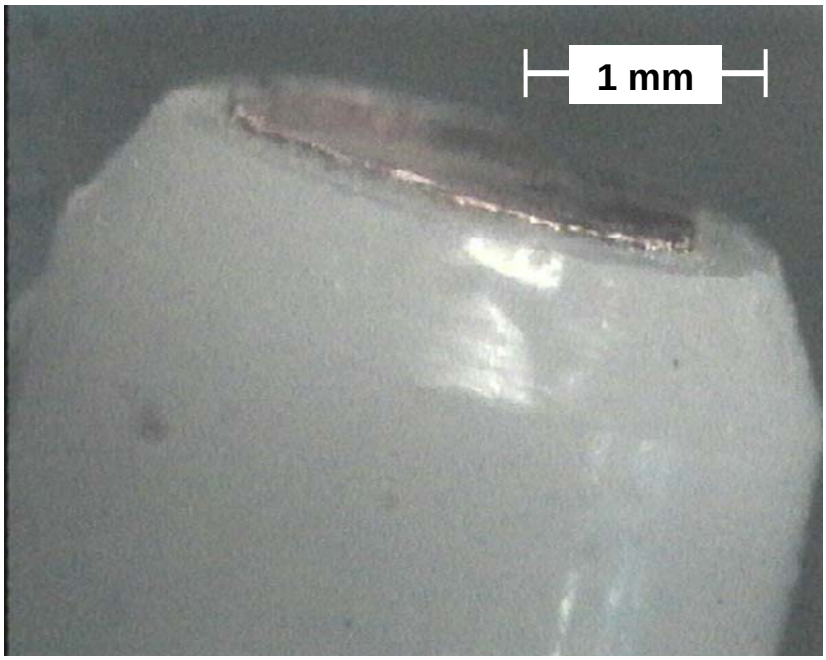

Figure 6.3 Zirconia ferrule sensor.

6.3.2 Diaphragm preparation

Load cycling decreases the sensor hysteresis (see Chapter 7). The foil was exposed to between 500 and 2000 tension load cycles prior to cutting and bonding the diaphragm onto the zirconia ferrule. This load cycling was performed using a H5K-S Universal Testing Machine supplied by Housfield Ltd (Load cell 99-999-1026), as described in Appendix I.

As discussed in Section 5.6, applying a load that corresponds to twice the maximum working stress can increase the diaphragm stability, however, the load should not exceed the proportional limit. For example, the maximum equivalent stress for a sample copper foil with a thickness of 9 μm was 57 MPa (see Section 5.11) if the maximum working pressure was 600 kPa. Therefore, a load corresponding to a maximum stress of around 130 MPa, which is less than the proportional limit for this material, should increase the diaphragm stability and decreases the sensor hysteresis.

The effect of diaphragm roughness on the sensor response was discussed in Section 5.3. Polishing the diaphragm increases the possibility of producing a good sensor from 30% to about 50% and this decreases possible irregularities observed in the response of some sensors (see Section 6.3.6.1). Polishing can also provide a more reflective diaphragm.

The polishing process is very easy. Glass was used as a pad and foils were placed onto the glass. A soft cotton cloth was chosen; its surface soaked with oil and then a polishing material was put on the cloth. The polishing material used for this work was Micoid Diamond Compound with particles of a size less than 1 micrometer from LECO Corporation. (This paste compound is commonly used for metallography.) Roughness measurements for the various foils, including a copper foil before and after polishing are presented in Table 6.6 (the roughness symbols used in this table are defined in Section 5.3).

Table 6.6 Roughness of foils (measured by Suffest-4, MITUTOYO Ltd)

No.	Commercial Name	R_q (μm)	R_a (μm)	R_z (μm)	R_{max} (μm)
1	Roll Wrap, aluminium (PHIL TAYLOR)	0.21	0.19	0.84	1.27
2	Foil- Stronger than ordinary, aluminium (MUTIX ALFOIL)	0.31	0.29	1.16	1.95
3	Metalic Cello, aluminium (WRAP SENSATION)	0.12	0.10	0.32	0.53
4	Aluminium Foil, thickness 55 μm	0.17	0.15	0.73	0.90
5	FOIL, aluminium 1145-O (ALL FOILS)	0.16	0.12	0.52	1.03
6	FOIL, aluminium 1145- H19 (ALL FOILS),0.01”	0.30	0.27	1.46	1.82
7	FOIL, aluminium 1145- H19 (AL FOILS),0.015”	0.38	0.35	1.81	2.19
8	FOIL, copper 110 as rolled (ALL FOILS)	0.11	0.09	0.48	0.68
9	FOIL, copper (MICRO HARD) before polishing	0.10	0.09	0.42	0.56
10	FOIL, copper (MICRO HARD) after polishing	0.04	0.03	0.2	0.26
11	Glass	0.01	0.01	0.04	0.05

The results show that this method of polishing can substantially decrease the roughness even for initially low roughness foils. Repeating the polishing process for high roughness foils yield similar results. To decrease the roughness to less than the values shown in Table 6.6, it is necessary to use a polishing material with smaller particles and glass with very low roughness as the pad.

Cutting the diaphragm for zirconia ferrule substrate sensors was easily performed using scissors. Diaphragms with an outside diameter of around 2 mm were generally created for zirconia ferrule substrate sensors. For the hypodermic tube sensors, cutting the diaphragm required some practice. In the case of the hypodermic tube

sensors, the diaphragm was cut in the form of a cross which was then clamped to the side of the tube and finally wrapped across the top of the tube.

6.3.3 Adhesive preparation

For the film and double sided tape adhesives, the diaphragm diameter is related to the size of the hole made in the film and tape. As the diaphragm diameter has a strong influence on sensor pressure sensitivity and natural frequency (see Section 5.11), creating the hole in the adhesive is critical.

Holes can be created using a fibre if the film and tape adhesives were placed under tension. However, precise control of the hole diameter was not possible as in practise, the material removed to create the hole remained partly attached to the rest of the adhesive layer. For the thicker film adhesive and double sided tape, making a hole using fibre was not practical as the fibre would break. The best method to create the necessary hole was to pierce the adhesive using a copper wire with a diameter of 0.1 mm. This wire should be heated before quickly touching the adhesive.

One part liquid adhesives require little preparation, but for two part epoxies, mixing must occur in the appropriate ratio otherwise it may not cure properly. The construction repeatability will be reduced as will the performance of each sensor. Extra care should be taken during mixing, because ideally a homogeneous mixture on the molecular scale should be produced.

6.3.4 Substrate preparation

The only preparation necessary for the zirconia ferrule substrates is cleaning. Washing the ferrule front face with a solvent provides better bonding of the diaphragm and the substrate. Inserting a cleaved fibre soaked with a solvent removes foreign matter from inside the hole. Any microscopic particles will affect the sensor’s performance if they cover part of the fibre core.

The hypodermic tube requires some preparation. The plastic component that mates with the syringe should be removed from the hypodermic tube and it is necessary to grind a flat surface perpendicular to the tube axis. This surface should be of a high quality with minimum roughness otherwise a flat diaphragm without creasing is not achievable. The cleaning process prior to diaphragm and fibre bonding was similar to that adopted for zirconia ferrule substrates.

6.3.5 Diaphragm bonding

Applying pretension to the diaphragm was generally necessary in order to prevent creasing of the diaphragm if a hypodermic tube was used as substrate. One side of the hypodermic tube was then bonded with instant liquid adhesive (to decrease construction time) and one side of the diaphragm was bent onto the tube. After the adhesive had cured, the process was repeated around the other sides of the tube.

The method of diaphragm bonding onto the zirconia substrate was more complicated. After preparing the zirconia ferrule (see Section 6.3.4), a fibre with its buffer entirely removed, was inserted inside the substrate to prevent possible penetration of liquid adhesive inside the hole. The substrate was placed in the chuck of a high speed drill (maximum speed 30000 rpm) and the face of the substrate was covered with liquid adhesive. The liquid adhesive was usually placed on the face of the substrate using a fibre or very small hypodermic tube. Experience showed that thinner bonding layers were produced if only a small amount of adhesive was initially placed on the substrate. The whole process was observed using a stereo microscope to make sure that the adhesive covered the entire front face of the substrate but did not penetrate inside the hole.

The substrate was then spun for about 1 minute in the high speed drill and then the fibre inside the hole was extracted from the substrate via its front face. This prevented possible penetration of liquid adhesive inside the hole. To confirm that no adhesive penetrated the hole, a fibre connected to the interrogation system was inserted in the ferrule and if the optical power decreased during insertion, a fibre soaked with a solvent was inserted into the hole and then removed a number of times.

The zirconia ferrule was inserted into a tight fitting plastic tube which had an inside diameter equal to the outside diameter of the substrate. A fibre connected to the interrogation system was also inserted inside the ferrule hole to a distance of about 10 μm from the front face. The plastic tube into which the zirconia substrate was inserted had a length approximately 1.5 times that of the zirconia substrate. The diaphragm was placed onto a second zirconia substrate which was then inserted into the tight fitting plastic tube.

The two zirconia substrates were then slowly moved towards each other until contact between the diaphragm and the adhesive layer was made. The length of the plastic tube and its tight fit with the ferrules minimised the possibility of relative lateral movement of the diaphragm, adhesive, and ferrule (hence the adhesive rarely went inside the hole during this process). A small amount of pressure was applied to the ferrules to ensure good bonding. The signal detector was used to monitor alignment between the fibre and the diaphragm. After the liquid adhesive was cured, the fibre was extracted from the zirconia substrate.

6.3.6 Fibre preparation & location

The fibre was cleaved using a cleaver (CT-07) supplied by Fujikura Ltd. Due to the high surface quality of the cleaved end, polishing was not required. However, it was necessary to inspect the cleaved end using a microscope in order to identify the flatness and angle of the cleave. A further indication of the cleave quality was obtained by connecting the fibre to the interrogation system, the reading the signal detector voltage was used to indicate the power level associated with the Fresnel reflection.

Prior to the method described in this section, the locating of the fibre was completed using the stereo microscope. In this method, after covering the substrate with a long working time liquid adhesive (e.g., Araldite 24 hour with about 1 hour working time) and before placing the diaphragm (see Section 6.3.5), the fibre was soaked with an instant liquid adhesive (e.g., Araldite 5 minute) and then the fibre was inserted inside the substrate. The cavity length was controlled using the stereo microscope to about 10-20 μm.

However, for the most successful sensors (which were constructed using zirconia ferrules as the substrate), locating the fibre in the substrate generally included two steps. Firstly, the fibre was inserted into the substrate to investigate the quality of the cavity and secondly, the fibre was bonded inside the cavity. These steps are described in detail below.

6.3.6.1 Investigation step

After the diaphragm was bonded to the ferrule zirconia substrate, the fibre was inserted into the 126 μm hole. The fibre was connected to the interrogation system and the output voltage was recorded with the computer. The substrate was then

installed in the lower jaws of the tension testing machine, and the fibre from the substrate was attached to the upper jaws of the machine. Efforts were made to have a good alignment between the fibre and the substrate hole. Good alignment is important as it can minimise any change of fibre angle as the cavity length is increased. (Changes of fibre angle may cause phase changes in the signal, which are then interpreted as a change of cavity length, so it is important to avoid angle changes if at all possible.)

Care should be taken when inserting the fibre to ensure that the diaphragm and the fibre do not make contact with each other, as this can destroy the diaphragm and also damage the end face of the fibre. The distance between the two jaws was at least 200 mm and the change of optical path length was less than 3 mm. The top jaw of the tension testing machine can be moved with very low velocity (0.001 mm/min).

Equation (5.3) is valid only for Gaussian speckle. Comparing the size of the optical fibre core, which is less than 5 μm, and the size of the roughness of the foils (presented in Table 6.6) indicates that this equation is not precisely appropriate for the present case, because there will be insufficient sampling for a Gaussian distribution. However, the equation can be used to evaluate the general effects of the speckle on the sensor performance.

For example, in the case of L=20 μm and D=5 μm and λ=790 nm, the size of the objective speckle from Eq. (5.3), is about 4 μm. This size is less than the core diameter and shows that there may be a few light and dark regions on the fibre surface. If this is the case, the sensor will not work or will respond irregularly. Increasing the pressure decreases the cavity length, but as this deflection was generally limited to be less than half the interrogation wavelength, the number of light and dark region remain almost constant and there may be no change of power from the sensor. However, this possibility decreases sharply for polished diaphragms.

The results from the investigation step for unpolished copper foil diaphragms (numbered 8 in Table 6.6, copper 110 as rolled, ALL FOILS) are presented in Fig. 6.4. The results from four nominally identical diaphragms bonded to zirconia substrates are presented in this figure.

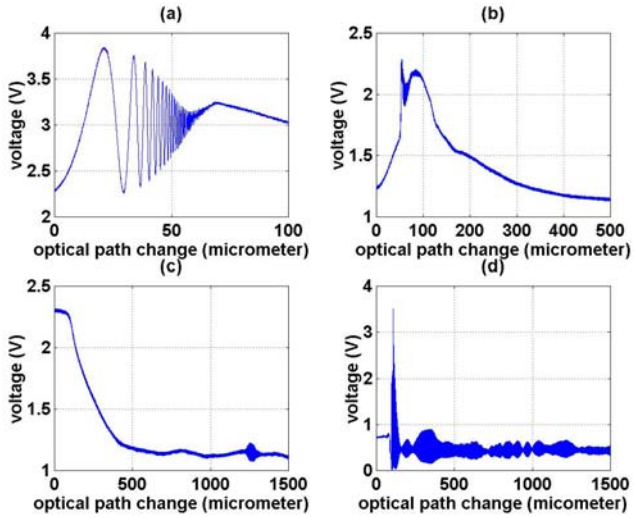

Figure 6.4 Signal voltage versus optical path change for unpolished copper foil diaphragms (number 8, Table 6.6).

The performance of the foil is completely different in all four experiments, which suggests that the Gaussian speckle equations cannot be used. In Fig. 6.4a, increasing the optical path length decreases the visibility and after about 70 μm, there are no more fringes to be observed. This can be related to changes of the polarization state. Increasing the optical path to values close to coherence length can also affect the results. Figure 6.5a presents the results from the same experiment as Fig. 6.4a, but zoomed in on optical path changes between 40 and 50 μm. These results indicate that a sensor with visibility of about 20% with a cavity length less than 20 μm can be constructed with this particular diaphragm and fibre arrangement.

A different diaphragm was made from the same kind of unpolished foil used in Fig. 6.4a, and the results are presented in Fig. 6.4b. The voltage first increases and then after some fringes, it decreases. This performance can again be related to changes of the polarization state. The same laser and interrogation system was used, and therefore, the change of response relative to Fig. 6.4a can also be related to the different levels of roughness. Figure 6.5b shows that a relatively low visibility sensor (about 7%) can be made using this diaphragm if an optical path of between 55 and 65 μm is used. Such a low visibility is not conducive to the construction of a high performance sensor, so it was not used for making a new sensor.

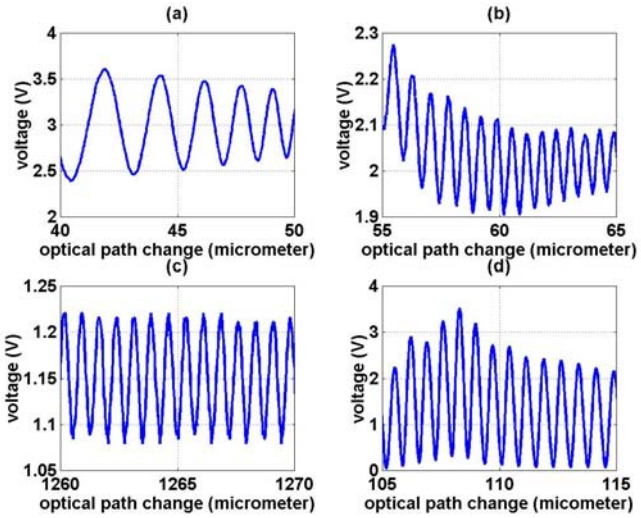

Figure 6.5 Signal voltage versus optical path change for unpolished copper foil diaphragms (number 8, Table 6.6). Parts a) to d) in this figure correspond to parts a) to d) in Fig. 6.4, but with different axes.

The particular arrangement used to produced Fig. 6.4c (although it was nominally identical with those used in Figs. 6.4a and b), gave a very different response. The voltage first decreases and then remains essentially constant. Some fringes do appear after changing the optical path by 1.2 mm (Fig. 6.5c). This response can be related to the polarization state in the beginning and white light interferometry (see Section 3.8.3) towards the end of the extension of the jaws. Figure 6.5c indicates that visibility for this arrangement was less than 5%, and therefore this diaphragm was not used for making a new sensor.

Figure 6.4d indicates a good response: fringes occur at the beginning of the fibre withdrawal, and the visibility decreases as the optical path increases. It also shows some nodes after the optical path changes about 100 μm, which indicates the existence of some white light interferometry and this can also be related to changes of polarization. Figure 6.5d indicates that using this diaphragm, a high visibility sensor with a long cavity length (>20 μm) can be constructed.

The results presented in Figs. 6.4 and 6.5 indicate that it is possible to make a good sensor even with a diaphragm which has an average roughness of 90 nm. However, it is expected that the probability of a successful sensor construction will be enhance if the roughness of the diaphragm can be decreased.

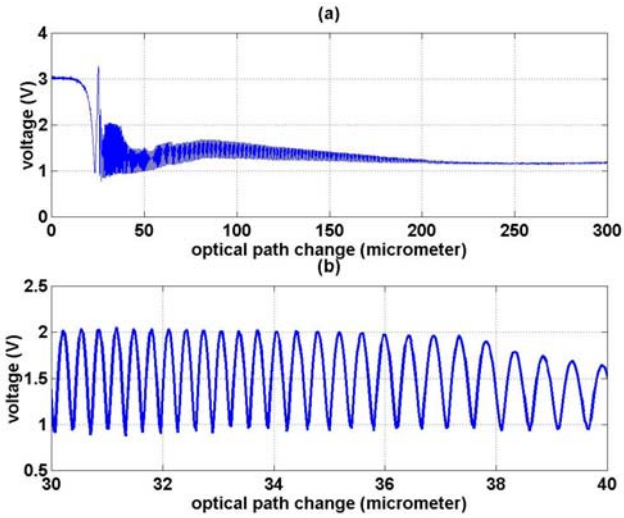

Figure 6.6 Signal voltage versus optical path change for a polished copper foil diaphragm (number 10, Table 6.6).

A copper foil with a thickness of about 9 μm and a very low roughness (produced by polishing, number 10, Table 6.6) was used to make a sensor. The diaphragm was bonded to a zirconia ferrule substrate with the liquid adhesive (Araldite 5 minute). The results from the investigation step are presented in Fig. 6.6.

Figure 6.6a shows that by polishing the foil, interferometry occurs for a long optical path even where only a small fraction of light is reflected back into the fibre from the diaphragm. This increases the probability of making a good sensor. Figure 6.6b shows a sensor with visibility of about 35% can be constructed from this arrangement. Furthermore, the wavelength of the interference fringes changes from approximately 300 nm to 550 nm and this cannot be related to the experimental errors such as misalignment or fibre elongation. This effect is probably related to diaphragm roughness.

6.3.6.2 Locating step

Diaphragms which showed high visibility during the investigation step, were selected for the second step which involved locating the optimal fibre position and bonding it into the ferrule. If the diaphragm did not show high visibility, its zirconia ferrule was used for a new diaphragm and the process of bonding the diaphragm was repeated.

Decreasing the cavity length increases the visibility in most sensors and decreases dispersion and noise (see Section 4.4.1). However, if the cavity length is very short

(less than 5 μm) and the air inside cavity is not evacuated, then errors during dynamic calibration will be large (see Section 8.8.3.2). Therefore, the final cavity length adopted for each sensor was between a minimum value of 5 μm and a maximum value of around 30 μm (the precise maximum value was identified during the investigation step).

Glue was applied halfway around the fibre and the fibre was then inserted into the hole again. The insertion process was stopped when the signal detector reached a voltage close to that obtained when a dummy diaphragm was placed in direct contact with the fibre (the fibre was cleaved again). Using this limiting voltage decreased the possibility of contact between the fibre and the diaphragm during the insertion process.

The metallic base of the ferrule was then glued in place and the fibre inside the ferrule was twisted within the hole in order to bond all sides of fibre to the substrate. The jaws of the tension testing machine were then made to move apart and when the voltage began to change, the change of distance was measured and the jaw movement was stopped at the distance identified in the investigation step. A slight vacuum was expected in this method (after increasing cavity length), however the value of the vacuum could not be identified.

After the required location was reached and the jaw motion terminated, the signal power continued to change. This change of power may be associated with the tension of the fibre, which also causes movement of the fibre during the adhesive curing process. In an attempt to eliminate this problem, low speed reverse movement for the top jaw was applied. While this helped, it did not completely resolve the problem, as shown in Fig. 6.7.

It is important that the glue in the substrate metallic base be homogenous. Dissimilarity of glue thickness can modulate the angle between the fibre and the diaphragm slightly during the curing process.

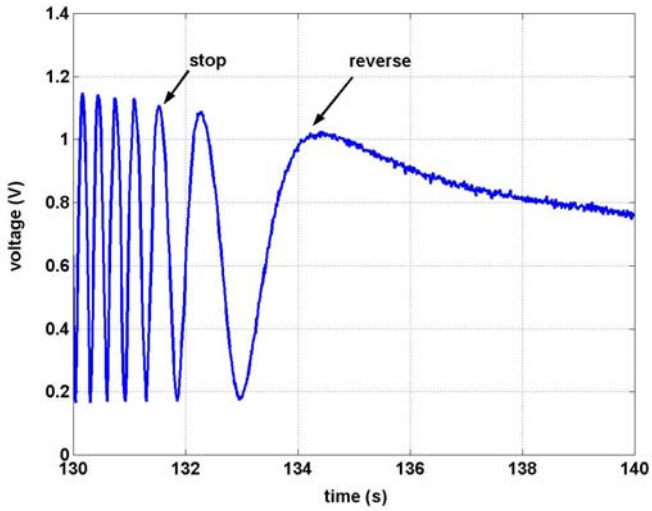

Figure 6.7 Change of signal voltage with time for a polished copper foil diaphragm (Number 10, Table 6.6) before and after stopping the tension machine jaw motion.

Many sensors were made using this polished diaphragm and on line cavity length control technique. However, after construction, some sensors still showed irregularity and low visibility. Approximately 50% of sensors worked acceptably well. The reason for irregularity in the response of some sensors can be related to the way the optical path changes. During step 1, only the optical path was changed. However, in a real sensor, as the pressure increases, not only does the distance between the diaphragm and fibre decrease, but the diaphragm also curves and thus changes the orientation of the diaphragm roughness relative to the fibre end face. Changes of diaphragm angle become very critical if the light is not reflected from the centre of the diaphragm. The actual diaphragm centre (or the position where the slope of the diaphragm in its deflected state is zero) may not coincide with the centre of the hole in the ferrule because of uncertainties in construction of the diaphragm bonding layer.

6.3.7 Sensor embedding

The fibre optic pressure sensors were embedded in a mounting bush before they were calibrated to make interchanging sensors relatively easy. The key components are illustrated in Fig. 6.8.

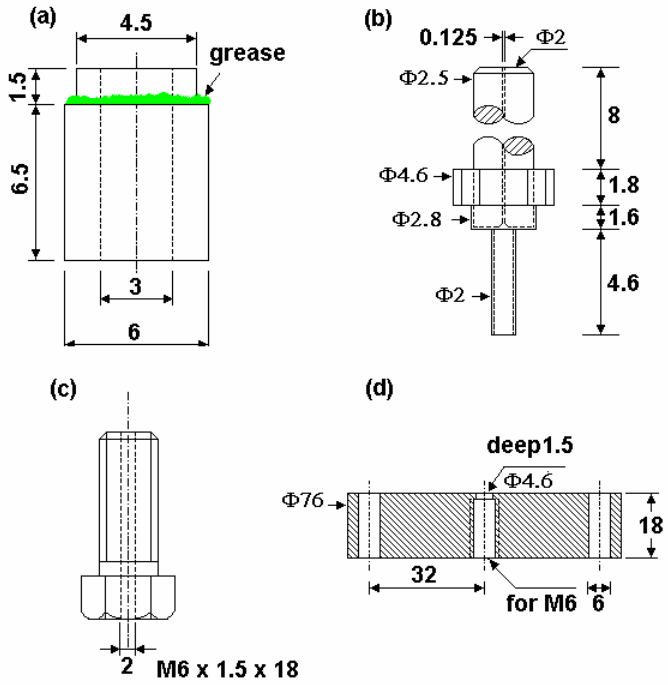

Figure 6.8 Sensor embedding components: a) mounting bush; b) zirconia ferrule; c) locking bolt; and d) end plate for shock tube. All dimensions are in mm.

The mounting bush is shown in Fig. 6.8a. Glue was applied to the sides of the sensor before they were inserted into the bush. The base of the sensor (Fig 6.8b) cannot physically go inside the bush. The length of the bush and the ferrule produces a flush mounted end for the sensor provided it is inserted hard up against the bush. Extra care was taken when embedding the hypodermic tube sensors as they lack the base to prevent proud mounting of the diaphragm.

A brass locking bolt is used to secure the mounting bush into the end plate, Fig. 6.8c. This is essentially a brass bolt with a long hole through its centre. The diameter of the hole is increased towards the ferrule to permit the locking nut to contact directly on the mounting bush.

The end plate has four clearance holes which allow it to be mounted directly on the end of the calibration tube. The end plate has a hole in the centre as shown in Fig. 6.8d to suit the locking bolt and mounting bush. Grease was put onto the sealing face of the mounting bush to prevent leakage during calibration and shock experiments.

6.3.8 Load cycling

The load cycling the foil prior to diaphragm bonding decreases the diaphragm hysteresis, however it is possible that some residual stress is created during the diaphragm preparation and bonding process. Furthermore, the diaphragm is not the only source of hysteresis – the adhesive can also contribute to the overall sensor hysteresis. Applying pressure load cycling to the sensors was found to be the most efficient means of reducing hysteresis effects (Chapter 7).

For the pressure load cycling, a small pressure chamber was constructed. The chamber was pressurised using the central compressed air supply. The pressure load cycling was controlled with solenoid valves and a PLC device. Between approximately 1000 and 2000 pressure load cycles were applied to the sensors before calibration and operation. Each cycle consisted of: 1) a chamber filling period (approximately 1 s); 2) a constant high pressure period (up to approximately 700kPa gauge for 4 s); 3) a chamber discharge period (approximately 1 s); and 4) a constant atmospheric pressure period (approximately 4 s). This load cycling was found to greatly reduce errors associated with sensor hysteresis (Chapter 7).

6.4 Quasi-Static calibration

6.4.1 Arrangement

After the fibre optic pressure sensors were constructed and the load cycling was completed, their performance was evaluated in the calibration tube. The arrangement of the calibration tube, which also serves as the short shock tube arrangement for dynamic experiments (Chapter 8), is presented in Fig. 6.9.

Compressed air (to maximum supply pressure of between 600-800 kPa gauge) was provided by the central compressed air supply. The compressed air entered the system through air valve V1 which controlled the flow rate. The filling line pressure can be read with the Bourdon gauge G1. The pneumatic filling system included a tank which made it easier to control the flow rate and damp fluctuations in system pressure (see Fig. 6.9). This tank could be isolated from the system by closing the valve V2.

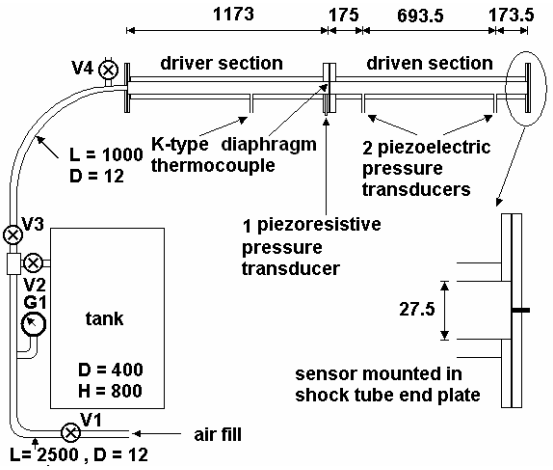

Figure 6.9 Short shock tube and pneumatic filling system. (This arrangement was also used for quasi- static calibrations). All dimensions are mm, not to scale.

Valve V3 is opened to allow the compressed air to fill the calibration tube. Valve V4 is closed during filling and, for the quasi-static calibrations, there is no diaphragm between the driver and the driven sections. The fibre optic sensor is located in the shock tube end plate and is connected to the optical interrogation system. A K-type thermocouple is also placed in the calibration tube to monitor any temperature changes of air inside tube. A piezoresistive pressure transducer (PTX 1400, DRUCK) is located in the middle of the tube to monitor the pressure. The output voltages from the fibre optic transducer, thermocouple and piezoresistive pressure transducer were all recorded with an A/D card (National Instruments AT-MIO 16E-10) and computer or oscilloscope. Closing V1 and opening V4 exhausts the air in the calibration tube.

The optical interrogation system was the same as that presented in Chapter 4, except that the optical isolation in the launching system was not used for some sensors due to their poor reflectivity.

The calibration process was quasi-static which implies that all data such as pressure, temperature and sensor output were recorded during the slow changes of air pressure inside the tube. The term, calibration duration includes both filling and discharging time which in most cases were approximately equal.

6.4.2 Pressure sensitivity

For the quasi-static calibrations to determine the pressure sensitivity, the calibration period was kept long to prevent large changes of temperature within the calibration

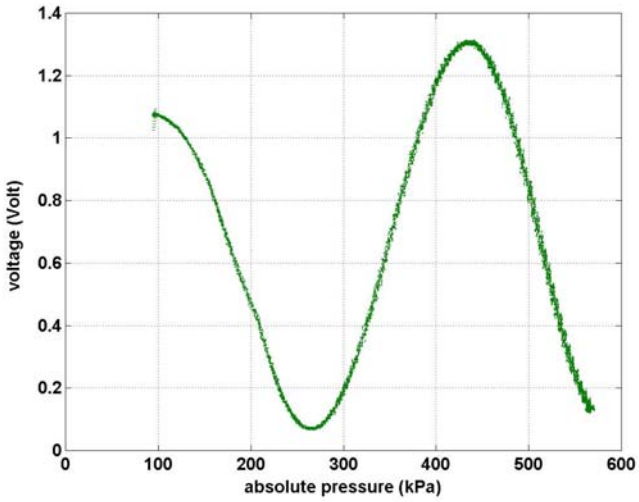

Figure 6.10 Pressure sensitivity of a sensor made with zirconia substrate and polished copper foil (Table 6.6, number 10).

tube (see Chapter 7). Figure 6.10 shows a typical sensor response obtained from the quasi-static pressure calibration process.

Most sensors showed pressure sensitivities somewhat higher than the values calculated using the equations presented in Chapter 5. Furthermore, due to construction variability, even sensors made with the same material and construction technique showed different pressure sensitivities. For example, for the sample copper diaphragm pressure sensor described in Chapter 5, pressure sensitivities between $2\pi/100$ and $2\pi/1200$ rad/kPa[1] were measured while the calculated pressure sensitivity (assuming fixed edge support) was about $2\pi/4800$ rad/kPa. These substantial differences may arise due to: 1) uncertainty in support conditions (see Section 5.11), diaphragm diameter, and adhesive thickness; 2) adhesive deformation and its contribution to diaphragm deflection (see Appendix E); 3) softening of the adhesive and diaphragm due to laser radiation (preliminary calculations indicate that the change of temperature could be around 10^{o}C); and 4) changes of room temperature which could alter the level of pretension within the diaphragm (see Section 5.8).

[1] Following the convention of most literature in this field, pressure sensitivities (and temperature sensitivities) are quoted in reciprocal form throughout this dissertation.

6.4.3 Temperature sensitivity

Ideally sensors should respond only to the parameter which they are designed to measure. Most pressure sensors have a measurable temperature sensitivity, and this is certainly true of the fibre optic pressure sensors constructed in this work. In this section, the quasi-steady temperature sensitivity of the sensors is evaluated through modelling and measurements.

6.4.3.1 Modelling

An increase in temperature causes the diaphragm, adhesive, and substrate to expand. It also leads to changes in the pressure and refractive index of the air within the cavity.

Assuming the volume of the air cavity remains constant with temperature (a good approximation – see below), the change of pressure within the cavity due to a change of temperature of around 3^{o}C will be in the order of 1%. A uniform temperature distribution is assumed and therefore, the change of temperature within the cavity cannot affect the optical path directly. The change of refractive index of air (MacPherson 1999) is about 3×10^{-7} K^{-1}. The pressure and refractive effects of air within cavity are therefore relatively small and will not be considered any further. However, thermal expansion effects are significant and these are considered in some detail below.

For simplicity, a conical model for the diaphragm shape is used. To evaluate the error in this approximation, the length of diaphragm in the conical model can be calculated as $(a^2+h^2)^{0.5}$, and the actual length of the diaphragm can be calculated using $\int_0^a \sqrt{\left(1+(dy/dr)^2\right)}\,dr$ where dy/dr can be calculated using Eq. (5.4). The error in the conical approximation can therefore be calculated and the results for deflections up to 100 μm are presented in Fig. 6.11. According to the results in Fig. 6.11, the maximum error is less than 1% if the deflection of the diaphragm is less than 20 μm.

The adhesive layer between the diaphragm and the substrate may affect the temperature sensitivity. The coefficients of thermal expansion of adhesives are usually greater than that for the zirconia and the diaphragm (80×10^{-6} m/m/^{o}C for Loctite 324; 16.4×10^{-6} m/m/^{o}C for copper; $5\text{-}10\times10^{-6}$ m/m/^{o}C for zirconia). Thus,

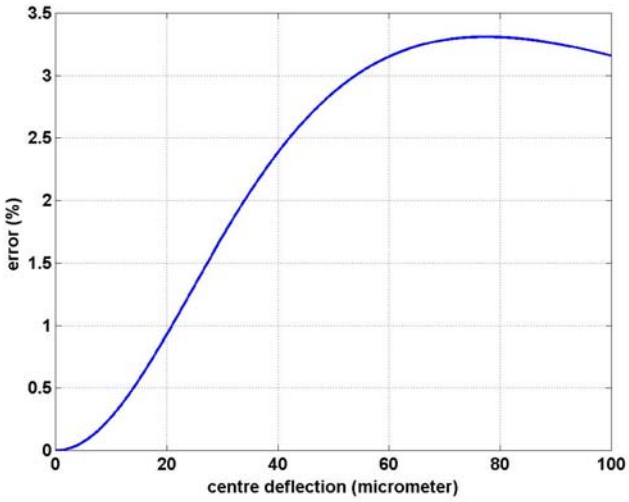

Figure 6.11 Relative error in diaphragm length from the conical model, cavity diameter 125 μm.

adhesives can have a major influence on the temperature sensitivity when the diaphragm is not under load.

However, all practical construction techniques will induce some form of diaphragm deflection and/or pretension. Furthermore, the case of a pressure load applied to the diaphragm is of primary importance. Therefore, it is the modulus of elasticity that should be considered in conjunction with the coefficient of thermal expansion in order to determine the likely impact of temperature changes on the adhesive. As the modulus of elasticity of the adhesive is negligible in comparison with that for copper (E=614 MPa for Loctite 324; E=40000 MPa for copper foil), the thermal effects that derive from the adhesive will be negligible (<1 nm) provided the adhesive layer is thin (<5 μm). In any case, the expansion of the adhesive would tend to increase the cavity length and therefore counteract the effect of diaphragm expansion (which tends to decrease the cavity length). Ignoring the effects of adhesive expansion should therefore lead to a conservative estimate (over estimation) of the temperature sensitivity.

Fibre optic pressure sensors discussed in this work are based on interferometry. This means that those factors that affect the strength of the two beams or the difference between the two beam optical paths can have an influence on the sensor output. Considering the short length of the fibre used in the interferometer (a few metres), the very short length of fibre inside the sensor (a few mm), and the fibre attenuation

coefficient, which is in the order of a few dB/km, the light attenuation is negligible (see Table K.3). The change of the fibre attenuation with temperature is in the order of 0.01 dB/km (see Strelite Optical Technologies and Kingfisher International), therefore the change of the beam strength due to temperature changes can be neglected.

A change of fibre temperature also has two kinds of effects on the beams phase. The first kind of effect is fibre expansion which alters both optical paths and does not influence the sensor output. The second kind of effect is modification of the refractive index of the fibre. This modification can alter the light output angle and it can modify the cavity length. The change of refractive index of all kinds of common fibres (SiO_2, quartz) is in the order of 10^{-5}/°C (Inatomi 2003) and can be neglected.

Assuming the initial cavity length is *cl*, the cavity length change due to the longitudinal expansion of the substrate is given by,

$$\Delta cl = cl \times \alpha_{substrate} \times \Delta T \tag{6.4}$$

where ΔT is temperature change.

Assuming the diaphragm is rigidly clamped around the edge of the hole (the radius of which is initially assumed to be independent of temperature), the expansion of the diaphragm (see Fig. 7.3c) will decrease the cavity length according to,

$$\Delta L = L_0 \times \alpha_{diaphragm} \times \Delta T \tag{6.5}$$

where L_0 is the initial length of the diaphragm. If the diaphragm has an initial deflection given by h_0, this expansion decreases the cavity length according to,

$$\Delta cl = \sqrt{(L_0 + \Delta L)^2 - a^2} - h_0 \tag{6.6}$$

Now the substrate radius will actually increase by the amount,

$$\Delta a = a \times \alpha_{substrate} \times \Delta T \tag{6.7}$$

where *a* is the initial substrate radius. This increase can increase the cavity length only when there is an initial deflection or there is a deflection due to the diaphragm expansion. This change of cavity length can be calculated using,

$$\Delta cl = \sqrt{(L_0 + \Delta L)^2 - a^2} - \sqrt{(L_0 + \Delta L)^2 - (a + \Delta a)^2} \tag{6.8}$$

The optical path change is twice that of the cavity length change (Eq. (3.4)). The results of this calculation are presented in Fig. 6.12 for two different initial cavity lengths and a 1°C temperature rise and 780 nm illumination. The substrate is a zirconia ferrule with a copper diaphragm diameter of 125 μm. The thermal expansion coefficients at room temperature (20°C) were taken as 7.5×10^{-6} K^{-1} and 16.4×10^{-6} K^{-1} for zirconia (Gauthier et al. 1995) and copper (Matweb 2002) respectively.

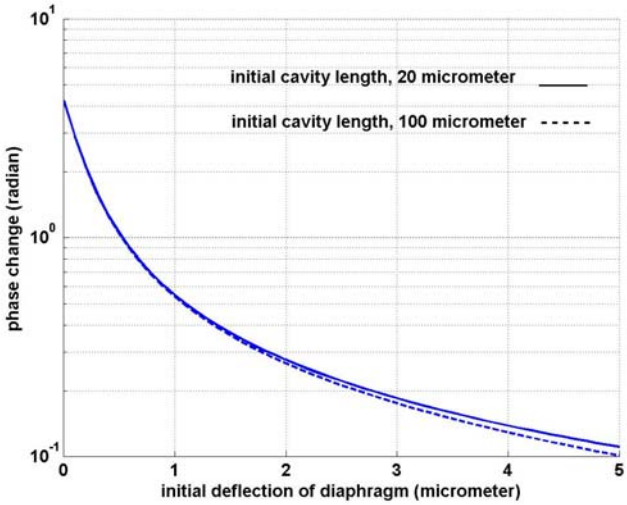

Figure 6.12 Estimated temperature sensitivity for a zirconia ferrule sensor with a copper diaphragm.

Figure 6.12 shows that the effects of the initial cavity length are negligible for initial lengths between 20 and 100 μm. The sensor shows very high temperature sensitivity. For example, in the case of no initial diaphragm deflection, the phase changes 4π/3 radian due to a 1°C rise of temperature. For a sensor with a pressure sensitivity of 2π/600 rad/kPa, an error of 400 kPa would develop if the temperature changed by 1°C.

Increasing the initial deflection of the diaphragm has a significant effect on the temperature sensitivity of the sensor. Using the previous example, 1 μm initial deflection of the diaphragm decreases the value of the error 400 kPa to 50 kPa. An initial deflection of 3 μm decreases this error to less than 20 kPa.

Figure 6.12 also shows that different temperature sensitivities will occur for different operating pressures. Increases in the operating pressure create larger diaphragm

deflections. Therefore, the sensor temperature sensitivity is reduced at higher operating pressure.

Values shown in Fig. 6.12 are appropriate only for very slow changes of temperature – the substrate and the diaphragm temperatures are assumed to be the same. Transient temperature effects are likely to alter these values. The present calculation is likely to overestimate the temperature sensitivity because the effects of the adhesive have been neglected. A thick layer of adhesive increases the optical path and compensates for the diaphragm expansion, which is the main source of temperature sensitivity.

6.4.3.2 Measurements

The temperature sensitivity of each sensor is slightly different due to construction variability. The temperature sensitivity of $2\pi/1.5$ rad/°C was calculated for a uniform temperature distribution without any initial deflection of the diaphragm (copper on zirconia substrate). In practice, a small initial deflection is expected due to the construction techniques

6.4.3.2.1 Sensor

A small temperature controlled environment was established to house a sensor (copper diaphragm on zirconia) and a thermocouple was placed in close proximity to the sensor to indicate the temperature. The lower half of the substrate support and the fibre remained outside the temperature controlled environment. The thermocouple temperature and the sensor output were recorded as the temperature slowly changed over a few degrees Celsius.

A number of different sensors (all copper on zirconia) were tested in this way yielding temperature sensitivities between $2\pi/2$ and $2\pi/10$ rad/°C. These temperature sensitivities are less than the calculated value for an initially flat diaphragm. An initial diaphragm deflection of 1 μm is sufficient to account for the measured temperature sensitivities.

6.4.3.2.2 Sensor and interrogation system

A sensor (zirconia ferrule with copper diaphragm) was connected to the optical interrogation system and the room temperature was changed using a heater. The heater was placed well away from the sensor in an attempt to ensure a reasonably

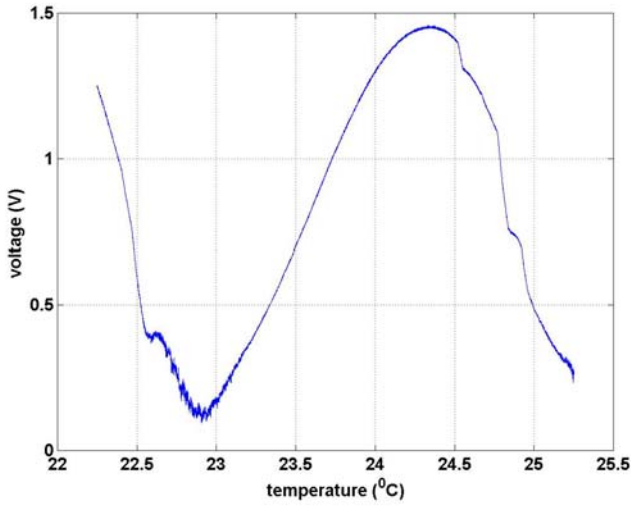

Figure 6.13 Variation of the signal from a zirconia ferrule sensor with a copper diaphragm and the interrogation system as a function of the ambient temperature.

uniform temperature across the sensor and interrogation system. A thermocouple was placed close to the sensor, and the sensor output and thermocouple signals were recorded. Results from this experiment are presented in Fig. 6.13.

The indicated temperature sensitivity was $2\pi/2.5$ rad/°C which is less than the value calculated for an initially flat diaphragm ($2\pi/1.5$ rad/°C). An initial diaphragm deflection of 0.3 μm is sufficient to account for this difference. Adhesive thickness effects may also contribute to this difference.

6.5 Calibration results & discussion

The success of the different construction techniques is measured by: 1) calibration run-to-run repeatability of the sensors; 2) consistency of pressure sensitivity produced by each construction method; 3) visibility of the sensor; 4) regularity of interferometer response; 5) temperature sensitivity; and 6) propensity for diaphragm leakage. Each of these factors is discussed for the different construction techniques. It should be noted that due to a lack of control in all factors affecting sensor response, only general performance is considered and there are considerable exceptions.

6.5.1 Calibration repeatability of each method

Repeatability of a sensor is one of the most important factors of sensor performance. A sensor should be repeatable otherwise it cannot be calibrated. In this thesis, a

repeatable fibre optic pressure sensor has a response that is virtually identical to its previous response under the same conditions (e.g. pressure, temperature, detector gain, etc). In practice, the difference between the two responses should be less than minimum sensible response or within the level of noise. The noise levels may be different for different sensors (e.g. see Section 8.8.3.2). To assess the repeatability of sensor calibration and operation, fibre optic pressure sensors were placed on the calibration tube (shock tube) and the pressure was applied three times without recording any data, the data was then recorded during the next three consecutive calibrations. A shock experiment was performed and the sensor was calibrated for a fourth time.

The results show that the sensors made with foils 1, 2 and 3 (Table 6.3) are not repeatable and their performance is completely different for every calibration due to plastic deformation of the diaphragm. Sensors made with metal foils that do not include plastic layers (foils 4-11, Table 6.3), show better repeatability. The sensors made with liquid adhesive techniques using zirconia ferrules provide the best repeatability. This is because thin adhesive layers could be achieved. However, if two part epoxies are used, poor mixing can significantly decrease sensor repeatability. The two hypodermic tube sensors do not have good repeatability and this is possibly related to relative movement of the two tubes. Tape adhesive sensors (one-sided and double-sided) were not repeatable due to the plastic deformation of the adhesive layers.

6.5.2 Consistency of sensitivity of each method

None of methods described in Section 6.3.1 provide consistent pressure sensitivity due to a lack of control of the diaphragm diameter and adhesive thickness. Hypodermic tube sensors provide better consistency in the pressure sensitivity and this is related to better control of the diaphragm diameter.

6.5.3 Sensor visibility

Sensor visibility varied from less than 5% to greater than 90%. The active control of the cavity length improves the probability of producing high visibility sensors. Short cavity length sensors (<5 μm) show the highest visibility and they show the best results in quasi-static calibration. However, they also show large errors in dynamic calibration (see Chapter 8). The reflectivity of the diaphragm also affects visibility.

Sensors made with metallic cello (foil number 3, Table 6.3) show good visibility. Polishing the foils increases visibility.

6.5.4 Regularity of sensor response

The term of regularity of sensor response refers to how closely the response approximates a standard fringe (sine curve). For example, some irregularities can be observed in Fig. 6.13 at a temperature of 22.6°C and at temperatures higher than 24.5°C. Two factors which affect the regularity of sensor response are: 1) diaphragm creasing during construction; and 2) the roughness of the diaphragm material. Diaphragm creasing was most likely for the one tube hypodermic sensors; the two hypodermic tube sensors show less creasing. No creasing was observed with the zirconia ferrule sensors. Polishing the foil material prior to diaphragm construction decreased sensor irregularity. The best results were observed using zirconia ferrule sensors with polished diaphragms.

6.5.5 Diaphragm leakage

The sensors do not work properly if there is any leakage between the air cavity and the external environment. To assess possible leakage, sensors were placed in the calibration tube and the pressure was increased. The rate of pressure change within the calibration tube was kept to a minimum in order to limit possible changes of temperature which could affect the sensor performance. The temperature was monitored with the K-type thermocouple. To minimise possible changes of the ambient temperature (which can affect the interrogation system), the time of the experiment was limited to 60 minutes. During this time, the tube pressure was maintained at a constant value of 300 kPa, the reference voltage was monitored and the signal voltage was recorded. Provided the reference voltage did not change during this time, any change in signal voltage during this time was assumed to be the result of leakage.

The sensors made using the zirconia ferrules and film adhesive did not show any leakage, but the hypodermic tube sensors and the sensors made with tape adhesives (on zirconia ferrule substrates) were prone to leakage. Zirconia ferrules with the diaphragms bonded using liquid adhesive occasionally exhibited a leakage. Applying a liquid adhesive around the diaphragm edges reduces the possibility of such leakage (however this is not advisable from a sensor hysteresis perspective, Chapter 7). A

few of the hypodermic tube sensors had a microscopic scratch on the diaphragm, which could not be fixed.

6.6 Conclusion

A variety of different sensor construction methods was investigated using different diaphragms, substrates, and adhesives. Sensors constructed from hypodermic tubes have a small outside diameter, however, they are prone to diaphragm leakage and creasing. Sensors constructed using the zirconia ferrule substrates are generally the better sensors. The quality of the diaphragm and the strength of the bond between the fibre and the zirconia ferrule are higher for the zirconia substrate sensors.

The potential for changes in the angle between the fibre and the diaphragm during the adhesive curing process is much lower in the case of the zirconia ferrule substrate sensors. Diaphragm bonding with tape adhesives does not produce good results due to the softness and plasticity of the tape adhesives. Useful sensors can be constructed using film adhesives and it is possible to apply pretension to the diaphragm during production. However, the lack of control during the required heating and cooling process makes it a less attractive option than the liquid adhesives.

The diaphragm roughness has a large impact on the sensor performance, and roughness should be minimised. Decreasing the rms roughness (R_a) to about 30 nm improves the sensor performance, however speckle effects remain and the performance of the diaphragm material should be assessed before final curing of the sensor. Optimising the cavity length for each sensor increases the possibility of quality sensor production to about 50%.

Most sensors showed a higher pressure sensitivity than calculated assuming fixed edge conditions. The edge support conditions are perhaps somewhere between fixed edge and simply supported conditions. Furthermore, the contribution of adhesive deformation on the diaphragm deflection increases the pressure sensitivity. The sensors made with the same material also show different pressure sensitivity. For example, for a zirconia substrate sensor with a copper diaphragm (thickness 9 μm), the calculated pressure sensitivity was $2\pi/4800$ rad/kPa but the measured pressure sensitivities were between from $2\pi/100$ to $2\pi/1200$ rad/kPa. This variation of pressure sensitivity can be related to different glue thickness, diaphragm diameter

and increases in the adhesive and diaphragm temperature due to the absorbed laser radiation.

The fibre optic pressure sensors show high temperature sensitivity. The temperature sensitivity of the sensor constructed with zirconia substrates and copper diaphragms was found to be between $2\pi/2$ and $2\pi/10$ rad/°C.

The temperature sensitivity of the optical interrogation system makes it important to calibrate the sensor before every experiment. The temperature sensitivity of the interrogation system does not affect the sensor performance during an actual shock tube experiment, as this is completed in a very short time. The interrogation system can be remote from the flow in which the measurements are being taken.

Chapter 7: Hysteresis effects

7.1 Introduction

Mechanical hysteresis operates in all materials and will therefore affect the performance of pressure sensors that utilize a diaphragm. An illustration of mechanical hysteresis can be seen in the stress-strain curves for most materials: usually the curves are not precisely aligned in the increasing and decreasing load directions. Mechanical hysteresis results from friction-like irreversibilities which are dissipated as heat. The mechanical hysteresis effects can be minimized through proper choice of material and working stress level. For example, crystalline materials yield low hysteresis errors and diaphragms made of monocrystalline silicon show minimal hysteresis effects (Di Giovanni 1982). However, other optically-addressed sensor construction issues such as: 1) price; 2) reflectivity; and 3) availability in foil or thin sheet form, could limit the use of low mechanical hysteresis materials in some cases.

The fibre optic pressure sensors constructed with the initial techniques described in Chapter 6 (those techniques that did not utilise any form of hysteresis minimisation) showed strong hysteresis effects. Such levels of hysteresis are not conducive to high precision pressure measurements in transient aerodynamic flows. In this chapter, the hysteresis effects associated with the quasi-steady calibration of the fibre optic pressure sensors are characterised (Section 7.2), and attempts are made to minimise the various contributions (Section 7.3). The success of hysteresis minimisation efforts is demonstrated by examining the quasi-static calibration results from sample pressure sensors (Section 7.4).

The sensors considered in this work were constructed from zirconia ferrules with aluminium and copper diaphragms (38.1 and 12.7 μm thick respectively). The diaphragms were bonded to the substrate using Araldite 5 minute. The fibre optic interferometer and calibration hardware are the same as those described in Chapter 6.

7.2 Sources of hysteresis

7.2.1 Diaphragm material

While the sensor cost is an important factor, an expensive diaphragm material could still be used provided a manufacturing method is developed that does not require much material. The diaphragm should be an optically reflective material that is available in thin foil or sheet form.

However, for the current work, a variety of low cost aluminium and copper foils supplied by All Foils Inc were used (Table 6.3). Figures 7.1 shows the results from tension tests on 38.1 μm aluminium foil (1145-H19) and 12.7 μm copper foil (110 as rolled). These tension tests were performed using a H5K-S Universal Testing Machine supplied by Housfield Ltd (with load cell 99-999-1026), as described in Appendix I. The results show that the hysteresis in the aluminium foil is 6% larger than it is in the copper foil (The hysteresis is currently defined as the residual strain when the load returns to zero divided by the peak strain experienced during the loading cycle).

Simulated sensor output signals accounting for the hysteresis identified in the tension testing of the aluminium (1145-H19) and copper (110) materials are presented in Figs. 7.2. For these simulations, the optical cavity transfer function was taken as

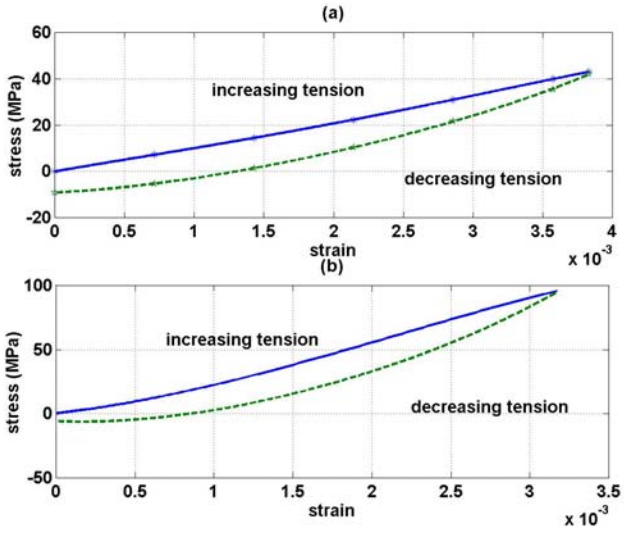

Figure 7.1 Tension test results for: a) 38.1μm thick aluminium foil (1145-H19); and b) 12.7 μm thick copper foil (110).

(MacPherson et al. 1998),

$$I_r = kI_0(1+V\cos\phi) \tag{3.5}$$

where V is cavity visibility which can be calculated using,

$$V = \frac{I_{\max} - I_{\min}}{I_{\max} + I_{\min}} \tag{3.6}$$

The factor k incorporates losses, and $I_{\max}$ and $I_{\min}$ are the cavity maximum and minimum reflected intensities respectively. I_r is measured intensity and ϕ is optical phase which is related to the optical path length according to

$$\phi = \frac{4\pi}{\lambda} nl \tag{3.4}$$

where λ is wavelength and nl is optical path length, n is the refractive of index of the medium and l is the cavity length.

Assuming a clamped edge support for the diaphragm, the deflection can be calculated using (Di Giovanni 1982),

$$y = \frac{3(1-\nu^2)\Delta p}{16Eh^3}(a^2 - r^2)^2 \tag{5.4}$$

where E is the modulus of elasticity, r is the distance from centre of the diaphragm, a is the radius of diaphragm (to the clamped support), ν is Poisson's ratio, h is the

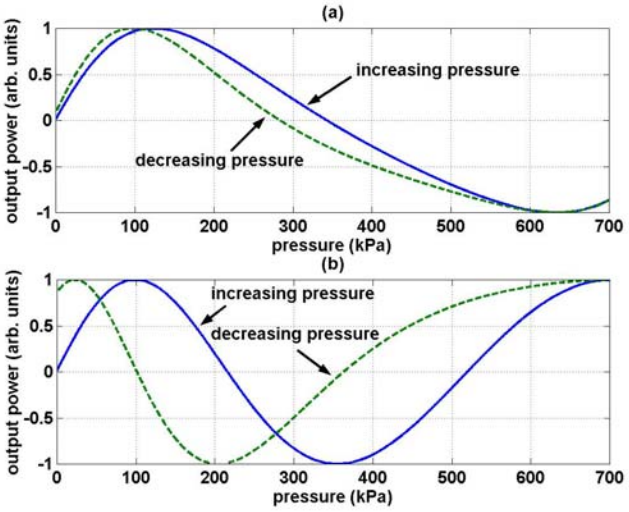

Figure 7.2 Simulated output signal for hysteresis in: a) 38.1 μm thick aluminium diaphragm (1145-H19); and b) 12.7 μm thick copper diaphragm (110).

thickness of diaphragm, and Δp is the difference in pressure across the diaphragm.

As different points within the diaphragm experience a different maximum stress, precise simulation of hysteresis effects in a diaphragm sensor requires data from a number of tension tests each inducing a different maximum stress. However, in the present simulations, the relative hysteresis behaviour of the materials is assumed to be independent of the actual maximum stress. The unsupported diaphragm diameter was taken as 0.4 mm for the aluminium diaphragm and 0.25 mm for the copper diaphragm in the simulations as these values are thought to be representative of the actual construction using the Araldite adhesive.

From Figs. 7.2, it is apparent that the mechanical hysteresis of the diaphragm material makes a significant contribution to the net hysteresis observed during sensor calibration. The maximum hysteresis effect for the aluminium and copper sensors over a calibration range of 700 kPa is around 50 kPa and 150 kPa respectively, and these values are unacceptably large. It should be noted that in the tension tests, aluminium showed more hysteresis than copper (see Fig. 7.1), but because the aluminium diaphragm is thicker, the sensor indicates lower hysteresis. Equations (5.6) and (5.8) show that increasing the thickness of the diaphragm decreases the stress (provided other parameters are held constant).

7.2.2 Diaphragm bonding material and arrangement

The hysteresis of the Araldite was not identified through tension testing. However, the adhesive is expected to have a hysteresis effect which plays an important role in the net sensor hysteresis.

Two methods have been used to bond the diaphragm to the ferrule as illustrated in Fig. 7.3. In first method (Fig. 7.3a), there is no bonding around the edge of the diaphragm and thus there is no bending stress near the diaphragm edge for this method. In the second method (Fig. 7.3b), the epoxy is around and on top of the diaphragm edge. With this first method, a moment could be transferred into the epoxy near the diaphragm edge.

To estimate the significance of bond hysteresis effects, a uniform distribution of shear stress was assumed for all points within the bonding material. For simplicity, it was also assumed that the diaphragm deflection decreases linearly from the centre to

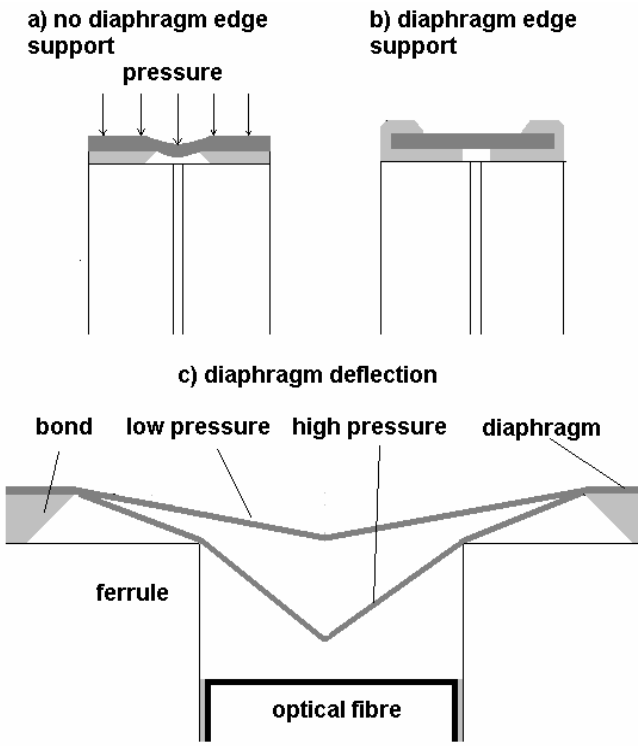

Figure 7.3 Illustration of diaphragm bonding and deflection: a) no diaphragm edge support; b) diaphragm edge support; and c) possible diaphragm deflection for low and high pressure.

the edge (a conical surface for the deflected diaphragm shape). When the minimum diameter of the bonded surface is larger than the inner diameter of the ferrule, two cases are possible as illustrated in Fig. 7.3c.

The value of *G* (the shear modulus) for increasing and decreasing diaphragm pressure will be a function of the shear stress and should ideally be measured. However, for the present modelling, two different but constant values for *G* are assumed to apply in the case of increasing and decreasing pressures.

Figure 7.4 illustrates the results of the present modelling for a 12.7 μm thick copper diaphragm (110) bonded to the ferrule using the Araldite epoxy (5 minute) with the two different edges conditions (illustrated in Fig. 7.3). Properties for the Araldite were estimated from available data (Hussey & Wilson 1996) which gives *E*=680 MPa for Araldite 2016. Estimated shear modulus values are *G*=230 MPa for an increasing load and 177 MPa for a decreasing load. The internal and external diameters of Araldite were taken as 0.4 mm and 2 mm respectively and its thickness was taken as 5 μm. Details of the calculation method are presented in Appendix E.

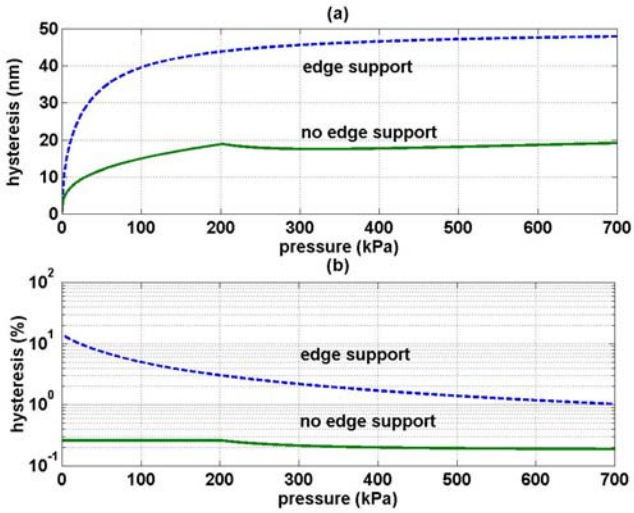

Figure 7.4 Estimation of diaphragm deflection hysteresis due to hysteresis in diaphragm bonding material (Araldite) for 12.7 μm thick copper diaphragm (110): a) absolute diaphragm deflection; and b) relative diaphragm deflection.

Figure 7.4 shows the result and it should be noted that only the effects of the bonding material are considered in this figure.

The results of the bond modelling presented in Fig. 7.4 indicate that the type of diaphragm edge restraint has an influence on the diaphragm deflection hysteresis. For example, if a pressure change of 700 kPa is imposed and then removed from the diaphragm with edge support (Fig. 7.3b), the cavity length obviously decreases and then increases, but will remain about 50 nm less than its initial length (see Fig. 7.4a). In the case of the diaphragm with no edge support (Fig. 7.3a), the corresponding hysteresis value is only about 20 nm (see Fig. 7.4a). The diaphragm without the edge support is confirmed as the more attractive configuration when it is recognised that the value of diaphragm deflection at maximum load in the case with edge support is less than in the configuration without edge support.

Figure 7.4b illustrates the relative hysteresis, which is defined as the diaphragm deflection that remains when the pressure is removed, divided by the diaphragm deflection (at r=0) at maximum pressure. For example if the pressure increases from zero to 700 kPa and then decreases to zero, the remaining deflection is about 1% of the deflection at 700 kPa for a diaphragm with edge support, and only 0.2% for a diaphragm without edge support. The kink in the no edge support curve in Fig. 7.4 at

about 200 kPa arises because the diaphragm deflection is large enough for the diaphragm to make contact with the substrate.

7.2.3 Confined air in the cavity

The air inside the cavity between the end face of the fibre and the diaphragm can also contribute to the net sensor hysteresis. To estimate the magnitude of this effect, it is first assumed that the diaphragm is subjected to a sudden change in external pressure which causes an adiabatic compression within the air cavity. It is then assumed that there is enough time for the air cavity temperature to return to the ambient temperature of the surrounding materials through a heat transfer process. Finally, it is assumed that the return of the external pressure to its initial value induces an adiabatic volume change in the cavity air. The diaphragm deflection (and hence the changes in air cavity volume) was calculated using Eq. (5.4). Results from this modelling are presented in Fig. 7.5. Details of the calculation are presented in Section 8.8.3.2.

Figure 7.5a indicates that maximum change of pressure within the confined air cavity is expected to be less than 1 kPa for the cavity lengths normally adopted in this work (generally greater than 10 μm) and hence it is reasonable to assume that the confined air pressure is essentially constant during the pressure calibration process. The change of temperature is also expected to be negligible (see Fig. 7.5b), and for a 10

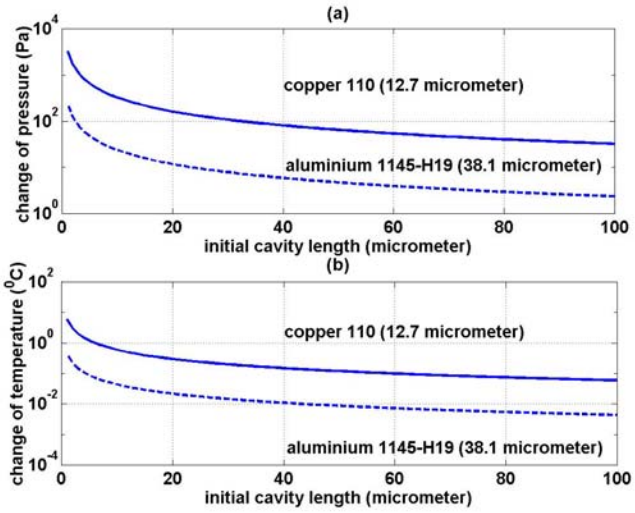

Figure 7.5 Maximum change of properties of air inside air cavity as a function of initial cavity length: a) pressure; and b) temperature.

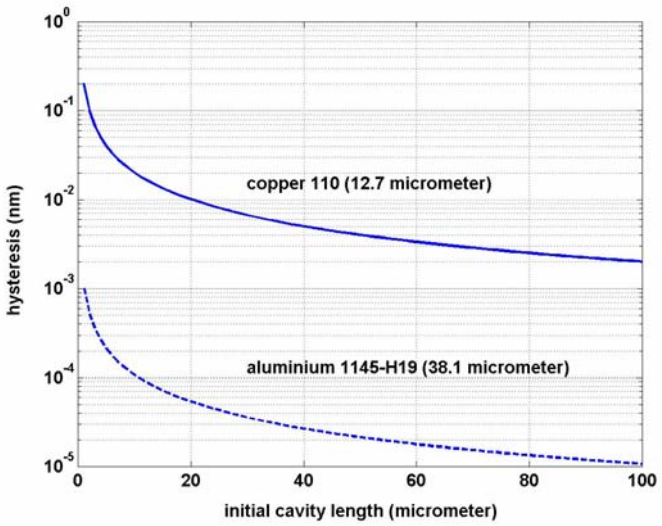

Figure 7.6 Apparent deflection hysteresis as a function of initial cavity length due to confined air inside cavity.

μm cavity length, the anticipated change is less than 0.1°C for the present calibration conditions. It should be noted that the change of diaphragm temperature would be even less than values that are presented in Fig. 7.5b which are for the cavity air temperature. This is because there is enough time for heat transfer and some heat will be absorbed by the substrate.

Figure 7.6 presents the apparent deflection hysteresis calculated from the current model and this figure is expected to provide an upper estimate for the magnitude of this effect. When the applied pressure returns to its initial value, the pressure of the confined air will be less than its initial value because of its lower temperature due to heat transfer.

7.2.4 Calibration tube

The temperature of the air inside the calibration tube changes during the charging and discharging process and this could affect the apparent sensor performance. To model these effects, the air is assumed to be an ideal gas and heat transfer to and from the tube walls is considered. Heat transfer on the internal and external surfaces of the calibration tube is thought to be of a similar magnitude to free convection around a horizontal cylinder, for which standard heat transfer correlations are available (Holman 1986). Furthermore, an equal time is considered for the increasing pressure and decreasing pressure phases of the calibration process. Details of the

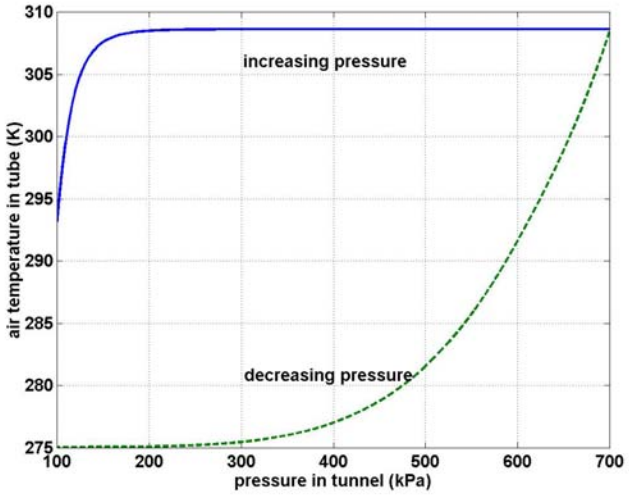

Figure 7.7 Air temperature inside the calibration tube due to changes of pressure over 1 min.

calculation are presented in Appendix F. Results from this model are presented in Figs. 7.7 and 7.8.

Figure 7.7 shows that substantial changes of temperature could occur within the tube. For example, on returning to the original pressure, the temperature is expected to be around 18°C lower than its initial value. Diaphragm temperature changes could be induced by such changes in tube air temperature, and as the diaphragm deflection

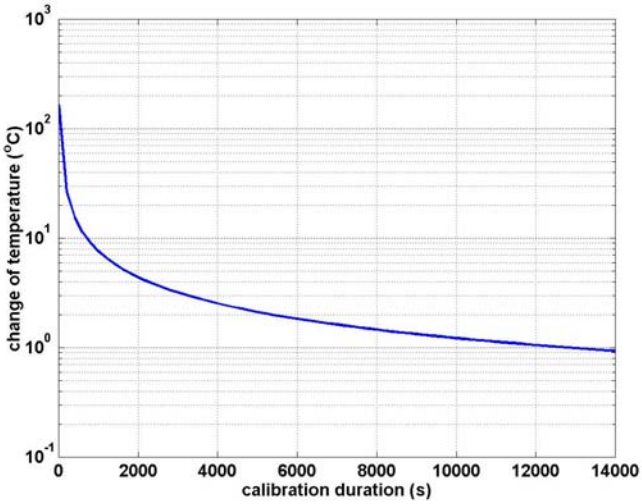

Figure 7.8 Influence of calibration duration on the change of temperature inside tube in maximum pressure of 700 kPa.

will have some temperature sensitivity, apparent sensor performance may be affected. Figure 7.8 presents the change of air temperature inside the tube when the pressure returns to its initial value as a function of the calibration process duration. A strong relationship between calibration tube air temperature and the duration of the calibration process is apparent. For example, Fig. 7.8 shows that to have only a 1°C change of temperature on returning to the initial pressure, at least 3 hours are required for the calibration process.

Experimental results show that the calculation overestimates the air temperature and calibration duration especially for a fast calibration as expected (refer to Appendix F). For example, according to Fig. 7.8, for a maximum change of air temperature inside the calibration tube of 26.5°C, the calibration duration should be longer than 120 s, but the experimental results show 200 s is required which implies an error of about 70%. This error decreases for slower calibrations. For example, for a 20 minutes calibration, the change of air temperature is 6.5°C and 4.5°C according to calculation and experimental results respectively. This indicates an error of about 45%.

7.2.5 Summary

Four potential sources of hysteresis were evaluated using tension test results and theoretical modelling. To amplify the previous results and compare the relative significance of each factor, two model sensors are considered: one with an aluminium foil diaphragm, and the other with a copper foil diaphragm. The thickness of the adhesive was assumed to be 5 μm and the supposed calibration duration was 1 hour for each sensor. Furthermore, the internal and external diameters of the diaphragm were taken as 0.4 mm and 2 mm and the edge supported bonding arrangement (Fig. 7. 3b) was assumed.

The pressure sensitivity for the aluminium diaphragm (38.1 μm thickness) was taken as $2\pi/800$ rad/kPa, and for the copper diaphragm (12.7 μm thickness) it was taken as $2\pi/530$ rad/kPa (both values were derived from Fig. 7.2). The temperature sensitivities were assumed to be $2\pi/12^{o}$C for both sensors (see Section 6.4.3). (The average initial temperature sensitivity is about $2\pi/6^{o}$C but it decreases when the diaphragm deflects).

The calculated effects of each factor on the performance of the sensor during quasi-static calibration were converted to a phase change and are presented in Table 7.1. The effects of material hysteresis and calibration duration are greater than other factors. The calculated effects for the calibration duration may be slightly overestimated because the temperature of the air and that of the sensor may be somewhat different due to a low convective heat transfer coefficient.

From the discussion in Sections 7.2.1 to 7.2.4, it should be clear that while the effects of material hysteresis and calibration duration are larger than the other factors, the adhesive and confined air in the cavity can play more significant roles in the net sensor hysteresis if a different construction is considered. For example, had a 50 μm bonding layer been assumed, the effects of the adhesive layer hysteresis would be significant (0.2 and 1.2 rad for aluminium and copper diaphragms respectively).

For the 20 μm cavity length, the effects of confined air are negligible and even the results presented in Table 7.1 are overestimated because in practice, there is enough time for heat transfer during quasi-static calibrations. However, for short cavity length sensors and very fast changes of pressure (such as occurs in shock experiments), the air cavity effects become important, as discussed in Section 8.8.3.2.

Table 7.1 Calculation of hysteresis effects for two model sensors

Factor contributing to hysteresis	Phase change (radians)	
	aluminium diaphragm (38.1 μm thick)	copper diaphragm (12.7 μm thick)
Diaphragm material	0.4	1.7
Adhesive (thickness 5 μm)	0.02	0.12
Air cavity (cavity length 20 μm)	0.002	0.0001
Calibration duration (1 hour)	1.6	1.6

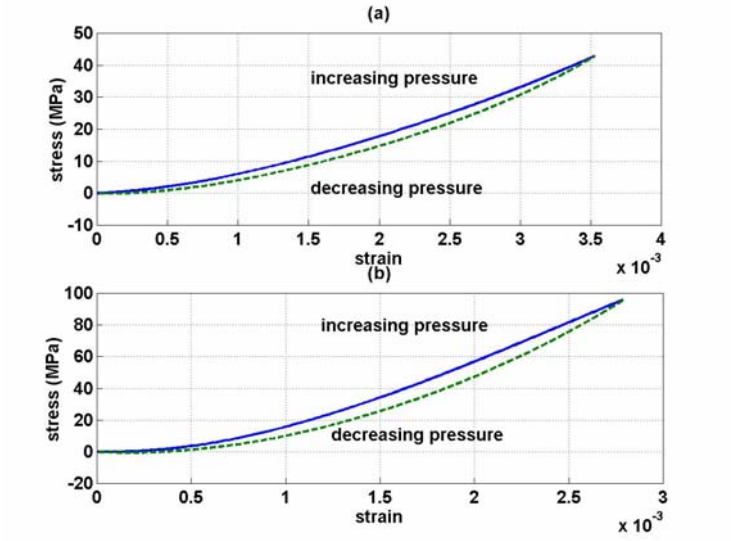

Figure 7.9 Tension test results after 500 tension load cycles for the: a) 38.1 μm thick aluminium foil (1145-H19); and b) the 12.7 μm thick copper foil (110).

7.3 Reduction of hysteresis

7.3.1 Diaphragm material

The hysteresis that derives from the quasi-static calibration duration is not an inherent sensor hysteresis issue. Therefore, the mechanical hysteresis of the diaphragm material is the main contribution to the hysteresis of the sensor itself. The mechanical hysteresis of the diaphragm material can be reduced through load cycling.

Tension test results for aluminium foil (1145-H19) and copper foil (110) after 500 tension load cycles are presented in Fig. 7.9. Figures 7.10a and 7.10b are the simulated output signals for sensors constructed with the aluminium (1145-H19) and copper (110) diaphragm materials after the 500 tension load cycles. These simulated output signals utilize the results in Fig. 7.9 and the modelling previously described in Section 7.2.1.

Comparing Fig. 7.2a and Fig. 7.10a, it can be seen that the tension load cycling with the aluminium material reduces the simulated hysteresis effect from around 50 kPa to 15 kPa. Similarly, through a comparison of Fig. 7.2b and Fig. 7.10b, it can be seen

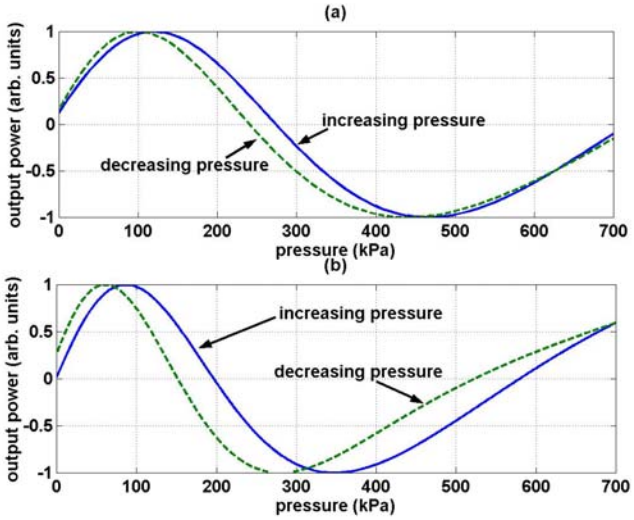

Figure 7.10 Simulated output signal accounting for hysteresis in diaphragm after 500 tension load cycles: a) 38.1 μm thick aluminium diaphragm (1145-H19); and b) 12.7 μm thick copper diaphragm (110).

that the simulated hysteresis effect in the copper diaphragm is decreased from around 150 kPa to 50 kPa.

While load cycling is expected to reduce the mechanical hysteresis effect, tension load cycling the foil material is unlikely to yield optimal results because: 1) microstructural changes may occur during the process of bonding the foil to the zirconia; and 2) the diaphragm stress state is not uniaxial tension. A more practical solution would be to pressure load cycle the diaphragm after bonding it to the zirconia. Results from both tension and pressure load cycling are presented in Section 7.4.

7.3.2 Diaphragm bonding material and arrangement

Mechanical hysteresis in the bonding material and the diaphragm bond arrangement play an important role in the overall sensor hysteresis problem. Based on the results of Section 7.2.2: 1) the bonding material should remain only on the surface of the diaphragm that faces the ferrule because the type of edge restraint can have an effect on the hysteresis; 2) a bonding material with a high shear modulus should be used to reduce the shear deflection; 3) the thickness of the bonding material should be low to minimize the shear deflection; 4) the bonding material should have an inherently low mechanical hysteresis of identifiable magnitude; 5) load cycling the bond may reduce the hysteresis effects; 6) the stress in the glue should be decreased by

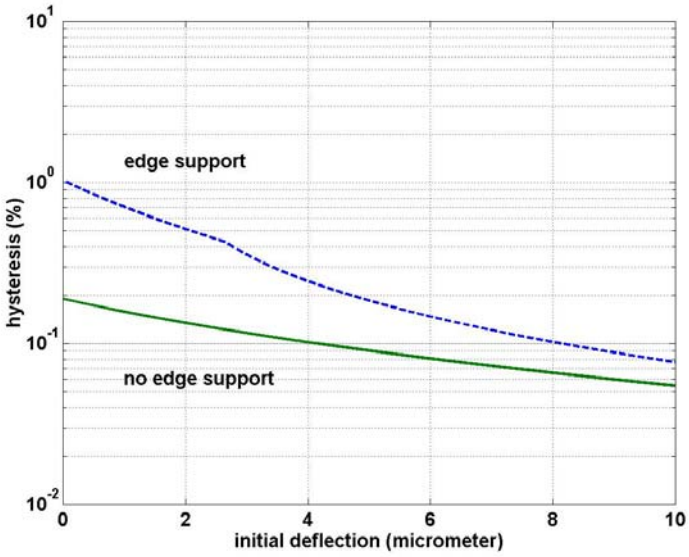

Figure 7.11 Effect of initial deflection on relative diaphragm deflection hysteresis due to hysteresis in diaphragm bond (Araldite).

increasing bonding area; and 7) an initial diaphragm deflection could reduce hysteresis. While this last point has not yet been directly discussed, it is suggested by the results in Fig. 7.5 which indicate that the relative hysteresis reduces with increasing diaphragm deflection.

The relative diaphragm deflection hysteresis for a pressure of 700 kPa as a function of the initial (zero pressure) diaphragm deflection is presented in Fig. 7.11. This is for the case of a 12.7 μm thick copper diaphragm (110) bonded to the ferrule with Araldite 5 minute, as discussed in Section 7.2.2.

Another consequence of providing an initial deflection when bonding the foil to the ferrule is the decrease in temperature sensitivity of the diaphragm deflection. Figure 7.12 illustrates the assumed conical geometry for the calculation of temperature sensitivity effects. (In section 6.4.2.1, it was demonstrated that this approximate modelling is likely to yield results that are accurate to within 3.5% for cavity lengths less than 100 μm.) The length L changes according to

$$L = L_0(1+\alpha\,\Delta T) \tag{6.5}$$

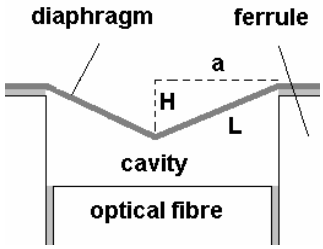

Figure 7.12 Sensor details and geometry for estimating temperature effects.

where L_0 is the initial deflected length, L is the deflected length after the temperature change, α is the thermal expansion coefficient, and ΔT is the change in temperature. The calculation of deflection due to temperature effects (ΔH – see Fig. 7.12) is a matter of geometry because the radius of the cavity (a) is assumed to remain constant. For a cavity diameter of 125μm and aluminium (α_{Al}=24 μm/m/°C), copper (α_{Cu}=16.4 μm/m/°C) and silicon (α_{Si}=2.49 μm/m/°C) diaphragms, the calculated temperature sensitivity is presented in Fig. 7.13a as a function of the initial diaphragm deflection.

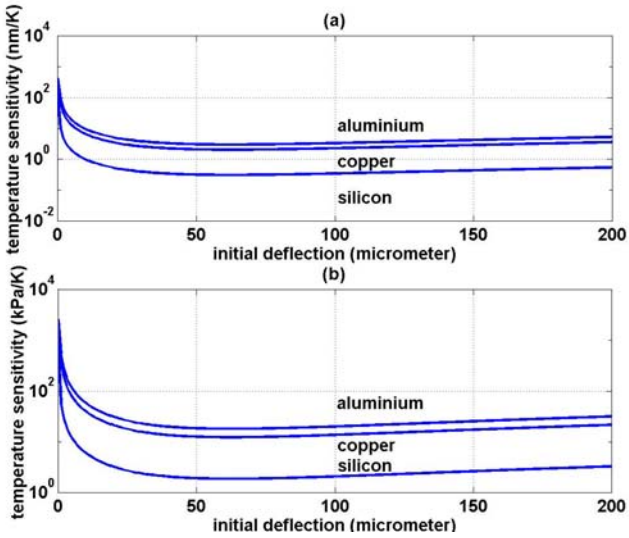

Figure 7.13 Variation of temperature sensitivity with initial diaphragm deflection expressed as a: a) deflection; and b) apparent pressure change.

In some applications it is more convenient to express the diaphragm deflection due to temperature effects as an apparent pressure change. Assuming a diaphragm pressure sensitivity of 0.167 nm/kPa, the results of Fig. 7.13a are expressed in terms of an

apparent pressure change in Fig. 7.13b. The results of this approximate modelling indicate that an initial deflection equal to diaphragm radius (62.5 μm) can decrease temperature sensitivity 500 times for a silicon diaphragm from 1000 to 2 kPa/°C.

The initial deflection also has a dramatic effect on the pressure sensitivity. However, the pressure sensitivity can be easily increased by selecting a thinner diaphragm without penalty in the temperature sensitivity.

7.3.3 Confined air in the cavity

The confined air in the cavity does not make a significant contribution to the apparent hysteresis observed during quasi-static pressure calibration. However, it does have an important effect when the diaphragm is shock-loaded as is demonstrated in Section 8.8.3.2.

7.3.4 Calibration tube

The change of air temperature in the calibration tube is likely to change the diaphragm temperature and may therefore contribute to the apparent hysteresis of the sensor. Calibrations should be performed over a long time period – perhaps as much as 3 hours or more, and the room temperature should remain fixed during calibration.

One practical way to reduce the change of temperature is to start charging and discharging slowly. Figure 7.7 indicates the temperature changes within the calibration tube has sharp slope at the beginning of both steps.

If in-situ calibration of the pressure sensor is not required, a more practical solution is to perform the pressure calibrations using a liquid medium instead of the air. In this case the calibrations could be performed rapidly.

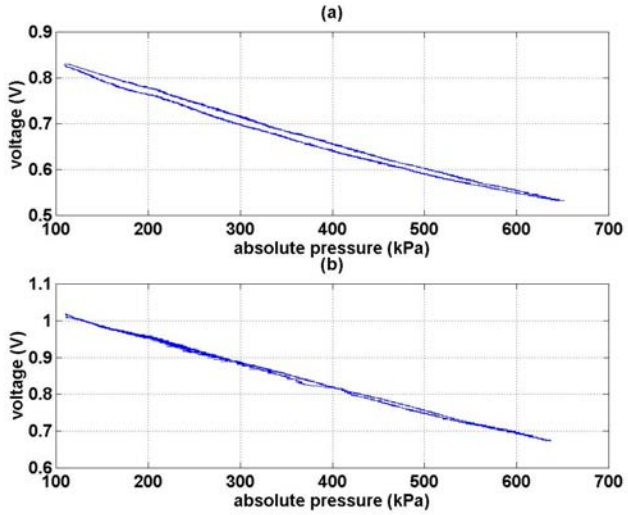

Figure 7.14 Calibration of a sensor with 12.7 μm thick copper (110) diaphragm: a) constructed after 500 tension load cycles applied to the foil material; and b) after 10 additional pressure load cycles applied to the finished sensor.

7.4 Experimental results

Based on the theoretical results provided in the previous sections (7.2 and 7.3), new sensor construction (as described in Chapter 6) and calibration techniques were employed and the results were compared with earlier techniques. The new construction techniques included a number of features: 1) load cycling to the diaphragm and the sensor were applied; 2) a thinner adhesive bonding layer was provided; 3) longer cavities were tested; and 4) the calibration duration was increased especially at the beginning of charge and discharge steps. Details of features 1, 2 and 3 were explained in Chapter 6.

Pressure calibrations were performed over a period of about 20 minutes. For this calibration duration, a maximum change in air temperature within the calibration tube of around 6°C is expected (see Fig. 7.8). The temperature of diaphragm will change by less than 6°C and because of initial diaphragm deflection, the temperature change in the calibration tube should not have a major affect on the results.

Figure 7.15a shows the calibration results from another sensor, which was constructed using the same method described above, one week after applying a cyclic tension load to the foil material. The calibration results shows around 100 kPa hysteresis. To reduce hysteresis in this sensor, a purpose-build pressure cycling tube

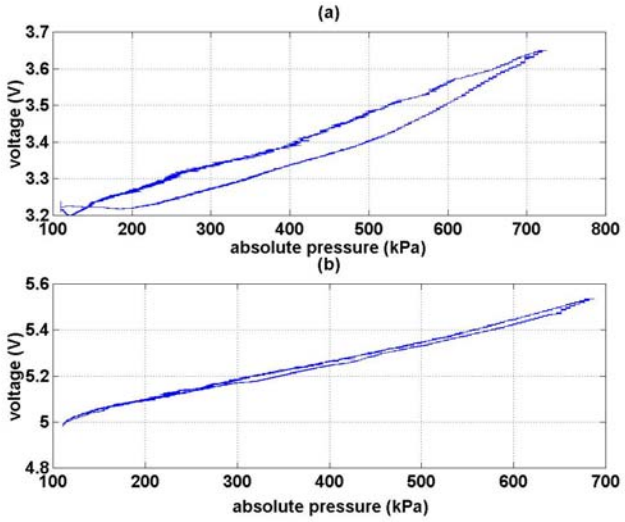

Figure 7.15 Calibration of a sensor made with 12.7 μm thick copper (110) diaphragm; a) after 500 tension load cycles applied to the foil material prior to sensor construction; and b) after 2000 pressure load cycles applied to the finished sensor.

was constructed. After 2000 pressure cycles over a range of 400 kPa, the sensor which had previously demonstrated around 100 kPa hysteresis (Fig. 7.15a) demonstrated less than 10 kPa hysteresis as is illustrated in Fig. 7.15b.

7.5 Conclusion

The hysteresis effects associated with fibre optically-addressed diaphragm pressure sensors have been investigated. It is demonstrated that without due attention to hysteresis issues, substantial problems are likely to be encountered. A number of techniques to reduce hysteresis effects have been proposed and investigated theoretically. Experimental results demonstrate the substantial reduction of hysteresis effects that can be achieved by: 1) tension load cycling the diaphragm material prior to bonding to the ferrule; 2) pressure load cycling subsequent to sensor construction; 3) reducing glue thickness and increasing bonding area; and 4) longer calibration period with slow beginning of charge and discharge steps.

Chapter 8: Shock tube experiments

8.1 Motivation and outline

Fibre optic pressure sensors have been constructed using the techniques discussed in Chapter 6 and their hysteresis minimized through pressure load cycling (Chapter 7). The pressure and thermal sensitivity such sensors has also been quantified (see Chapter 6). However, it is also necessary to determine the sensor performance under shock conditions in order to characterise their dynamic response. The shock tube experiments provide a measurement of the damped natural frequency of the diaphragm. Furthermore, the thermal response of the sensors needs to be quantified under transient conditions, because different transient temperature distributions can affect the thermal sensitivity.

Section 8.2 provides a general description of a shock tube and discusses analytical methods for one dimensional, inviscid, adiabatic shock flow. The particular shock tube arrangement, quasi-static calibration, and the fibre optic interrogation system used for this work are discussed in Sections 8.3 to 8.5. A piezoelectric pressure sensor and a quasi one-dimensional computational fluid dynamics program are used to evaluate the shock performance of the fibre optic pressure sensors. The response of a sample fibre optic pressure sensor under shock loading is presented and discussed in Section 8.8. This section also discusses the source of the errors observed in the fibre optic sensor response. Two kinds of thermal isolation layer were used and their thermal performance is assessed in Section 8.9. The response time and natural frequency of fibre optic sensors with and without thermal isolation layers are discussed in Section 8.10. The final section (8.11) describes the application of a fibre optic pressure sensor to the identification of an acoustic disturbance within the shock tube.

8.2 Ideal shock tube theory

Shock tubes are valuable but inexpensive gasdynamic instruments that have important applications in the study of high temperature gases, in the testing of supersonic bodies and hypersonic entry vehicles, and high power gasdynamic lasers (Anderson 1989). The basic configuration of shock tubes was illustrated in Section

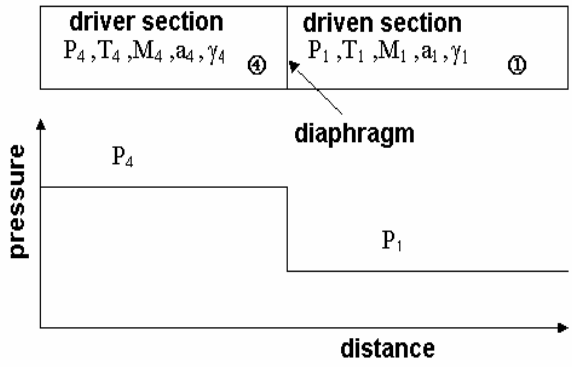

Figure 8.1 Initial conditions in a pressure-driven shock tube (after Anderson 1990).

2.6. A schematic illustration of the initial conditions within a shock tube is presented in Fig. 8.1.

Region 4 indicates the high-pressure section (the driver section) and region 1 indicates the low-pressure section (the driven section). The temperature, pressure and molecular weights are designated *T*, *P*, and *M* respectively and can initially be different for the two regions. After the diaphragm which separates the two regions ruptures, a normal shock wave propagates to the right (into region 1) with a velocity of *W*, while expansion waves (an expansion fan) propagates to the left (into region 4), as illustrated in Fig. 8.2.

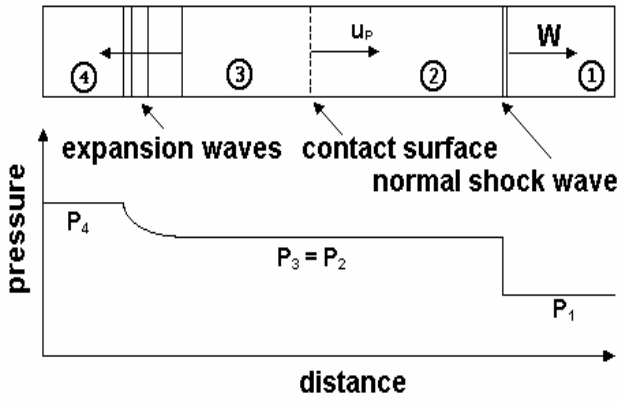

Figure 8.2 Conditions in a shock tube some time after diaphragm rupture (adapted from Anderson 1990).

Gas in region 4 travels towards region 1 with a velocity u_p, and the interface between driver and driven gases is called the contact surface (see Fig. 8.2). Region 2 consists

of shock compressed gas that was initially in region 1. Region 2 has a higher pressure than region 1 due to the effects of the normal shock. Region 3 is the region between the contact surface and expansion fan, and the gas in region 3 has the same velocity and pressure as the gas in region 2 (although the entropy in region 3 differs from that in region 2).

Analytical expressions for the flow conditions in regions 2 and 3 can be derived from the continuity, momentum, and energy equations (Anderson 1998). Such expressions (which are presented in Appendix J) do not include heat transfer and viscous effects, and further the driver and driven gases are assumed to be calorically perfect.

A reflected normal shock forms after the incident normal shock wave hits the end wall. The reflected normal shock propagates to the left with absolute velocity of W_R, shown in Fig. 8.3.

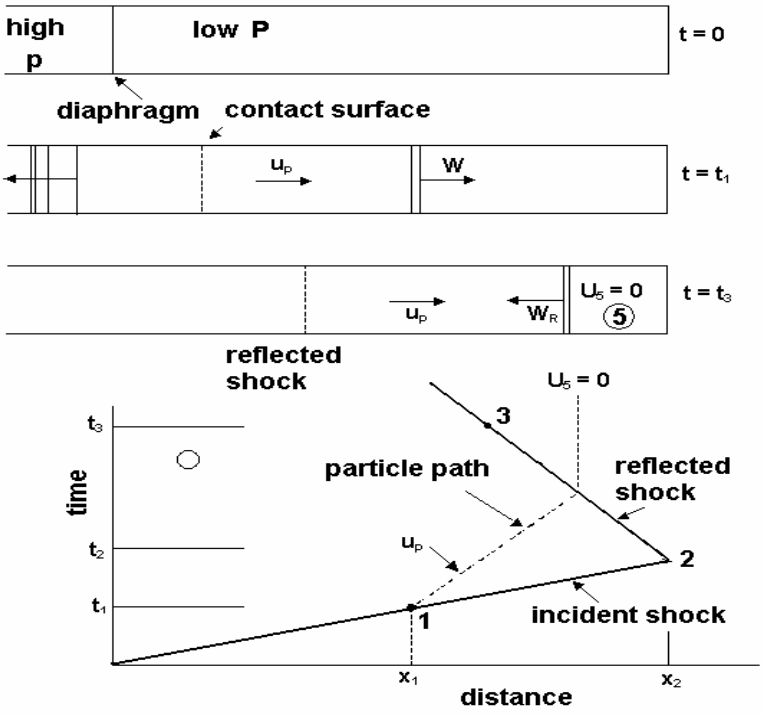

Figure 8.3 Conditions in a shock tube after shock reflection and an x-t diagram illustrates the shock trajectory (after Anderson 1990).

Region 5 is the region between the reflected normal shock and the end wall. The gas velocity in region 5 is zero ($u_5=0$). Analytical expressions for the conditions in region 5 are also available (again, see Appendix J), but as with the analytical expressions for regions 2 and 3, heat transfer, viscosity and caloric imperfections are

neglected.

Wave motion on an *x-t* (displacement-time) diagram is illustrated in Fig. 8.3. At time $t=0$, the diaphragm which is located at $x=0$ ruptures. The shock wave travels to the right, and is located at point $x=x_1$ after t_1 seconds. When the incident shock hits the end wall at $x=x_2$, it reflects toward the left with velocity W_R. At $t=t_3$, the reflected shock is at location $x=x_3$. Due to different velocities of incident and reflected shocks, their path slopes are different and equal to $1/W$ and $1/W_R$ respectively.

Particle motion can also be sketched on the *x-t* diagram. For example, a particle initially located at $x = x_1$ does not move until time t_1 because the incident shock has not yet reached the particle. The particle moves towards the end wall with velocity of u_p until the reflected shock brings it to rest. The complete dashed curve represents a particle path in the *x-t* diagram (Fig. 8.3).

As the temperature in regions 2 and 3 will differ from the tube wall temperature and there is a flow of a real (viscous) fluid in these regions, heat transfer and friction will induce some errors in the values calculated with the analytical expressions (Appendix J). Thus *x-t* diagrams like Fig. 8.3 are not precisely accurate. For example, the particle motions will not follow straight lines. To incorporate heat transfer and boundary layer friction in the shock tube simulations, a quasi one dimensional computational fluid dynamics program has been used as is discussed in Section 8.7.

8.3 Actual shock tube arrangement

Short and long shock tube arrangements were used. The short shock tube and the pneumatic filling system arrangement were presented in Fig. 6.3. The long shock tube arrangement is basically the short shock tube extended by 2.4 m. The long shock tube dimensions are presented in Fig. 8.4 and it uses the same pneumatic

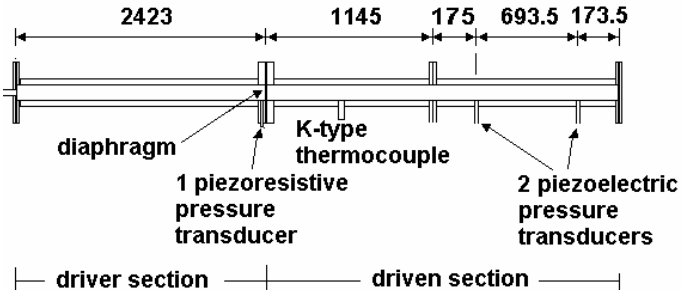

Figure 8.4 Long shock tube configuration.

filling system used with the short shock tube (Fig. 6.10).

A central compressed air system was used to fill the driver (and shock tube in the case of calibration) to a maximum pressure of 600 kPa gauge. The flow rate can be controlled by a valve on the filling line however, for a better control of the flow rate, a 100 litre tank was placed in series with the driver, as is described in Section 6.4. A vent valve was installed close to the filling point on the driver tube in order to exhaust compressed air from the shock tube after each experiment. During quasi-static calibration of the fibre optic sensors, the diaphragm was not placed between the driver and driven section. The piezoresitive pressure transducer was positioned in the middle of the shock tube to record the air pressure during calibration and the results were logged with an A/D board (National Instruments AT-MIO 16E-10).

Two piezoelectric pressure transducers shown in Fig. 8.4 were used to identify the incident shock speed during the shock experiments. The air temperature during the driver filling process (in the case of short shock tube arrangement) or quasi-static calibration (in the case of both arrangements) was identified using a K-type thermocouple.

The fibre optic pressure sensor was installed in the middle of the end plate (see Fig. 6.10) and was connected to the optical interrogation system, as shown in Fig. 6.10. The signal detector output was connected to either the oscilloscope (for shock experiments) or the A/D board (for the quasi-static calibrations).

8.4 Quasi-static calibration

Attempts were made to have the same conditions during quasi-static calibration and shock experiments. The fibre was taped to the bench to prevent any movement. The laboratory was equipped with ducted air conditioning however, because of high temperature sensitivity of the fibre optic sensor, the time between pre-calibration and shock experiments was kept to a minimum. Furthermore, calibration time was restricted to less than 10 minutes to minimise changes in the environment temperature during the calibration. The thermocouple that was mounted within the shock tube was connected to the A/D card or digital thermocouple reader, to indicate any temperature change. The maximum change in temperature within the shock tube during quasi-static calibration was limited to less than 1^{o}C. Also, care was taken to

prevent any physical change in the fibre optic sensor arrangement during the placement of the diaphragm into the shock tube.

Post-shock calibrations were also carried out after each shock experiment. Most sensors typically change very little (up to 10%) if at all in between their pre- and post-shock calibrations. A few sensors showed a considerable change between their pre- and post-shock calibrations, and some sensors did not survive the process of shock experimentation. However, the performance of all the sensors during about the first 105 ms following shock reflection was acceptable, which indicates that when sensor damage occurred, it most likely occurred after the initial shock reflection process.

8.5 Optical system

The fibre optic pressure sensors were calibrated before every shock tube experiment. Environmental parameters such as pressure and temperature affect not only the sensor, as discussed in Chapter 6, but also the optical system. The length and curvature of the optical fibre and the quality of the connection in the splicer can all affect the signal intensity.

The optical system used in the quasi-static calibrations and shock tube experiments is shown in Fig. 8.5. Attempts were made to increase the signal-to-noise ratio. All end faces of the optical fibre, apart from the fibre connected to the sensor, have an 8-degree angle to minimize the return of back reflections to the optical system. To increase optical power, a single wavelength interrogation system (see Section 3.8.1)

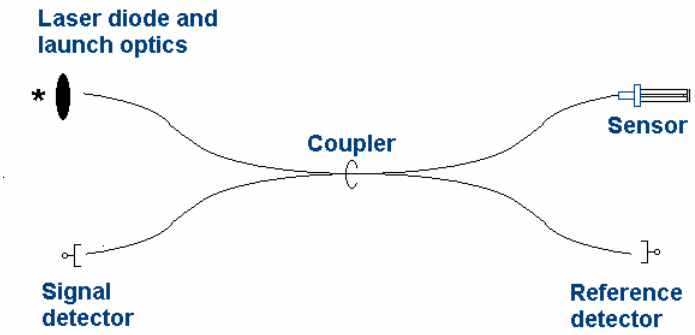

Figure 8.5 One wavelength interrogation system and sensor used in shock tube experiments.

was used and the optical isolation in the launching system was removed. These conditions allow the use of lower gain in the signal detector and thus reduced the detector response time as discussed in Appendix H.

Two laser diodes were used as the light source at different times throughout the shock tube experiments. Their powers were 20 and 30 mW and their wavelengths were 789 and 790 nm respectively. Details of these lasers are presented in Table K.1. Details of the reference detector (photodiode with in-house amplifier) and the signal detector (Thorlabs PDA55) are presented in Appendix K. The reference detector and signal detector gain were optimised depending on the input optical power, which may vary from sensor to sensor.

8.6 Piezoelectric pressure transducer

A commercial piezoelectric pressure transducer was used as a reference to assess the performance of the fibre optic pressure sensors. The transducer was a PCB model 112A22, and it was flush-mounted in the end wall of the shock tube.

As discussed in Section 2.3.5, such pressure transducers can only measure dynamic pressure as they have a finite discharge time constant, DTC (usually defined as the time taken for the step response signal to decay to 37% of its initial value). The DTC for this transducer is greater than 1 second according to the manufacturer, but it can change depending on the coupling circuit. The transducer was covered with a 0.4 mm thick layer of RTV to isolate it from temperature effects, and this layer is expected to alter the transducer dynamics slightly. The DTC was measured for the sensor covered by RTV and it was in fact greater than 8 seconds (as shown in Appendix L). The manufacturer quotes the rise time for this transducer as less than 2 μs (in its uncoated state).

The transducer output was recorded with the Tektronix TDS420A oscilloscope generally at a scan rate of 250 kSample/s during the shock experiments. The recorded voltage was converted to a text file, and based on the transducer sensitivity, the recorded voltage was converted to a pressure.

To identify the appropriate sensitivity for the piezoelectric transducer, in-situ shock wave calibrations were performed. The measured shock tube initial conditions and the shock speed measured from the transit time between the two piezoelectric

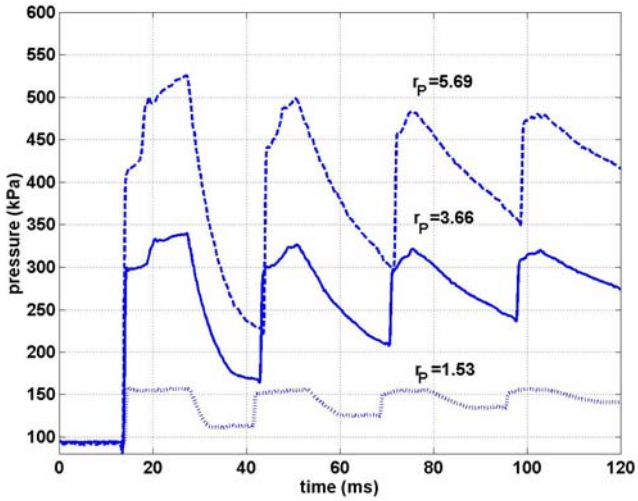

Figure 8.6 Pressure measurements from the piezoelectric transducer for 3 different shock tube diaphragm pressure ratios.

transducers on the side of the shock tube (see Fig. 8.4) were combined with the analytical shock relations (Appendix J) to calculate the reflected shock pressure. These values of pressure and the measured transducer output voltage indicated a sensitivity of 8.2 mV/kPa.

The results from the piezoelectric pressure transducer in the long shock tube arrangement are presented in Fig. 8.6 for different shock tube diaphragm pressure ratios, r_p. In this figure, the reference time scale is arbitrary – the results have been offset to align the shock arrival times at each pressure ratio.

8.7 Simulation of shock tube performance

The piezoelectric pressure transducer mounted in the end plate is not able to provide all the information, such as the shock-compressed air temperature, which is necessary to analyse the fibre optic pressure sensor performance. Furthermore, due to spatial limitations, the piezoelectric sensor could not be mounted in the same plate as the fibre optic sensor being tested. The initial filling conditions and shock tube diaphragm rupture pressures could not be controlled precisely, and therefore, slightly different reflected shock conditions were obtained for the piezoelectric and fibre optic pressure sensors.

The approach adopted in this work is to treat the piezoelectric measurements as the benchmark and demonstrate that reasonable numerical simulations of these pressure

histories are possible. After this validation work is completed, the numerical simulations can then be used to assess the performance of the fibre optic transducers.

8.7.1 CFD program and modelling

The simulations were performed using the CFD program was written by Jacobs (1994a). This program, which is known as L1d, is a quasi one dimensional gas dynamic routine in which the facility is modelled as a linear array of circular pipes (of variable cross sectional area) that are aligned with the x-axis. The program can model heat transfer, wall shear stress and high temperature gas effects. There are however some limitations in the modelling. For example, all area variations must be gradual. Buttsworth, Jacobs & Jones (2002) found that for accurate simulation of flow discharge through a contraction, cross sectional area changes across each cell should be less than about 10%. This is in contrast to the sudden area transitions that are often found in real facilities. Furthermore, the simulation does not model the turbulent mixing at the contact surface, and the boundary layer momentum and energy loses are modelled using a fully developed pipe flow model. Hence the post shock boundary layer modelling may be somewhat inaccurate (Jacobs 1994a), and this in turn may lead to inaccuracies in the predicted reflected shock conditions.

Different modelling options were considered in order to identify simulations with highest fidelity. In the first simulation, only the driver and driven sections, with the dimensions given in Fig. 8.4 were considered – the compressed air filling tube and reservoir connected to the driver were ignored. The air was assumed to be calorically perfect and this is a good approximation for the present shock strengths as the maximum temperature of the compressed gas did not exceed 427 K. The effects of viscosity (momentum loss through shear stress at the wall) were included in the simulations.

The simulations require the specification of initial conditions of the gas (e.g., temperature, pressure, and velocity) in the driver and driven section of the tube immediately prior to diaphragm rupture. The initial conditions for the driven section were the laboratory temperature and the local atmospheric pressure which was generally around 94 kPa (at the University of Southern Queensland in Toowoomba, the location of the laboratory). The initial conditions for the driver section were

identified from the air temperature and pressure measurements made immediately before diaphragm rupture.

The initial velocity throughout both the driver and driven sections was taken as zero. This is likely to be a good assumption for the driven section as there was not flow into or out of this section prior to diaphragm rupture. Although there was some flow into the driver section at the time of diaphragm rupture, the maximum velocity in the driver section at the time of diaphragm rupture is estimated as only 0.27 m/s. As this maximum velocity occurred at the junction of the air filling tube and the driver tube, and it is a low speed relative typical contact surface speeds developed in the present experiments (about 200 m/s for r_P=3.66), the zero velocity approximation should not affect the simulation of the incident shock.

8.7.2 Initial validation of simulations

The experimental results from the piezoelectric pressure transducer, and the adiabatic and non adiabatic flow simulations are presented in Fig. 8.7. The wall temperature was assumed to be constant and equal to the room temperature for the non adiabatic flow simulation. The time scale for the simulated results in Fig. 8.7 is relative to the time of diaphragm rupture (the start of the simulation). In Fig. 8.7 and all subsequent figures where experimental data is compared with the computational simulations, the time scale for the experimental data has been offset so that the time of shock arrival

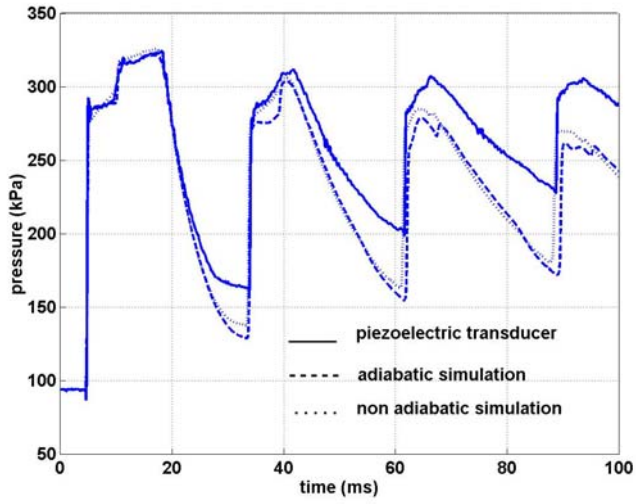

Figure 8.7 Comparison between the results provided from piezoelectric transducer and adiabatic and non-adiabatic viscous simulations ignoring the air filling tube (r_P=3.66).

at the end plate matches the simulated shock arrival time.

Referring to Fig. 8.7, the adiabatic simulation is in good agreement with the piezoelectric pressure transducer for the first 18 ms following shock reflection at this pressure ratio. In the non adiabatic simulation, the pressure immediately behind the reflected shock is too low, but the gradual pressure rise behind the reflected shock (between about 5 and 10 ms on the scale in Fig. 8.7) is too large relative to the piezoelectric pressure measurements. The remainder of the simulations were performed using the adiabatic option in L1d.

The difference between the adiabatic simulation and piezoelectric sensor becomes considerable as the full strength of the reflected expansion waves arrive at the sensor. This corresponds to the time at which the effects of the driver filling arrangement would appear. The presence of the driver filling arrangement (not modelled in this simulation) is expected to cause weaker expansion waves, because compressed air still enters the driver after diaphragm rupture, and a fraction of the expansion waves pass into the driver filling arrangement and do not reflect. The arrival of the expansion waves at the upstream end of the driver section augments the flow of air from the filling tube into the driver tube.

One main factor that should be considered in all CFD programs is the number of segments and their lengths. It is important to select sufficient segments that converge the results. Appendix M shows the simulation in three different segment lengths. Considering the results, the minimum segment length is about 40 mm for driven region and 10 mm for 0.5 m length behind the bursting diaphragm. In this case, the value of mean pressure is converged but the duration of pressure rise after the first reflected shock is about 0.5 ms and can be reduced by selecting more segments. If the number of segments increases by about 4 times (see Table M.1), the duration of pressure rise decreases to about 0.1 ms. A further decrease is also possible but it increases the time which is required for the computer to complete its calculation.

8.7.3 Model optimisation – addition of filling tube

Exact modelling of the driver filling arrangement was not possible due to the sharp changes of diameter, however a 6 m length of tube was included in an attempt to improve the simulation. The actual length of the tube between the driver and the

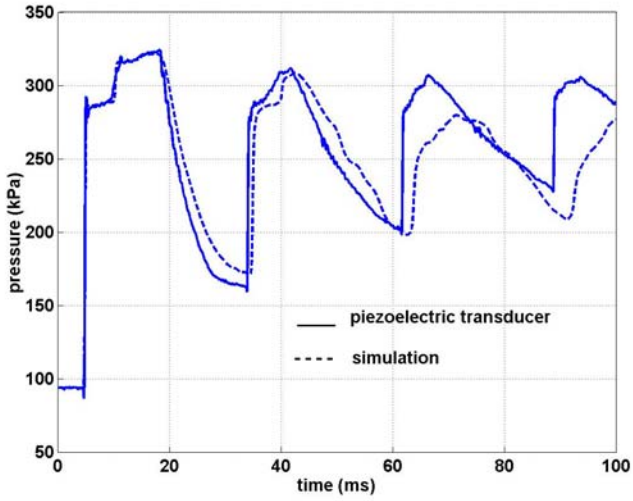

Figure 8.8 Comparison between the results from piezoelectric transducer and adiabatic viscous flow simulation considering 6 m filling tube and change of diameter to the driver section over 0.2 m (r_P=3.66).

reservoir was only 1 m (see Fig. 6.9) but the additional length was included in this simulation in an attempt to simulate the effects of the reservoir. The change of diameter between the driver and the filling tube was assumed to occur over 0.2 m. The initial velocity of air in the filling tube was taken as zero as was the case for the air in the driver section at the time of diaphragm rupture. The initial pressure and temperature of the air in the filling tube was assumed to be the same as those values for the air already in the driver section.

The results from the piezoelectric sensor and the adiabatic, viscous flow simulation (including the 6 m filling tube) are presented in Fig. 8.8. Reflected shock conditions are the same as in the first simulation, and the addition of the air filling tube has decreased the magnitude of the pressure drop associated with the expansion waves. However, the presence of the 6 m filling tube and the 0.2 m transition zone between the filling tube and the driver section caused a delay in the arrival of the shock at about 35 ms on the scale in Fig. 8.8.

To overcome the delay in arrival of the second shock, the transition between the driver and the filling tube was shortened to 0.01 m. The results from this simulation are presented in Fig. 8.9. All of the other initial conditions and parameters remained the same as in the previous simulation. The figure also includes the simulation for a 5 m air filling tube.

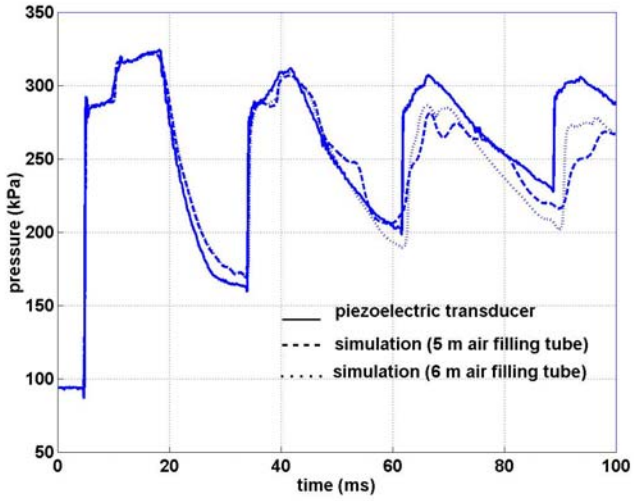

Figure 8.9 Comparison between the results from piezoelectric transducer and adiabatic, viscous flow simulations considering 5 m and 6 m filling tubes and change of diameter to the driver section over 0.01 m (r_P=3.66).

Referring to Fig. 8.9, it is apparent that the reduced transition length improves the fidelity of the simulation up to approximately 40 ms on the scale in Fig. 8.9. It is concluded that the reflected shock pressure can be simulated for about 35 ms following shock arrival at this pressure ratio.

To provide an independent test of the performance of the current modelling, simulations of the two other diaphragm pressure ratios (for which data was obtained

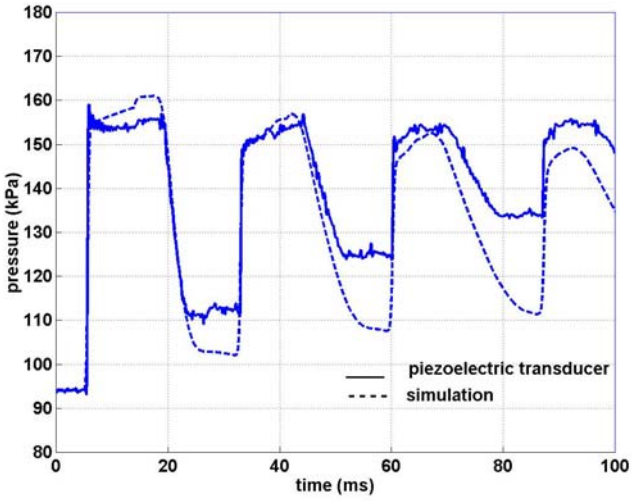

Figure 8.10 Comparison of piezoelectric pressure transducer response with simulated reflected shock pressures for diaphragm pressure ratio, r_P=1.75. (Adiabatic, viscous flow simulation with 5 m air filling tube and change of diameter over 0.01 m).

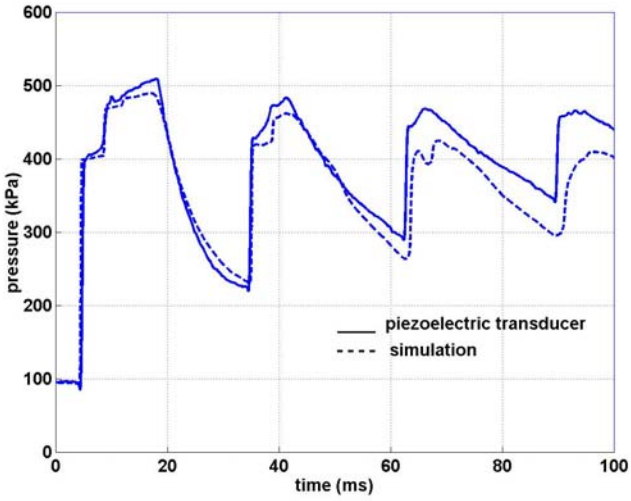

Figure 8.11 Comparison of piezoelectric pressure transducer response with simulated reflected shock pressures for diaphragm pressure ratio, r_P=5.69. (Adiabatic, viscous flow simulation with 5 m air filling tube and change of diameter over 0.01 m).

with the piezoelectric transducer) were also performed using an adiabatic, viscous flow with an assumed 5 m air fill tube. For these simulations, the diameter change between the filling tube and driver section also occurred over a length of 0.01 m. Results are presented in Fig. 8.10 for r_P=1.75 and Fig. 8.11 for r_P=5.69.

A summary of the experimental and simulated results for the three different pressure ratios presented in Figs. 8.9 to 8.11 is presented in Table 8.1. Of the various parameters presented in Table 8.1, the simulated change associated with the first reflected shock (ΔP_1) is in closest agreement with the experimental values (the error is less than 1% for all three pressure ratios). This effectively indicates that the simulated reflected shock pressures are in close agreement with the analytical predictions because: 1) the pressure transducer was calibrated using analytical predictions of reflected shock pressure based on the measured shock speed; and 2) if the simulated shock speed was not in agreement with the experimental value (to within 5 %), a slight adjustment was made to the initial pressure in the driver section. The simulation for the pressure ratio r_P=3.66 is the most accurate, except in the magnitude of the pressure change associated with the second reflected shock (ΔP_2). The simulated rate of pressure rise immediately after the first reflected shock (dP_1/dt) is greater than that for piezoelectric transducer at the pressure ratio r_P=1.75, but the simulated rate of pressure rise is less than that indicated by piezoelectric transducer

at the other two pressure ratios. This indicates that the simulated effects of viscosity at the lowest pressure ratio are greater than the actual effects, but at the higher pressure ratios, the trend is reversed.

The magnitude of pressure drop through the reflected expansion wave (ΔP_{expn}) has the largest error (30%) at lowest pressure ratio (r_P=1.75) but the error is substantially reduced at the higher pressure ratios (7% and 9% for r_P=3.66 and 5.69 respectively). The pressure change associated with the second reflected shock has minimum error at the high diaphragm pressure ratios. The comparative trends for the rate of pressure rise immediately following the second reflected shock (dP_2/dt) are similar for those associated with dP_1/dt.

The slope of a line, which connects the pressure peaks across consecutive shock-expansion cycles, is denoted dP_{max}/dt. Experimental values for this parameter are negative, indicating the peak pressure decreases over time (e.g., compare the experimental peak values of pressure in Fig. 8.11 at approximately 18, 42, and 67 and 93 ms). The simulations overestimate this rate of pressure drop at all three pressure ratios, but is in closet agreement with the experimental results for pressure ratio of 3.66.

Table 8.1 Comparison of pressure results for the shock tube: measured values from the piezoelectric transducer and the simulated values from L1d.

Parameter	Shock tube diaphragm pressure ratio at rupture, r_p								
(symbols as defined	1.75			3.66			5.69		
in the text)	L1d	Exp.	Error	L1d	Exp.	Error	L1d	Exp.	Error
ΔP_1 (kPa)	61.1	60.8	<1%	192	191	<1%	306	305	<1%
dP_1/dt (kPa/ms)	0.43	0	-	0.6	1.8	-	1.6	4.3	-
ΔP_{expn} (kPa)	58	44	30%	149.5	161.5	7%	259	284	9%
ΔP_2 (kPa)	47.9	40	20%	100	120	17%	190	215	12%
dP_2/dt (kPa/ms)	1	0.5	-	4	4.3	-	6.7	8.8	-
dP_{max}/dt (kPa/s)	-4	0	-	-0.18	-0.08	-	-0.3	-0.01	-

8.8 Sensor Response

8.8.1 Overview of experiments

The shock response of the fibre optic sensors is presented and discussed in this section. The value of reflected shock pressure indicated by a sample fibre optic pressure sensor is the focus of Section 8.8.2, and Section 8.8.3 discusses potential sources of the errors in the indicated pressure. All experiments reported in this chapter were performed using fibre optic pressure sensors constructed from zirconia ferrules as the substrate and liquid adhesives (Araldite 5 minute and Araldite 24 hour) to bond the diaphragm (9 μm thick copper foil) as such constructions have shown superior repeatability (Chapter 6).

The results of the fibre optic experiments discussed here are often presented after filtering the data with a digital filter with a cut off frequency of 2.5 kHz. The high temperature sensitivity of the sensor makes it necessary to perform a quasi static calibration just before the shock experiment (the pre-shock calibration). A quasi static pressure calibration was also performed immediately after the shock experiment (the post-shock calibration) to assess the sensor for possible damage and repeatability. For the results presented in this section, the pre-shock calibration and post-shock calibration agreed to within 10%. Even when the results of pre- and post-shock calibrations did not agree, there was still good agreement with the simulations indicating that the shock reflection process affects the sensor after the recording time.

The same basic shock tube arrangement used in the piezoelectric sensor experiments (Section 8.6) was used for testing the fibre optic pressure sensors. Cellophane was used as the diaphragm material and depending on the required bursting pressure, two or three layers of cellophane were used to achieve higher bursting pressures, and a single sheet of cellophane was lightly sanded to achieve low bursting pressures. A thermocouple placed in the driven section of the shock tube was used to indicate any leakage between the two sections prior to the desired rupturing pressure.

8.8.2 Sample sensor response

This experiment was performed using a sensor without any thermal isolation layer. Although this sensor registered a 2 ms delay time in the heat gun test (described in

Appendix C, the expected delay time for conditions of the reflected shock experiment was 0.2 ms (see Appendix A). This delay time may arise because of oxidation, dust, oil or possibly the thin layer of glue.

The shock tube diaphragm pressure ratio was 1.53 (P_{atm}=94 kPa, P_{burst}= 144 kPa) and the experiment was performed using the long shock tube configuration (see Fig. 8.4). As it turns out, this diaphragm pressure ratio is identical to one for which piezoelectric pressure transducer data is available. Nevertheless, this was not normally the case (as will be seen in later sections) and the validation exercise of Section 8.7 is well justified.

The sensor used in this experiment showed around 20 kPa hysteresis when calibrated to a maximum pressure of 600 kPa. The signal detector was set on gain 4 and therefore had a response time of around 2.8 μs (see Appendix H). The oscilloscope sample rate was set to 250 kSample/s. Dry and wet bulb temperatures were 22^{o}C and 17^{o}C respectively.

The fibre optic pressure measurement and L1d simulation for this experiment are shown in Fig. 8.12. (The L1d simulation consisted of adiabatic, viscous flow, the 5 m filling tube and a diameter transition between filling tube and driver section distributed over 0.01 m – see Section 8.7.)

Pressure contours from the simulation of this experiment are presented in Fig. 8.13.

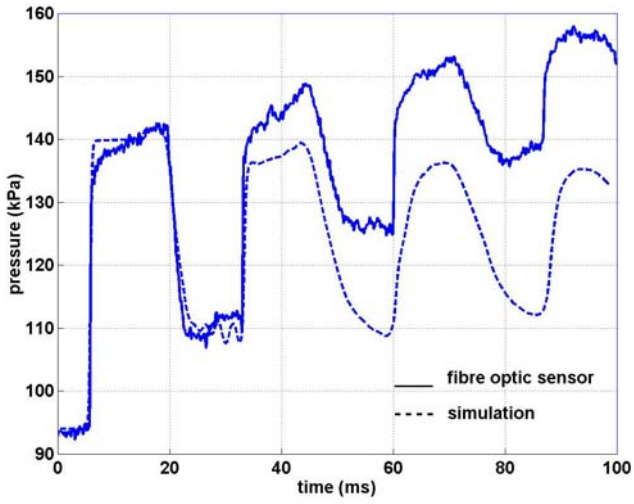

Figure 8.12 Sample fibre optic pressure sensor response in a shock experiment.

The movement of particles on the interface of the driver and the driven sections (*x=0* at *t=0*) are indicated with a dashed line in Fig. 8.13. The diaphragm ruptures at *t=0*, and after about 5.5 ms, the shock reaches the end plate where the sensor is located. After the shock reflects from the end plate and the sensor, the pressure increases sharply. The simulation indicates that the reflected shock pressure should be 140 kPa, where as the fibre optic sensor shows 134 kPa immediately after the reflected shock – an error of 13% – as detailed in Fig. 8.14a.

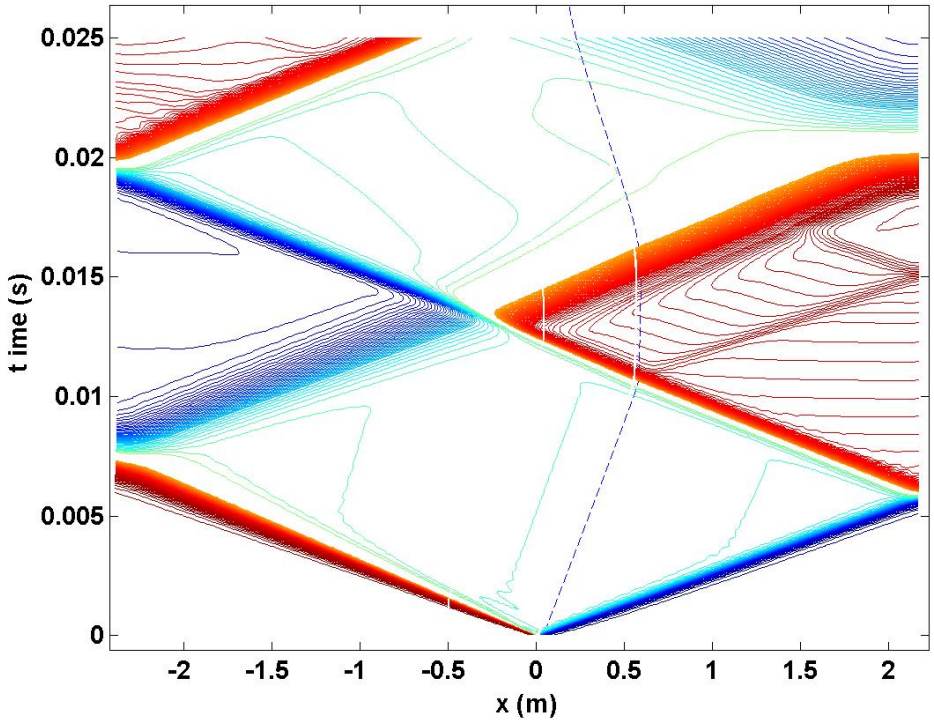

Figure 8.13 Pressure contours in the form of an x-t diagram from a simulation of the sample fibre optic pressure sensor experiment.

The adiabatic simulation does not show any change in pressure during the 9 ms following shock reflection (Fig. 8.12 and 8.14). However, a slight increase of pressure is expected due to the heat transferred from the post shock flow (in region 2, Fig. 8.2) to the tube walls. The rate of pressure increase indicated by the piezoelectric transducer at similar reflected shock conditions is 0.4 kPa/ms. The rate of pressure increase indicated by the fibre optic sensor is approximately 0.5 kPa/ms (see Fig. 8.14a for details) – about 20% higher than the rate indicated by the piezoelectric transducer.

At time t=14.7 ms on the scale in Fig. 8.12, the sensor and simulation show a sharp increase of pressure of about 2 kPa, and this effect is shown in greater detail in Fig. 8.14b. This additional compression is a consequence of the interaction between the reflected normal shock and the interface which moves towards the sensor, as shown in Fig. 8.13.

The expansion waves, which travel into the driver gas, are reflected from the upstream end of the shock tube. These expansion waves arrived at the sensor at t=18 ms (on the scale in Figs. 8.12 and 8.14). There is good agreement between the sensor and simulation (maximum difference of 2 kPa) after the expansion waves arrive at the sensor, Fig. 8.4c. The simulation of the air filling tube attached to the driver (see Section 8.7) produces the fluctuations that appear on the simulation at around t=26 ms (see Fig. 8.14c). The average value of pressure indicated by simulation does not change during the next 4 ms. The sensor shows an apparent 3 kPa increase of pressure during this time, which is possibly associated with the filling tube and reservoir gas dynamics.

A second normal shock (reflected from the upstream end of the shock tube) arrives at the sensor end wall at about t=32.8 ms (on the scale in Figs. 8.12 and 8.14d) and both the sensor and simulation show a sharp increase of pressure at this time. The sensor and simulation both indicates a change in pressure of 27 kPa associated with this shock (Fig. 8.14d).

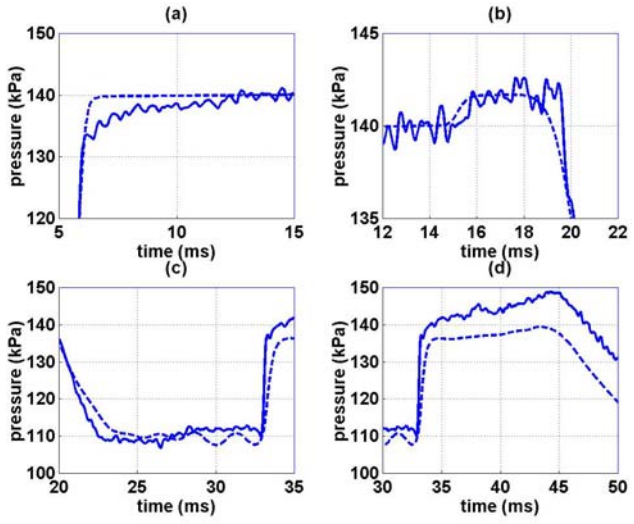

Figure 8.14 Detailed view of Fig. 8.12 at different stages in the reflected shock experiment.

The piezoelectric pressure transducer indicates that the maximum pressure reaches approximately the same value with consecutive shock reflections from the end wall (see Fig. 8.7 and note pressure values at 18, 42, 67, and 93 ms) whereas the simulated peak values decrease slightly with consecutive shocks. It is argued that this difference is caused by imperfect modelling of the filling tube and reservoir (Section 8.7), so the piezoelectric result is taken as correct. The peak pressure indicated by the fibre optic sensor actually increased by about 5 kPa with each consecutive shock-expansion cycle (Fig. 8.12), and this is clearly incorrect.

8.8.3 Error sources

Four kinds of errors are observed in the performance of the fibre optic sensors in shock tube experiments of the type illustrated in Section 8.8.2.

The indicated pressure immediately after the reflected shock is lower than the pressure measured by the piezoelectric transducer and the simulated value (by up to 30%).

The indicated pressure after the reflected shock increases at a rate much higher than that measured by the piezoelectric pressure transducer.

The peak indicated pressure increases at each consecutive shock-expansion cycle in contrast to the measurements from the piezoelectric transducer.

The indicated pressure drop with the arrival of the expansion waves is lower in magnitude than values measured by the piezoelectric transducer.

In this section, the potential sources of these errors are discussed and evaluated.

8.8.3.1 Calibration process

A change of air temperature inside the shock tube during quasi-static calibration is sufficient to cause errors No. 1 and No. 4. During quasi-static calibration, the air temperature increases slightly even during a slow calibration process, as discussed in Section 7.2.4. The magnitude of the error depends on the temperature sensitivity of the sensor and the value of the air temperature rise during calibration.

In contrast, during the shock tube experiments, the sensor is not affected by heat transfer from the shock compressed air inside the shock tube, prior to estimated delay time. This situation causes an error in the pressure indicated by sensor.

8.8.3.2 Air within cavity

The pressure of the confined air in the cavity increases during diaphragm deflection and has the potential to contribute errors No. 1 and No. 2, although it would tend to decrease error No. 4.

During a slow calibration process, there is enough time for heat transfer to occur and the process can be assumed to be isothermal. Due to the fast deflection of the diaphragm during shock loading, the process cannot be assumed to be isothermal. An isentropic process is likely to be a better approximation for the initial compression of the confined air in the cavity. For a given volumetric compression ratio, higher pressures results from an isentropic compression than from an isothermal compression. Higher pressures within the cavity for shock loading relative to quasi-static calibration tend to reduce the diaphragm deflection. This condition induces an error and the sensor will indicate lower pressure. However, some time after the initial shock loading, heat transfer from the confined air in the cavity decreases the pressure inside the cavity and the pressure indicated by the sensor will increase.

To evaluate this effect, the change of cavity volume will be $\Delta V = \pi a^2 y_0/3$ where a is the diaphragm radius and the diaphragm deflection in centre is y_0. (This is the exact solution obtained by integrating Eq. (5.4).) If the cavity length, initial pressure and final pressure within the cavity are h, P_1, and P_2 respectively, for an isothermal process,

$$P_2 = P_1 \frac{h}{h - y_0/3} \tag{8.10}$$

During an isentropic process, the value of $(PV)^k$ remains constant and the final pressure can be calculated as,

$$P_2 = P_1 \left(\frac{h}{h - y_0/3} \right)^k \tag{8.11}$$

where k can be assumed to be 1.4 for air in an isentropic process. The difference between these two pressures causes an error that is equal to,

$$\Delta P = P_1 \left[\left(\frac{h}{h - y_0/3} \right)^k - \left(\frac{h}{h - y_0/3} \right) \right] \tag{8.12}$$

The results from this equation for an initial pressure of 94 kPa and 3 different diaphragm deflections are shown in Fig. 8.15.

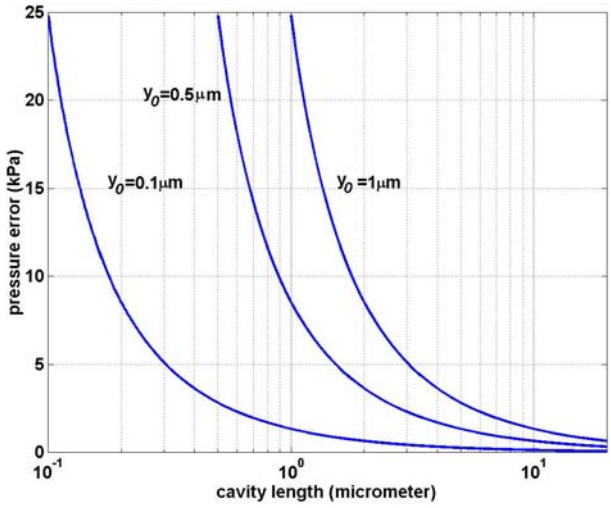

Figure 8.15 Pressure error due to compression of confined air in the cavity.

The sensor discussed in Section 8.8.2 had a cavity length of about 15 μm (measured with the method discussed in Chapter 6) and its centre deflection during the shock loading was about 0.1 μm (estimated from the results of the pre-shock calibration), so the magnitude of the pressure error is about 0.1 kPa (from Fig. 8.15) which is negligible for the present operating conditions.

The change of temperature of the confined air within the cavity has the potential to contribute to all four errors. The refractive index of air depends on the temperature (dn/dT=3×10^{-7} /^{o}C, MacPherson 1999). The change of refractive index alters the optical path length (Eq. 3.4), and therefore, the change of temperature of the confined air can contribute to error No. 1 and No. 4. Heat transfer from the confined air to the diaphragm can also contribute to errors No. 2 and No. 3.

The change of temperature of the confined air within the cavity can be calculated using a method similar to the pressure rise calculation. The rise of temperature can be calculated as,

$$\Delta T = T_1\left[\left(\frac{h}{h-y_0/3}\right)^{k-1}-1\right] \tag{8.13}$$

where T_1 represents initial absolute temperature of air within the cavity. Figure 8.16 shows the air temperature change as a function of cavity length for 3 different

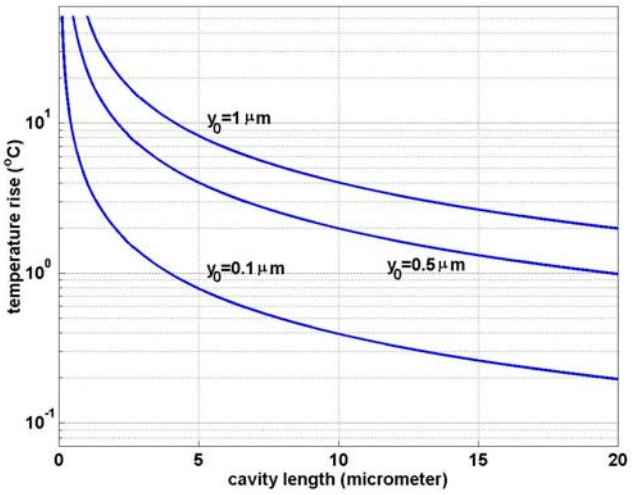

Figure 8.16 Temperature rise of confined air within the cavity due to compression.

diaphragm deflections.

Figure 8.16 indicates that for a short cavity sensor (0.1 μm), the rise of temperature is high (more than 50^{o}C) if the centre diaphragm deflection is 0.1 μm. However, for a 15 μm cavity length sensor as discussed in Section 8.8.2, the rise of temperature is about 0.3^{o}C for the 0.1 μm shock induced deflection. This rise of temperature is not sufficient to have an impact through a refractive index change and hence does not contribute to errors No. 1 and No. 4. However, the rise in air cavity temperature can contribute to errors No. 2 and No. 3 through thermal expansion of the diaphragm with heat transfer from the compressed air in the cavity.

To evaluate possible contribution of air cavity temperature rise to error No. 2, the sensor in Section 8.8.2 is again considered. The sensor in Section 8.8.2 had temperature sensitivity of about $2\pi/6$ rad/^{o}C and a pressure sensitivity of about $2\pi/360$ rad/kPa. Assuming the convective heat transfer in the cavity leads to a coefficient of about 12.7 J/kg^{o}C (see Appendix A), the maximum apparent rate of pressure change indicated by the sensor (treating the diaphragm as a lumped thermal mass), is 0.02 kPa/ms. The apparent rate of pressure change due to this effect will decrease with time due to the rise of diaphragm temperature and drop of confined air temperature. Assuming: 1) all the thermal energy from the compression is transferred to the diaphragm (although it would never happen because a significant fraction of this heat will transfer to the zirconia substrate); 2) only the diaphragm

adjacent to the cavity absorbs and retains this heat (although it will never happen because some will be conducted to the outer parts of diaphragm); and 3) no heat is convected to or from the external surface of the diaphragm, the maximum increase of apparent pressure can be only 0.02 kPa.

Clearly for the sensor discussed in Section 8.8.2, the thermal effect from the confined air in the cavity is also negligible. However, both pressure and temperature effects associated with the confined air can play an important role if the cavity length is comparable to the diaphragm deflection. For example, if a sensor has the same temperature and pressure sensitivity as the sensor discussed in Section 8.8.2, but the sensor has a cavity length of 1 μm and a diaphragm deflection of 0.5 μm, the pressure error after shock reflection (contributes to error No. 1) increases by 8.5 kPa and the apparent rate of pressure rise (contributing to error No. 2) increases to about 2.2 kPa/ms. In this case, the temperature rise in cavity will be 50^{o}C.

Short cavity sensors show good performance during quasi-static calibration. Their visibility is higher (visibility up to 95%) and their noise is lower than long cavity sensors. For example, it was found that for a sensor with a cavity length of 1 μm, the noise was less than 50% of the noise associated with a sensor with a cavity length of 10 μm. However, due to a larger pressure and temperature rise of the confined air during shock loading, large errors were observed during shock tube experiments. Evacuating the air from the cavity can diminish these effects.

8.8.3.3 Substrate expansion

Expansion of the substrate can stretch the diaphragm and increases the cavity length. This effect has the potential to increase error No. 1 and decrease errors No. 2, No. 3 and No. 4. However, its actual contribution will be very small because the substrate in the vicinity of the cavity is isolated from thermal effects during the first few milliseconds following shock reflection by the presence of the copper diaphragm. A thermoelastic simulation was performed using ANSYS (a finite element program) with a 1 mm diameter copper diaphragm on a zirconia substrate. The simulation indicated that during the first millisecond, there was less than 0.3 nm change of cavity length.

8.8.3.4 Friction effects

During the shock experiments, deflection of the diaphragm creates shear forces and motion between the diaphragm and glue, the substrate and air. Such friction effects may contribute to errors No. 1, No. 3 and No. 4.

Shear sensitivity due to gas movement across the diaphragm face is not thought to have a large influence because the sensors were mounted in the centre of the shock tube end plate and the construction is nominally axisymmetric. Furthermore, the flow velocity at the end plate is zero in the one dimensional model, and in reality is likely to be negligible in the present context.

During quasi-static calibration, changes of pressure occur at a maximum rate of around 10 kPa/s. Ideally the reflected shock loading occurs in an infinitesimal time, and even if it is assumed that the loading is distributed over one microsecond, the loading rate would be 50 GPa/s, which is five million times faster than during the quasi-static calibration. The friction between materials is related to loading speed. At low speed, friction effects are relatively small but increase rapidly at high speed where frictional forces can be proportional to speed squared due to the Stribeck effect (Dunpont et al. (2002); Richard (2000); Berg (2002)).

8.8.3.5 Temperature distribution on diaphragm

The temperature sensitivity of the sensor was calculated in Section 6.4.3. In that calculation, a uniform temperature distribution was assumed throughout the diaphragm. However, this is not the case during the shock experiments particularly when there is no thermal isolation layer on the diaphragm. The temperature on the side of the diaphragm that is in contact with the shock tube air increases due to the shock compression (see Appendix A). A finite time is required for the thermal wave to reach the other side of the diaphragm. This temperature gradient through the thickness of the diaphragm reduces the pressure induced deflection of the diaphragm until the temperature becomes uniform within the diaphragm. This phenomenon has the potential to contribute errors No. 1, No. 2 but would tend to reduce error No. 4.

For a copper diaphragm with a thickness of 9 μm exposed to a reflected shock pressure of 140 kPa, the sudden increase of diaphragm surface temperature is calculated to be 0.03^{o}C (see Appendix A). Using the ANSYS finite element program,

it is calculated that less than 1 μs is required for the temperature difference across the diaphragm to be less than 0.01^{o}C. Thus, this temperature gradient effect cannot make a contribution to the observed errors.

However, if a thicker diaphragm is used, the thermal penetration time will. For example, for a copper diaphragm with a thickness of about 55 μm, the thermal penetration time increases to about 16 μs. Such a thermal gradient effect could be eliminated by using a thermal isolation layer on the diaphragm. In this case, the thermal isolation layer should not contribute to the stiffness of the diaphragm. Low viscosity grease can be used as the thermal isolation layer (see Section 8.9.2).

8.8.3.6 Heat transfer from air in tube to diaphragm

The temperature rise within the shock compressed air, which is dependent on shock tube diaphragm pressure ratio, can be about hundreds of centigrade and will affect the diaphragm performance. Heat transfer to the diaphragm increases its temperature and causes it to expand. The sensor will therefore indicate an apparent rise of pressure which is actually a heat transfer effect. However, for sensors which have a thermal delay time longer than the duration of the reflected shock process (which is less than 1 μs), this heat transfer effect should not contribute to error No. 1.

For the sample sensor discussed in Section 8.8.2, the thermal delay time was around 0.3 ms, heat transfer is not expected to affect the sensor before this time. In any case, heat transfer will tend to increase the apparent pressure not reduce it, as is the case with error No. 1. Furthermore, as shown in Section 8.9 and Appendix A, the heat transfer effect is gradual and it is not likely to have a significant contribution to the rise of pressure indicated by the sensor immediately after shock reflection. The heat transfer may contribute to errors No. 2, No. 3 but is likely to reduce error No. 4.

8.8.3.7 Viscoelastic effects

An elastic material follows Hooke's law and immediately responds to an applied load and reaches its final strain (neglecting strain wave effects). In contrast, a viscous fluid continues to deform until the load is removed. In reality, no material follows Hook's law or Newton's viscosity law perfectly. Viscoelastic materials are materials that when they are subjected to a load, behave somewhere between the ideals of elastic and viscous materials. Viscoelastic materials show an immediate strain but

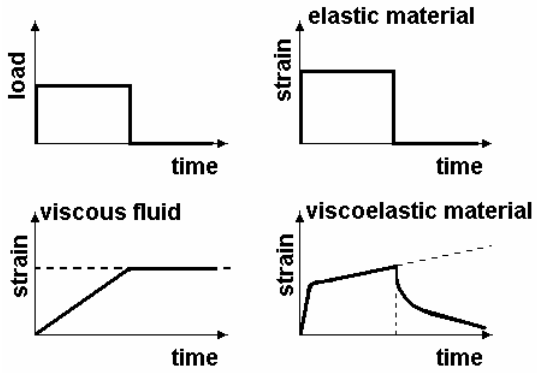

Figure 8.17 Comparison of strain response for elastic, viscous and viscoelastic materials under a constant load for a limited time (after Haddad 1995).

deformation continues until unloading occurs. Figure 8.17 shows the performance of different model materials exposed to a sudden constant load for a limited time.

Materials such as polymers, polymeric base composites, inorganic polymeric materials (i.e. silicon and glass resins), synthetic rubber like materials, commercial plastics, and natural or synthetic textile fibres (i.e. wood, paper, and board) can all show strong viscoelastic phenomenon (Haddad 1995). Some special behaviours of viscoelastic materials include: 1) increase of strain during constant stress (i.e. creep); 2) decrease of stress during constant strain (relaxation); 3) variable stiffness due to stress rate; and 4) hysteresis during cyclic loads (Lakes 1998).

As previously explained, a small percentage of hysteresis remains in the fibre optic sensor even after applying load cycling (Section 7.4). As the magnitude of the pressure induces a maximum stress that is far below the elastic limit of the diaphragm, it can be concluded that viscoelasticity plays a role in the sensor performance.

All materials including metals (especially at high temperature) and human bones (Lakes 1998) show some degree of viscoelasticity. However, the adhesives used to bond diaphragm to the substrate are likely to be the main source of this effect in the sensor. Richardson and Crook (1998) report that even for an exotic adhesive used in the space shuttle's reusable solid rocket motor nozzle and other rocket motor nozzles, some degree of viscoelasticity is apparent.

The contribution of viscoelasticity to the errors observed during shock loading could not be quantified in this work due to the unavailability of necessary adhesive

specifications. However, it was observed that for sensors made with a thicker layer of adhesive, not only did the level of hysteresis increase (as discussed in Chapter 7), but the percentage of error No. 1 also increased. It is believed that the one main source of all errors (especially No. 1 and No. 2) is related to the viscoelasticity of the adhesive. Incomplete mixing of the two parts of the epoxy can sharply increase the viscoelastic effect, as was observed in some sensors.

The concepts of hysteresis and viscoelasticity should be distinguished. If a material that has no viscoelasticity is subjected to an increasing and then decreasing load, it may still shows a hysteresis effect. In this case, the path (on a stress-strain diagram) will be different, but the start and end points are ideally the same. The difference between the two paths (the increasing and decreasing load paths) is only related to the magnitude of load and is not related to the loading speed (ideally). For example, if an increasing load is applied and reaches a maximum value, the strain at the maximum load point remains constant. For consecutive identical load cycles, the path in the strain-stress diagram is the same and is not related to the interval between two loads. Therefore, the non-repeatability of a sensor is not directly related to hysteresis.

On the other hand, for a viscoelastic material, the width of the hysteresis loop is a function of load speed and the interval between application of the increasing and decreasing loads. Ideally, no hysteresis will be seen if two sudden loads equal in magnitude but opposite in direction are applied with a time interval between them approaching zero. Furthermore, due to permanent deformation, the start and end point on the stress-strain diagram will not be the same – the difference between the start and end points is related to load speed and the interval between the loading and

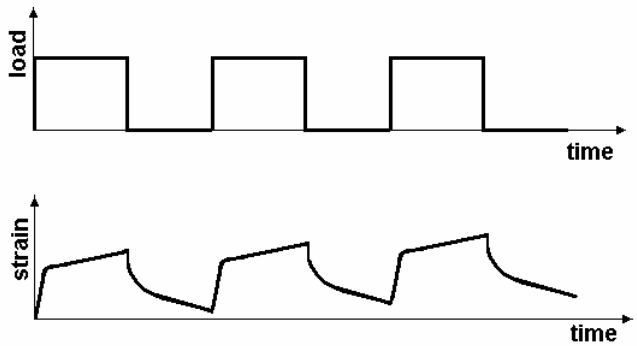

Figure 8.18 Model response of a viscoelastic material to a cyclic load.

unloading phases. The process becomes totally non-repeatable due to viscoelasticity effects.

Figure 8.18 shows the expected response of a viscoelastic material under cyclic load, based on the idealised viscoelastic material model of Fig. 8.17. The loading picture in Fig. 8.18 is somewhat similar to the pressure loading that is applied to the fibre optic pressure sensors in the shock experiments. The strain picture is somewhat similar to the apparent pressure response of the fibre optic pressure sensors.

8.8.3.8 Hysteresis

Hysteresis was discussed in Chapter 7. The hysteresis was minimized by load cycling prior to the sensor calibration, however the remaining hysteresis has the potential to account for errors No. 3 and No. 4.

The adhesive is the main source of hysteresis as discussed in Section 8.8.3.7, however, the diaphragm material hysteresis was not completely eliminated (Chapter 7) and it can affect the sensor response. Due to hysteresis, the magnitude of pressure drop following the expansion wave is less than the actual value and this error adds to the other errors and increases the apparent pressure during the following shocks.

8.9 Isolation layer thermal performance

In Section 8.8.3, potential sources of error in the sensor response during the shock experiments were discussed. Some errors were related to heat transfer from the air inside the shock tube to the sensor (diaphragm and substrate). Heat transfer can be prevented from affecting the diaphragm for a limited time using a thermal isolation layer. In this section, effects of two isolation layers on the sensor thermal response are discussed.

8.9.1 Aerosolve as thermal isolation layer

In an attempt to reduce the effects of heat transfer, a thin layer of Aerosolve Clear Cote 540 was applied to a sensor constructed using a copper diaphragm (9 μm thick) bonded to a zirconia ferrule substrate with a liquid adhesive (Araldite 5 min.). Clear Cote 540 is a plastic-like material that is applied as a spray and is used as a protective coating for printed circuit boards and other electronics. According to the manufacturer, Clear Cote 540 has good electrical insulation properties, excellent

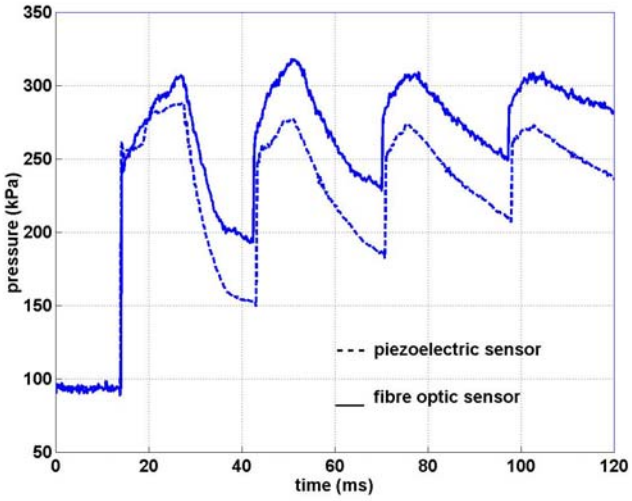

Figure 8.19 Comparison of piezoelectric pressure transducer and fibre optic pressure sensor coated with Aerosolve Clear Cote 540.

adhesion and it also provides a tough protective layer. The delay time for this coated sensor was 3.5 ms measured with the heat gun test described in Appendix C. The expected delay time for this coated sensor with the reflected shock conditions was 0.3 ms (see Appendix A).

The thin layer Clear Cote 540 had a slight effect on sensor pressure sensitivity: it was reduced from $2\pi/500$ rad/kPa (uncoated) to $2\pi/520$ rad/kPa (coated), a difference of about 4%. Although the contribution of this layer to diaphragm deflection was relatively small, it had a substantial effect on the sensor hysteresis, increasing it from 15 kPa to 35 kPa (when calibrated over a 600 kPa range).

The conditions of the reflected shock experiment performed with this sensor were close to one of the experiments performed with the piezoelectric pressure transducer. The difference in ambient temperature was 0.7^{o}C (higher temperature for the fibre optic sensor experiment), and the difference in diaphragm bursting pressure was about 10 kPa (higher for fibre optic sensor experiment). As this pressure difference resulted in a change of diaphragm bursting pressure ratio of only 3%, in this case it is possible to take the results from the piezoelectric sensor as the reference (instead of using the CFD simulation as the reference). The results from the two sensors are shown in Fig. 8.19.

The results show reasonable agreement immediately following the initial reflected

shocks, although the fibre optic sensor indicates a pressure that is low by 8 kPa. Considering 10 kPa higher bursting pressure in the fibre optic sensor equipment, this 8 kPa translates to about 12%, and this is consistent with the results discussed in Section 8.8.2. Clearly the error in pressure shown by the fibre optic sensor immediately after shock reflection is not related to heat transfer (from the air inside the shock tube to the diaphragm) because the expected delay time in this case was about 0.3 ms.

The slope of the pressure rise after the reflected shock for the fibre optic sensor is about 4 kPa/ms compared with 1 kPa/ms for the piezoelectric transducer. This slope does not change greatly after expected delay time, and this indicates that the effect of heat transfer is gradual (as discussed in Appendix A). As previously discussed, the main source of error appears to be a viscoelasticity effect in the adhesive. An increase in the hysteresis for the sensor due to Clear cote 540 layer may be attributed to a higher viscoelasticity effect. A minor source of error may be a change of temperature during calibration and different friction coefficients in the slow calibration and the fast shock experiment.

The fibre optic sensor shows a pressure 18 kPa higher than the piezoelectric sensor just prior to the expansion waves arriving at the sensor. This is due to a slightly higher shock tube diaphragm bursting pressure and thermal effects (heat transfer from the air within the shock tube to the sensor). The cavity length for this sensor was about 12 μm and the confined air within the cavity is not expected to have any effect on the sensor performance as discussed in Section 8.8.3.2.

Following the expansion wave, the fibre optic sensor indicates a pressure drop of 120 kPa compared with 140 kPa for the piezoelectric transducer. This error is a combination of viscoelastic (including hysteresis) and heat transfer effects.

It was anticipated that the maximum pressure indicated by the sensor would increase during consecutive shock-expansion pressure cycles (as described in Section 8.8.3) but the sensor does not show such effects. The fact that such an increase is not observed may be related to the temperature difference on the two sides of isolation layer as discussed in Section 8.8.3.5. It is difficult to estimate the magnitude of this effect due to the unidentified thickness of the isolation layer and the lack of exact thermal and mechanical properties of Clear Cote 540.

In conclusion, a thin layer of Clear Cote 540 can be used to decrease heat transfer effects. However, as the layer provides a slight contribution to the overall stiffness of the (composite) diaphragm, it increases hysteresis and viscoelastic effects. It also lowers the pressure sensitivity of the sensor. Using a thicker layer can greatly affect the sensor performance and induces non-repeatability. Thermal protection layers should not contribute to the diaphragm stiffness.

8.9.2 Grease as thermal isolation layer

A layer of grease on the diaphragm was also tested as a candidate method to minimize transient thermal effects. To minimize the effects of viscoelasticity (i.e. hysteresis), low viscosity grease was chosen. The chosen grease was Kopr Kote manufactured by Jet-Lube. This grease is a low friction (Kopr Kote data sheet n.d.) lubricant and is recommended in applications where high temperature (up to 800^{o}C), high torque, high pressure, and sealing or corrosion presents a problem (MIN Grease products n.d.). Two experiments were performed with the same sensor: 1) before covering the sensor with grease; and 2) after covering the sensor with grease. The delay time measured without the layer of grease was less than 0.5 ms in the heat gun arrangement. This sensor was used in the shock tube only a few days after its construction and therefore, the minimum delay time was expected. The thickness of the grease was about 0.3 mm and the sensor with this layer indicated a thermal delay time of around 108 ms in the heat gun test. The delay time was expected to be about 90 ms in the reflected shock experiment (calculated using the method of Appendix A). The results obtained with and without the grease layer are presented in Fig. 8.20.

The grease has a small affect on the pressure sensitivity (less than 2%) and it seems to decreases the hysteresis (12 kPa to 10 kPa). This decrease can be related to the thermal effects that arise during calibration – a layer of grease lowers a change of diaphragm temperature during calibration.

The reflected shock results (Fig. 8.20) are similar to the Clear Cote 540 results (Fig. 8.19) in that the layer of grease does not reduce error No. 1 (errors are 30% and 27% for the cases without grease and with grease respectively) and No. 2. The maximum pressure indicated by the sensor keeps increasing during consecutive shock-expansion cycles even with the layer of grease. The slope of pressure rise following

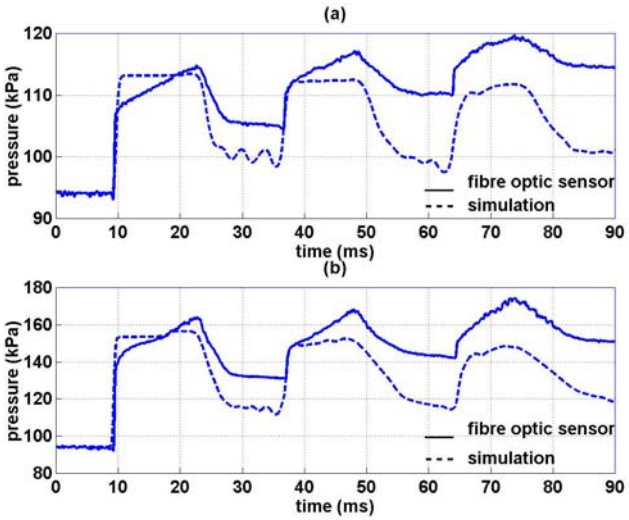

Figure 8.20 Comparison of fibre optic pressure sensor performance: a) without grease; and b) with grease thermal isolation layer.

the reflected shock (error No. 2) in the case without grease is 0.7 kPa/ms and in case with grease it is 1.9 kPa/ms. It is difficult to attribute this difference to the grease because the pressure ratio for the two experiments was different.

To evaluate the effects of grease on sensor performance just after shock reflection (errors No. 1 and No. 2), a sensor without grease, 0.3 mm thickness grease, and 1 mm thickness grease was tested. The sensor does not show a significant change in pressure sensitivity due to the 1 mm grease layer (<4%) and the hysteresis is reduced, as discussed previously. For sensors with grease layers, the expected delay time is longer than the data acquisition time so no heat transfer effects are expected for the sensor with the grease layers. In contrast, the expected delay time for the sensor without grease was about 0.3 ms. The results are presented in Fig. 8.21.

The thickness of the grease layer has little impact on error No. 1. For conditions of no grease, 0.3 mm grease, and 1 mm grease, error No. 1 is 13%, 22%, and 20% respectively. Furthermore, error No. 2 does not change due to the grease layer (for all cases is about 3 kPa/ms). The results demonstrate that the apparent increase of pressure immediately after shock reflection is not related to heat transfer from the air within the shock tube to the sensor for two reasons. Firstly, the bursting pressure ratio in Fig. 8.21a was greater than Fig. 8.21c and the higher pressure ratio induces

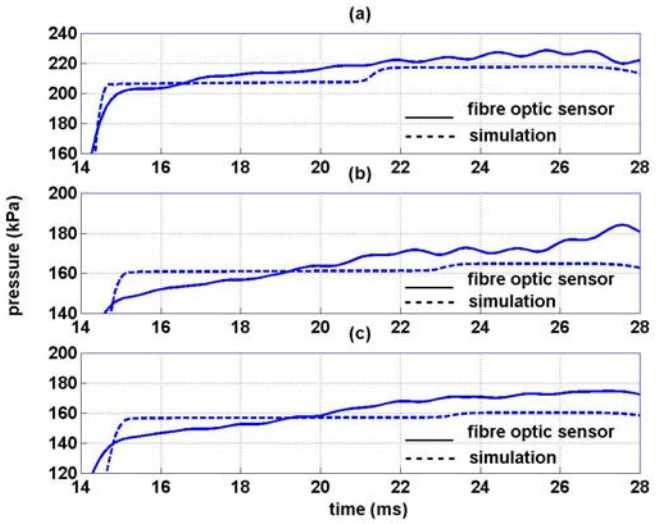

Figure 8.21 The effect of grease layers on reflected shock performance of a fibre optic pressure sensor: a) No grease; b) 0.3 mm grease; c) 1 mm grease.

higher temperature within the shock tube. Heat transfer to the sensor increases proportionally for greater temperature differences. According to the results provided from simulation and considering equations presented in Appendix A, the heat transfer for Fig. 8.21 is expected to be 60% higher than it was for Fig. 8.21c. Secondly, the sensor in Fig. 8.21c was covered with grease which increases delay time. Heat transfer from an increase of temperature in the cavity is not expected due to the long cavity length of 10 μm used for this sensor construction (see Section 8.8.3.2).

In summary, grease layers do not contribute to the diaphragm stiffness and therefore do not reduce the pressure sensitivity considerably. The grease does not reduce errors No. 1 and No. 2, however, it does decrease error No. 3 and protects the sensor from heat transfer (see Appendices A and C, and Section 6.4.3). The results also show the effect of heat transfer on sensor performance is gradual (for the shock tube diaphragm pressure ratios up to 5) and the main source of errors is a viscoelastic effect in the diaphragm adhesive.

8.10 Sensor response time

The performance and shock response of fibre optic sensors at frequencies less than 2.5 kHz (the cut-off frequency for the digital low pass filter) was discussed in

Section 8.9. The response time of the sensors and their natural frequency are the subject of this section.

8.10.1 Without thermal isolation layer

The sensors show a wide variation in pressure sensitivity even for nominally identical constructions. For example, for a copper foil diaphragm with a thickness 9 μm, pressures of between 100 and 1000 kPa were required for a 2π phase change. It is believed that such variations are due to different effective diaphragm diameters and different glue thickness – a consequence of the construction variability. A substantial pressure was not applied to the diaphragm while the glue was setting in order to avoid possibility of the glue penetrating inside the hole. Thus, some variation in effective diaphragm diameter is therefore expected. For example, even if only 0.06 mm around the hole is not bonded, the diaphragm diameter is doubled relative to the nominal 126 μm and therefore the sensor's pressure sensitivity increases 16 times (see Eq. (5.4)). Due to the contribution of the adhesive elasticity to the diaphragm deflection, any change in adhesive thickness can affect the sensor pressure sensitivity, as discussed in Appendix E.

Sensors also show variability in natural frequency and damping ratio. A change of diaphragm diameter affects the sensor natural frequency (Eq. (5.49)). The damping ratio is closely related to adhesive thickness. Thicker adhesive layers increase the sensor damping ratio due to viscoelastic effects. Figure 8.22 shows the shock response of three sensors operated in the long shock tube (the data has not been processed with a digital filter). Only the first 4 ms following shock reflection is presented in this figure.

The sensor of Fig. 8.22a exhibited a low damping ratio and its response time was about 6 μs. Most sensors, which are made with the techniques described in Chapter 6 were overdamped. Figures 8.22b and 8.22c shows some illustrative results for overdamped sensors. The sensor in Fig. 8.22b had a response time of about 10 μs with errors No. 1 and No. 2 of about 18% and 1.3 kPa/ms respectively. Figure 8.22c

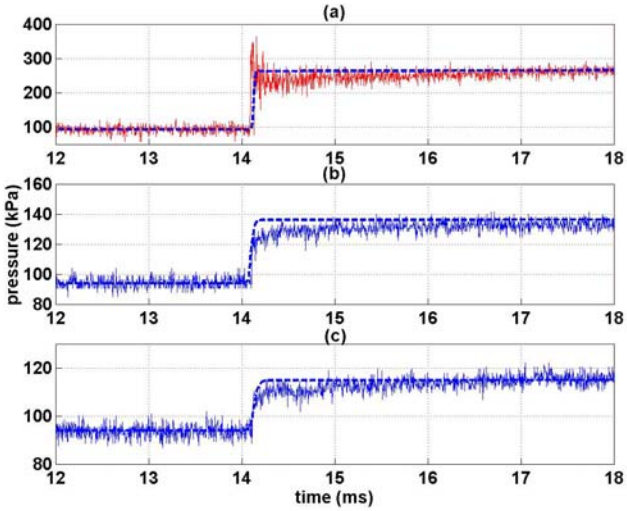

Figure 8.22 Comparison between simulation (broken line) and experimental response of the fibre optic pressure sensor with different damping ratio: a) low damping ratio sensor; b) high damping ratio sensor; and c) very high damping ratio sensor.

shows a higher damping ratio for a sensor whose response time was about 25 μs with errors No.1 and No.2 of about 25% and 2 kPa/ms respectively. It was observed that most sensors that indicated a larger error No. 1 simultaneously indicated a larger error No. 2. This leads to the conclusion that the source of these two errors (No. 1 and No. 2) is the same, namely, viscoelasticity.

8.10.2 Grease as isolation layer

To evaluate the effects of grease on sensor response time, a number of sensors were deliberately constructed with large diaphragm diameters and the adhesive thickness was minimized. To achieve this, the ferrule was covered with glue and the glue was swept by a fibre, the ferrule was then spun at a high speed (30000 rpm). Most sensors made with this method showed a leakage because of insufficient bonding material between the diaphragm and the ferrule. However, a few sensors did not indicate a leakage (less than 10% of all sensors made using this method).

The response of the sensor to normal shock loading is presented in Fig. 8.23a. The sensor shows a relatively low damping ratio. With the method described in Appendix B, the undamped and damped natural frequencies of the sensor are estimated as 167.2, and 167 kHz respectively, and the damping ratio was found to be 0.08.

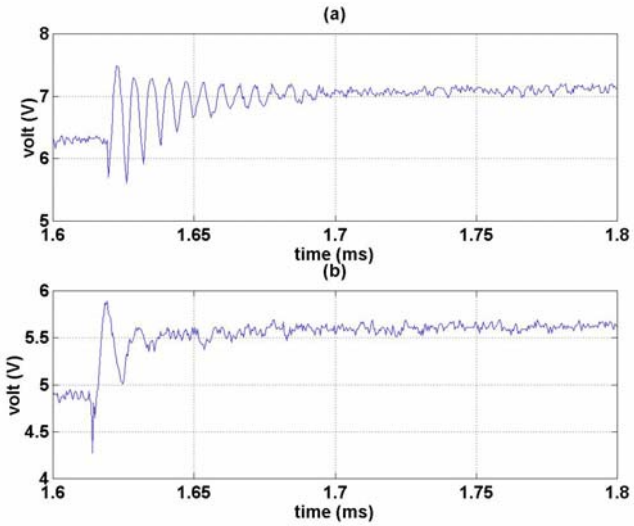

Figure 8.23 Effect of grease on diaphragm natural frequency: a) no grease; and b) 0.3 mm grease.

A layer of grease (Kopr Kote) 0.3 mm thick was then applied to the same sensor which was then tested to determine its shock response. The sensor response is presented in Fig.8.23b. The layer of grease decreased its natural frequency, as discussed in Appendix G. According to the properties of the grease and the copper diaphragm material presented in Appendix A and Section 5.10 respectively, and using Eq. (5.50), the expected natural frequency of the diaphragm is f=80 kHz. The actual damped natural frequency is about 90 kHz (from Fig. 8.23b) and the undamped natural frequency and damping ratio are 94 kHz and 0.25 respectively. The difference between the calculated (80 kHz) and experimental (94 kHz) natural frequencies can largely be attributed to the approximate nature of the grease thickness measurement. An increase in the damping ratio can have an advantage in that it reduces the settling time. The settling time is defined as the time for the response to reach and stay within ±2% of its final value. Fig. 8.23 shows that the grease layer decreased the settling time from 80 μs to 50 μs.

8.11 Shock tube disturbance identification

A fibre optic pressure sensor made with a copper diaphragm bonded onto a zirconia ferrule with liquid adhesive (Araldite 5 minute) was mounted in the end plate of the short shock tube arrangement. The results for this experiment are presented in Fig. 8.24. Part a of this figure shows the results over a total record length of 120 ms and

part b shows the results over a period of about 1 ms following shock reflection.

The sensor indicated a disturbance following each of the reflected shocks. The first disturbance began about 35 μs after shock reflection and the disturbance was repeated on a number of occasions after the same interval of time. The results from the simulation of this particular experiment, indicate that the temperature was 403.5 K within the reflected shock region (ie immediately behind the first reflected shock). The sound speed was therefore calculated as 402.5 m/s and hence if the period of the disturbance is 35 μs, the distance travelled by the disturbance is around 14.1 mm which closely corresponds to the radius of the tube (13 mm).

On inspection of the end wall mounting arrangement with the short shock tube, an annular gap was identified as illustrated in Fig. 8.25. The throat to the annular cavity had a dimension of approximately 0.5 mm. This cavity certainly has the potential to create the observed disturbance as has been illustrated in axisymmetric simulations of this configuration.

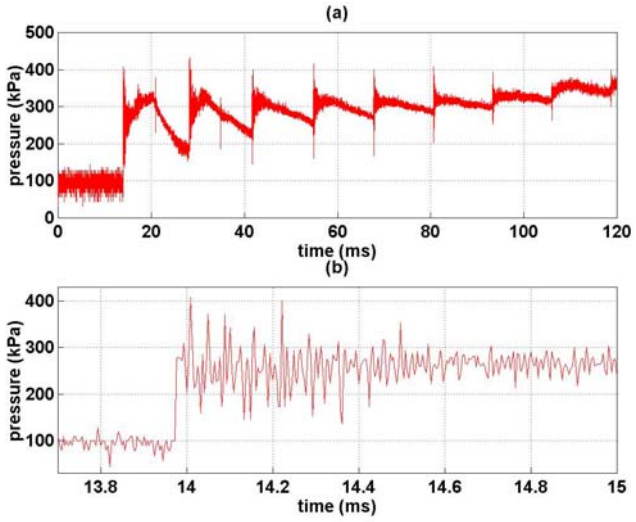

Figure 8.24 Shock response of a fibre optic pressure sensor in the short shock tube: a) Shock response for about 100 ms; b) Shock response for about 1 ms.

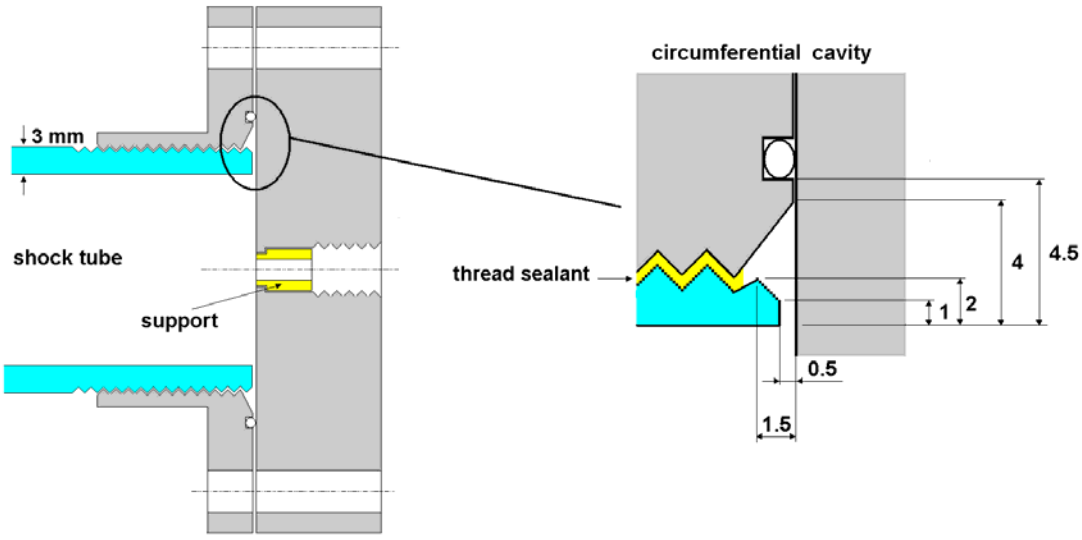

Figure 8.25 Illustration of shock tube end plate arrangement. Dimensions in mm.

The long shock tube was then inspected. It also had an annular gap, although of slightly smaller extent than the gap that existed in the short shock tube configuration. After filling the gap in the long shock tube arrangement with a plastic putty (Plasti-Bond heavy duty from Selleys) and machining the face of the flange flat, the fibre optic pressure sensor was again tested. Figure 8.26 shows the results from this

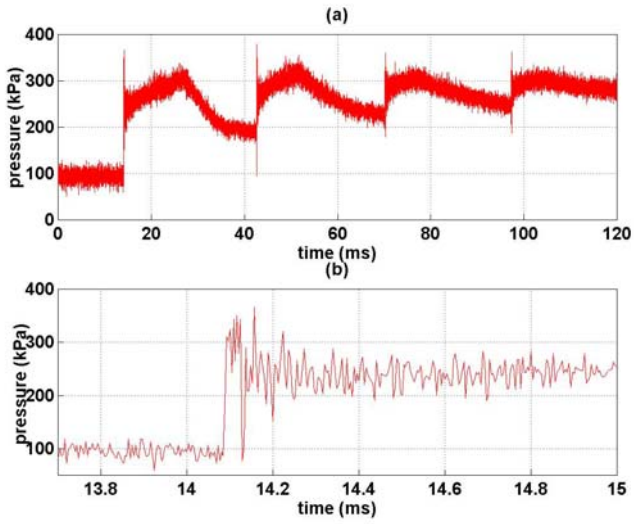

Figure 8.26 Shock response of a fibre optic pressure sensor in the long shock tube (with elimination of annular gap): a) Shock response for about 100 ms; b) Shock response for about 1 ms.

experiment. Although there is still some effect approximately 25 μs after shock reflection, the extent of the disturbances that were previously observed has been greatly reduced.

8.12 Conclusion

Various fibre optic pressure sensors were tested within the shock tube, and results were compared with those obtained using a piezoelectric pressure transducer and a numerical simulations performed using a quasi one dimensional computer program.

Sensors with a very short cavity (around 1 μm) showed lower noise in comparison with relatively long cavity sensors (>10 μm). However, the short cavity sensors showed considerable errors in the shock experiments due to the substantial change of temperature of confined air inside the cavity.

In quasi-static calibration, due to the contribution of the adhesive elasticity to the diaphragm deflection and the uncertainty in the actual diaphragm diameter, the diaphragm pressure sensitivity was larger than the expected values.

Viscoelastic effects especially in the adhesive, affect the sensor performance both in quasi-static calibration and in the shock experiments. Viscoelastic effects contribute to sensor hysteresis and therefore hysteresis cannot be completely eliminated through load cycling. In the shock experiments, most sensors showed a high damping ratio. This damping ratio is related to the adhesive thickness. Lower damping ratios were achieved by decreasing the adhesive thickness. The natural frequency of sensors was reduced due to the contribution of the adhesive to diaphragm deflection.

Using a thermal isolation layer which contributes to the diaphragm stiffness (such as Aerosolve Clear Cote 540) affects the sensor performance and increases the hysteresis. Using a thermal isolation layer, which does not contribute to diaphragm stiffness (such as a low viscosity grease) can protect the sensor from heat transfer effects and decrease errors in quasi-static calibration and shock tube experiments. It has been found that the grease can also increase the damping ratio of the sensor . An increase in damping ratio for a sensor, which originally has a low damping ratio, can be useful as it reduces its settling time.

Fibre optic pressure sensors made with a copper foil (9 μm thickness) showed a natural frequency of up to 500 kHz and pressure sensitivity of between $2\pi/1000$ and

$2\pi/100$ rad/kPa. Their response time was between 4 and 100 μs and can be used to measure fluctuations with a frequency up to 250 kHz.

These sensors measure shock pressure with an error of up to 30%. These errors can be calibrated for each sensor. The magnitude of error is almost constant for each sensor and the sensors always underestimate the actual reflected shock pressure (with a variation of up to 10%).

Fibre optic pressure sensors show a false pressure rise after every shock. The rate of this apparent increase in pressure does not change significantly (for pressure ratio up to 5.66) and can be calibrated.

The accuracy of pressure indicated by the fibre optic sensor decreases after it is hit by a second shock due to viscoelasticity effects. Therefore, these sensors can be used for the period between two shocks. In this case, the sensor should be covered with a layer of thermal isolation to decrease heat transfer effects.

Chapter 9: Conclusion

9.1 Introduction

The research presented in this thesis has mainly concerned the development of Fabry-Perot fibre optic pressure sensors, and in particular, the diaphragm used with these sensors. This chapter summarizes the main conclusions from this work and discusses possible improvements to the sensor design and interrogation systems. The improvements suggest in this chapter can be grouped into three categories. Firstly, some modifications to the current design that may improve sensor performance; secondly, some minor changes to the basic configuration; and finally, some major changes to the configuration.

9.2 Principal achievements

Extrinsic Fabry-Perot fibre optic pressure sensors were designed to be employed in transient aerodynamic facilities. The principle achievements were:

- high spatial resolution (in the order of 0.1 mm);
- high temporal resolution (natural frequency of up to 900 kHz);
- wide pressure range (100 kPa- 1200 kPa);
- pressure accuracy within 10% of mean pressure; and
- low cost sensor (less than $10 Australian)

The sensor was successfully employed in locating the source of disturbances in a shock tube.

9.3 Summary

The value of a low cost fast response pressure sensor which is able to work in the harsh hypersonic flow environment produced by a transient wind tunnel was argued in Chapter 1. To make a useful addition to the array of sensor options that are currently available to experimentalists working in this field, the new pressure sensor should have a spatial resolution of around 1 mm or less. Ideally, the sensor should

not be temperature sensitive, but an achievable compromise would be to take advantage of the transient flow environment and ensure that the sensor is protected from hot flow for the duration of the useful test time. The thermal shielding should not decrease the sensor bandwidth to less than 100 kHz. Provided an inexpensive sensor can be produced, such design goals are realistic with current technology as the sensor could be operated in a sacrificial mode – the damaging particle impacts and additional heat transfer, which normally occur after the useful test flow has finished, would be acceptable.

Some basic pressure sensors including those that have the potential to be used in the transient flow environments were discussed in Chapter 2. Most sensors did not suit the transient conditions and design goals outlined in Chapter 1 with the exception of piezoelectric transducers, piezoresistive transducers, bar gauges and pressure sensitive paints.

Currently, pressure sensitive paints can be employed for bandwidths up to 10 kHz but they indicate a high temperature sensitivity (1%/^{o}C) and it is not possible to shield them while maintaining their pressure sensitivity and bandwidth. Piezoresistive and piezoelectric transducers are commercial devices that generally have a wide bandwidth, but they are expensive and must be shielded from the flow which generally makes their temporal response unacceptably low. Their spatial resolution is at best on the order of 1 mm. Bar gauges are in-house constructed devices that can be considered as a special form of piezoelectric transducers. They can be constructed with sufficiently low rise time (generally around 4 μs or less), but their long lengths may be inappropriate in some applications and their pressure sensitive diameter is quite large (at least 3 mm). Bar gauges can be only produce useful data for a short period which depend on their length.

Chapter 3 which dealt exclusively with fibre optic pressure sensors, provided a selective review of fibre optic pressure sensors and interferometers. Fabry-Perot fibre optic pressure sensors have the potential to be used in applications outlined in Chapter 1. They have already been used in a turbomachinery application by workers at Heriot-Watt University and have a spatial resolution of around 0.2 mm and a temporal response such that fluctuation to more that 200 kHz were detected. Their pressure resolution in the full-scale test facilities was about 0.5 kPa. Fabry-Perot

fibre optic pressure sensors have the potential to satisfy the design requirements of a new transducer for transient wind tunnels.

Chapter 4 reviews some key features of fibre Fabry-Perot interrogation system components, including some important design factors and their limitations. The interrogation wavelength that was selected (780-790 nm) is the lowest interrogation wavelength used in fibre optic communication systems. This interrogation wavelength has some advantages such as lower cost and simplicity (e.g., there is no need to use a frequency dither), and leads to the production of sensors with a higher natural frequency and higher pressure sensitivity. However, the disadvantages of this operating wavelength include higher dispersion, more difficulty in launching light into the fibre and higher sensitivity to diaphragm roughness.

One important step in the design of the Fabry-Perot fibre optic pressure sensor is the diaphragm. Chapter 5 presents the important factors and the essential equations in the design of the diaphragm. According to the calculations, a thin copper diaphragm (about 10 μm) with a diameter of 125 μm can provide the required pressure sensitivity (pressure range to 600kPa gauge in this work), along with the desired spatial and temporal resolution. Effects of pretension on the diaphragm strength and natural frequency were discussed. According to the calculations, pretension slightly improves the diaphragm performance. However, applying high pretension during construction is not practical if a liquid adhesive is to be used to bond the diaphragm to the substrate. Changes in the pretension are likely to occur between construction and operation of the sensor due to changes of environmental temperature or viscoelastic effects in the adhesive and these effects will alter the diaphragm performance. Thick layers of thermal isolation on the diaphragm considerably reduce the natural frequency of the diaphragm. However, a thin thermal isolation layer (on order of 0.1 mm) for a 9 μm thick copper diaphragm can be applied without a considerable reduction of natural frequency (less than 17%).

Construction techniques for a variety of foils, adhesives and substrates were discussed in Chapter 6. Using a hypodermic tube as a sensor substrate leads to a sensor with a small outer diameter (about 0.4 mm), however their temporal resolution was not high due to the relatively large internal diameter (around 0.2 mm). Some irregularities were observed in these sensors due to possible creasing of the diaphragm during construction. The zirconia ferrule substrate showed better results

but decreasing their outer diameter through a machining operation is time consuming due to their hardness. More reliable construction techniques (and hence sensors) were developed using liquid adhesives than with tape and film adhesives, especially if a thin layer of liquid adhesive was applied between the substrate and the diaphragm. The construction rate success finally achieved using zirconia ferrule substrates, a liquid adhesive, polished diaphragms and active control of cavity length was about 50%. Reduced viscoelastic effects within the adhesive layer were also attained with a very thin bonding layer (<5 μm) between substrate and diaphragm. However, in this case, the construction success rate was limited to less than 10% because the diaphragm bonding layer was prone to leakage.

The effects of diaphragm roughness were identified. The results showed that producing a diaphragm with rms roughness reduced from 100 nm to 40 nm increases the rate of construction success. Active control of the cavity length during the curing of the adhesive used to bond the fibre also increases the rate of construction success and can generally yield sensors with higher visibility.

The pressure sensitivity of sensors constructed from a copper diaphragm with a thickness of 9 μm was between $2\pi/100$ and $2\pi/1000$ rad/kPa. These pressure sensitivities are much higher than the calculated values ($2\pi/4800$ rad/kPa assuming a clamped diaphragm). The main sources of error were identified as uncertainty in the actual diaphragm support conditions, the actual diaphragm diameter, and the thickness of the bonding layer.

The sensor temperature sensitivity was also modelled and measured. The sensors indicated variable temperature sensitivity. For a flat copper diaphragm (thickness 9 μm) and zirconia ferrule substrate, the sensor temperature sensitivity was calculated as $2\pi/1.5$ rad/^{o}C but this value can be decreased if an initial deflection is present. Constructing a flat diaphragm under pretension can decrease the sensitivity to environmental temperature change, but due to relaxation of the adhesive, such a sensor could not be stored for a long period. Furthermore, a flat diaphragm actually has a higher temperature sensitivity than a curved diaphragm under loaded conditions. An initial deflection of the diaphragm was therefore recommended in order to decrease the sensor temperature sensitivity during loading. The measured temperature sensitivities were between about $2\pi/2$ and $2\pi/10$ rad/^{o}C. This lower

temperature sensitivity relative to the calculated value is believed to be due to the effects of adhesive expansion (which were not considered in the modelling). Additional contributing factors include the initial diaphragm deflection was caused by a possible partial vacuum in the cavity which is derived from cavity length adjustment during fibre adhesive curing.

The sensors made with the initial construction techniques showed considerable hysteresis. The possible sources and their contributions to the net sensor hysteresis were discussed in Chapter 7. According to the results, the diaphragm and bonding layer material hysteresis, air within the cavity, and a change of temperature of air within the calibration tube during quasi-static calibration are all possible sources of hysteresis. By tension load cycling the diaphragm material, pressure load cycling the diaphragm following construction, using a thin bonding layer, using a larger bonding area, and increasing the duration of the calibration process, sensor hysteresis can be greatly reduced. The air within the cavity can contribute to the sensor hysteresis only if the sensor has a short cavity (<5 μm).

The responses of the fibre optic pressure sensors to shock loading were presented in Chapter 8. The sensors show errors of up to 30% in comparison with results provided from the piezoelectric transducer. The fibre optic sensors also show an apparent increase of pressure after the reflected shock. It was demonstrated that the primary source of these errors was not related to thermal effects associated with heat transfer from the shock compressed air or from the compression of air within the cavity (for a sensors with a cavity length >5 μm). The main source of error is believed to be viscoelastic effects within the bonding layer adhesive. Decreasing the bonding layer thickness decreases the error. However, by using the results of the dynamic shock calibration, the maximum error can be limited to less than 10%.

Heat transfer from the air inside the shock tube to the sensor can contribute to the apparent increase of pressure. This effect can be eliminated within the measurement period by using a thin thermal isolation layer on the exposed surface of the diaphragm. Two types of thermal isolation layer were tested – a plastic coating for the diaphragm and a low viscosity grease. Either layer can be successfully used to isolate the diaphragm from heat transfer for a reasonable period of time (tens of milliseconds for a 0.3 μm thick layer of grease if the shock tube diaphragm pressure ratio is less than 5.69). However, the plastic coating was less successful than the

grease as it made a small but significant contribution to the diaphragm stiffness. The sensors without any thermal isolation showed natural frequencies of up to 900 kHz and damping ratios of between 0.05 and 1.5 (depending of the construction parameters such as thickness of the adhesive). Using a thermal isolation layer decreases the sensor natural frequency and increases its response time. However, this may actually be of benefit for sensors with naturally low damping ratios as it decreases the diaphragm settling time and extends the flat portion of the frequency response spectrum to higher frequencies.

The sensor was applied to the identification of strong disturbances in the end wall region of the shock tube. It was found that the origin of the disturbances was a small annular gap at the junction between the tube and the end wall. It was demonstrated that the magnitude of the noise was greatly reduced by virtually eliminating the annular gap.

9.4 Future work

The performance of the Fabry-Perot fibre optic pressure sensors can be improved with some modification to the design and construction techniques. These modifications include evacuating the air from within the cavity and using stiffer adhesives that are less susceptible to viscoelastic effects. Furthermore, some changes in the interrogation system could also improve the sensor performance.

9.4.1 Potential improvements to current design

If the cavity length is longer than 5 μm, evacuating the air from within the cavity will not measurably affect performance. However, a vacuum in the cavity would permit shorter cavity sensors to operate effectively. Shorter cavity sensors can decreases dispersion (see Section 4.4.1) and noise. Choosing a light source, which has a narrower spectral width, cannot assist in decreasing dispersion and noise because it also decreases the SBS threshold power (see Section 4.4.3.1).

In this work, some attempts were made to evacuate the air within the cavity prior to gluing the diaphragm to the substrate. The vacuum that was achieved was about –70 kPa. The main problem with this technique was related to the liquid adhesives which generally failed to dry or create a sufficiently strong bond under the relatively low

pressure conditions. Loctite 324 (see Table 6.4) was the only adhesive which was found to provide good bonding under the low pressure conditions. However, this adhesive requires an activator which of necessity was applied the diaphragm and consequently produced an irregularity in the reflected light.

The main source of non-repeatability and hysteresis that persists after applying the load cycling is believed to be related to the adhesive which forms the diaphragm bonding layer. Reductions in bonding layer thickness (which in turn reduce the shear deflection of the bonding layer) can be achieved using a very low viscosity liquid adhesive. When cured, the adhesive should ideally have a high modulus of elasticity and bonding strength, and if an evacuated cavity is required, the adhesive must obviously be capable of curing at the low pressure conditions. Unfortunately, the specification sheets for most adhesives do not include all the desired data, and an adhesive that would yield substantial performance improvements at moderate cost has not yet been identified.

Using a diaphragm material with a low coefficient of thermal expansion will reduce the sensor temperature sensitivity, especially if the diaphragm is constructed with an initial deflection. An initial deflection will actually increase the sensor temperature sensitivity in comparison with a pretensioned flat diaphragm if the sensor is unloaded. However, in the usual case of a loaded diaphragm, the temperature sensitivity can be decreased through the provision of an initial deflection.

Polishing commercial foils can decrease their roughness and improve their optical performance when used as diaphragms. For example, in the case of the 9 μm thick copper foil used in this work, polishing decreased its rms roughness from 100 nm to about 40 nm and improved its optical performance (see Section 6.3.6.1). However, even lower roughness is achievable (down to about few nm) using Chemical Mechanical Planarization (CMP) technique and is expected to have beneficial effects on the fibre optic transducer.

Some modifications to the interrogation system could also improve the sensor performance. Using polarization maintaining or single polarization fibres could improve the visibility, decreases polarization mode dispersion, and reduce the system sensitivity to fibre bending. Choosing a longer interrogation wavelength (e.g., 1310 nm) should also decreases the scattering (Eq. (4.13)).

The signal to noise ratio is an important factor, especially for measuring low intensity and high frequency fluctuations. The level of noise is relatively high for the current application and should be reduced. Improvements could be made through optical, mechanical, thermal and electrical modifications. Using a single polarization fibre or polarization maintaining fibre would reduce noise derived from random changes of polarization conditions in an interrogation system (see Section 4.4.4). Electromagnetic shielding of detectors and amplifier conductors may also be useful (see Section 4.6.1.3). Reducing the sensing area of the detector also reduces the noise. Laser and room temperature control reduces the thermal noise which especially affects the dark current (see Section 4.6.1.3). Decreasing the sensor cavity length has a significant effect on sensor noise (see Fig. 3.9). However in this case, the cavity should be evacuated otherwise it will induce other errors (see Section 8.8.3.2).

9.4.2 Major changes of configuration

The main source of sensor non-repeatability is believed to be related to the bonding layer. In this section, some configurations that can eliminate bonding layer contribution in the diaphragm deflection are suggested.

9.4.2.1 Diaphragm improvement

Using a rigidly supported diaphragm can minimize the contribution of the bonding layer deflection to the overall diaphragm deflection and thereby reduces the effect of adhesive viscoelasticity. Four possible diaphragms arrangements are presented in Fig. 9.1.

In Fig. 9.1, the diaphragm and diaphragm support form a pressure sensitive end cap that is bonded onto the substrate. The end cap should be constructed in one piece. Care should be taken such that the adhesive does not penetrate between the substrate and the diaphragm support region. As the diaphragm support region would be much thicker than the diaphragm itself, it should have virtually not contribution to the diaphragm deflection. As the diaphragm will be in direct contact with the substrate, the adhesive will have virtually no contribution to the diaphragm deflection provided there is a compressive load due to the applied pressure. However, if the measurand pressure becomes less than the pressure within the cavity, the adhesive will

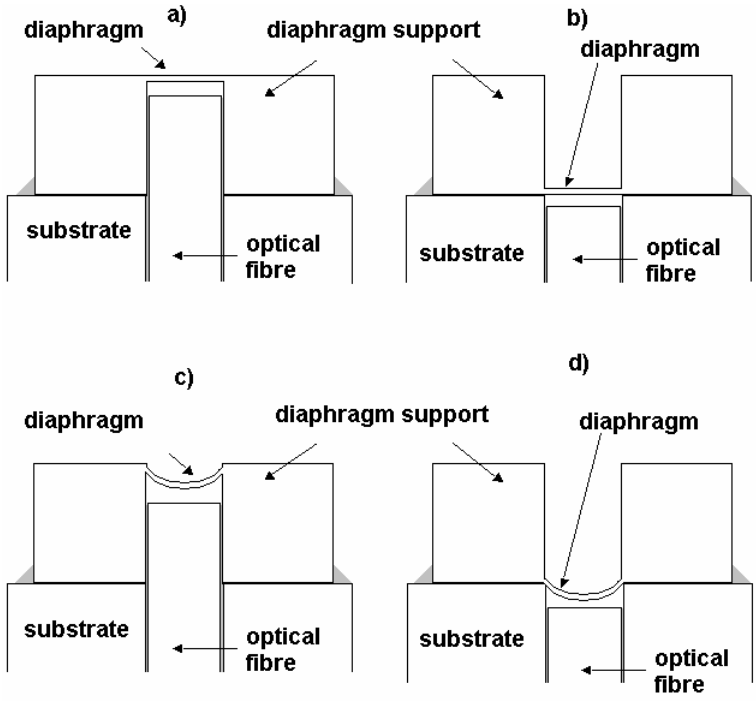

Figure 9.1 Four possible arrangements for a rigidly supported diaphragm

contribute to the deflection. If the air within the cavity is evacuated, the adhesive will not contribute to the diaphragm deflection.

Provided the end cap is constructed in one piece, the support conditions for the diaphragm will closely approximate those of a clamped edge (fixed edge) diaphragm. The anticipated deflection is therefore expected to be much lower than for a diaphragm with a similar thickness and diameter constructed according to the configuration used in this work. The estimated natural frequency of such diaphragms should similarly be in close agreement with predictions based on the clamped edge (fixed edge) diaphragm model.

In Fig. 9.1 parts a and c, the thickness of the diaphragm support region should be much larger than the cavity length so that the fibre can be bonded within the end cap itself. The temperature sensitivity of these sensors is expected to be decreased due to the same thermal expansion of the diaphragm and the diaphragm support region. Figure 9.1b shows a different scheme in which the fibre is not required to be inserted into the end cap. However, depending on the length of the cavity on the exposed surface of the diaphragm, the sensor may have a pneumatic resonance that impedes

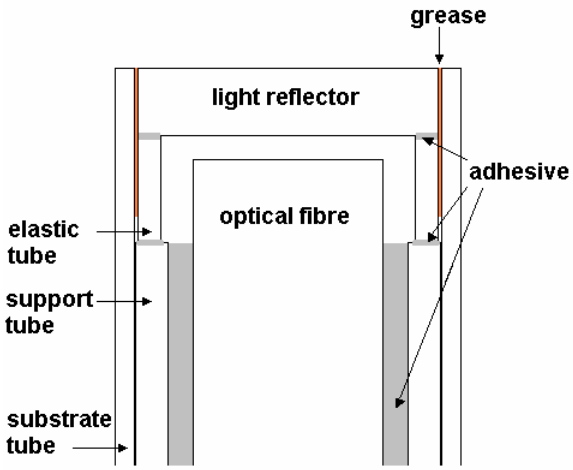

Figure 9.2 Proposed configuration for a new Fabry-Perot fibre optic pressure sensor.

the measurement of high bandwidth fluctuations. In the arrangements illustrated in Fig. 9.1c and 9.1d, curved diaphragms are suggested to decrease temperature sensitivity during loading. However, a curved diaphragm may introduce other problems such as the light reflected from the diaphragm not returning to the small core of the single mode optical fibre.

The diaphragms described in Fig. 9.1 can be constructed using a vacuum deposit. The variation of diaphragm thickness is probably possible using some obstructs before glass. Optimising the diaphragm construction process is required and can be subject of a mechanical project for bachelor or master course.

9.4.2.2 Fabry-Perot hypodermic tube sensors

As discussed in Chapter 6, the main problem with the hypodermic tube sensors was a creasing of the diaphragms. Furthermore, the bonding layer will also have a substantial contribution to the diaphragm deflection. Both these problems could be solved using a new configuration illustrated in Fig. 9.2.

In the configuration presented in Fig. 9.2, a light reflector is used instead of a diaphragm. The light reflector is designed so that it does not experience any substantial bending during the measurement. Instead, the light reflector translates due to the elastic action of the elastic tube (see Fig. 9.2). The elastic tube is supported by the support tube, and this support tube is fixed to the housing tube. The bonding on the ends of the elastic tube is not expected to contribute to the translation of the

reflector, especially when the elastic tube is under compression. The optical fibre is inside the first tube but is not bonded to it, to provide relative motion.

Preliminary calculations show that this system could realistically have a high natural frequency. For example, considering a steel hypodermic tube 25G (see Table 6.2) with outside and inside diameters of 0.5 mm and 0.3 mm respectively, a length of 20 mm provides a pressure sensitivity of 2π/3.6 rad/ MPa. In this case, the natural frequency of the tube can be calculated using (Timoshenko, Young & Weaver 1974),

$$\omega_n = \frac{\pi}{l}\sqrt{\frac{E}{\rho}} \tag{9.1}$$

According to Eq. (9.1), the natural frequency of this arrangement would be 800 kHz. Buckling is not a particular limitation for the short tube considered here as the pressure, which will cause buckling, is greater than 100 GPa in the present example.

It should be noted that in the configuration of Fig. 9.2, the support tube and substrate tube are bonded using a liquid adhesive. This adhesive can contribute to the change of the optical path length. Choosing a support tube with an outer diameter close to the inner diameter of the substrate tube can minimize the contribution. This can also be achieved by increasing the length of the two tubes. Choosing a thicker substrate tube and decreasing the internal diameter can eliminate the adhesive viscoelasticity effect on sensor performance.

9.4.3 Closure

Fabry-Perot fibre optic pressure sensors can be employed to measure fluctuation with bandwidths up to 200 kHz with a maximum error of 10% for a limited time (around 10 ms). The pressure resolution for such sensors is less than 10 kPa in quasi-static calibration over a range of 600 kPa. However, these sensors show high temperature sensitivity and some non-repeatability due to viscoelasticity of the adhesives used to bond the diaphragm to the substrate. Some new configurations were suggested and there are good prospects for eliminating or substantially reducing these problems.

References

American Society for Testing and Materials 1998. Standard test methods of tension testing of metallic foil. ASTM E345-93.

Abbitt, JD, Fuentes, CA & Carroll, BF 1996, 'Film-based pressure-sensitive-paint measurements', Optics Letters, vol. 21, no. 22, pp 1797-9.

Amos, SW 1990, *Principles of transistor circuits*, 7th edn, Butterworth, London.

Anderson, JD 1989, *Hypersonic and high temperature gas dynamics*, McGraw-Hill, New York.

Anderson, JD (Jr.) 1990, *Modern compressible flow*, 2nd edn, McGraw-Hill, New York.

Asai, K 2001, 'Analyses of high speed gas flows using molecular sensor technology', Japanese National Aerospace Laboratory, Year 2000 Report, viewed Jan. 2003, <http://www.nal.go.jp/fluid/eng/mosaic/detail/e3_1/>.

Beckwith, IE 1975,"Development of a high Reynolds number quiet tunnel for transition research", *AIAA Journal*, vol. 13, pp 300-6.

Berg, S 2002, "High-frequency measurements of interfacial friction using quartz crystal resonations integrated into a surface forces apparatus", *Physical Review E*, American Physical Society, vol. 65, article no. 026119.

Bejan, A 1995, *Convection Heat Transfer*, Wiley & Sons, New York.

Bentley, JP 1989, *Principles of measurement systems*, 2nd edn, Wiley & Sons, New York.

Bertone, N & Webb, P n.d., “Noise and stability in PIN Detectors”, viewed Jan. 2003, <http;//opto.perkinelmer.com /library /papers/tp7.htm>.

Brown, B.E. 1965, *Modern optics*, Reinhold publishing corporation, New York.

Buttsworth, DR 2001, “Assessment of effective thermal product of surface junction thermocouples on millisecond time scales”, *Experimental Thermal and Fluid Sciences*, vol. 25, pp. 409-20.

Buttsworth, DR, Jacobs PA & Jones, TV 2002, ‘Simulation of Oxford university gun tunnel performance using a quasi-one-dimensional model’, *Shock Waves*, vol. 11, pp. 377-383.

Buttsworth, DR, & Ahfock, AL 2003, “A Pulsed LED System for Schlieren Flow Visualisation”, Technical Report TR-2003-01, Faculty of Engineering and Surveying, University of Southern Queensland.

Carstens, JR 1993, *Electrical sensors and transducers*, Regents and Prentice Hall, New Jersey.

Cherin, AH 1983, *An Introduction to optical fibers*, McGraw Hill, New York.

Cloud, G 1998, *Optical methods of engineering analysis*, Cambridge University Press, Cambridge.

Cochrane, PT 1998, ‘Fibre optic surface roughness measurement’, MSc thesis, University of Waikato, viewed Jan. 2003, <www.physics.uq.edu.au/people/cochrane /pubs/mastersThesis.pdf>.

Crisp, J 1999 , *Introduction to fiber optics*, Newnes, Oxford.

Culshaw, B 1986, *Optical fibre sensing and signal processing*, Peter Peregrinus Ltd, London, UK.

Dakin, J, Culshaw, B 1998, *Optical fiber sensors*, Artech house Inc., vol. 1, Boston.

Dally, JW, Rifley, WF & McConnell, KG 1993, *Instrumentation for engineering measurements*, 2nd edn, John Wiley, New York.

Davies, L & Lippaitt, J 1964, 'Evaluation of a modified 3/8" diameter pressure-bar gauge for shock tube studies', National physical laboratory aero, note 1029 A.R.C. 26360 Hyp. 456.

Di Giovanni, M 1982, *Flat and Corrugated Diaphragm Design Handbook*, Marcel Dekker Inc., New York.

Doebellin, EO 1990, *Measurement systems, application and design*, 4th edn, McGraw Hill, New York.

Donnel, LH 1976, *"Beams, plates and shells"*, McGraw-Hill, New York.

Doolan, CJ 1997, 'A Two-Stage Free-Piston Deriver Hypervelocity Expansion Tubes', PhD thesis, University of Queensland, Australia.

Dunpont, P, Hayward, V, Armstrong, B & Altpeter, F 2002, 'Single Elasto-Plastic Friction Models', University of Wisconsin Milwaukee, Milwaukee, USA, viewed Jan. 2003, <http://www.uwm.edu/People/bsra/ftp/ElastoPlastic>.

Eggins, B 1996, *Biosensors*, Wiley and Teubner, Chichester.

Figliola, FS & Beasley, DE 2000, *Theory and design for mechanical measurements*, 3rd edn, John Wiley, New York.

Finkelstein, L & Grattan, KTV 1994, *Concise encyclopaedia of measurement & instrumentation*, Pergamon Press Ltd., Oxford.

Gander, MJ, Macpherson, WN, Barton, JS, Reuben, RL, Jones, JDC, Stevens, R, Chana, KS, Anderson, SJ & Jones, TV 2002, 'Embedded micromachined fibre optic

Fabry-Perot sensors in aerodynamics application', *Sensors 2002 Proceedings of IEEE*, June 12-14, pp 1707-12.

Gauthier, MM, Drgolich, KS, Ferjutz, K, Garverick, LM, Lampman, HF, Sheppard, LM, Wheaton, ND & Woods, MS 1995, 'Engineered materials handbook desk edition', *ASM International Handbook Committee*, ASM International, OH.

Gengel, YA 1998, *Heat Transfer*, McGraw-Hill, New York.

Germain, PD & Hornung, HG 1975, 'Transition on a slender cone in hypervelocity flow', *Experiments in Fluids*, vol. 22, pp. 183-190.

Goff, DR 1999, *Fiber optic reference guide*, 2nd edn, Butterworth-Heinemann, MA, USA.

Goodfellow, Catalogue c. 1998/1999, Goodfellow Cambridge Limited, Cambridge, Great Britain, <http:\\www.goodfellow.com>.

Gopel, W, Hesse, J & Zemel, JN 1989, *Sensors, a comprehensive survey*, VCH publishers Inc., vol. 1, New York.

Gratton, KTV & Meggitt, BT 1995, *Optical fiber sensor technology*, Chapman & Hall, London.

Gratton, KTV & Meggitt, BT 1999, *Optical fiber sensor technology*, Kluwer academic publishers, vol. 3, Netherlands.

Guenther, R 1990, *Modern Optics*, John Wiley, New York.

Haddad, YM 1995, *Viscoelasticity of engineering materials*, Chapman & Hall, London.

He, Y & Morgan, RG 1994, 'Transition of compressible high enthalpy boundary layer flow over a flat plate', *Aeronautical Journal*, vol. 98, pp. 25-34.

Hecht, E & Zajac, A 1982, *Optics*, 7th edn, Addison Wesley, Boston.

Hecht, J 2002, *Understanding fiber optics*, 4th edn, Prentice-Hall International, London.

Holman, JP 1986, *Heat transfer*, 6th edn, McGraw-Hill, New York.

Huang, A, Ho, CM, Jiang, F & Tai, YC 2000, 'MEMS transducers for aerodynamics-a paradym shift', *AIAA Paper 2000-0249*, 38th Aerospace Sciences Meeting & Exhibit, NV, USA.

Hussey, B & Wilson, Jo (comps) 1996, *Structural adhesives directory and databook*, Chapman-Hall, London.

Inatomi, Y 2003, 'Measurement of temperature and concentration dependences of refractive index of Hen-egg-white Lysozyme solution', The Institute of Space and Astronautical Science, Japan, viewed Aug. 2003, <http://staff.aist.go.jp/yin-dachuan/Thermooptic.pdf>.

Jacobs, PA 1994a, 'Numerical simulation of transient hypervelocity flow in an expansion tube', *Computers in Fluids*, vol. 23, no. 1, pp. 77-101.

Jacobs, PA 1994b, 'Quasi one dimensional modelling of a free piston shock tunnel', *AIAA Journal*, vol. 32, no. 1, pp 137-145.

Joenathan, C 1998, 'Speckle photography, shearography and ESPI', Handbook of optical metrology, Artech House, London, viewed Jan. 2003, < http://www.rose-hulman.edu/~joenatha/speckle1.html>.

Kingfisher International Pty Ltd, viewed Sep. 2003, <http://www.Kingfisher .com.au/appnotes/A08.htm>.

Kingston, RH 1995, *Optical sources, detectors, and systems*, Academic Press, San Diego.

Klein, MV & Furtak, TE 1986, *Optics*, John Wiley, New York.

Kopr Kote data sheet by Jet-Lube Inc., Moreau marketing & sales, USA, Winston-Salem, NC, viewed Jan. 2003,<http://www.rmoreau.com/copper.pdf>.

Krohn, DA 1988, *Fiber optic sensors, fundamentals and applications*, Instrument society of America, U.S.A.

Lagakos, N, Cole, JH & Bucaro, JA 1987, 'Microbend fiber optic sensor', Applied Optics, vol. 26, no. 11, June, pp 2171-80.

Lakes, R. 1998, Viscoelasticity notes adapted from viscoelastic solids, University of Visconsin, CRC press, viewed Jan. 2003, <http://silver.neep.wisc.edu/~lakes /VEnotes.html>.

Lothian, GF 1980, *Optics and its uses*, Van Nostrand Reinhold, New York.

M-System Technology Inc. n.d., Product Bulletin no. 12, Japan, Osaka, viewed Jan. 2003, <http://www.m-system.com/english/service/PB12.pdf>.

MacPherson, WN, Kilpatrick, JM, Barton, JS, Jones, JDC, Chana, KS, Anderson, JS, Jones, TV & Buttsworth, DR 1998, 'Miniature fibre optic pressure sensor for high resolution measurements in turbomachinery applications', European Workshop on Optical Fibre Sensors, Culshaw, B & and Jones, JDC (Eds), *Proceedings of SPIE*, vol. 3483, pp. 200-4.

MacPherson, WN 1999, *Fibre optic sensors for applications in Turbomachinery research*, PhD thesis, Heriot-Watt University, UK.

MacPherson, WN, Kilpatrick, JM, Barton, JS & Jones, JDS 1999, 'Miniature fibre optic pressure sensor for turbomachinery applications', *Rev. Scientific Instr.*, vol. 70, no. 3, pp. 1868-74.

MacPherson, WN, Gander, MJ, Barton, JS, Jones, JDC, Owen, CL, Watson, AJ & Allen, RM 2000 "Blast pressure measurement with a high bandwidth fibre optic pressure sensor," *Meas. Sci. Technology*, vol. 11, pp. 95-102.

Macrossan, MN, Chiu, HH, Mee, DJ 2001, 'A Test facility for hypervelocity rarefied flows', 22nd International Symposium on Rarefied Gas Dynamics, July 2000, Sydney, Australia, *American Institute of Physics Conference Proceedings*, vol. 585, pp. 772-9.

Matweb material property data 2002, Automation Creation Inc. Blacksburg, VA, viewed Jan. 2003, <http://www.matweb.com>.

Mayinger, F & Feldmann, O 2001, *Optical measurements, techniques and applications*, 2nd edn, Springer, Berlin.

MIN Grease products n.d., MID North Petroleum, Australia, Mulgrave, Victoria, viewed Jan. 2003, <http://www.midnorth.com.au/products/nfgrease.html#Jet-Lube %20Kopr-Kote>.

Morgan, RG 1997, 'A Review of the use of expansion tubes for creating superorbital flows', *AIAA Paper 97-0279*, 35th Aerospace Sciences Meeting and Exhibit, Reno, NV.

Moseley, PT & Crocker, AJ 1996, *Sensor materials*, Institute of Physics Publishing Ltd., Bristol.

Mudford, NR, Stalker, RJ, Shields, I 1980, 'Hypersonic nozzles for high enthalpy nonequilbrium flow', *The Aeronautical Quarterly*, vol. 31, pp. 114-31.

Neely, AJ & Morgan, RG 1994, 'The superorbital expansion tube concept, experiment and analysis', *The Aeronautical Journal of the Royal Aeronautical Society*, vol. 98, pp. 97-105.

Neely, AJ 1995, 'Experimental and analytical study of a pilot superorbital expansion tube for aerothermodynamic testing to 13 km/s in air', PhD thesis, University of Queensland.

Owen, FK 1975, 'Comparison of wind tunnel transition and free stream disturbance measurements', *AIAA Journal*, vol. 13, 266-9.

Pal, BP 1992, *Fundamentals of fibre optics in telecommunication and sensor systems*, Wiley eastern limited, New Delhi.

Pedrotti, FL & Pedrotti, LS 1987, *Introduction to optics*, Prentice-Hall, New Jersey.

Pitotech Co. Ltd. 2002, 'What is Pressure Sensitive Paint?', Taiwan, Chang Hua, viewed Jan. 2003, <http://www.pitotech.com.tw/k4h61.htm>.

Pownall, T (trans.) 1993, *Sensors, principles & applications*, Prentice Hall International Ltd, UK.

Richard, C 2000, 'On the identification and haptic display of friction', PhD thesis, Stanford university, USA.

Richardson, DE & Crook, RA 1998, 'Time-dependent nature of adhesive EA946', Associated Business publications International, USA, viewed Jan. 2003, <http: //www.nasatech.com/Briefs/Dec98/MFS31161.html>.

Schairer, ET 2002, 'Optimum thickness of pressure sensitive paint for unsteady measurements', *AIAA Journal*, vol. 40, no. 11, Nov., pp. 2312-18.

Schultz, DL & Jones, TV 1973, 'Heat-transfer Measurement in Short-duration Hypersonic Facilities', *North Atlantic treaty organization*, AGARDograph , no. 165.

Sharifian, SA, Buttsworth, DR 2000, 'Deflection of a Pretensioned circular diaphragm due to Aerothermal loading', *EMAC 2000 Proceedings*, Engineering Mathematics and Applications Conference, RMIT, Melbourne, pp 247-50.

Sharp company c. 1990, Laser diode user's manual.

Shigley, EJ 1986, *Mechanical engineering design*, McGraw-Hill, 1st metric edn, New York.

Stark, B. n.d., 'Material properties', Jet propulsion Laboratory, USA, Passadena, California, viewed Jan. 2003, <http://nppp.jpl.nasa.gov/docs/JPL%20PUB%2099-1D.pdf>.

Sterlite optical Technologies, viewed Sep. 2003, <http://www.sterliteoptical.com/sterlitejava/sotl/pmdlite.jsp>.

Stewart, JE 1996, *Optical principles and technology for engineers*, Marcel Dekker, New York.

The engineering toolbox, viewed Jan. 2003, <http://www.engineeringtoolbox.com/Sound/SoundSpeedOfSound.htm>.

Timoshenko, S., Young, D.H. & Weaver, W (Jr.) 1974, *Vibration problems in engineering*, Wiley, New York.

Tongue, BH 2002, *Principles of vibration*, 2nd edn, Oxford University Press, Oxford, pp 171-173.

TPC training systems 1979, *Pressure measurement, application of pressure instrumentation to industrial process*, Technical Publishing Company, IL. USA.

Van Wylen, GJ & Sontag, RE 1994, *Fundamentals of classical thermodynamics*, 4th edn, Wiley, New York.

Weik, MH 1997, *Fiber optics standard dictionary*, 3rd edn, Chapman & Hall, New York.

White, FM 1991, *Viscous fluid flow*, 2nd edn, McGraw-Hill, New York.

Young, M 1992, *Optics and lasers*, 4th edn, Springer-Verlag , New York.

Yu, FTS & Yang, X 1997, *Introduction to optical engineering*, Cambridge University Press, Cambridge, UK.

Yu, FTS, Yin, S 2002, *Fiber optic sensors*, Marcel Dekker Inc., New York.

Appendices

Appendix A: Thermal isolation under reflected shock conditions

The measured delay time described in Appendix C is not valid for reflected shock conditions. The sudden surface temperature rise of the thermal isolation layer and the magnitude of the temperature rise within shock tube can influence the delay time. To estimate the delay time under the reflected shock conditions, it is necessary to first identify the heating conditions (convective heat transfer coefficient and driving temperature difference) in the standard test, and then compare this result to that obtained under reflected shock conditions.

Heat transfer in the standard test

There are many books available which recommend heat transfer correlations. According to the configuration of the standard test, which is described in Appendix C, it is reasonable to assume that the sensor and its support have a diameter of 3 mm. The airflow approaching the sensor will form a boundary layer that wraps around the sensor. The fluid particles on the centre line will strike the sensor at the stagnation point, bringing the fluid to a complete stop (Gengel 1998). Boundary layer separation will not occur on the face of the sensor.

Equation (7.48) of White (1991, p. 516), which was actually developed for high-speed plane stagnation flow, can also be applied to incompressible conditions (with the appropriate value of *K*, the normalised velocity gradient at the edge of the stagnation point boundary layer) and axisymmetric conditions (by modifying the coefficient from 0.570 to 0.763). The expression becomes,

$$q_w = 0.570\,\mathrm{Pr}^{-0.6}(\rho_e \mu_e K)^{1/2}\left(\frac{\rho_w \mu_w}{\rho_e \mu_e}\right)^{0.1}(h_e - h_w) \qquad \text{(A.1)}$$

Viscosity, density and Prandtl number are denoted by ν, ρ, Pr and subscripts *e* and *w* indicate external and wall condition, respectively. Enthalpy in the external flow and at the wall which are denoted by h_e and h_w and should not be confused with *h* which represents convection coefficient. The flow parameters on the jet centreline upstream of the sensor are taken as external values, and ambient (room) conditions as the wall values. The hot air jet flow is not compressible and the pressure is assumed

to be atmospheric pressure. In Eq. (A.1), the enthalpy difference is calculated from $h_e - h_w = C_{po}(T_e - T_w)$, where C_{po} is evaluated at an average temperature. By considering the heat transfer relationship, $q_w = h(T_e - T_w)$ in which h is now the heat transfer coefficient, it is found that an expression for the heat transfer coefficient is

$$h = 0.570\,\mathrm{Pr}^{-0.6}(\rho_e \mu_e K)^{1/2}\left(\frac{\rho_w \mu_w}{\rho_e \mu_e}\right)^{0.1} C_{po} \tag{A.2}$$

According to Eq. (7.50c) of White (1991), the velocity gradient of a flat-nosed cylinder in an incompressible flow can be estimated using,

$$\frac{K.D}{V_\infty} = \frac{\pi}{2} \tag{A.3}$$

The flow velocity in the jet was measured as 2.5 m/s near the sensor and the sensor support diameter was 3 mm. Using these values in Eqs. (A.2) and (A.3), and by assuming the wall temperature of 20^{o}C and external temperature of 70^{o}C (measured in the jet) with appropriate thermal properties of air (e.g., Table A.5 from Holman (1986)), the value of h in the standard test is estimated as

$$h = 120\ \mathrm{W/m^2/K}$$

Bejan (1995) shows the value of h is constant in the area very close to the stagnation point, but increases as the outer radius of the body is approached. The lowest value for h (nearly 120 W/m^2/K) will be considered, as this value will lead to a conservative estimate for the thermal delay time.

For the situation in which transient heat conduction is coupled with a convective boundary condition at the surface of the solid, Holman (1986) presents the equation,

$$\frac{T - T_i}{T_\infty - T_i} = 1 - erf(X) - \left[\exp\left(\frac{hx}{k} + \frac{h^2 \alpha \tau}{k^2}\right)\right] \times \left[1 - erf\left(X + \frac{h\sqrt{\alpha \tau}}{k}\right)\right] \tag{A.4}$$

where $X = x/(2\sqrt{\alpha \tau})$

and the new symbols have the following meaning:

k thermal conductivity (W/m/K)

T temperature (K)

T_i initial temperature of solid (K)

T_∞ temperature of convective fluid (K)

x distance from surface (m)

α thermal diffusivity (m^2/s)

τ time (s)

It should be noted that in Eq. (A.4) only the thickness of the isolation layer was considered. The thickness of the diaphragm was ignored. The effect of the diaphragm thickness for a thin diaphragm made with a high thermal conductive coefficient is negligible. For example, as discussed in Section 8.8.3.5, the time at which a copper diaphragm with thickness of 9 μm reaches a uniform temperature on both sides (to within 0.01°C) is less than 1 μs.

Figure A.1 shows the results from Eq. (A.4) for three different convection coefficients for the conditions of the experiment in Section 8.9.1 (T_i=22.5°C,

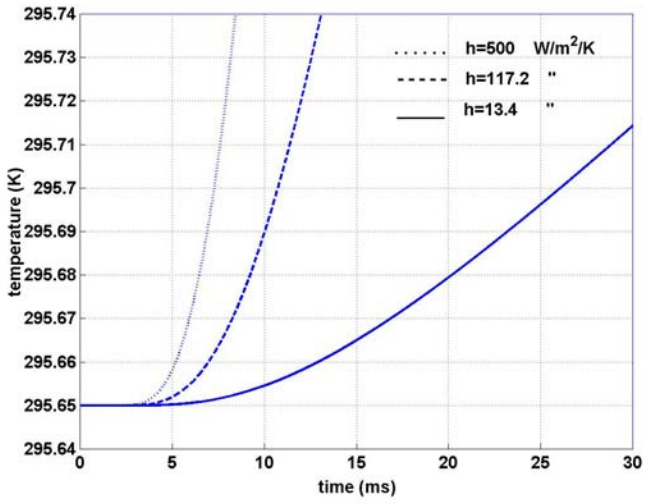

Figure A.1 Effect of convection on the estimated surface temperature rise on a diaphragm covered with a 0.1 mm thick thermal isolation layer (Aerosolve Clear Cote 540).

T_∞ =119.85°C), assuming the thickness of the thermal isolation layer (with properties k= 0.19 W/m/K and α=1.16×10^{-7} m^2/s) is equal to 0.1 mm. Delay time measured in the standard test was about 3.5 ms, as discussed in Appendix C. The actual thermal delay period, which is terminated when the temperature rise produces an effect that is greater than the sensor noise, is strongly dependent on the magnitude of the

convection. For example, the delay time for h equal to 500, 117.2 and 13.4 W/m^2/K, is estimated as 7.3, 10.7 and 26 ms respectively (taking a rise in temperature of 0.05 ^{o}C as the smallest measurable temperature change which creates a recognizable change of voltage greater than noise).

Heat transfer behind reflected shock

In contrast to the convective conditions associated with the standard test, there is (ideally) no movement of the air in contact with the sensor immediately following shock reflection. In the reflected shock situation the initial heat transfer process is perhaps best characterised by transient conduction in both the sensor and the air.

Assuming semi-infinite one dimensional heat conduction, there will be a step in the surface temperature of the thermal isolation layer upon shock reflection, which is given by Buttsworth (2001),

$$\frac{T - T_s}{T_a - T_s} = \frac{TP_a}{TP_a + TP_s} \tag{A.5}$$

Where T is the temperature, TP is the thermal product $(\rho.c.k)^{1/2}$, and ρ, c, k are the density, specific heat and thermal conductivity, respectively. Subscript a indicates air (at reflected shock conditions) and s indicates the substrate. Applying Eq. (A.5) to the conditions of experiment 2 where a spray is used as thermal isolation layer, and assuming properties of polyurethane are close to those of the Aerosolve Clear Cote 540 spray (ρ=1090 kg/m^3, c =1500 J/kg/K , k= 0.19 W/m/K and α=1.16 x 10^{-7} m^2/s , Matweb (n.d.)), the temperature rise at the surface of the thermal isolation becomes ΔT=1.47^{o}C .

The one dimensional transient heat conduction equation,

$$\frac{\partial^2 T}{\partial x^2} = \frac{1}{\alpha}\frac{\partial T}{\partial \tau} \tag{A.6}$$

can be solved in order to estimate the delay time associated with a temperature change of 0.05^{o}C at a depth of 0.1 mm due to a surface temperature step of 1.47^{o}C. When this equation is solved for semi infinite conditions (Holman 1986) with the substrate composed entirely of the Aerosolve Clear Cote 540 spray (properties estimated above), the estimated delay time is 0.3 ms. This temperature rise is gradual but it can affect the sensor due to their high thermal sensitivity. (see Section 6.4.3)

The exact properties of the grease, Kopr Kote, could not be identified. Properties of unused oil presented by Bejan (1995) have been adopted as representative values: ρ, c_p , k and α are taken as 884 kg/m^3, 1910 J/kg/K, 0.144 W/m/K and 8.53×10^{-8} m^2/s.

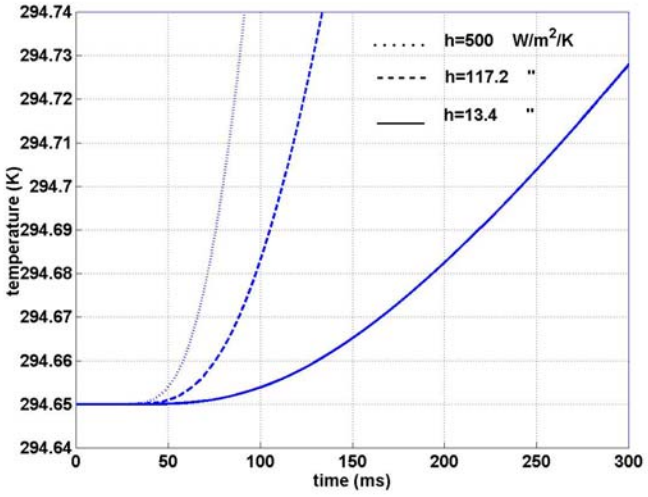

Figure A.2 Effect of convection on the estimated surface temperature rise on the diaphragm covered with a 0.3 mm thick thermal isolation layer (grease Kopr Kote).

Using the approach adopted with the spray thermal isolation layer, a delay time associated with the grease layer (thickness of 0.3 mm) under reflected shock conditions can be calculated for the experiment of Section 8.9.2, Fig. 8.20b (T_i=21.5^{o}C, T_∞ =64.85^{o}C). From Eq. (A.5), the surface temperature change at shock reflection is estimated as ΔT= 0.57 K, and according to Eq. (A.6), the delay time for a 0.05 K change of temperature at a depth of 0.3mm is 92 *ms*.

The reflected shock gas in contact with the sensor will not remain stationary for this length of time because of multi dimensional effects. To determine if natural or forced convection effects at the shock tube end wall could affect the delay time, a range of results for different heat transfer coefficients are presented in Fig. A.2. As shown in Fig. A.2, the temperature does not increase during the shock experiment due to the convection in the shock tube. For example, to increase temperature by 0.05^{o}C, a heating time of 240 ms is required.

Appendix B: Response of a viscous damping system to a step force

A sudden change of pressure at the sensor during shock reflection vibrates the sensor diaphragm. The vibration of the diaphragm can be modelled as shown in Fig. B.1. The step input of force occurs at the time t_0 and the response (displacement) begins at zero, grows to a maximum, and then dies down as it oscillates about f_0/k.

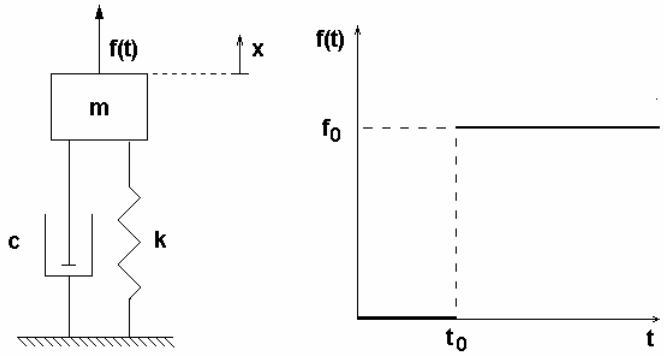

Figure B.1 Configuration of a viscous damping system and a step force.

According to example 3.2 of Tongue (2002), for a system shown in Fig. B.1, if the excitation is a step input force, the response can be calculated from Eq. (B.1),

$$x(t) = \frac{f_0}{k}(1 - e^{-\xi \omega_n t}\cos(\omega_d t)) - \frac{\xi\, f_0}{k\sqrt{1-\xi^2}} e^{-\xi \omega_n t}\sin(\omega_d t) \qquad \text{(B.1)}$$

where,

c linear damping coefficient

f_0 step input force

k spring constant

m mass

t time

ω_d damped natural frequency, $\omega_d = \omega_n\sqrt{1-\xi^2}$

ω_n natural frequency

ξ damping ratio, $c/(2m\omega_n)$

Within the shock tube, the input is a pressure step and the output is the diaphragm movement, which is registered as a voltage and then interpreted as a pressure using the quasi-static calibration. If the force is applied gradually, the final system response is f_0/k or the static response. Equation B.1 can be rewritten for the pressure sensor problem as,

$$P(t) = P_0(1 - e^{-\xi.\omega_n t}\cos(\omega_d t)) - \frac{\xi.P_0}{\sqrt{1-\xi^2}} e^{-.\xi\omega_n t}\sin(\omega_d t) \qquad \text{(B.2)}$$

Where P_0 is actual applied pressure step and $P(t)$ is the sensor output.

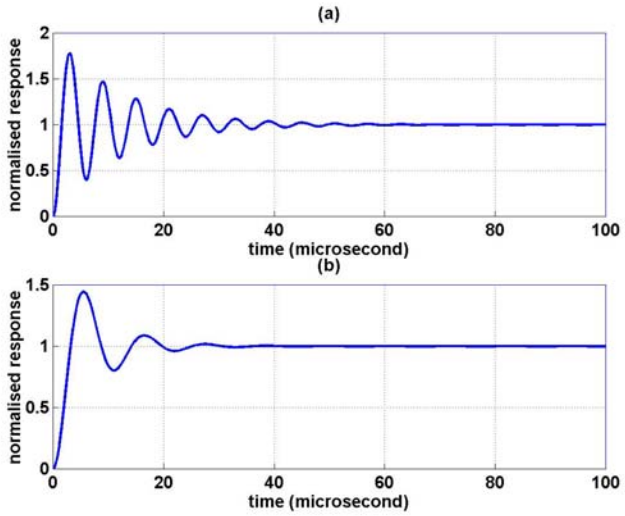

Figure B.2 Response a viscous damping system to a step force: a) damping ratio 0.08; b) damping ratio 0.25.

Equation B.2 is illustrated in Fig. B.2a for conditions of the experiment discussed in Section 8.10.2 (Fig. 8.23a), where the damped natural frequency was 167 kHz. The damping ratio for Fig. B.2a was adjusted to produce ten recognisable fluctuations as was the case in Fig. 8.23a. The 50% overshoot in Fig. 8.23a is not a reliable indication of damping ratio due to the nonlinear relationship between deflection and voltage. The damping ratio chosen for Fig. B.2a was ξ=0.08, and thus the undamped natural frequency is calculated as 168 kHz.

For Fig. 8.23b, where the damped natural frequency is 90 kHz and three recognizable fluctuations were observed (Fig. 8.23b), a damping ratio ξ=0.25 suited the

experimental results. In this case, the undamped natural frequency was calculated as 94 kHz.

Appendix C: Measurement of thermal delay time of fibre optic pressure sensors covered with a thermal isolation layer

Fibre optic pressure sensors constructed with the methods described in Chapter 6 indicated a high temperature sensitivity. This high temperature sensitivity makes it necessary to protect the sensor from the high temperature flow within the shock tube. This can be achieved for a limited time (the delay time) using a thermal isolation layer which ideally does not contribute to diaphragm stiffness but simply delays the arrival of the temperature rise at the diaphragm. Two thermal isolation layers were used in this work: 1) a grease (Kopre Kote); and 2) Aerosolve Clear Cote 540. The grease was easily applied to the sensor and its thickness was measured. Aerosolve was applied as a spray and its thickness could not be measured accurately. In this appendix, an arrangement for the measurement of thermal delay time and the effect of Clear Cote 540 on delay time is discussed.

Experimental arrangement

A 2 kW hot air gun was used as a thermal source. The hot air gun was placed horizontally at a distance of 25 cm from the sensor. The sensor and a K-type thermocouple were also placed close to the centre of the airflow, horizontally aligned with the sensor. A piece of wood was placed between the air gun and the sensor. The thermocouple and the sensor signals were amplified and recorded using the A/D card (Nation Instruments AT-MIO 16E-16). The interrogation system for the fibre optic sensor was the same as that described in Section 8.5.

The hot air gun was switched on and the piece of wood was kept between the gun and the sensor to protect the sensor from the hot air flow. A period of one minute was required to allow the hot air gun to reach its final steady temperature. The piece of wood was then rapidly removed and the change of output voltage from the sensor and the thermocouple were recorded. The vertical movement of the piece of wood appeared to assist the airflow impinge on the sensor and the thermocouple simultaneously, reducing possible errors.

The air speed from the hot air gun in the vicinity of the sensor was 2.5 m/s (measured using a Pitot tube). The temperature rise indicated by the thermocouple rapidly increased to around 55^{o}C. The data were recorded at 10 kSample/s for 12 seconds. A sample of the results obtained from these experiments is presented in Fig. C.1.

A method for the measurement of the thermal isolation layer (Aerosolve Clear cote 540) thickness was not developed. However, to establish a relationship between the spraying period and thermal delay time, a standard spraying method was used. In this method, the spray nozzle was horizontally aligned with the sensor at a distance of 25 cm. The sensor was aligned on the spray centreline to within about ±10 mm.

Results

The sensors were sprayed and their thermal delay times were measured. Figure C.1 shows the results from a sample experiment. Figures C.1a and C.1b show the result for the fibre optic sensor, and Figs. C.1c and C.1d show the thermocouple response from the same experiment. Due to noise in the fibre optic pressure sensor signal, the measurement of delay time is somewhat uncertain. Point 1 in Figure C.1b indicates the time that the thermocouple senses the heat flow and starts to respond. Point 2 indicates the time at which the fibre optic sensor signal rose above the noise floor. The thermal delay time was taken as the difference in time between points 1 and 2.

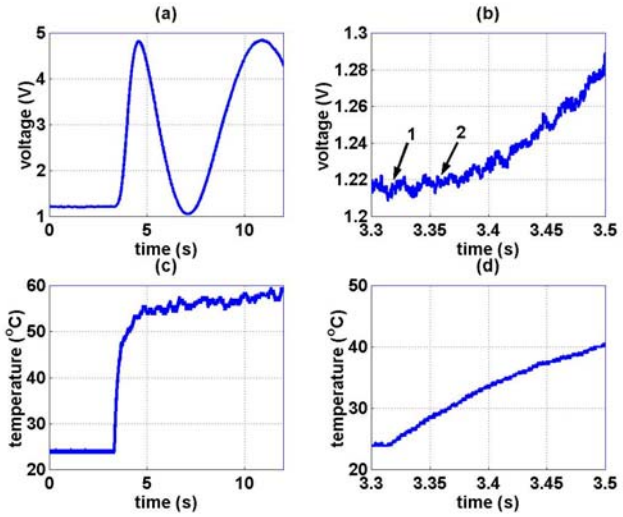

Figure C.1 Measurement of thermal delay time of fibre optic pressure sensor: a,b) fibre optic pressure sensor response; c,d) thermocouple response.

Different definitions for the delay time are possible and this can influence the results. However, the definition illustrated in Fig. C.1 was applied consistently throughout this work.

The results of the experiments are summarised in Fig. C.2. The result show that even a sensor without a thermal isolation layer has a delay time of a few milliseconds.

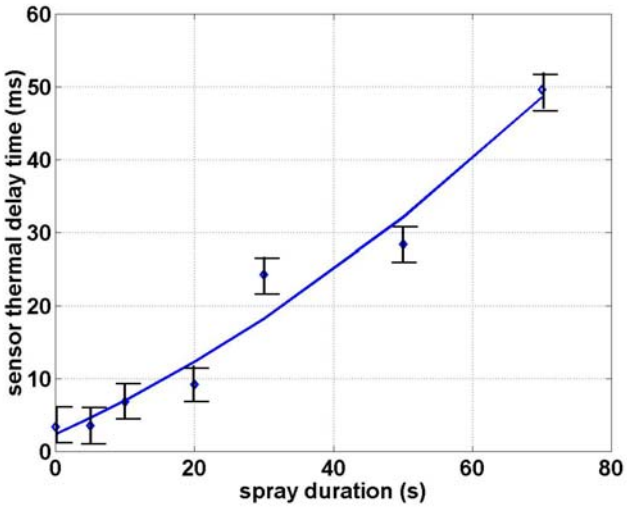

Figure C.2 Fibre optic pressure sensor thermal delay time as a function of spray duration.

Figure C.2 shows that the relationship between spray duration and thermal delay time is approximately linear. It was found that there is a relationship between the sensor shelf time and its thermal delay time. For a newly constructed sensor, the thermal delay time is the shortest (about 0.3 ms), but it can increase up to 5 ms for a one month old sensor.

Appendix D: Effects of diaphragm material on sensor hysteresis

According Di Giovanni (1982, p. 132), tensile stresses (other than those from bending) become significant when the deflection of the diaphragm is more than 10% of its thickness. The wavelength of the interrogation light was about 780 nm, and the minimum diaphragm thickness used was around 12.7 μm. For calibration and analysis convenience, it is desirable that the defection be a fraction of wavelength, around λ/4. Hence tensile stress (or the membrane effect) is not considered, and perfect diaphragm bending theory is assumed.

According to this bending theory (Di Giovanni 1982), radial and tangential stresses within the clamped circular diaphragm can be calculated as,

$$\sigma_r = \pm\frac{3}{8}\frac{pa^2}{h^2}\left[(3+\nu)\frac{r^2}{a^2}-(1+\nu)\right] \tag{5.6}$$

$$\sigma_\theta = \pm\frac{3}{8}\frac{pa^2}{h^2}\left[(3\nu+1)\frac{r^2}{a^2}-(1+\nu)\right] \tag{5.8}$$

and the deflection can be calculated using,

$$y = \frac{3(1-\nu^2)\ p}{16Eh^3}(a^2-r^2)^2 \tag{5.4}$$

where

a radius of diaphragm

E modulus of elasticity

h diaphragm thickness

p pressure difference across diaphragm

r radial distance

y deflection

ν Poisson's ratio

Equations (5.4), (5.6) and (5.8) are valid for thin diaphragms where their thickness is less than 20% of their diameters. Furthermore, the diaphragm deflection should not exceed 30% of its thickness. Other limitations are discussed in Section 5.7.

The maximum stresses that occur at the edges ($r=a$), and the maximum deflection that occurs at the centre ($r=0$), are given by,

$$\sigma_{r,\max} = \pm\frac{3}{4}\frac{pa^2}{h^2} \tag{5.7}$$

$$\sigma_{\theta,\max} = \mp\frac{3}{8}\frac{pa^2}{h^2}(1+\nu) \tag{5.9}$$

$$y_0 = \frac{3(1-\nu^2)p}{16Eh^3}a^4 \tag{5.5}$$

The maximum equivalent stress at $r=a$ can be calculated using,

$$\sigma_{eq} = \frac{3}{4}\frac{pa^2}{h^2}\sqrt{1+\nu^2} \tag{D.1}$$

A program was written which calculates the deflection and the maximum equivalent stress for the sensor when the load increases. It calculates E from the results of the tension test, so E is different for increasing and decreasing loads. This program calculated maximum stress in maximum pressure and will change hysteresis diagram to suit it. For example, if there is a 10% greater strain in downward load in half of maximum load in a tension test, it will calculate 10% more strain in half of a new maximum load in the sensor. Furthermore, E in return, is variable and is equal to tangent of stress-strain curve.

It is known that when the distance between the end face of fibre and the diaphragm changes, the power at the signal detector will be modulated due to interferometry. This relationship approximately sinusoidal (see Eq. (3.5)) and it is related to $2y_0$ (see Eq. (3.4)). Hence it is assumed that the voltage from the signal detector is related to y_0 according to,

$$V \propto \sin(2y_0) \tag{D.2}$$

The results for copper and aluminium foil, where their strain-stress curves were presented in Fig. 7.1, are shown in Fig. 7.2. According to the results, the material

hysteresis has a major contribution to the fibre optic pressure sensor hysteresis (see Table 7.1).

Appendix E: Effects of adhesive on sensor hysteresis

Deflection of the adhesive (which bonds the diaphragm to the substrate) contributes to the diaphragm deflection. In similarity with other materials, the deflection characteristics of adhesives can be different for increasing and decreasing load. The contribution of the adhesive hysteresis to the overall sensor hysteresis is estimated in this appendix for two bonding arrangements, and two kinds of diaphragm deflection as illustrated in Fig. 7.3.

Edge supported diaphragm

The deflection of the adhesive which forms the bonding layer is affected by radial stress σ_r and not tangential stress σ_θ for a symmetrical diaphragm and bonding layer. The radial stress for a clamped diaphragm can be calculated using,

$$\sigma_r = \pm\frac{3}{8}\frac{pR_i^{\,2}}{h^2}\left[(3+\nu)\frac{r^2}{R_i^{\,2}} - (1+\nu)\right] \tag{5.6}$$

where the $\pm$ indicates the tension and compression side of the diaphragm respectively. The maximum radial stress occurs at the edges ($r=R_i$),

$$\sigma_{r,\max} = \pm\frac{3}{4}\frac{pR_i^{\,2}}{h^2} \tag{5.7}$$

For the definition of the symbols used in the above equations, see Fig. E.1 and the nomenclature section at the end of this appendix.

The radial stress for a clamped diaphragm is zero at the centre-thickness plane of the diaphragm and it increases proportionally with distance from this plane. The radial stress at edges of diaphragm causes shear stresses within the bonding layer. Since the fully clamped edge equations are being used to model the edge supported diaphragm, it is consistent to assume that the adhesive provides symmetrical resistance to diaphragm deflection on the upper and lower sides of the diaphragm for $r>R_i$. Therefore, the radial force that must be supported by in bonding layer between diaphragm and substrate will be,

$$F_r = \sigma_{r\max} * h/2 * 1/2 * 2\pi\, R_i \tag{E.1}$$

and this force will attempt to push the adhesive layer away from the centre of the diaphragm (for a pressure acting downwards on the diaphragm). A force with equal magnitude but opposite direction will be acting on the adhesive bonding layer on the upper surface of the diaphragm.

As the adhesive layer has a modulus of elasticity that is much smaller than the modulus of the diaphragm (e.g., the modulus of Araldite is less than 5% of the modulus of copper) it is reasonable to assume a uniform shear stress distribution across the bonding layer. The shear stress can therefore be calculated from,

$$\tau = \frac{F_r}{\pi(R_o^{\,2} - R_i^{\,2})} \tag{E.2}$$

The shear stress calculated using Eq. (E.2) causes a shear strain within the adhesive (uniform throughout its thickness) which can be calculated using,

$$\gamma = \frac{\tau}{G} \tag{E.3}$$

The radial deflection around the edge of the diaphragm on the upper and lower surfaces can be calculated using $t_g \times \gamma$.

No edge support diaphragm

For a diaphragm with no edge support, the radial stress can be calculated using the simply supported diaphragm model which gives,

$$\sigma_r = \frac{3}{8}\frac{pR_i^{\,2}}{h^2}\left[(3+\nu)\left(1-\frac{r^2}{R_i^{\,2}}\right)\right] \tag{5.14}$$

However, at the edges ($r=R_i$) the radial stress is zero. Hence a different approach to that adopted with the edge supported diaphragm is required.

In contrast with the clamped edge diaphragm where the membrane stresses were negligible in comparison with stress caused by bending (see Section 5.11), for a simply supported diaphragm, the membrane radial stress at the edge are the only radial stresses and these can be calculated using (Di Giovanni 1982),

$$\sigma_r = \left(\frac{3-\nu}{1-\nu}\frac{EH^2}{4R_i^{\,2}}\right) \tag{E.4}$$

For the case of a diaphragm with no edge support, the tension stress caused by membrane effect is uniform around the edge and can be calculated from,

$$F_r = 2\pi R_i h \sigma_r \tag{E.5}$$

Shear stress and bonding layer deflection can now be calculated using a similar to that adopted with the clamped diaphragm.

Computer program

A computer program was written to calculate the bonding layer deformation and its contribution to sensor hysteresis. Two different values of shear modulus *G* for increasing and decreasing loads were specified inputs for the program and in each case the adhesive deflection was calculated from equations presented in this appendix.

If the inner diameter of diaphragm is greater than the cavity diameter, the diaphragm can contact the substrate during deflection and this will change the effective diameter of diaphragm. This process can alter the deflection and stress induced in the bonding layer.

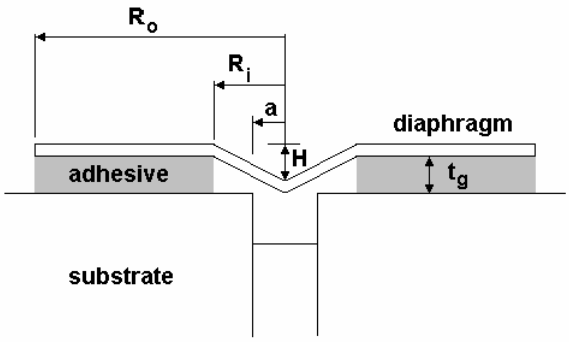

Fig. E.1 Deflection of diaphragm under load and bonding layer.

To estimate this effect (see Fig. E.1), it is first recognised that contact can only occur if,

$$\frac{H_0}{R_{i0}} \geq \frac{T_g}{R_{i0} - a} \tag{E.6}$$

If the inequality of (E.6) is satisfied, it is still possible that the contact does not occur due to the lack of sufficient adhesive deflection. The program again considers the

effect of adhesive deflection on *H* and a new internal diameter and its possible effect on the geometry is determined. The new internal diaphragm diameter and deflection can be calculated (assuming the length of diaphragm does not change due to contact) from,

$$L_0 = \sqrt{R_{i0}{}^2 + H^2} \tag{E.7}$$

$$R_i = R_{i0} - \gamma T_g \tag{E.8}$$

$$H = \sqrt{L_0{}^2 - R_i{}^2} \tag{E.9}$$

and the inequality of (E.6) becomes,

$$\frac{H}{R_i} > \frac{T_g}{R_i - \gamma T_g} \tag{E.10}$$

where the subscripts 0 designates the initial approximation.

If the inequality of Eq. (E.10) is now satisfied, then contact occurs and the new *H* can be calculated using,

$$L_1 = \sqrt{T_g{}^2 + (R_i - a - \gamma T_g)^2} \tag{E.11}$$

$$L_2 = L_0 - L_1 \tag{E.12}$$

$$H = T_g + \sqrt{L_2{}^2 - a^2} \tag{E.13}$$

The program was executed for a copper foil (thickness 12.7 μm) and Araldite 2016 with a thickness of 5 μm. The estimated shear modulus values were *G*=230 MPa and *G*= 177 MPa for increasing and decreasing loads respectively. The results for edge supported diaphragms and those with no edge support at different pressures were presented in Fig. 7.4. According to the results, edge supported diaphragms have a greater contribution to the sensor hysteresis than those with no edge support. The contribution of adhesive hysteresis to overall sensor hysteresis increases at higher pressures but its relative magnitude decreases. It should be noted that the effect of adhesive hysteresis proportionally increases for higher thickness of the adhesive layer.

The actual diaphragm is neither a clamped edge or a simply supported configuration. Nevertheless, bonding only one side of the diaphragm to the substrate means the

support conditions will more closely approximate those of no edge support which appears attractive for the minimisation of hysteresis effects.

Nomenclature

E	modulus of elasticity
F_r	radial force
G	shear modulus
h	diaphragm thickness
H	diaphragm deflection at centre
L	half diaphragm length
p	pressure
r	distance from diaphragm centre
R_i	internal radius of bonding layer
R_o	external radius of bonding layer
T_g	bonding layer thickness
γ	shear strain
ν	Poisson's ratio
σ_r	radial stress
$\sigma_{r,\,max}$	maximum radial stress
τ	shear stress

Appendix F: Change of air temperature within the calibration tube

Air within the calibration tube experiences changes of temperature due to the change of pressure. This affects the accuracy of the pressure sensitivity calibration because unfortunately the sensor will also have some temperature sensitivity. The approximate calculation presented in this appendix establishes a relationship between the calibration period and the anticipated change of temperature within the tube.

The first law of thermodynamics for a uniform state uniform flow (USUF) process with one entrance, where the change of kinetic and potential energy is negligible, can be written as (Van Wylen & Sontag 1994, Eq. (5.54)),

$$Q + m_i h_i = m_2 u_2 - m_1 u_1 \tag{F.1}$$

Heat transfer, mass, specific enthalpy, and specific internal energy are designated as *Q*, *m*, *h* and *u* respectively. Subscripts *1*, *2*, and *i* indicate the initial, final and entrance conditions respectively.

The conservation of mass law for one entrance can be written as,

$$m_i = m_2 - m_1 \tag{F.2}$$

The definition of enthalpy gives,

and

$$\begin{aligned} u_2 &= h_2 - p_2 v_2 \\ u_1 &= h_1 - p_1 v_1 \end{aligned} \tag{F.3}$$

The combination of Eqs. (F.1), (F.2), and (F.3) yields,

$$Q + m_2 (h_i - h_2 + P_2 v_2) = m_1 (h_i - h_1 + P_1 v_1) \tag{F.4}$$

From the definition of specific volume,

$$m = V / v \tag{F.5}$$

where *V* is volume of the calibration tube. Air is assumed to be an ideal gas, and therefore,

$$\Delta h = C_{po} \Delta T \tag{F.6}$$

$$v = \frac{R.T}{P} \tag{F.7}$$

Pressure, temperature, specific gas constant and the specific heat at constant pressure are denoted by P, T, R, and C_{po} respectively.

Applying Eqs. (F.5), (F.6), and (F.7) in Eq. (F.4) yields,

$$T_2 = \frac{T_i}{1 + \frac{R}{P_2 C_{po}} \left[\frac{C_{po}}{v_1} (T_i - T_1) + P_1 - P_2 - Q/V \right]} \tag{F.8}$$

The overall heat transfer rate for a hollow cylinder in a convection environment on its inner and outer surface, can be expressed by (Holman 1986, Eq. (2.14)),

$$\dot{Q} = \frac{T_2 - T_0}{\frac{1}{\hbar_i A_i} + \frac{\ln(r_o / r_i)}{2\pi K L} + \frac{1}{\hbar_o A_o}} \tag{F.9}$$

The heat transfer coefficient, tube radius, convection surface area, thermal conductivity of the tube and the tube length are denoted by $\hbar$, r, A, K, and L respectively. Internal and external conditions are designated with i and o subscripts respectively. Temperature within the calibration tube and the air temperature outside of the calibration tube are denoted by T_2 and T_0 respectively.

The free convection coefficient from the horizontal cylinder to the external air at atmospheric pressure can be calculated using (Holman 1986, Table 7.2),

$$\hbar = 1.32(\Delta T / d)^{0.25} \quad \text{if} \quad 10^4 < \mathrm{Pr_f.Gr_f} < 10^9 \tag{F.10}$$

$$\hbar = 1.24(\Delta T)^{1/3} \quad \text{if} \quad \mathrm{Pr_f.Gr_f} > 10^9 \tag{F.11}$$

These equations are for the external surface of cylinders. The heat transfer inside the cylinder may be a combination of free and forced convection especially in a short period calibration. The changing air pressure within the tube also makes it difficult to determine the exact heat transfer coefficient. For simplicity, the heat transfer coefficient inside the tube is also calculated from Eqs. (F.10) and (F.11). The actual heat transfer coefficient on the inside of the tube is larger than this free convection value, so it is expected that the present model will overestimate the temperature change, especially during fast calibrations. Other factors that have not been considered and will lead to further overestimation of the required calibration time are the heat capacity of the tube and the humidity of the air.

The temperature of the air inside the tube during the discharge process can be calculated in a similar manner giving,

$$T_4 = \frac{T_e}{1 + \frac{R}{P_4.C_{po}}\left[\frac{C_{po}}{v_3}(T_e - T_3) + P_3 - P_4 - Q/V\right]} \qquad \text{(F.12)}$$

where subscripts 3 and 4 indicate the conditions at the beginning and at the end of the tube discharge and *e* shows the condition of the exhaust air. In practice, conditions of 3 and 2 are the same because the air is discharged immediately after charging the tube.

A computer program was written to calculate the temperature inside the calibration tube as a function of the calibration period. A small step in pressure was applied and the corresponding temperature inside the tube (T_2 or T_4) was calculated. In the following step, these calculated temperatures were taken as the initial conditions. The results from this modelling are presented in Figs. 7.7 and 7.8, and are also discussed in Section 7.2.4.

Appendix G: Natural frequency of a pretensioned circular diaphragm with clamped edges and thermal isolation layer

The particular type of pressure sensor of interest in this appendix consists of a nominally flat circular diaphragm that is clamped at the edges and is optically-addressed using a single-mode fibre optic cable, as described in Chapter 4. Previous sensor constructions (MacPherson et al. 1999) have not utilised a pretensioned diaphragm and thermal protection layer and have demonstrated a temperature sensitivity that needs to be considered in many applications. Pretensioning of a diaphragm can reduce the possibility of 'snap-through' buckling of the diaphragm and temperature sensitivity, as discussed in Section 5.8. However, the effect of pretensioning and a thermal isolation layer on the natural frequency of the diaphragm has not yet been discussed – it is the subject of this appendix.

Governing equations

Natural frequency of a circular diaphragm clamped at the edges.

The differential equations governing the potential and kinetic energy of an axisymmetric diaphragm clamped at the edges under a symmetrical load are given by (e.g., Timoshenko, Young & Weaver 1974),

$$PE = \pi D \int_0^a \left(\frac{\partial^2 y}{\partial r^2} + \frac{1}{r}\frac{\partial y}{\partial r}\right)^2 r\,dr \tag{G.1}$$

$$KE = \pi \rho h \int_0^a \dot{y}^2\, r\,dr \tag{G.2}$$

where

$$D = \frac{Eh^3}{12(1-\nu^2)} \tag{G.3}$$

In deriving Eqs. (G.1) and (G.2), it is assumed that the diaphragm material is perfectly elastic, homogenous, and isotropic. It is also assumed that the diaphragm has a uniform thickness that is small in comparison to its diameter.

Using the following nondimensional parameters:

$$Y = \frac{y}{a} \ , \ R = \frac{r}{a} \ , \ H = \frac{h}{a} \tag{G.4a,b,c}$$

$$T = \frac{\sigma_T}{\frac{E}{12(1-\nu^2)}} \tag{G.4d}$$

$$P = \frac{p}{\frac{E}{12(1-\nu^2)}} \tag{G.4e}$$

$$T^* = \frac{T}{H^2} \tag{G.4f}$$

$$P^* = \frac{P}{H^3} \tag{G.4g}$$

so that,

$$\frac{dy}{dr} = \frac{dY}{dR} \tag{G.5a}$$

$$\frac{d^2y}{dr^2} = \frac{1}{r_0}\frac{d^2Y}{dR^2} \tag{G.5b}$$

Eqs. (1) and (2) can be rewritten,

$$PE = \pi D \int_0^1 \left(\frac{\partial^2 Y}{\partial R^2} + \frac{1}{R}\frac{\partial Y}{\partial R}\right)^2 R dR \tag{G.6}$$

$$KE = \pi \rho h r_0^{\ 4} \int_0^1 \overset{o}{Y}^2 R dR \tag{G.7}$$

In the case $T^* = 0$, the nondimensional diaphragm deflection is given by Sharifian & Buttsworth (2000),

$$W = \frac{P^*}{64}(1-R^2)^2 \cos \omega t \tag{G.8}$$

Applying Eq. (G.8) in Eqs. (G.6) and (G.7) leads to

$$PE = \frac{\pi D P^{*2}}{384} \cos^2 \omega t \tag{G.9}$$

$$KE = \frac{\pi \rho h r_0^{\ 4} P^{*2}}{40960} \omega^2 \sin^2 \omega t \tag{G.10}$$

The total potential and kinetic energy is constant during vibration so,

$$\frac{d}{dt}(PE + KE) = 0 \tag{G.11}$$

By substituting Eqs. (G.9) and (G.10) into Eq. (G.11), the following expressions for natural frequency are obtained:

$$\omega = \frac{1}{a^2}\sqrt{\frac{320D}{3\rho h}} \tag{G.12}$$

$$f = \frac{10.33}{2\pi a^2}\sqrt{\frac{D}{\rho h}} \tag{G.13}$$

According to Timoshenko, Young & Weaver (1974), if a power series (order 6) is used for *R*, the fundamental diaphragm frequency can be written,

$$f_0 = \frac{10.21}{2\pi a^2}\sqrt{\frac{D}{\rho h}} \tag{G.14}$$

Natural frequency of a pretensioned clamped circular diaphragm.

Equation (G.10) is still valid for the calculation of the kinetic energy but a new equation should be established to calculate the potential energy.

The relation between stresses and deflection has been described as (Donnel 1976),

$$\sigma_r = \frac{f_r}{h} - \frac{12Dz}{h^3}\left(\frac{d^2y}{dr^2} + \frac{\nu}{r}\frac{dy}{dr}\right) \tag{G.15}$$

$$\sigma_\theta = \frac{f_\theta}{h} - \frac{12Dz}{h^3}\left(\frac{1}{r}\frac{dy}{dr} + \nu\frac{d^2y}{dr^2}\right) \tag{G.16}$$

and because of symmetry,

$$\sigma_{r\theta} = 0 \tag{G.17}$$

Assuming then that the diaphragm pretensioning is due to a uniform biaxial load, the radial and tangential forces per unit can be written,

$$f_r = f_\theta = h\sigma_{pt} \tag{G.18}$$

Substituting Eq. (G.18) into Eqs. (G.15) and (G.16) leads to

$$\sigma_r = \sigma_{pt} - \frac{12Dz}{h^3}\left(\frac{d^2y}{dr^2} + \frac{\nu}{r}\frac{dy}{dr}\right) \tag{G.19}$$

$$\sigma_\theta = \sigma_{pt} - \frac{12Dz}{h^3}\left(\frac{1}{r}\frac{dy}{dr} + \nu\frac{d^2y}{dr^2}\right) \tag{G.20}$$

The general relations for strains in cylindrical coordinates are given by (Donnel 1976),

$$\varepsilon_{rr} = \frac{du}{dr} + \frac{1}{2}\left(\frac{dy}{dr}\right)^2 - z\frac{d^2y}{dr^2} \tag{G.21}$$

$$\varepsilon_{\theta\theta} = \frac{u}{r} - \frac{z}{r}\frac{dw}{dr} \tag{G.22}$$

The potential energy may be expressed as (Timoshenko, Young & Weaver 1974),

$$d(PE) = \frac{1}{2}(\sigma_r\varepsilon_{rr} + \sigma_\theta\varepsilon_{\theta\theta})r\,dr\,d\theta\,dz \tag{G.23}$$

due to the symmetry of load, diaphragm shape, and boundary conditions. Because of the small deflection assumption, the amount of radial displacement (u) and its derivative is negligible (Timoshenko, Young & Weaver 1974). Furthermore, $(dy/dr)^2$ is negligible compared with (d^2y/dr^2), so

$$\varepsilon_{rr} = -z\frac{d^2y}{dr^2} \tag{G.24}$$

$$\varepsilon_{\theta\theta} = -\frac{z}{r}\frac{dy}{dr} \tag{G.25}$$

By introducing the above equations and substituting Eqs. (G.19) and (G.20) into Eq. (G.23), the following expression for potential energy can be obtained,

$$PE = \pi D\int_0^a [(\frac{d^2y}{dr^2})^2 + (\frac{1}{r}\frac{dy}{dr})^2 + \frac{2\nu}{r}\frac{dy}{dr}\frac{d^2y}{dr^2}]rdr \tag{G.26}$$

The above equation can be written in nondimensional form with the aid of Eq. (G.5),

$$PE = \pi D\int_0^1 [(\frac{d^2Y}{dR^2})^2 + (\frac{1}{R}\frac{dY}{dR})^2 + \frac{2\nu}{R}\frac{dY}{dR}\frac{d^2Y}{dR^2}]RdR \tag{G.27}$$

The equations for the deflection of a pretensioned circular diaphragm due to uniform loading are presented in (Sharifian & Buttsworth 2000). For a harmonic vibration, the deflection can be multiplied by cos ωt, so

$$Y = V\cos\omega t \tag{G.28}$$

where

$$V = a_0 + a_2R^2 + a_4R^4 + a_4\sum_{n=3}^{\infty} b_nR^{2n} \tag{G.29}$$

$$a_4 = \frac{\frac{P^*}{4}}{16 + T^*(2 + \sum_{n=3}^{\infty} n b_n)} \tag{G.30}$$

$$b_n = T^{*(n-2)} \quad \frac{1}{4^{n-3} n!^2} \tag{G.31}$$

$$a_2 = \frac{16}{T^*} a_4 - \frac{P^*}{4T^*} \tag{G.32}$$

$$a_0 = -a_2 - a_4 - a_4 \sum_{n=3}^{\infty} b_n \tag{G.33}$$

Substituting Eq. (G.28) into Eq. (G.27), gives

$$PE = \phi \cos^2 \omega t \tag{G.34}$$

where

$$\phi = \pi . D \int_0^1 \left(\left(\frac{d^2 V}{dR^2} \right)^2 + \left(\frac{1}{R} \frac{dV}{dR} \right)^2 + \left(\frac{2\nu}{R} \frac{dV}{dR} \frac{d^2 V}{dR^2} \right) \right) R dR \tag{G.35}$$

Kinetic energy can be rewritten by using Eqs. (G.7) and (G.28)

$$KE = \psi \omega^2 \sin^2 \omega t \tag{G.36}$$

where

$$\psi = \pi \ \rho \ a^2 \int_0^1 R V^2 dR \tag{G.37}$$

The sum of potential and kinetic energy during vibration is constant, so using Eqs. (G.34) and (G.36) in Eq. (G.11), the natural frequency can be written as,

$$\omega = \sqrt{\frac{\phi}{\psi}} \tag{G.38}$$

and

$$f = \frac{1}{2\pi} \sqrt{\frac{\phi}{\psi}} \tag{G.39}$$

Defining the normalised frequency as

$$f^* = \frac{f}{f_0} \tag{G.40}$$

where f_0 is the natural frequency for a non-pretensioned diaphragm, which is defined by Eq. (G.14), natural frequency for a pretensioned diaphragm can be written,

$$f^* = \frac{a^2}{10.21}\sqrt{\frac{\phi\,\rho\,h}{D\,\psi}} \tag{G.41}$$

Substituting Eqs. (G.35), (G.37) and (G.39) into Eq. (G.40), yields,

$$f^* = \frac{1}{10.21}\sqrt{\frac{\int_0^1\left(\left(\frac{d^2V}{dR^2}\right)^2+\left(\frac{1}{R}\frac{dV}{dR}\right)^2+\frac{2\nu}{R}\frac{dV}{dR}\frac{d^2V}{dR^2}\right)RdR}{\int_0^1 V^2 RdR}} \tag{G.42}$$

Natural frequency of a clamped circular diaphragm with thermal isolation layer

A thermal isolation layer is used to isolate or protect the sensor from thermal effects when it is operated within transient aerodynamic environment. This layer is made with a soft material such as grease and it is not expected to support any load, so it will not affect potential energy during vibration. Thus, Eq. (G.9) or (G.34) can still be used for the potential energy. However, the isolation layer will alter the kinetic energy because an additional mass will be vibrating with the diaphragm.

In cylindrical coordinates, the mass of an element of diaphragm and thermal protection layer are,

$$dm = 2\pi\ \rho\, h\, r\, dr \tag{G.43}$$

$$dm' = 2\pi\ \rho'\, h'\, r\, dr \tag{G.44}$$

A normalised mass per unit area for the thermal layer can be defined as,

$$M = \frac{\rho' h'}{\rho\, h} \tag{G.45}$$

Using Eqs. (G.43), (G.44), and (G.45) in Eq. (G.7), leads to

$$KE = (1+M)\pi\ \rho\, h\, a^4 \int_0^1 \overset{o}{Y}^2\, RdR \tag{G.46}$$

When this expression is substituted into Eq. (G.11), the equation for the natural frequency of a diaphragm with a thermal isolation layer when there is no pretension,

$$f\ = \frac{10.21}{2\pi a^2}\sqrt{\frac{D}{\rho h(1+M)}} \tag{G.47}$$

The equation for the natural frequency of a diaphragm with pretension and a thermal protection layer can be now obtained by substituting Eqs. (G.46) and (G.34) into Eq. (G.11). Equation (G.40) is used to simplify the resulting expression and the coefficient 10.33 is substituted with 10.21 for consistency with Eq. (G.14) giving,

$$f^* = \frac{1}{10.21}\sqrt{\frac{\int_0^1 [(\frac{d^2V}{dR^2})^2 + (\frac{1}{R}\frac{dV}{dR})^2 + \frac{2\nu}{R}\frac{dV}{dR}\frac{d^2V}{dR^2}]R\,dR}{(1+M)\int_0^1 V^2\,R\,dR}} \qquad \text{(G.48)}$$

By comparing Eqs. (G.47) and (G.48) with Eqs. (G.14) and (G.42) respectively, it is clear that either with or without pretension, the natural frequency is scaled by $(1/(1+M))^{0.5}$ when a thermal isolation layer is used.

Results and discussion

The results presented in Fig. G.1 were obtained using Eq. (G.48) with the series evaluated to n=40 and dR=0.001. It is estimated that numerical results produced in this manner are within 1×10^{-4} % of the exact solution. In Fig. G.1, the first natural frequency (in dimensionless form) is plotted for different values of M as a function of pretensioning. It is clear that the first natural frequency increases with an increase

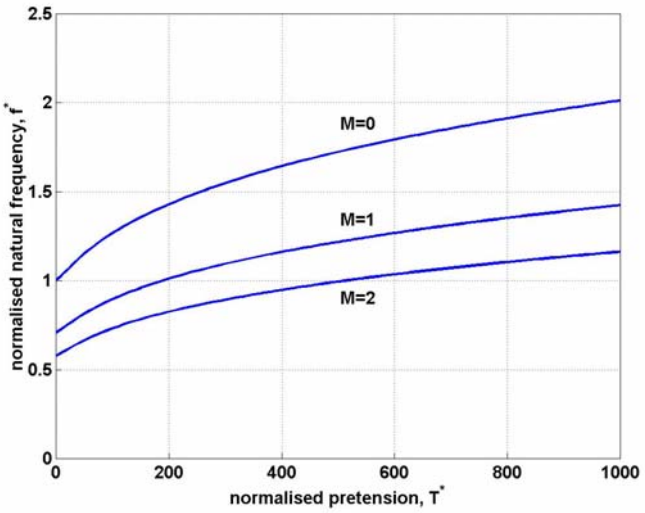

Figure G.1 Effect of pretension and thermal protection layer on the first natural frequency of the diaphragm, ν=0.3.

in pretension and decreases with an increase in thickness and density of the thermal isolation layer.

The maximum value of T^* is 1000, because larger values are unlikely to be realised in practice due to material property limitations. For example, in the case T^*=1000 and H=0.01 (a very thin diaphragm), if it is assumed that ν=0.3 and E≅100 GPa, then $\sigma_{PT} \cong 900$ MPa which would probably be close to, if not beyond, the yield or ultimate strength of the diaphragm material.

Nomenclature

a	diaphragm radius
D	flexural rigidity of diaphragm
E	elastic modulus
f_r	radial force per unit length
f_θ	tangential force per unit length
f	natural frequency
f^*	normalised natural frequency
h	diaphragm thickness
h'	thickness of thermal protection layer
H	normalised thickness
KE	kinetic energy
m	diaphragm mass
m'	thermal protection layer mass
M	normalised mass per unit area for thermal layer, $\rho' h' / \rho h$
p	differential pressure on the diaphragm
P	dimensionless p
P^*	P normalised using H^3
PE	potential energy

r distance from centre of diaphragm

R dimensionless r

t time

u radial displacement

T dimensionless σ_{pt}

T^* T normalised using H^2

V normalised maximum deflection of diaphragm

y deflection of diaphragm

Y normalised y

z distance from middle plane of diaphragm

ε_{rr} radial strain

$\varepsilon_{\theta\theta}$ tangential strain

ν Poisson's ratio

ρ density of diaphragm material

ρ^* normalised density, $\rho'.h' / \rho.h$

σ_{PT} stress due to pretensioning

σ_r radial stress

$\sigma_{r\theta}$ shear stress

σ_θ tangential stress

Appendix H: Measurement of receiver response time

The response time of the receiver depends on the amplification of the electrical circuit and bias voltage. Response time measurements for the two types of receiver used in this work are presented in this appendix.

Details of the two types of receiver used in the work are presented in Appendix K. For the receiver based on the PLD-DSI-500-R20-FC7 photodiode, all the response time data was obtained directly after the transimpedence stage of the in-house constructed amplification circuit.

Both the PLD-DSI-500-R20-FC7 and the PDA55 receivers were irradiated for a period of between 5 μs and 10 μs by an amber LED that was driven with a pulsed current supply (Buttsworth & Ahfock 2003). The measured rise and fall time for the current delivered to the LED was around 0.1 μs regardless of the period of irradiation. The LED response time quoted by the manufacturer is 10 ns, so it is concluded that the light input to the receivers was a square pulse with a rise and fall time around 0.1 μs.

Data were recorded using a digital storage oscilloscope usually set to a sample rate of 1 GSample/s. A sample of the measured data is presented in Fig. H.1. A computer program was written to determine the rise and fall times which are defined as the time for the voltage increases or decreases between the 10% and 90% levels as indicated in Fig. H.1.

The results for the two different receivers at their various gains setting are presented in Table H.1 and H.2. The measured response times for the PDA55 with gain settings of 1 and 2 may be inaccurate because these value are approaching the rise/fall time values for the LED pulsed current circuit.

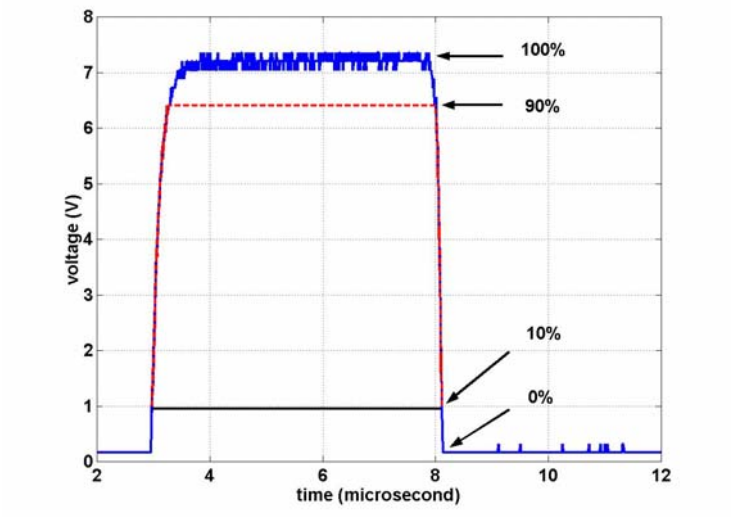

Figure H.1 An example of the receiver response time measurement (PDA55, gain 2).

Table H.1 Response time measurements for PLD-DSI-500-R20-FC7 receiver

Resistance (kΩ)	Rise time (μs)	Fall time (μs)	Response time (μs)
1	0.36	0.13	0.36
10	0.5	0.6	0.6
100	1.2	2	2
1000	7.2	14	14
10000	16	70	70

Table H.2 Response time measurements for PDA55 receiver

Gain No.	Rise time (μs)	Fall time (μs)	Response time (μs)	Rise time (μs)	Fall time (μs)	Response time (μs)
	with 50 Ω termination			with no 50 Ω termination		
1	0.16	0.08	0.16	0.16	0.12	0.16
2	0.25	0.16	0.25	0.16	0.12	0.16
3	0.4	0.4	0.4	0.8	1.0	1
4	1.6	1.8	1.8	1	2.8	2.8
5	3.2	8	8	4	8	8

Appendix I: Modulus of elasticity for copper foil

To measure the modulus of elasticity of a thin foil, tension tests were performed using a H5K-S universal testing machine, supplied by Housfield Ltd (with the load cell 99-999-1026). This testing machine can perform tests in a user defined speed range of 0.001 mm/min to 1000 mm/min. The particular load cell permits a maximum load of up to 2.5 kN. The extensometer has an estimated accuracy of ±0.05% without load, and the load cells have an estimated accuracy of ±0.5% indicated load and the maximum load sampling rate was 200 Hz.

The foil testing standard ASTM E345-93 (American Society for Testing and Materials 1998) and Sample type A with the shape shown in Fig. I.1 were adopted. The results from a sample copper foil are presented in Fig. I.2.

The most important factor to be derived from the foil testing is the modulus of elasticity as this is one of the critical factors in diaphragm design. This modulus of elasticity can vary significantly for different alloys of the same material and even materials with the same composition can have different moduli depending on their production.

Some irregularity due to slippage of the sample within the jaws of the machine is apparent in Fig. I.2 for strains less than about 0.1%. However, this slippage does not compromise the measurement of the modulus of elasticity. From Fig. I.2, the modulus E=40 ±5 GPa was identified for a copper foil. The main source of error in this measurement is related to the sample dimensions which have an estimated uncertainty of ± 0.5 mm.

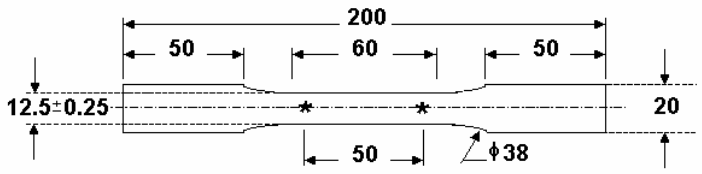

Figure I.1 Sample type A in ASTM standard E345-93, sample length 200 mm and gage length is 50 mm. All dimensions are mm.

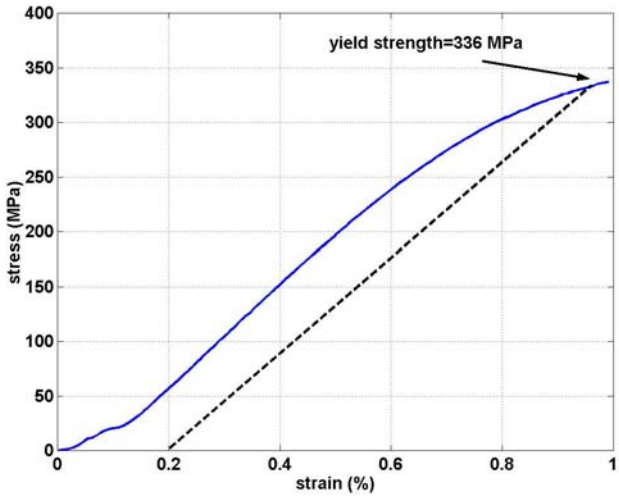

Figure I.2 Experimentally determined stress-strain diagram for a copper foil (9μm thickness).

The yield strength indicated in Fig. I.2 is likely to be a slightly conservative estimate (for the 0.2% strain offset) because of the slippage effect that appears to have occurred at a strain of around 0.1%.

Appendix J: Shock tube equations

This appendix presents the principal equations for one dimensional, inviscid, adiabatic shock flow. The subscripts indicate the regions introduced in Figs. 8.2 and 8.3. All equations are derived from continuity, momentum and energy equations for a calorically perfect gas and do not include heat transfer and viscous effects (Anderson 1990).

$$\frac{P_2}{P_1} = 1 + \frac{2\gamma}{\gamma+1}(M_s{}^2 - 1) \tag{J .1}$$

$$W = a_1\sqrt{\frac{\gamma+1}{2\gamma}(\frac{P_2}{P_1} - 1) + 1} \tag{J.2}$$

$$u_p = \frac{a_1}{\gamma}(\frac{P_2}{P_1} - 1)\left(\frac{\frac{2\gamma}{\gamma+1}}{\frac{P_2}{P_1} + \frac{\gamma-1}{\gamma+1}}\right)^{1/2} \tag{J.3}$$

$$\frac{T_2}{T_1} = \frac{P_2}{P_1}\left(\frac{\frac{\gamma+1}{\gamma-1} + \frac{P_2}{P_1}}{1 + \frac{\gamma+1}{\gamma-1}\frac{P_2}{P_1}}\right) \tag{J.4}$$

$$\frac{\rho_2}{\rho_1} = \frac{1 + \frac{\gamma+1}{\gamma-1}\left(\frac{P_2}{P_1}\right)}{\frac{\gamma+1}{\gamma-1} + \frac{P_2}{P_1}} \tag{J.5}$$

The Mach number for the reflected normal shock wave is defined as $M_R = (W_R + u_p) / a_2$, because it propagates into region 2 and the particle velocity is u_p towards the reflected shock wave which is moving into region 2 with a velocity W_R (in the laboratory frame of reference). The properties associated with the reflected shock can be calculated from the equations,

$$\frac{M_R}{M_R{}^2 - 1} = \frac{M_s}{M_s{}^2 - 1}\sqrt{1 + \frac{2(\gamma-1)}{(\gamma+1)^2}(M_s{}^2 - 1)\left(\gamma + \frac{1}{M_s{}^2}\right)} \tag{J.6}$$

$$P_5 = p_2 + \rho_2(W_R + u_p)^2 - \rho_5 W_R{}^2 \tag{J.7}$$

$$\rho_5 = \rho_2 \frac{(W_R + u_P)}{W_R} \tag{J.8}$$

$$T_5 = T_2 + \frac{(W_R + u_P)^2 - W_R^{\ 2}}{2c_{po}} \tag{J.9}$$

where

a speed of sound

c_{po} specific heat of perfect gas

M_s moving incident normal shock Mach number (W/a_1)

P absolute pressure

T absolute temperature

u_p particle velocity

W absolute velocity of incident normal shock wave

ρ density

γ ratio of specific heats

Appendix K: Details of fibre optic components

Details of the fibre optic components used in this research are presented in this appendix. The data presented here has been extracted from manufacturers catalogues and specification sheets.

Lasers

Five different laser diodes manufactured by Sharp were used. They are single transverse mode lasers and their details are presented in Table K.1

Table K.1 Specifications for laser diodes (Sharp c. 1990)

Parameter	LT025MD0	LT024MD0	LT024MD0	LT026MD0	LT026MD0
T_c (^oC)	25	25	25	25	25
P_o (mW)	30	20	20	3	3
I_{th} (mA)	54.2	42.8	38.3	39.7	41.5
I_{op} (mA)	92.1	68.8	65	48.4	51
η(mW/mA)	0.79	0.77	0.75	0.35	0.32
λ_p (nm)	790	786	789	784	785
I_m (mA)	0.25	0.12	0.12	0.91	1.02
$\theta_{\parallel}$ (degree)	8.1	9.3	9.6	10.5	10.1
$\theta_{\perp}$ (degree)	25.7	27.3	28.1	29.2	32.3
$\Delta\phi_{\parallel}$ (degree)	0.4	0.4	0.5	-0.5	-0.9
$\Delta\phi_{\perp}$ (degree)	1.4	1.5	1.2	2.1	1.8
Manufactured	October 99	May 99	May 99	July 96	July 96

Where the symbols presented in Table K.1 have the following meanings:

I_m monitor current – the current through the photodiode at a specified reverse bias voltage when the laser diode is producing its specified typical power output

I_{op} operating current

I_{th} threshold current

P_0 optical power output

T_c case temperature

$\Delta\phi_{\parallel}$ the deviation of the optical axis of the beam from mechanical axis of the package, parallel to the junction plane

$\Delta\phi_{\perp}$ the deviation of the optical axis of the beam from mechanical axis of the package, perpendicular to the junction plane

η differential efficiency- the ratio of optical power change to change in forward current

λ_p the wavelength of light emitted by the laser diode

$\theta_{\parallel}$ full radiation angle at the half maximum intensity points parallel to the junction plane

$\theta_{\perp}$ full radiation angle at the half maximum intensity points perpendicular to the junction plane

Launch system and Lenses

Launching light into a single mode fibre optic requires a system with high precision. The selected launch system was KT112 from Throlabs Inc. This system provided two locations for the collimating and focusing lenses. It also provided relative movement of the focused light from the laser and the optical fibre in the 3 axis directions.

An aspheric lens C230TM-B *f*=4.5 mm AR coated 600-1050 nm from Lastek Ltd was used to collimate the output light from the laser. This lens was installed in the launch system. The focusing lens used was a C220TM-B AR coated 600-1050 nm and *f*=11 mm from the same company. These lenses were placed into the collimation tube LT230P-B, which is also from Lastek Ltd.

Optical isolator

An optical isolator IO-D-785 from OFR Inc was used. The details of the isolator are presented in Table K.2.

Table K.2 Details of optical isolator

Parameter	Value
Wavelength range (nm)	760-810
Aperture (mm)	1.75
Use/tune between (nm)	±2
Rotation @ 782 nm	42^o
Faraday rotator transmittance	0.52
Input polarizer transmittance	0.965
Output polarizer transmittance	0.965
Total forward transmittance	0.45
Isolation (dB)	-41.3
Maximum optical power (mW)	80

Optical fibre

Single mode SMC-AO780B was used and its details are presented in Table K.3.

Table K.3 Details of optical fibre SMC-AO780B

Parameter	Value
Operating wavelength	780 nm
Core diameter	4.9 μm
Mode field diameter@ 780 nm	5.4 ± 1 μm
Cladding Diameter	125 ± 2 μm
Fibre Diameter	245±15 μm
Core/clad concentricity	≤1 μm
Clad concentricity	≤2 μm
Refractive index of primary coating	1.54
Refractive index of secondary coating	1.53
NA	0.11±0.02
Cut-Off wavelength	730±60 nm
Attenuation @780 nm	≤4 dB/km

Coupler

A bi-directional 2×2 coupler from Sifam Fibre Optic Inc was purchased. Although the coupling output was nominally 50-50, there differences in the power delivered to

each leg at the 780 nm wavelength. This coupler was made with a single mode fibre optic SMC-AO780B (manufactured by Lucent) and its details are presented in Table K.4.

Table K.4 Details of the coupler

Parameter	Value
Operating wavelength (nm)	780
Core diameter (μm)	4.9
Mode field Diameter (μm)	5.4±1
Cladding Diameter (μm)	125±2
Buffer Diameter (μm)	245±15
Cut-off wavelength (μm)	730±60
NA	0.11±0.02
Attenuation at Operating wavelength (dB/km)	≤ 4
Refractive Index of Primary Coating	1.54
Refractive Index of Secondary Coating	1.53
Core/clad concentricity (μm)	≤ 1
Clad Concentricity (μm)	≤ 2

Splice

The temporary splices used in this work were ULTRAsplice supplied through Thorlabs Inc. This splice includes a capillary tube and is especially designed for single mode optical fibre (yellow body). They were already loaded with index matching gel and they can be used approximately four times without recharging the index matching gel. The index matching gel was purchased to fill the capillary tube so that it can be used for more than four times.

Receivers

Five silicon PIN photodiodes, PLD-DSI-500-R20-FC7 with in-house constructed transimpededence amplifier circuits were used in the research. The PIN photodiodes were supplied by PL-LD Inc and their details are presented in Table K.5. The transimpedence amplification circuits include selectable feedback resistors (1, 10, 100, 1000, and 10000 kΩ), which give five different gains. Furthermore, the in-house

constructed amplifier circuit included two optional ×10 gain stages (giving a total of 15 different gain settings).

Table K.5 Details of photodiodes PLD-DSI-500-R20-FC7

Parameter	Value
Active Diameter (μm)	500
Responsivity (A/W) @ 780 nm	0.5-0.52
Capacitance (pF) @ -10 V	2
Response Range (nm)	400-1000
Dark Current (nA) @ -10 V	0.06-1.0
Response Time (ns)@ -10 V	1.0-2.0
Capacitance (pF)@ -10 V	2.0
NEP ($W/Hz^{0.5}$)@ -10 V	$8.5x10^{-15}$
Minimum Breakdown Voltage (V)@ 10μA	40

Two other PIN photodiodes packed as the detector PDA55 supplied by Thorlabs Inc were also used and their details are presented in Table K.6.

Table K.6 Details of detector PDA55

Parameter	Value
Active area (mm×mm)	3.6×3.6
Response range (nm)	320-1100
Peak response (A/W) @ 960 nm	0.6
Responsivity (A/W) @ 780nm	0.52
Bandwidth	DC to 10 MHz
Output impedance (50Ω)	0 to 5 V
Output impedance	0 to 10 V
Gain steps (dB)	0,10,20,30,40

The detectors have 5 different gains and the performance at each setting is in Table K.7.

Table K.7 Details of detector PDA55 at the different gain setting

Parameter	Value				
	Gain 1	Gain 2	Gain 3	Gain 4	Gain 5
Gain (dB)	0	10	20	30	40
NEP ($W/Hz^{0.5}$) @ 960 nm	1×10^{-11}	8×10^{-12}	5×10^{-12}	5×10^{-12}	4×10^{-12}
Transimp. gain(V/A)	1.5×10^{4}	4.7×10^{4}	1.5×10^{5}	4.7×10^{5}	1.5×10^{6}
Transimp. gain with 50 Ω (V/A)	0.75×10^{4}	2.35×10^{4}	0.75×10^{5}	2.35×10^{5}	0.75×10^{6}
Bandwidth (MHz)	10	2.3	0.700	0.170	0.060
Maximum rms noise (mV)	0.44	0.40	0.46	0.60	1.0
Offset (mV)	15	15	20	50	100

Cleaver

A high precision fiber cleaver from Fujikura (model CT-07) was used. It has two fibre guides within the same adapter plate. The first guide can hold fibres with a coating diameter of 900 μm and cleaves an uncoated length between 10 mm and 20 mm. The second guide is for a coating diameter of 250 μm and cleaves an uncoated length between 6 mm and 20 mm.

Appendix L: Discharge time constant for piezoelectric pressure transducer

Piezoelectric pressure transducers cannot be used to measure static pressure because their output reduces over time as the charge decays. In measurements presented in Chapter 8, the maximum duration of the experiments was 120 ms. Therefore, it is necessary to confirm the discharge time constant (DTC) for the piezoelectric pressure transducer did not affect the results. That is, the DTC for the transducer should be much longer than 120 ms (see Section 8.6).

According to the manufacturer (PCB), the DTC for this particular piezoelectric transducer should be greater than 1 s, however, the coupling circuit and thermal isolation layer used on the diaphragm (see Section 8.6) can affect the DTC, and therefore it should be measured.

The piezoelectric pressure transducer and associated end plate was placed on the end of the calibration in the place of the fibre optic pressure sensor end plate tube (see Figs. 6.8, 6.9 and 8.4). The air pressure within the tank was increased to 600 kPa gauge while the valve V3 was closed (see Fig. 6.9). After about 10 minutes, when the air temperature reached room temperature, the valve V3 was opened and the pressure inside the calibration tube increased suddenly. A K-type thermocouple was also

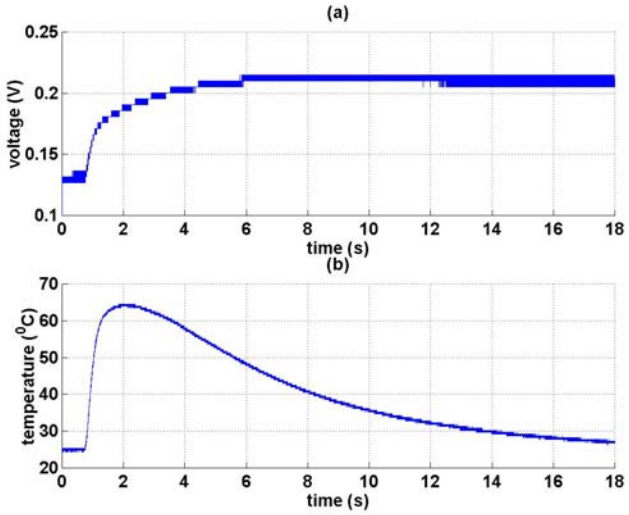

Figure L.1 Identification of discharge time constant of a piezoelectric pressure transducer: a) piezoelectric output; b) thermocouple output.

placed inside the tube to measure the air temperature. The piezoelectric pressure transducer and the thermocouple outputs were recorded with an A/D card (National Instruments AT-MTO 16E-10) and a computer. The results are presented in Fig. L.1.

Figure L.1a shows the output of the piezoelectric pressure transducer. The piezoelectric output increased rapidly over a period of about 1 s after which a slower rise in apparent pressure occurred. This slower rate of increase is believed to be as a result of heat transfer from the hot air within the calibration tube to the transducer. The air temperature increased by about 40^{o}C as shown in Fig. L.1b and dropped due to the heat transfer.

Although precise interpretation of the results is complicated by the probable contribution of temperature effects, the results show that the piezoelectric transducer output does not decrease for about 12 s following the pressure increase. As the data was recorded in the reflected shock experiments for a maximum duration of only 120 ms following shock reflection (Chapter 8), it can be concluded that the piezoelectric transducer output was not affected by discharge time constant.

Appendix M: Discretisation effects in the L1d simulations

The length of the cells used in the L1d simulation can affect the results. The effects of discretisation of the numerical solution are discussed in this appendix.

As described in Section 8.7.3, the best simulations results were obtained by modelling the filling system with a 6 m air filling tube and treating the transition between the filling tube and the driver section as occurring over a 0.01 m length. To improve the initial development of the flow into the driven section when the diaphragm bursts, the driver section was divided into two regions. The last 0.5 m of the driver region (closest to the bursting diaphragm), was a higher resolution region.

Table M.1 The length of cells (in mm) in coarse, medium and fine resolution simulations.

	Region				
Resolution	air filling tube	Diameter transition	Driver	Last 0.5 m of the driver	Driven
Coarse	300	10	38.5	10	43.7
Medium	150	2	19.2	5	21.9
Fine	75	1	9.6	2.5	10.9

The program was executed using three different resolutions producing coarse, medium and fine simulations. The initial lengths of cells in each simulation are presented in Table M.1, and some selected results for the three simulations are shown in Fig. M.1. The initial pressures and temperatures for these simulation were: 1) driver section: 343.9 kPa and 295.65 K; and 2) driven section: 93.9 kPa and 295.65 K.

The pressure results from the 3 levels of discretisation are in agreement and do not show any significant difference in the level of mean pressure produced by the various wave effects. The main difference between the simulations is in the sharpness of pressure changes.

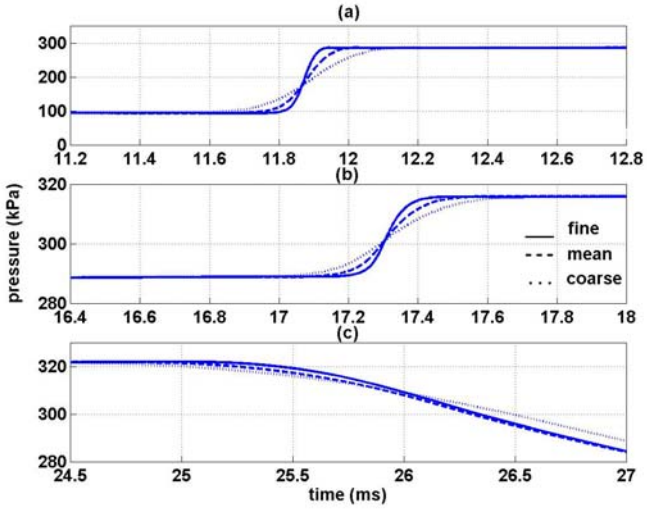

Figure M.1 The effects of segments length on simulation: a) during first reflected shock; b) during pressure rise caused by interaction between the reflected normal shock and the interface; and c) during expansion waves reflection.

Figure M.1a shows the pressure jump for the first reflected shock at the end plate of the shock tube. The pressure rise occurs over a period of about 0.5, 0.3 and 0.1 ms for coarse, medium and fine simulations respectively. The same results can be observed for Figs. M.1b which presents the change of pressure caused by the interaction between the reflected normal shock and the interface (the tailoring wave). The duration of the tailoring wave pressure rise was 0.5, 0.4 and 0.3 ms for the coarse, medium and fine simulations respectively. Fig. M.1c presents the results during the arrival of the reflected of the expansion waves.

The simulations presented in Chapter 8 were generally obtained using initial cell sizes close to that of the coarse simulation presented in this appendix. The exception is the results presented in Figs. 8.22 for which an initial cell length in the driven region of 2.5 mm was used in order to increase the sharpness of the simulated reflected shock pressure step.